Investigation of Thermopower Waves based Energy Sources

A thesis submitted in fulfilment of the requirements for the degree of Doctor of Philosophy

Sumeet Walia

BEng.

School of Electrical and Computer Engineering

RMIT University

Aug 2013

Investigation of Thermopower Waves based Energy Sources

Sumeet Walia

(Doctor of Philosophy)

2013

RMIT University

Declaration

I certify that except where due acknowledgement has been made, the work is that of the author alone; the work has not been submitted previously, in whole or in part, to qualify for any other academic award; the content of this thesis is the result of work which has been carried out since the official commencement date of the approved research program; any editorial work, paid or unpaid, carried out by a third party is acknowledged; and, ethics procedures and guidelines have been followed.

…….

Sumeet Walia

Aug, 2013

Acknowledgements

There have been many people whose help has ensured the completion of this dissertation. First and foremost, I would like to thank my senior supervisor Prof. Kourosh Kalantar-zadeh for his guidance, encouragement and supervision during my PhD candidature. His persistent assistance on my experiments and research papers were of great help. Certainly, his passion for research was a great motivation for me throughout my PhD candidature. I would also like to thank my second supervisor Dr. Sharath Sriram for his valuable ideas and discussions on my research work.

During my PhD, I have had an opportunity to collaborate with several people in interdisciplinary fields, specifically, Professor Michael Strano from Massachusetts Institute of Technology (USA), Associate Professor Rodney Weber from the Australian Defence Force Academy (Canberra) and Dr Serge Zhuiykov from the Commonwealth Scientific Industrial Research Organisation (CSIRO). These people provided fantastic insights and creative ideas for my work.

I would also like to thank current and former researchers and students within the School of Electrical and Computer Engineering: Dr. Madhu Bhaskaran, Dr. Haidong Zheng, Dr. Jian Zhen Ou, Dr, Michael Breedon, Dr. Haneef Yacoob, Dr. Jerry Yu, Mr. Sivacarendran Balendhran, Mr. David Yao, Ms. Pyshar Yi, Mr. Adam Chrimes, Mr. Charan Shah, Mr. Ahmad Sabirin, Mrs. Rozina Abdul Rani, Mr. Majid Nour, Mr. Kyle Berean, Mr. Hussein Nili, Mr. Jos Campbell, Mrs. Rosemalini Ab Kadir for their assistance and for providing an excellent research environment.

My work would not have been possible without access to state-of-the-art equipment and facilities and I would like to thank the people and technical staff who work hard to keep these facilities operational. Specifically, Mr. Yuxun Cao, Mr. Paul Jones of the Microelectronics and Materials Technology Centre, RMIT University and Mr. Philip Francis from the RMIT Microscopy and Microanalysis facility for their assistance and advise throughout the duration of my candidature.

My research would not have been possible without the financial support from the Australian government in the form of the Australian Postgraduate Award (APA). I would also like to

acknowledge the additional financial support from the School of Electrical and Computer Engineering and the Commonwealth Scientific Industrial Research organisation (CSIRO).

I am also very grateful to my parents and my sister for their continuous support and encouragement.

Abstract

Miniaturisation of energy sources is critical for the development of the next generation electronic devices. However, reduction in dimensions of none of the commonly used energy generation technologies including batteries, fuel cells, heat engines and supercapacitors have resulted in efficient and reliable energy sources with high specific powers (power-to-mass ratio). Recently, the new concept of energy generation based on thermopower waves has shown promise for miniaturization. In such sources, exothermic chemical reactions of a reactive fuel are coupled to charge carriers of a thermoelectric (TE) material in its affinity, resulting in an intense thermal wave that self-propagates along the surface of the TE materials. This wave simultaneously entrains charge carriers, resulting in a large current. If the TE material also has a high Seebeck coefficient, a large output voltage and subsequently large specific power output are obtained. As the thermal wave results in a power output, it is called a thermopower wave.

This PhD research aimed at creating thermopower wave based energy sources with large enough output voltages and specific powers viable for driving electronic circuits. Before the commencement of this research, only one type of thermopower wave system based on multi walled carbon nanotube (MWNT) TE cores had been reported. Although the MWNT based thermopower wave system generated specific powers as large as 7 kW/kg, the voltage and oscillation amplitudes generated using that system was too low (in the order of 20-50 mV) for any practical application. The author of this thesis identified that the low Seebeck coefficient of MWNTs (–80 μV/K) was the main reason for such small output voltages. Therefore, to achieve the aims of this PhD research program, the PhD candidate developed a set of innovative research goals as follows: (1) exploring potential core TE materials that exhibit a high Seebeck coefficient (S), electrical conductivity (σ) and moderate thermal conductivity (κ), (2) designing thermopower wave systems by incorporating such core TE materials to generate high amplitude oscillatory voltages, while maintaining a high specific power, and (3) understanding the influence of thermal conductivity of the core material and the substrate on the behaviour of thermopower waves.

In order to realize the aforementioned goals, the author comprehensively reviewed the TE properties of conventional TE materials such as bismuth telluride (Bi_2Te_3), antimony telluride (Sb_2Te_3) as well as TE transition metal oxides (TMOs). Additionally, the author reviewed strategies that can be used for tuning the S, σ and κ of the selected materials. Based on the literature review, the author chose the appropriate core TE materials to develop thermopower wave devices in the thin film geometry. As such, the author implemented his research in four distinct stages such that the work in the earlier stages could provide the platform for the subsequent work.

In the first stage, the author demonstrated thermopower wave systems based on thin films of Bi_2Te_3. Bi_2Te_3 was implemented due to its high S (~ –200 μV/K) and σ (10^5 S/m). As Bi_2Te_3 exhibits a low κ, the author devised a novel strategy by placing it on thermally conductive alumina (Al_2O_3) substrate to compensate for this deficiency. The Bi_2Te_3 based thermopower wave sources generated voltages and oscillations higher (at least 150 %) than MWNT based thermopower wave sources, while maintaining a high specific power in the order of 1 kW/kg. A comprehensive theoretical analysis of the system was carried out and the influence of substrate thermal conductivity was studied by concurrently developing thermopower wave devices based on terracotta substrates that exhibit extremely low thermal conductivity compared to Al_2O_3.

In the second stage, the author implemented a novel combination of p-type Sb_2Te_3 and n-type Bi_2Te_3 as the core TE materials with complimentary semiconducting properties, to show the generation of voltage signals with alternating polarities. For the first time, the phenomenon of thermopower waves was demonstrated using a p-type TE core material (Sb_2Te_3 in this case), in which the majority charge carriers are holes.

Due to fundamental deficiencies of Bi_2Te_3 and Sb_2Te_3, thermopower wave systems based on them could not generate voltages exceeding 200 mV. To make thermopower wave systems practically applicable, larger output voltages are desired, while maintaining a large specific

power. As a result, the author searched for alternatives. A thorough literature review revealed that TMOs can potentially solve this problem as some of them can offer a high S and σ as well as moderate thermal conductivity κ simultaneously.

As such, in the third stage, the author implemented zinc oxide (ZnO), which is a TE TMO, for the first time as the core material in thermopower wave sources. It was shown that both S (~ –500 μV/K at 300 °C) and σ (~ 4×10^3 S/m at 300 °C) of ZnO increased at elevated temperatures. By incorporating ZnO as the core TE material, the PhD candidate obtained voltages and oscillation amplitudes at least 200 % higher than any previously demonstrated thermopower wave systems (in the order of > 500mV), while maintaining a high specific power (~ 0.5 kW/kg).

In the final stage, in order to exceed voltages larger than 1 V, the PhD candidate identified that manganese dioxide (MnO_2), which is another TE TMO, can exhibit exceptionally large S and moderate σ at elevated temperatures. As a result, the author implemented MnO_2 as the core TE material. It was shown that the S of MnO_2 increased dramatically with temperature, exhibiting a peak value of approximately –1900 μV/K at 350 °C. Consequently, voltages large enough (~1.8 V) to drive small electronic circuits were obtained, while maintaining high specific powers in the order of 1 kW/kg. The author also provided novel fundamental insights to explain the increase in Seebeck coefficient of such TE TMOs at elevated temperatures.

In summary, the author believes that this PhD thesis provides the readers with an in-depth analysis of thermopower wave sources based on thin films of conventional TE materials including p-type Sb_2Te_3 and n-type Bi_2Te_3 as well as TE TMOs. The author also believes that this study has contributed significantly towards establishing thermopower wave sources as a viable miniaturised energy generation technology.

List of symbols

S	Seebeck coefficient
σ	electrical conductivity
κ	thermal conductivity
κ_{phonon}	phonon thermal conductivity
$\kappa_{electron}$	electron electrical conductivity
c_v	electronic specific heat per volume
v	electron velocity
v_s	velocity of sound
L_{ph}	phonon mean free path
L	Lorenz number
k_B	Boltzmann constant
h	Planck constant
τ	electron relaxation time
d_w	diameter of wire
a	cross sectional width
n	carrier concentration
e	electronic charge
μ	electron mobility
m^*	carrier effective mass
F_i	Fermi energy
T	temperature
Λ	electron mean free path
c_p	specific heat
ρ	density of fuel
w	concentration of fuel
Q	heat of reaction
A	pre-exponential rate constant

c	wave propagation velocity
E	activation energy
R	universal gas constant
S/V	surface to volume ratio

List of abbreviations

AFM	atomic force microscopy
ALD	atomic layer deposition
ac	alternating current
dc	direct current
CVD	chemical vapour deposition
DOS	density of states
DFT	density functional theory
2DEG	two-dimensional electron gas
EBE	electron beam evaporation
GPR	gas phase reaction
LPR	liquid phase reaction
LED	light emitting diode
MBE	molecular beam epitaxy
MOCVD	metal organic chemical vapour deposition
PLD	pulsed laser deposition
QDSL	quantum dot superlattice
RF	radio frequency
RTA	relaxation time approximation
SEM	scanning electron microscopy
SNW	segmented nanowire
SSR	solid state reaction
SPS	spark plasma sintering
TE	thermoelectric
TMOs	transition metal oxides
TPF	thermoelectric power factor
VDWE	Van der Waals epitaxy
XRD	x-ray diffraction

List of figures

Table of contents

Chapter 1

Introduction

1.1 Motivation

Miniaturisation of energy sources, while maintaining or enhancing their energy discharge capabilities is one of the greatest technological challenges of our time. Researchers envision micro/nano scale systems whose realization is hampered by the lack of sufficiently small power sources. Such miniaturised power sources are extremely vital for future micro/nanoscale advanced electronics, telecommunications systems as well as implantable bio-devices. These future systems include cardioverter-defibrillators the size of apple seeds, implanted unobtrusively in a heart patient to automatically control heart arrhythmias. Also, such small scale energy generation systems could possibly apply localized high energies to muscles or attack cancerous cells *in vivo* with localized pulses of large energies [1]. Another possible application for these puny powerhouses is in "smart dust"— sensors that float in the air, collecting information about temperature, airborne pollutants, and other characteristics [1, 2].

Commonly used energy generation systems include batteries, fuel cells, supercapacitors and heat engines. However, all of them have failed to be miniaturised while maintaining their specific energy (energy to mass ratio) and specific powers (power to mass ratio).

Although there have been recent advances in designing thin films based 3-D Li-ion micro/nano batteries [3], their specific energies and powers are still low (0.4 kWh/kg and 0.3 kW/kg, respectively at 10-15 μm thickness) [4-6]. A reduction in size of such sources gives rise to problems such as ionic flow disruption around electrodes as well as electrical shorts that hamper their ability to perform effectively [7]. Additionally, microlithography

processes have proved cumbersome and expensive to transfer to batteries [8]. Although, a few newer technologies such as small stacked micro fuel cells (~ 200 μm thick) [9], may become promising sources to power future micro/nano scale systems, but despite many years of research and innovation, fuel cells of this size are yet to produce sufficiently large specific powers. Fuel cells designed to work with microscale systems exhibit specific powers less than 0.1 kW/kg [1, 10] [11].

Energy can also be stored and released at high rates using technologies such as supercapacitors. It has been shown that that they can exhibit a specific power as high as 10 kW/kg [12-14]. The major disadvantage of supercapacitors is their high self-discharge rate. This renders them impractical for long-term energy storage as they have to be charged frequently in order to maintain the stored energy.

Energy can also be generated using systems such as heat engines. However, they don't typically scale to the sizes needed for the next generation of technologies, either. To date, scaled-down heat engines with dimensions of the order of 1 mm can only sustain specific powers of only around 0.1 W/kg which is a minute fraction of the 0.2 kW/kg that average lithium-ion batteries achieve [1, 15].

Thus, none of the aforementioned technologies have so far enabled reliable miniaturized power sources with high specific power. It seems that a mere miniaturization of the current energy sources cannot simply solve the problem. Therefore, new technologies at small dimensions can possibly be the answer.

MIT's Strano Laboratory, first demonstrated a new approach to energy storage and power generation. Their experimental system generated power in a way that has no macroscopic analogy. In their work, they developed aligned arrays of multiwalled carbon nanotubes (MWNTs) wrapped in a several-nm-thick cyclotrimethylene-trinitramine (TNA) annular coating (Figure 1.1) [16-18]. By coating the MWNTs with a reactive fuel (TNA in their case)

and ignition at one end sets off a combustion wave along the nanotube was generated. This combustion wave created a strong electric current along their propagation direction and was called a 'thermopower wave' because it transmitted energy from one place to another, by coupling with the nanotube's electrical carriers, setting them in motion along the conducting nanotube. The moving heat source swept the coupled electrical carriers along, an effect which was called electron entrainment. The carriers all moved together in a single direction, creating an electrical current that is extremely large relative to the mass of the system. The propagation of the charge carriers was governed by the thermoelectric (TE) effect—the voltage that results from a temperature differential across a material. The specific power generated by the MWNT based thermopower wave system exceeded the best lithium-ion batteries currently available by as much as 3-4 times [1]. It was also demonstrated that the highest specific powers (~7 kW/kg) were obtained from the thermopower devices with the smallest masses (0.01-0.1 mg) [18].

Thermopower wave generators are remarkable in other ways. For instance, before the ignition, the chemical energy is stored in the chemical bonds of the fuel indefinitely. Therefore, such sources do not suffer from any self-discharge. They also have simple designs (Figure 1.1), which can take advantage of standard industrial micro- and nanofabrication technologies. Another feature of thermopower wave sources, is their ability to generate an oscillatory voltage signal, unlike energy sources such as batteries, fuel cells, supercapacitors and heat engines that are capable of producing only direct current (dc) power [16].

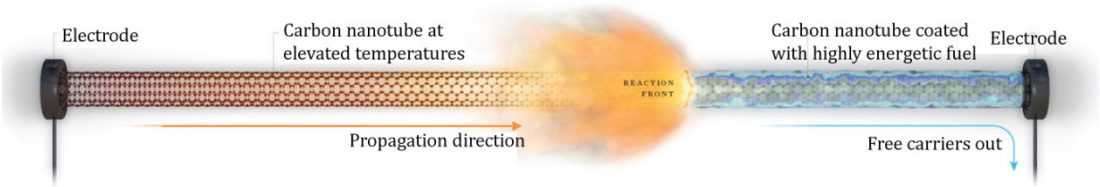

Figure 1.1: Schematic representation of a MWNT based thermopower wave system (not to scale). (Reproduced with permission from Ref [1].)

Although the aforementioned results were encouraging, there is much to be investigated before thermopower wave generators could be developed into a commercially viable power source. The main limitation of the MWNT based thermopower wave sources is the low voltage (generally 30–50 mV) and small oscillation amplitudes (10-15 mV) generated, although voltages as large as 200 mV were reported [17]. Such voltages aren't enough for most applications. Therefore, as with any energy generation system, the main challenge is to maximize the output power from thermopower wave systems. This can be potentially achieved by increasing the output voltage (by using materials with high Seebeck coefficient (S)) and boost the current by decreasing the internal resistance of the core TE materials. Therefore, an ideal TE material for thermopower wave systems should exhibit a high Seebeck coefficient (S) and high electrical conductivity (σ). Contrary to conventional TEs, thermopower wave sources benefit from a moderate to high thermal conductivity (κ) as it facilitates the sustained propagation of the reaction. Hence, thermopower wave sources based on materials exhibiting the aforementioned properties need to be investigated in order to achieve high output voltages enabling such sources to be used as micro/nano energy sources.

1.2 Objectives

The research work for this PhD thesis was based on developing thermopower wave systems in thin film geometries using different core TE materials that exhibit high S and σ and moderate to high κ, so that output voltages large enough for practical applications could be obtained.

In order to solve the challenges of this PhD thesis, the author made informed choices regarding the incorporation of a variety of materials as TE cores in thermopower wave sources. He studied conventional TE materials including bismuth telluride (Bi_2Te_3) and

antimony telluride (Sb_2Te_3) whose TE properties have been widely examined. The PhD candidate then extended his studies to TE transition metal oxides (TMOs) such as zinc oxide (ZnO) and manganese dioxide (MnO_2), which have been much less investigated for their TE properties. The author of this thesis focussed his attention on developing thermopower wave devices based on thin films of the aforementioned materials. The author chose to develop thermopower wave devices in thin film geometries due to its distinct advantages. Thin films allow the deposition of different layers with varying TE and thermal conductivity properties in order to control the propagation of the thermopower waves. Additionally, it allows the alteration of the surface roughness which can be used to increase the amount of solid fuel that can be placed over the TE layer. The compatibility of thin films with current microchips standards, which are all lithographically obtained in two dimensions (2D) is an added advantage.

Bi_2Te_3 and Sb_2Te_3 are the most commonly used TE materials. In order to increase the output voltage from thermopower wave sources, Bi_2Te_3 and Sb_2Te_3, with respective absolute Seebeck coefficients of ~200 μV/K and 160 μV/K, could be used instead of carbon nanotubes (CNTs) that exhibit an absolute *S* of only 80 μV/K [17, 19, 20]. Advantageously, both Bi_2Te_3 and Sb_2Te_3 also have high electrical conductivities of the order of 10^4–10^5 S/m [21-23]. This combination of their high Seebeck coefficient and electrical conductivity made these two materials potential candidates for applications in thermopower wave generators. Bi_2Te_3 and Sb_2Te_3 do not exhibit high thermal conductivities that are required for the successful self-propagation of thermopower waves. As a result, the PhD candidate designed a viable system for the propagation of thermopower waves by placing Bi_2Te_3 and Sb_2Te_3 onto thermally conductive substrates such as alumina (Al_2O_3) to compensate for this deficiency. The role of the highly thermally conducting alumina substrate is to provide a pathway for the thermal conduction across the sample thereby assisting the self-propagation of the thermopower waves.

The incorporation of Bi_2Te_3 and Sb_2Te_3 by the PhD candidate was a critical choice as both these materials exhibit complementary semiconducting properties (Bi_2Te_3 is n-type while Sb_2Te_3 is a p-type TE material). The work conducted by Strano *et al.* at MIT was based only on n-type MWNTs in which electrons were the majority carriers [18], and it was not clear whether the same phenomenon can be observed for p-type core. By demonstrating thermopower wave devices based on n and p-type materials the author showed that the same phenomenon also extended to hole dominant semiconducting TE materials. Additionally, it was shown that a combination of such n and p-type materials resulted in output voltage signals with alternating polarities.

The next approach by the PhD candidate was to investigate TE TMOs such as ZnO and MnO_2. These materials turned out to be potential candidates, as they demonstrated an ideal combination of the required characteristics (a high S, σ and moderate κ) at elevated temperatures. Contrary to Bi_2Te_3 and Sb_2Te_3, such TE TMOs are non-toxic and abundant in nature. Additionally, TMOs are stable at extremes of temperatures which is a desirable feature for the high temperature thermopower wave reaction. As such, they can lead to the development of low cost and safe functional thermopower wave systems.

ZnO a n-type semiconducting oxide was an outstanding candidate as the core TE material for thermopower based energy sources as it exhibited a high Seebeck coefficient (~ –200 μV/K at room temperature) which increased by ~150% at 300 °C which is the temperature regime in which the thermopower wave systems operate. Its high electrical conductivity at such elevated temperatures (of the order of 10^3 S/m), moderate thermal conductivity (15 W/m.K) and good chemical stability were also desirable features for implementation in thermopower wave sources [24-26].

MnO_2 was another TE TMO that was applied as the core material in thermopower wave sources due to its exceptionally high Seebeck coefficient, especially at elevated temperatures (–1900 μV/K at 300 °C). Similar to ZnO, its electrical conductivity was also enhanced as the

temperature increased, thereby resulting in a high thermoelectric power factor (TPF- defined as $S^2\sigma$) of the order of 10^3 μW/m.K^2 [27-29].

In the thermopower wave sources developed by the author of this thesis, the temperature gradient was achieved by the combustion of a reactive fuel. The author used nitrocellulose [$C_6H_8(NO_2)_2O_5$] as the highly reactive solid fuel due to its large enthalpy of reaction (4.75×10^6 J/kg) which helped in achieving a high temperature gradient. Although TNA exhibits a much higher enthalpy compared to nitrocellulose, there are legal restrictions on its use in Australia, therefore it could not be procured for the author's experiments.

Throughout his PhD, the author focussed on increasing the output voltages obtained from thermopower wave sources, while mainitaing a high specific power. The gaps were highlighted by the PhD candidate and as such the primary objectives of this PhD work were targeted towards those gaps as follows:

1. The author of this thesis generated new knowledge by preparing a comprehensive text reviewing the TE properties of conventional TE materials such as Bi_2Te_3 and Sb_2Te_3 as well as TMOs in pure, doped and non-stoichiometric forms. The developed literature was especially important as there is no comprenesive review on the properties of TE TMOs. Based on this analysis, the author made informed choices regarding the core TE materials to be implemented in thermopower wave sources developed during his PhD research.
2. The author of this thesis first demonstrated thermopower wave systems in a thin film geometry using Bi_2Te_3 , a conventional TE material. This was the first demonstration of thermopower wave generation in a thin film geometry using core TE materials other than MWNTs. Theoretical modelling was also carried out in order to assess and predict the behaviour of thermopower waves. The author also examined the influence of various parameters such as the thermal conductivity and the wave propagation velocities on the behaviour of the thermopower waves. It was shown that these systems are able to produce

higher voltage and oscillation amplitudes than previously demonstrated thermopower wave systems using MWNT cores

3. For the first time, the author provided a comparison of thermopower wave systems based on two complementary core TE materials (p-type Sb_2Te_3 and n-type Bi_2Te_3). By implementing a combination of such p and n type core TE materials, an output voltage with alternating polarities can was obtained.
4. For the first time, the author demonstrated the incorporation of TMOs as the core TE materials in thermopower wave sources. TE TMOs such as ZnO and MnO_2 were used due to their high S, σ and moderate κ resulting in the generation of very high oscillatory output voltages compared to any previously developed thermopower wave system. Additionally, the author also provided a fundamental insight into the enhancement of Seebeck coefficient with increasing temperature in such TE TMOs.
5. Furthermore, the author also used the experimental results to assess the influence of the thermal conductivity of the core TE materials and the substrates to assess its impact on the wave propagation velocities and the oscillatory behaviour of the voltage signals.

1.3 Thesis organisation

This thesis is primarily dedicated to developing thin film based thermopower wave sources using different core TE materials to maximise the voltage output, while maintaining a high specific power. The major sections of this thesis are as follows:

In Chapter 2, the author will provide the literature review of this thesis. The chapter will discuss the theory governing the key TE parameters of S, σ and κ for bulk and low dimensional TE materials. The author will then overview the strategies that are implemented to tune the aforementioned key TE parameters. A detailed discussion of the TE properties of Bi_2Te_3, Sb_2Te_3 and TMOs in pure and doped states will be presented.

In Chapter 3, the author will demonstrate his work on Bi_2Te_3 based thermopower wave sources. In this chapter the author will show thermopower wave generation by coupling the exothermic chemical reaction of nitrocellulose to charge carriers in Bi_2Te_3 films supported by alumina (Al_2O_3) or terracotta (baked natural polysilicate) substrates. Al_2O_3 and terracotta were used as substrates because of their contrasting thermal conductivities which helped to assess the effect of thermal properties of the system on the thermopower waves. It will be shown that devices based on Bi_2Te_3/Al_2O_3 generated self-propagating thermopower waves, which resulted in larger voltages and oscillatory amplitudes (~ 150 %) than the MWNT-based thermopower wave systems. The author will also provide a theoretical analysis to describe the behaviour of thermopower waves for nitrocellulose/Bi_2Te_3/substrate system.

In Chapter 4, the author will present a detailed comparison of thermopower wave sources based on TE cores with complementary semiconducting properties (p-type Sb_2Te_3 and n-type Bi_2Te_3). Such a contrast ensured that the voltage output from these thermopower wave sources, with identical characteristics (one based on Bi_2Te_3 and the other based on Sb_2Te_3), produced both positive and negative polarities. The combination of these two resulted in an alternating signal, which is required for practical applications.

In Chapter 5, the author will present the implementation of a TE TMO (ZnO in this case) as the core TE material in thin film thermopower wave sources for the first time. ZnO based thermopower devices were capable of generating significantly larger voltages and oscillation amplitudes than any previously reported systems (>200%). The Seebeck coefficients and the electrical conductivities of the ZnO films at elevated temperatures will also be discussed to assess the behaviour of the system.

In Chapter 6, the author will cover his work on the development of MnO_2 thin films' based thermopower wave sources which resulted in exceptionally high output voltages (~1.8 V). New insights into the fundamentals of the enhancement of Seebeck coefficient in TE TMOs such as ZnO, MnO_2 at elevated temperatures will be presented by the author. A full analysis

of the system by characterizing the device before and after the thermopower wave propagation and also its Seebeck coefficient, electrical conductiviy, output voltage profile, specific power and thermopower wave propagation velocities will also be included.

Finally, in Chapter 7, the author will present concluding remarks and suggest possible future works.

References

[1] M. S. Strano and K. Kalantar-Zadeh, "NanoDynamite," *Spectrum, IEEE,* vol. 48, pp. 44-49, 2011.

[2] B. W. Cook, S. Lanzisera, and K. S. J. Pister, "SoC issues for RF smart dust," *Proceedings of the IEEE,* vol. 94, pp. 1177-1196, 2006.

[3] S. J. Dillon and K. Sun, "Microstructural design considerations for Li-ion battery systems," *Current Opinion in Solid State and Materials Science,* vol. 16, pp. 153-162, 2012.

[4] T. Djenizian, I. Hanzu, and P. Knauth, "Nanostructured negative electrodes based on titania for Li-ion microbatteries," *Journal of Materials Chemistry,* 2011.

[5] N. J. Dudney, "Thin film microbatteries," *Journal of Material Science and Engineering B,* vol. 116, p. 245, 2005.

[6] M. Chen, J. P. Vogt, and G. A. Rincón-Mora, "Design methodology of a hybrid micro-scale fuel cell-thin-film lithium ion source," in *Circuits and Systems, 2007. MWSCAS 2007. 50th Midwest Symposium on*, 2007, pp. 674-677.

[7] S. Sekido, "Solid state micro power sources," *Solid State Ionics,* vol. 9-10, pp. 777-781, 1983.

[8] D. A. Lowy and A. Patrut, "Nonobatteries: Decreasing Size Power Sources for Growing Technologies," *Recent Patents on Nanotechnology,* vol. 2, pp. 208-219, 2008.

[9] R. Hahn, S. Wagner, A. Schmitz, and H. Reichl, "Development of a planar micro fuel cell with thin film and micro patterning technologies," *Journal of Power Sources,* vol. 131, pp. 73-78, 2004.

[10] C. Xie, J. Bostaph, and J. Pavio, "Development of a 2 W direct methanol fuel cell power source," *Journal of Power Sources,* vol. 136, pp. 55-65, 2004.

[11] J. D. Morse, "Micro-fuel cell power sources," *International Journal of Energy Research,* vol. 31, pp. 576-602, 2007.

[12] H. Nakanishi and B. A. Grzybowski, "Supercapacitors Based on Metal Electrodes Prepared from Nanoparticle Mixtures at Room Temperature," *The Journal of Physical Chemistry Letters,* vol. 1, pp. 1428-1431, 2010.

[13] P. Simon and Y. Gogotsi, "Materials for electrochemical capacitors," *Nature Materials,* vol. 7, pp. 845-854, 2008.

[14] L. L. Zhang and X. S. Zhao, "Carbon-based materials as supercapacitor electrodes," *Chemical Society Reviews,* vol. 38, pp. 2520-2531, 2009.

[15] M. Gad-el-Hak, *MEMS: Design and fabrication* vol. 2: CRC press, 2010.

[16] J. T. Abrahamson, W. Choi, N. S. Schonenbach, J. Park, J.-H. Han, M. P. Walsh*, et al.*, "Wavefront Velocity Oscillations of Carbon-Nanotube-Guided Thermopower Waves: Nanoscale Alternating Current Sources," *ACS Nano,* vol. 5, pp. 367-375, 2010.

[17] W. Choi, J. T. Abrahamson, J. M. Strano, and M. S. Strano, "Carbon nanotube-guided thermopower waves," *Materials Today,* vol. 13, pp. 22-33, 2010.

[18] W. Choi, S. Hong, J. T. Abrahamson, J. H. Han, C. Song, N. Nair*, et al.*, "Chemically driven carbon-nanotube-guided thermopower waves," *Nature Materials,* vol. 9, pp. 423-429, 2010.

[19] R. Jin, Z. X. Zhou, D. Mandrus, I. N. Ivanov, G. Eres, J. Y. Howe*, et al.*, "The effect of annealing on the electrical and thermal transport properties of macroscopic bundles of long multi-wall carbon nanotubes," *Physica B-Condensed Matter,* vol. 388, pp. 326-330, 2007.

[20] P. Kim, L. Shi, A. Majumdar, and P. L. McEuen, "Thermal transport measurements of individual multiwalled nanotubes," *Physical Review Letters,* vol. 87, 2001.

[21] L. M. Goncalves, P. Alpuim, G. Min, D. M. Rowe, C. Couto, and J. H. Correia, "Optimization of Bi_2Te_3 and Sb_2Te_3 thin films deposited by co-evaporation on polyimide for thermoelectric applications," *Vacuum,* vol. 82, pp. 1499-1502, 2008.

[22] C. B. Satterthwaite and R. W. Ure, "Electrical and Thermal Properties of Bi_2Te_3," *Physical Review,* vol. 108, p. 1164, 1957.

[23] K. Wojciechowski, E. Godlewska, K. Mars, R. Mania, G. Karpinski, P. Ziolkowski*, et al.*, "Characterization of thermoelectric properties of layers obtained by pulsed magnetron sputtering," *Vacuum,* vol. 82, pp. 1003-1006, 2008.

[24] P. Jood, R. J. Mehta, Y. L. Zhang, G. Peleckis, X. L. Wang, R. W. Siegel*, et al.*, "Al-Doped Zinc Oxide Nanocomposites with Enhanced Thermoelectric Properties," *Nano Letters,* vol. 11, pp. 4337-4342, 2011.

[25] K. H. Kim, S. H. Shim, K. B. Shim, K. Niihara, and J. Hojo, "Microstructural and thermoelectric characteristics of zinc oxide-based thermoelectric materials fabricated using a spark plasma sintering process," *Journal of the American Ceramic Society,* vol. 88, pp. 628-632, 2005.

[26] K. P. Ong, D. J. Singh, and P. Wu, "Analysis of the thermoelectric properties of n-type ZnO," *Physical Review B,* vol. 83, 2011.

[27] P. H. Klose, "Electrical properties of manganese dioxide and manganese sesquioxide," *Journal of the Electrochemical Society,* vol. 117, pp. 854-&, 1970.

[28] F. F. Song, L. M. Wu, and S. Liang, "Giant Seebeck coefficient thermoelectric device of MnO_2 powder," *Nanotechnology,* vol. 23, 2012.

[29] A. Ul Islam, R. Islam, and K. A. Khan, "Studies on the thermoelectric effect in semiconducting MnO_2 thin films," *Journal of Materials Science-Materials in Electronics,* vol. 16, pp. 203-207, 2005.

Chapter 2

Literature review

2.1 Introduction

In the previous chapter, the author highlighted the importance of developing thermopower wave sources as an alternative energy generation technology. Prior to the research conducted by the author of this thesis, only one thermopower wave system that was based on multi walled carbon nanotube (MWNT) thermoelectric (TE) cores had been reported [1]. It was highlighted that the output voltages and oscillation amplitudes from thermopower wave sources needed to increase to establish it as a viable technology. The author chose to develop thermopower wave devices in thin film geometries and highlighted its advantages in the previous chapter. The author also explained that in order to achieve higher voltages with larger oscillations while maintaining a high specific powers, core thermoelectric (TE) materials with high Seebeck coefficients (S), electrical conductivities (σ) and moderate thermal conductivities (κ) are required.

In this chapter, the author will review the TE properties of bismuth telluride (Bi_2Te_3), antimony telluride (Sb_2Te_3) which are conventional TE materials and various transition metal oxides (TMOs) in their intrinsic, various stoichiometry and doped forms. The theory governing the key TE parameters of κ, σ and S for the aforementioned materials in bulk and low dimensional form will be discussed, along with effects of morphological tuning and stoichiometric changes on these parameters. The author of this thesis prepared this important review in order to highlight the key considerations that are required to successfully develop thermopower wave systems for this PhD research and choose the most suitable core TE materials to incorporate in the thermopower wave devices.

This chapter also includes an extended review on the techniques that are implemented to tune the key TE parameters of the materials. A comprehensive text covering the TE

properties of TMOs does not exist in literature. As such, a major portion of the contents of this review was submitted to the Journal Progress in Materials Science.

The author will organise this chapter into 3 major categories. These include the theory governing the key TE parameters (S, σ and κ) for bulk and low dimensional Bi_2Te_3, Sb_2Te_3 and TMOs, strategies to tune their TE parameters and a review of their TE properties.

2.2 Basic principles of thermoelectricity

The fundamental factors that govern TE properties are thermal conductivity (κ), electrical conductivity (σ) and Seebeck coefficient (S). The performance of TE materials is generally assessed by the figures of merit (ZT) defined as $S^2\sigma/\kappa$, and the thermoelectric power factor (TPF) defined as $S^2\sigma$. In this section, we present an overview of the main equations governing the aforementioned TE parameters for bulk three dimensional (3D) and low dimensional (2D, 1D and 0D) structures.

2.2.1 Thermal conductivity

Thermal conductivity is the ability of a material to conduct heat. The main contributors to the thermal conductivity are phonons and charge carriers (electrons and holes). The overall thermal conductivity (κ_{total}) of a material is defined as [2, 3]:

$$\kappa_{total} = \kappa_{phonon} + \kappa_{electron} \quad (1)$$

where, κ_{phonon} is the lattice thermal conductivity due to acoustic phonons travelling through the crystal lattice and $\kappa_{electron}$ is the electronic thermal conductivity due to charge carriers. Phonons and charge carriers can undergo scattering due to other phonons, lattice defects, impurities, electrons, grain boundaries and interfaces [4]. Such scattering then results in changes of thermal conductivity. The fundamentals of κ_{phonon} and $\kappa_{electron}$ for bulk as well as low dimensional materials are discussed next.

2.2.1.1 Bulk (3D) materials

For semiconducting and insulating TE materials, acoustic phonons are the major contributors to $\kappa_{total.}$ However, for highly doped and non-stoichiometric TE materials the electronic thermal conductivity also plays an important role. For bulk materials, the kinetic theory of gases defines the κ_{phonon} and $\kappa_{electron}$ as:

$$\kappa_{phonon} = \frac{1}{3} \upsilon_s C_v L_{ph} \tag{2a}$$

$$\kappa_{electron} = \frac{1}{3} c_v \upsilon \Lambda = L\sigma T \tag{2b}$$

where υ_s is the velocity of sound, C_v is the heat capacity at constant volume, L_{ph} is the phonon mean free path, c_v is the electronic specific heat per volume, v is the electron velocity that can be assumed to be the Fermi velocity v_F, Λ is the electron mean free path, L is the Lorenz number (2.45×10^{-8} $V^2.K^2$), σ is the electrical conductivity, and T is the temperature in Kelvin.

C_v and υ_s are typically temperature independent for $T > 300$K; hence at high temperatures, κ_{phonon} primarily depends on L_{ph} and can be largely attributed to phonon-phonon scattering [5].

On the other hand, $\kappa_{electron}$ depends on the electron mean free path. The Wiedemann-Franz law as shown in Eq. 2b states that $\kappa_{electron}$ is directly proportional to σ and T, so that any variation in $\kappa_{electron}$ affects σ. Hence, the only TE parameter that is independent of the electronic band structure is κ_{phonon}.

In semiconducting materials, phonons are the majority contributors to κ_{total}, making it possible to tune their κ_{total} with a negligible effect on σ. A comprehensive theoretical analysis of κ has been provided elsewhere [3]. In order to improve the performance of TE materials for conventional applications such as cooling and energy scavenging, a reduction in κ_{phonon} is desirable. In theory, the minimum κ_{phonon} is achieved when the mean free path of the phonons

is no more than the interatomic spacing of the constituent atoms [6]. Limiting L_{ph} by confining phonons can help achieve this goal. Such a confinement can be obtained by creating low dimensional materials, which are described next.

2.2.1.2 2D materials

A two-dimensional (2D) quantum well structure consists of a very thin layer of material that is nanometers thick in one dimension and semi-infinitely large in the other two dimensions. 2D quantum well structures are likely to reduce the κ_{total} of TE materials compared to their bulk counterparts because phonons mainly scatter at the interfaces, while the motion of the electrons can be confined parallel to the layers. $\kappa_{electron2D}$ is a strong function of the thickness of layers (W). For 2D quantum well structures, $\kappa_{phonon2D}$ and $\kappa_{electron2D}$ along the x-axis (Figure 2.1 (a)) have been defined as [7, 8]:

$$\kappa_{phonon2D} = \frac{k_B}{2\pi^2 v}\left(\frac{k_B}{h}\right)^3 T^3 \int_0^{\theta/T} \frac{\tau_c \xi^4 e^{\xi}}{(e^{\xi}-1)^2} d\xi \tag{3a}$$

$$\kappa_{electron2D} = \frac{\tau h^2}{4\pi W}\left(\frac{2k_B T}{h^2}\right)^2 \left(\frac{m_y}{m_x}\right)^{1/2} k_B \left(3F_2 - 4\frac{{F_1}^2}{F_0}\right) \tag{3b}$$

where, k_B is the Boltzmann constant, h is the Planck constant, e is the electron charge, $m_{x,y,z}$ are the three components of the effective mass, θ is the Debye temperature, $\xi = h\omega / k_B T$ ($h\omega$ being the phonon energy), T is the absolute temperature, τ is the electron relaxation time and is defined as $\tau = \mu_x m_x / e$ where μ_x is the mobility along the x-axis (Figure 2.1 (a)), v is the velocity of sound, F_i are the Fermi-Dirac functions and τ_c is the combined phonon relaxation time due to all resistive processes (which include boundary scattering, mass difference scattering, scattering at dislocations and Umklapp scattering processes), which is governed by the Matthiessen's rule (see ref. [8] for details). According to Eq. 3a, the theoretical value of $\kappa_{phonon2D}$ is strongly influenced by the phonon-phonon energy, its relaxation time τ_c, which is a function of the quantum well dimension and temperature.

$\kappa_{electron2D}$ depends only on two effective mass components of the electrons as shown in Eq.3b. This is because, unlike phonons, electrons can only move in a 2D motion parallel to the layers due to the quantum confinement. Additionally, a stronger confinement (by decreasing

W) is expected to increase $\kappa_{electron2D}$. However, the result of reducing *W* is generally a decrease in the overall thermal conductivity. This is especially useful in engineering ZT when both Seebeck coefficient and electrical conductivity of the material remain constant. 2D Bi_2Te_3 and Sb_2Te_3 have also been shown to exhibit enhanced TPFs and ZTs [9, 10]. There are also practical examples of employing 2D TMOs such as TiO_2, cobalt oxides and manganese oxides [11] with increased ZTs and will be discussed in their relevant sections. The application of 2D TE materials with increased ZT values [11] has been demonstrated in energy scavenging at elevated temperatures that will also be discussed later.

2.2.1.3 1D materials

Hicks *et al.* developed a theoretical model and predicted that materials in 1D form (such as quantum wires, nanobelts and nanorods) can result in further reduction of $\kappa_{electron}$, compared to bulk and 2D structures [12]. The thermal conductivity of phonons in 1D structures were theoretically modelled by Zou and Balandin [13]. The equations describing κ_{phonon} and $\kappa_{electron}$ for 1D structures are [12, 13]:

$$\kappa_{phonon1D} = \frac{k_B}{2\pi^2 v}\left(\frac{k_B}{h}\right)^3 T^3 \int_0^{\theta/T} \frac{\tau_c \xi^4 e^{\xi}}{(e^{\xi}-1)^2} d\xi \times \left[1 - \frac{24}{\pi} G(\eta(\xi), p)\right] d\xi \qquad (4a)$$

$$\kappa_{electron1D} = \frac{2\tau}{\pi a^2}\left(\frac{2k_B T}{h^2}\right)^{1/2} (m_x)^{-1/2} {k_B}^2 T \left(\frac{5}{2} F_{3/2} - \frac{9{F_{1/2}}^2}{2F_{-1/2}}\right) \qquad (4b)$$

where, *a* is the width of a 1D structure with a square cross section, m_x is the effective mass component in the *x* direction (Figure 2.1 (b)), *v* is the phonon group velocity, *T* is the temperature, θ is the Debye temperature, $\xi = h\omega / k_B T$ ($h\omega$ being the phonon energy), Λ is the phonon mean free path ($\Lambda(\xi) = v(\xi)\tau_c(\xi)$), η is the ratio between the wire width and Λ ($\eta(\xi) = a\pi/\Lambda(\xi)$), *p* is a parameter which characterizes the interface roughness and its effect on the phonon scattering. The value of *p* represents the probability of a phonon undergoing diffusive scattering (refer to [13] for additional details). Other parameters have been defined in Eq. 3a & 3b.

The theoretical ZT calculations using Eqs.4a and 4b for a 1D structure show that it strongly depends on its width. For widths smaller than the thermal de Broglie wavelength of the carriers, the ZT increases significantly with decreasing the width of the 1D structure. 1D structures of Bi_2Te_3 and Sb_2Te_3 have been shown to alter their thermal conductivities [10, 14-20]. TMOs such as ZnO and TiO_2 have also been extensively synthesised in 1D morphologies (nanorods, nanoribons and nanotubes) [21, 22] and the thermal conductivity of such materials are strongly affected by such morphological manipulations [21].

2.2.1.4 0D materials

Unlike 2D or 1D structures, the carriers in 0D structures such as quantum dots are confined in all directions. The transport mechanism in 0D structures is thus different from others, in the sense that unconventional conduction behaviour such as tunnelling is required to maintain its electronic conductivity. Therefore, 0D structures such as quantum dot superlattices (QDSLs) and segmented nanowires (SNWs) were proposed to provide a conduction pathway. As the name suggests, such segmented structures consist of a series of interwoven quantum dots of two different materials (Figure 2.1 (c)). The electronic transport along the wire axis occurs by tunnelling between adjacent quantum dots. Furthermore, due to the wire boundaries and interfaces between the quantum dots, the phonon conduction along the wire axis is impeded, resulting in a reduced lattice thermal conductivity.

The lattice thermal conductivity for 0D structures ($\kappa_{phonon0D}$) such as QDSLs and SNWs comprising of two different materials *A* and *B* is defined as [23, 24]:

$$\frac{L}{\kappa_{phonon0D}} = \frac{L_A}{\kappa_{phononA}} + \frac{L_B}{\kappa_{phononB}} + 4\left(\frac{1}{C_A v_A t_{AB}} + \frac{1}{C_B v_B t_{BA}}\right)\left(1 - \frac{t_{AB} + t_{BA}}{2}\right) + \frac{3}{d_w}\left(\frac{L_A}{C_A v_A \propto_A} + \frac{L_B}{C_B v_B \propto_B}\right) \quad (5)$$

where, $C_{A,B}$ is the heat capacity, $v_{A,B}$ is the sound velocity of the nanodot material, $L_{A,B}$ is the length of the material's segment, t_{AB} and t_{BA} are the average transmissivity of phonons from quantum dot *A* to *B* and vice versa, $\alpha_{A,B}$ is the geometric factor that depends on the aspect ratio (L_A/d_w or L_B/d_w) of the quantum dots in which d_w is the diameter of the wire. The first two terms in Eq.5 account for the intrinsic phonon scattering events, while the third and

fourth terms account for the contribution of the segment interface and the wire boundary scattering processes to the $\kappa_{phonon0D}$. It is evident that the segment length, the choice of materials *A* and *B*, as well as the aspect ratio of the quantum dots play a vital role in determining $\kappa_{phonon0D}$ and hence, the design of the QDSL or SNW structure is the most important factor governing the thermal properties. In order to quantify the electronic contribution of the thermal conductivity ($\kappa_{electron0D}$) in a QDSL or SNW structure, the Kroenig-Penney model is used. This model determines the dispersion relation $E_{n,m}(k)$ for the electrons that move along the axis in the *n,m* sub-band of the wire experiencing a square periodic potential [25], where *k* is a 1D wave vector that describes the energies of these electrons in the square potential [24]. The electronic band structure of each sub-band is highly dependent on the segment length (L_A or L_B), the potential barrier height and the transport effective masses [24].

The constant relaxation time approximation is used for calculating the following fundamental integrals for the conduction band [23]:

$$K_{(\alpha)} = \frac{4\tau}{\pi^2 h^2 {d_w}^2} \sum_{n,m} \int \frac{1}{g_{n,m}(E)} (E_{n,m} - E_F)^{\alpha} \left(-\frac{\delta f}{\delta E}\right) dE \tag{6a}$$

$$g_{n,m}(E) = \frac{2}{\pi} \left(\frac{\delta E_{n,m}}{\delta \kappa}\right)^{-1} \tag{6b}$$

where, α=0,1 or 2, τ is the relaxation time of the carriers, E_F is the Fermi energy, *f(E)* is the Fermi-dirac distribution function and $g_{n,m}(E)$ is the density of states of the *n,m* sub-band, which is defined in Eq. 6b. The electronic component of the lattice thermal conductivity in 0D structures ($\kappa_{electron0D}$) is defined as [23]:

$$\kappa_{electron0D} = \frac{1}{T} \left(K_{(2)} - \frac{K_{(1)}^2}{K_{(0)}}\right)^{1/2} \tag{7}$$

From Eq. 6a, b & 7, it is clear that $\kappa_{electron0D}$ is strongly dependent on the diameter of the SNWs, as well as the carrier relaxation time. However, as discussed before, the electronic contribution towards the thermal conductivity in semiconducting TE materials is generally much lower, compared to the phonon contribution at small diameters. The superlattice

interfaces in 0D structures such as SNWs are expected to enhance the phonon scattering to further suppress the thermal conductivity compared to the bulk form [26].

The above discussion shows that a reduction in the dimensionality of the system can result in a reduced lattice thermal conductivity, due to the phonon mean free paths being limited by the nanostructuring, and consequently increased phonon scattering. This can potentially enhance the efficiency of TE materials for energy scavenging applications, while can increase the performance of temperature sensors, which are based on such structures.

2.2.2 Electrical conductivity

The electrical conductivity of TE materials in bulk and low dimensional form has been extensively studied [27-30]. It has been shown that quantum confinement of charge carriers alters the electronic density of states (DOS). Various nanostructuring and doping techniques can be employed to alter the carrier concentrations by adjusting the bandgap and surface energy in such TE materials [27]. In this section, we will discuss the theoretical equations that govern the electrical conductivity of TE materials in bulk and low dimensional forms.

2.2.2.1 Bulk (3D) materials

For bulk TMOs, the electrical conductivity can be defined in a simplistic form as follows [2, 25]:

$$\sigma = n(E)e\mu(E) = n(E)e^2\frac{\tau(E)}{m^*} \tag{8}$$

where, $n(E)$ is the density of carriers which is a function of the density of states $g(E)$, e is the electronic charge, $\mu(E)$ is the differential carrier mobility, $\tau(E)$ is the relaxation time and m^* is the carrier effective mass.

The m^* of many TE materials such as Bi_2Te_3, Sb_2Te_3 and TE TMOs TiO_2 and layered cobalt oxides is relatively large [2, 31, 32]. Additionally, they also suffer due to short relaxation times [33-35]. As a result, the charge carrier mobilities of many TE materials can be relatively small. The carrier concentrations of bulk TE materials, which is affected by the

thermionic effect, depend on their bandgap and temperature. As a result, the carrier mobilities and concentrations in TE materials can be tuned using various doping and nanostructuring techniques.

2.2.2.2 2D materials

The electrical conductivity of TE materials can be enhanced by fabricating quantum well structures, which result in the quantum confinement of carriers. For a 2D quantum well structure discussed previously in section 2.2.1.2, Hicks *et al.* defined the electrical conductivity (σ_{2D}) as [7]:

$$\sigma_{2D} = \frac{1}{2\pi W}\left(m_x^* m_y^*\right)^{1/2} F_0 e \mu_x \left(\frac{2k_B T}{h^2}\right) \tag{9}$$

where, W is the quantum well width, m_x^* and m_y^* are the effective mass components in the x and y direction (in the plane of the 2D material) respectively, F_0 is the Fermi energy, e is the electron charge, μ_x is the mobility, T is the temperature, k_B is the Boltzmann constant and h is the Planck's constant. In such structures the electrons are confined only to a 2D motion that is parallel to the layers. Eq.9 shows that a reduction in W enhances σ_{2D}. In TMOs, the Fermi level can be adjusted using various doping techniques and methods that control stoichiometry. The Fermi level of TE materials is a strong function of morphology and the temperature [36]. As expected, enhanced electrical conductivities have been demonstrated in 2D morphologies of Bi_2Te_3, Sb_2Te_3 [10] and TMOs such as MoO_3, CoO_2 and ZnO nanobelts [37] [38] [39].

2.2.2.3 1D materials

In morphologies such as one-dimensional nanorods, nanotubes or nanobelts of TE materials, σ is predicted to increase by reducing the cross sectional area of the structure. Such enhancement is mainly due to increased charge carrier mobilities *via* changes in DOS [40, 41]. σ in such 1D structures is defined as [12]:

$$\sigma_{1D} = \frac{1}{\pi a^2}(m_x^*)^{1/2} F_{-1/2} e\mu_x \left(\frac{2k_B T}{h^2}\right)^{1/2} \quad (10)$$

where, a is the width of a 1D structure with a square cross section, m_x^* is the effective mass component in the x direction. Other parameters have been defined in Eq. 9. Additionally, σ can be tuned by changing the Fermi levels, which result in the carrier concentration change as well [42] [43].

Conventional TE materials such as Bi_2Te_3, Sb_2Te_3 and TMOs such as TiO_2 and ZnO are widely synthesised in various 1D morphologies [14-22]. As predicted, σ in such quasi-1D structures is shown to increase compared to the bulk forms [42]. The carrier concentrations in such structures can be adjusted by the use of suitable dopants [42, 44]. There are many good review articles that cover the topic of electrical conductivity in various 1D TE structures [42, 45].

2.2.2.4 0D materials

QDSL or SNW structures, described in section 2.2.1.4, allow for electrical conduction through mechanisms such as tunnelling or hopping. Well-separated discrete energy states of the segments alter the fundamental properties such as DOS and bandgap energy in an alternating manner along the 1D wire [46, 47]. At the same time, the 0D characteristics, and in particular the electrical conductivity, of each quantum dot is maintained by the energy differential of the conduction or valence bands between the two constituent materials that form the wire [24]. The electrical conductivity for such 0D structures is defined as [23, 24]:

$$\sigma_{0D} = e^2 K_{(0)} \quad (11)$$

$K_{(\alpha)}$ is defined in Eq. 6a. It can be seen from Eq.11 that the σ_{0D} is a strong function of the diameter as well as the electronic DOS. An enhanced σ is expected in QDSL and SNW structures with reducing diameters. This is mainly because of the increased carrier relaxation times in such low dimensional structures [47].

2.2.3 Seebeck coefficient

The Seebeck coefficient is the magnitude of the induced voltage divided by the temperature gradient across a material. The Seebeck effect is caused by charge-carrier diffusion and phonon drag. TE materials such as Bi_2Te_3, Sb_2Te_3 and TE TMOs such as TiO_2, ZnO, CoO and MnO_2 exhibit large Seebeck coefficients. Such a high *S* usually arises from high effective masses (m^*) due to electronic correlations [48] or from electron–electron interactions [49]. An enhancement in the *S* can be achieved by altering the DOS through nanostructuring techniques. The theory governing the *S* of bulk and low dimensional TE materials is presented in this section.

2.2.3.1 Bulk (3D) materials

For semiconducting TE materials in bulk form, the simplified Seebeck coefficient can be estimated by the following expression [2]:

$$S_{bulk} = \frac{8m^*\pi^2 k_B^2}{3eh^2} T \left(\frac{\pi}{3n}\right)^{2/3} \tag{12}$$

where, *n* is the carrier concentration, m^* is the carrier effective mass, *e* is the electronic charge, *T* is the temperature, *h* is Planck's constant and k_B is the Boltzmann constant.

Eq.12 shows that a higher m^* results in larger Seebeck coefficients. Bi_2Te_3, Sb_2Te_3 and TMOs usually exhibit high effective carrier masses, which explain the high *S* values observed in these materials. From Eq. 12 it is also predicted that in an increase in *T* also enhances *S*. Enhanced *S* has been observed in Bi_2Te_3, Sb_2Te_3 and many TMOs such as ZnO and MnO_2 at elevated temperatures [50, 51] and will be discussed in their relevant sections.

2.2.3.2 2D materials

2D quantum well structures can result in enhanced *S* of TE TMOs materials due to changes in the Fermi energy of the carriers as well as the electronic DOS. For a 2D quantum well structure, the Seebeck coefficient is defined as [7]:

$$S_{2D} = -\frac{k_B}{e}\left(\frac{2F_1}{F_0} - \chi^*_{2D}\right) \quad (13a)$$

$$\chi^*_{2D} = \frac{1}{k_B T}\left(E_F - \frac{\pi^2 k_B^2 T^2}{12E_F} - \frac{h^2\pi^2}{2m_z^* W^2}\right) \quad (13b)$$

where, k_B is the Boltzmann constant, e is the electron charge, E_F is the Fermi energy, T is the temperature, m_z^* is the component of the effective mass, W is the quantum well width and F_i are Fermi-Dirac functions. χ^*_{2D} is the reduced chemical potential for quasi-2D structures.

The decrease in W of the quantum well is predicted to result in an enhanced S as can be seen from Eq. 13a & b. Additionally, the electron filtering (i.e. only high energy electrons can pass while others are scattered) [52] in such low-dimensional heterostructures is expected to decouple the S and σ, allowing fairly independent control over these properties. The phenomenon of electron filtering is explained in more detail elsewhere [47, 53]. Enhanced S has been demonstrated in 2D structures of Bi_2Te_3 and Sb_2Te_3 [9, 10]. In 2D TMOs, an increase in S has also been experimentally observed. Ohta *et al.* demonstrated dramatic increases in S (up to ~ 5 times) for 2D electron gas (2DEG) systems based on doped TiO_2 which will be discussed in detail in Section 2.4.3.3 [54, 55]. 2D layered cobalt oxides and rhodium oxide also show higher S compared to their bulk forms [56, 57].

2.2.3.3 1D materials

Bi_2Te_3. Sb_2Te_3 and TMOs are widely synthesised in various 1D morphologies [20, 22, 58-60]. Size reduction to a single dimension is expected to enhance S due to the altered DOS. The S for a 1D structure is defined as [12]:

$$S_{1D} = -\frac{k_B}{e}\left(\frac{3F_{1/2}}{F_{-1/2}} - \eta\right) \quad (14)$$

where, F_i is the Fermi Dirac function, e is the electronic charge, k_B is the Boltzmann constant and $\eta = \zeta/k_B T$ is the reduced chemical potential, in which ζ is the chemical potential relative to the lowest bound state. In a 1D structure, S is influenced by the Fermi level of the carriers

(Eq.14), which in turn is strongly influenced by the width of the 1D structure (see ref.[12] for details). Hence, an enhancement of *S* is predicted with decreasing width of the 1D structure. *S* is also a function of the energy derivative of the electronic DOS [61]. As the dimensionality decreases, an increase in Seebeck coefficient is expected because of changes in the DOS due to quantum confinement [7, 8, 12, 62]. As predicted, the *S* of 1D structures of Bi_2Te_3, Sb_2Te_3 and TE TMOs such as ZnO nanowires is shown to increase due to quantum confinement [14-20, 45].

2.2.3.4 0D materials

QDSL and SNW structures as described in section 2.2.1.4 exhibit sharper DOS compared to higher dimensional structures, due to the superlattice-like structure along the wire axis (Figure 2.1 (c)). An electronic structure with sharp maxima in the DOS like this is predicted to be the best for TE materials [46, 63]. Due to their unique electronic band structure and sharp density of states, an enhancement of *S* is expected in QDSLs and SNWs [46].

The Seebeck coefficient of a segmented nanowire is defined as [23, 24]:

$$S_{0D} = -\frac{1}{eT}\left(\frac{K_{(1)}}{K_{(0)}}\right) \tag{15}$$

From Eq. 6 a, b and 15 it is obvious that a sharp maximum in the electronic DOS (Figure 2.1 (d)) will result in a strong increase in the Seebeck coefficient. As the diameter is decreased, the size quantisation effects prevail, resulting in an enhanced *S*. Experimentally, QDSLs and SNWs of materials such as Bi_2Te_3, PbTe have been shown to enhance *S* [23, 64-70] [46]. The increase of *S* in such 0D TMO structures is expected to be pronounced. Even though metal oxide based SNWs have been synthesized [42, 71], there are no reports investigating their Seebeck coefficients. This presents a vast potential for future work in the field of TE TMOs.

From the discussion in this section, it is evident that reducing the dimensionality of TE materials offers opportunities to tune the key TE parameters of κ, σ and *S* independently.

There has been a continuous development in the synthesis techniques of TE materials in various morphologies. This allows flexibility in their fabrication which can be carried out at both large and small scales using liquid and gas phase deposition techniques, allowing tuning of their TE properties at low dimensions to engineer TE materials with high TPFs and figures of merit. Recent review articles comprehensively discuss the latest developments in the synthesis of nanostructures of TE materials [70, 72].

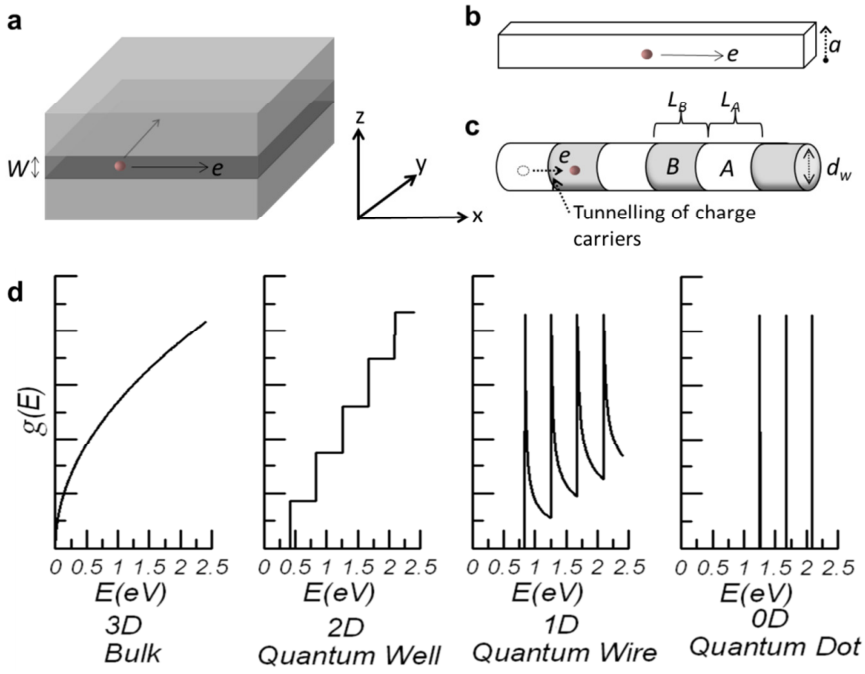

Figure 2.1: (a) A 2D quantum well structure with width W, (b) 1D conductor (nanowire) with a square cross section of width a, (c) a segmented nanowire superlattice of diameter d_w comprising of quantum dots (0D) of alternating materials A and B, with respective segment lengths L_A and L_B. (d) Energy dependence of the electronic DOS in 3D, 2D, 1D and 0D materials. ((c), (d) Reproduced with permission from [24] and [25].)

2.3 Strategies to tune and alter TE parameters

The performance of TE materials is assessed on the basis of the application. Applications of TE materials can be classified into four major categories: (1) cooling and refrigeration, (2) energy scavenging from heat, (3) sensors and (4) thermopower wave sources. For cooling, refrigeration, and energy scavenging, a high TPF along with a low κ is desirable [73, 74]. Sensors generally require high S and low κ, while σ can be either high or low depending on

the type of sensor. Thermopower wave sources require a high TPF and benefit from a high κ [1, 50, 75, 76]. Hence, the tuning of the key TE parameters depends on the application.

Furthermore, a fundamental understanding of the carrier transport processes contributing to the TE effect is required. There are however, many complexities in determining the key quantities in electron and phonon transport both theoretically and experimentally [77-79]. Tuning of transport properties of TE materials, such as reducing electronic thermal conductivity [80] or reducing the bipolar effect [81, 82], is possible. In their recent review papers, Minnich *et al.* [79] and Zebarjadi *et al.* [77] have extensively covered the challenges and strategies for improving our understanding of carrier transport processes.

In this section, the techniques that are commonly used to alter the materials' key TE parameters are briefly discussed.

2.3.1 Optimization using stoichiometry and doping technique

The incorporation of dopants and altering of stoichiometry are widely employed for adjusting the TE parameters of of materials such as Bi_2Te_3 and Sb_2Te_3 and TMOs [83-87]. The type of application plays a crucial role in determining the correct technique in this regard [88]. For cooling, refrigeration, heat scavenging and sensing applications, methods that reduce κ_{phonon} are generally desirable. Crystal disorder in the unit cell can be created by doping or altering stoichiometry of the materials' crystal lattice [30]. Such manipulations change the vibrational properties of the crystal and influence κ_{phonon} [2] or by introducing additional scattering sites for phonons, thereby limiting κ_{phonon} [19, 89-92]. $\kappa_{electron}$ is also affected by changing the stoichiometry and doping level in TE materials. $\kappa_{electron}$ depends on the electrical conductivity of the material (Eq. 2b) and is also a function of the Fermi level and charge carrier concentration, which are directly affected by changes of stoichiometry or incorporation of dopants [3]. In many refrigeration and heat scavenging applications, high electrical conductivity is desired, which generally directly increases $\kappa_{electron}$. However, this is not desirable as it enhances the exchange of heat between two sides. Hence, doping,

compositing and processes altering the oxygen deficiency can be implemented to achieve the desired thermal conductivity. Conversely, in thermopower wave sources, high TPF and κ are desirable. This can be achieved by the use of metallic dopants. Such dopants result in enhanced TPFs in Bi_2Te_3, Sb_2Te_3 and TMOs such as ZnO and CoO_2, which will be discussed in details in section 2.4 [93-105] [106].

After incorporating dopants and altering the stoichiometry, the most challenging issue is the determination of electronic band structures [77]. Theoretical methods such as density functional theory (DFT) can help; however, underestimation of the band gap by DFT calculations generally results in inaccuracy of theoretical predictions of the Seebeck coefficient and the bipolar effect [77]. Many methods have been developed to address this issue, such as the dynamical mean-field theory (DMFT) [107] [108].

The calculation of electron mobility and carrier lifetime is even more challenging. First principles calculations can only be performed on limited supercell sizes and the inclusion of long range potentials is difficult [77]. More importantly, inelastic scattering mechanisms at the elevated operating temperatures renders relaxation time approximations (RTA) calculated from first-principles and DFT mostly invalid [109, 110]. The details of carrier lifetimes in many TE materials are still relatively unknown. Hence, an improved fundamental understanding of the mechanisms governing the formation, stability, and properties of interfaces is required [52].

2.3.2 Substructuring

In engineering TE materials, it is generally desirable to decouple κ_{phonon} and $\kappa_{electron}$. For many refrigeration and heat scavenging applications it is desired to adjust κ_{phonon} without affecting σ (hence $\kappa_{electron}$). Substructuring (or segmentation) approaches are suggested to be efficient for such manipulations. Substructuring relies on a periodic arrangement of layers with different electron and phonon transport characteristics, resulting in a complex material structure with distinct regions providing particular functionalities (Figure 2.2). For many

refrigeration and heat scavenging applications, an ideal TE material would comprise a high mobility semiconductor region entwined with a phonon scattering region that houses disordered structures (dopants and lack of stoichiometry), without affecting the carrier mobilities of the other region [2]. A detailed discussion on the substructuring approach is provided in another review [2]. TE materials occurring as natural superlattices can provide an independent control of transport properties, providing an excellent platform to engineer high performance TE materials. TMOs such as the doped cobalt oxide systems are a classic example of the benefits of substructuring approach, which will be discussed in detail later [111]. Another advantage of TMOs is that they can be fabricated in a variety of well-studied structures and a large number of synthesis techniques to fabricate them in different morphologies and structures have been well-established, making the substructuring approach highly attractive in order to tune their TE parameters according to the desired application.

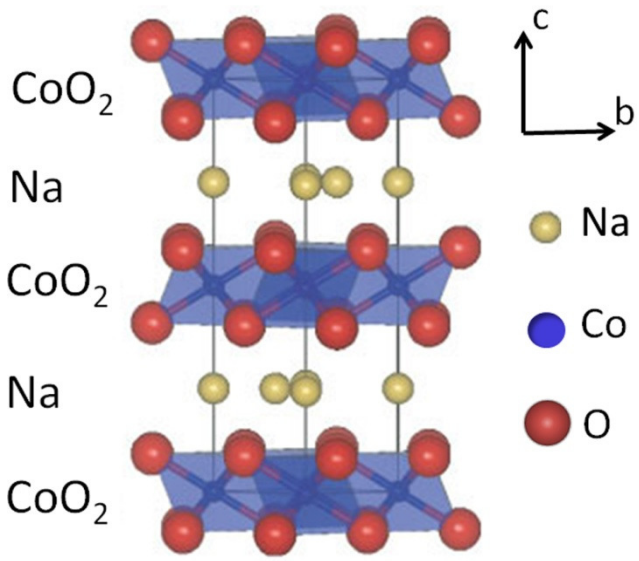

Figure 2.2: Schematic depiction of the substructuring approach in doped cobalt oxide, comprising of ordered CoO_2 layers that are separated by disordered layers (of Na dopant) to achieve a good electrical conductivity and poor phonon conductivity. (Reproduced with permission from [38].)

2.3.3 Nanostructuring

As discussed earlier, the S, σ and κ for conventional 3D crystalline TE materials are interrelated and cannot be controlled independently. Any increase in σ results in an enhanced

$\kappa_{electron}$ (Eq. 2b). Additionally, a change in the Fermi level and carrier concentration affects both $\kappa_{electron}$ and κ_{phonon}.

At the nanometer scale, there are significant changes to the electronics of TE materials (see section 2.2), which allow for alternative techniques to control the S, σ and κ in a relatively independent manner. In nanostructured materials, quantum confinement effects [47] and surface properties become much more important, and result in properties that are changed from those of the bulk forms. The quantum confinement of carriers in nanostructured TE materials is predicted to enhance both their TPF and ZT (see section 2.2) [62]. Additionally, it is well known that nanostructuring of TE materials alters their Fermi level and carrier concentration [27]. Nanostructures also introduce additional scattering mechanisms. If the spacing between the nanoparticles is larger than the electron mean free path (MFP), they will act as an additional source of electron scattering in the host material. If however, the spacing is smaller than the electron MFP, the scattering mechanisms will become much more complex since the leakage of the electron wave into the nanoparticles is no longer negligible [77, 112]. The nanostructuring technique has resulted in enhanced TPFs and ZTs in Bi_2Te_3, Sb_2Te_3 and TMOs such as TiO_2, ZnO, cobalates and manganates which will be discussed in detail in Section 2.4 [54] [101] [113, 114].

In addition to the electronics of TE materials, their phonon propagation properties and as a result κ_{phonon} can be tuned *via* nanostructuring (see section 2.2.1), resulting in enhanced phonon scattering and altered phonon mean free paths [114]. If the dimensions of semiconducting TE materials are smaller than the mean free path of the phonons, but larger than the mean free path of the charge carriers, a reduction in κ_{phonon} can be obtained due to boundary scatterings, without affecting σ. Dressalhaus *et al.* have reviewed the latest developments in nanostructured TE materials such as Bi_2Te_3 and Sb_2Te_3 based materials [70], while Koumoto *et al.* have reviewed the progress in the development of nanostructured TE TMOs [11].

Nanostructuring can be implemented to decrease the lattice thermal conductivity by introducing many interfaces with spacing smaller than the phonon mean free path. Although reducing lattice thermal conductivity through alloying and/or nanostructuring techniques has been the most effective way to improve performance of TE materials for conventional applications, details of phonon transport mechanisms are still not very well understood [79]. Even in bulk form, theoretical and experimental determination of quantities such as phonon mean free path is still a challenge [79]. Phonon transport models based on Callaway model of thermal conductivity [115] usually require adjusting various fitting parameters causing inconsistency in the models fundamental predictions such as phonon's wavelength and mean free path. Calculations of the thermal conductivity and phonon mean free path in TE materials using combined density functional theory (DFT) [116, 117] and molecular dynamics (MD) [118-120] simulations on the other hand are difficult and computationally costly because of the extremely complex crystal structure of alloys and misfit layered oxides. Moreover, the introduction of many interfaces in the material *via* nanostructuring adds more complexity to the problem.

The problem is even more complex in case of electron transport. In case of heavily doped complex TE materials, the standard analysis based on the Boltzmann equation with the assumption that the mean free path is much larger than the de Broglie wavelength leads to inaccurate results [79, 121]. Nanostructuring further complicates the problem as the interfaces introduce complex scattering mechanisms that should be accounted for in theoretical analysis [122]. Therefore, modeling the transport phenomena in bulk and nanostructured TE materials would require more powerful tools such as the non-equilibrium Green's functions with the inclusion of electron wave effects [79].

2.3.4 Compositing

It is suggested that composites can be useful in controlling TE parameters of Bi_2Te_3, Sb_2Te_3 and TMOs, as they can be designed to show high density of the interfaces [123], that can be used for adjusting both phonon and electron scattering. An excellent review article

discussing the impact of the bulk composite engineering approaches on S, σ and κ can be seen in ref. [79]. Composites of materials such as Bi_2Te_3, Sb_2Te_3 and TMOs have resulted in enhanced TPFs, which will be discussed later in the relevant sections [10, 124] [101, 125-129].

2.4 Bi_2Te_3, Sb_2Te_3 and TMOs- TE properties

In this section, the TE properties of Bi_2Te_3, Sb_2Te_3 and TMOs will be discussed. An overview of their crystal structures and their TE properties in pure and doped states will be presented. Additionally, different synthesis methods of these TE materials will be illustrated. For further information regarding the structures, properties and synthesis of Bi_2Te_3, Sb_2Te_3 and TMOs, the readers can refer to comprehensive text books in this field [130-132].

2.4.1 Bi_2Te_3

2.4.1.1 Crystal structure

Bi_2Te_3 is a n-type semiconducting material with a bandgap of ~ 0.20 eV [133]. A detailed description of its electronic band structure exists elsewhere [134, 135]. It exhibits a rhombohedral crystal structure [136] comprising of 5 atoms in a unit cell [137, 138] and is stable up to temperatures of ~ 525 K [82]. The TE properties of Bi_2Te_3 in a pure and doped form have been widely investigated and are discussed next.

2.4.1.2 TE properties of pure Bi_2Te_3

Bi_2Te_3 is the most widely used TE material at room temperature. In a pure bulk form, it exhibits S of approximately –190 μV/K and a high σ of the order of 10^5 S/m [139]. Its thermal conductivity is ~ 1 W/m.K [18]. Its TPF and ZT is of the order of 10^3 μW/m.K^2 and 0.4, respectively, at 298 K (room temperature). Theoretical models suggest that a reduction in dimensionality can result in enhanced TPFs due to significant changes in the density of states (section 2.2) [7, 12]. The TE properties of low dimensional morphologies of Bi_2Te_3 such as nanotubes, nanowires and nanosheets have been extensively investigated [14-19]. As predicted, such nanostructures show enhanced TPFs and ZTs of the order of

2.4×10^3 μW/m.K^2 and 0.96 respectively mainly on account of enhanced S and smaller κ [140-142].

Such high TPFs makes Bi_2Te_3 an attractive candidate for thermopower wave sources. Their low thermal conductivities can be compensated by placing them on thermally conductive substrates such as alumina (Al_2O_3).

2.4.1.3 TE properties of doped and composite Bi_2Te_3

The doping and compositing techniques are commonly utilised to alter S, σ and κ of Bi_2Te_3 in order to enhance the TPFs and ZTs. The incorporation of dopants provides additional scattering sites for phonons, thereby suppressing the phonon thermal conductivity. Doped Bi_2Te_3 has been shown to exhibit TPFs and ZTs of the order of 5×10^3 μW/m.K^2 and 1 respectively [83-86]. The compositing strategy has also been widely employed to adjust the TE parameters of Bi_2Te_3 [82, 128, 143]. Many Bi_2Te_3 composites and superlattice structures have been studied and ZTs as high as 2.4 have been observed for its superlattice with Sb_2Te_3 [10, 124]. Composites of Bi_2Te_3 in low dimensional morphologies such as nanowires and nanotubes have also been reported [144, 145]. Such structures have been shown to consistently exhibit ZTs higher than one [69, 70, 146, 147]. A review article covers the most recent advances in the development of low dimensional TE Bi_2Te_3 [70].

2.4.1.4 Methods of synthesis

Various liquid and vapour phase techniques have been shown to synthesise Bi_2Te_3 in a variety of morphologies. Commonly used liquid phase techniques include hydrothermal [144] and electrochemical methods such as electrodeposition [139, 148].

Vapour phases techniques such as RF magnetron sputtering [149], pulsed laser deposition (PLD) [150], thermal evaporation [151], metal organic chemical vapour deposition (MOCVD) [152], flash evaporation [153] are also used to synthesise Bi_2Te_3.

2.4.2 Sb_2Te_3

2.4.2.1 Crystal structure

Sb_2Te_3 is a p-type semiconductor with a bandgap of ~ 0.28 eV [20]. Similar to Bi_2Te_3, it exhibits a rhombohedral crystal structure with 5 atoms in a unit cell [138]. A detailed description of its electronic band structure is provided elsewhere [135]. Sb_2Te_3 is stable up to temperatures of ~ 550 K. The TE properties of pure and doped Sb_2Te_3 are discussed next.

2.4.2.2 TE properties of pure Sb_2Te_3

Sb_2Te_3 is a widely studied TE material. In a pure bulk form, it exhibits S, σ and κ of 180 μV/K, 10^4 S/m and 2.5 W/m.K respectively [154] [155]. The TPF of bulk Sb_2Te_3 has been reported to be of the order of 10^2 μW/m.K^2 [155]. The TE properties of Sb_2Te_3 has also been investigated for a variety of low dimensional morphologies such as nanowires[20] and nanosheets [156]. As predicted (section 2.2), such nanostructures show enhanced TPFs and ZTs of the order of 10^3 μW/m.K^2 and 0.58 respectively at 420 K [156]. Such an increase is mainly attributed to increased S (~210 μV/K) and lower κ (~0.76 W/m.K) achieved as a result of quantum confinement. Such high TPFs make Sb_2Te_3 a plausible candidate for implementation as the core TE material in thermopower wave sources. Additionally, such a p-type semiconducting material can be used to demonstrate thermopower wave propagation in materials with hole dominant electrical conduction. A thermopower wave system based on such a p-type material has never been developed so far and will be demonstrated by the author of the thesis in chapter 4 of this thesis.

2.4.2.3 TE properties of doped and composite Sb_2Te_3

The doping technique is widely used to alter the TE properties of Sb_2Te_3. The incorporation of dopants can be used to tune the key TE parameters of Sb_2Te_3 in a manner described in section 2.3.1. Several reports on doped Sb_2Te_3 and its TE properties exist in literature [86, 157-162]. Such doped Sb_2Te_3 has been shown to demonstrate TPFs and ZTs of the order of 10^3 μW/m.K^2 and 0.6 respectively. Compositing of Sb_2Te_3 has also been demonstrated to alter its key TE parameters [82, 124, 163]. Several Sb_2Te_3 composites have been shown to exhibit high ZTs [125-128]. The maximum ZT has been reported to be 1.56 at 300 K for

$Bi_{0.52}Sb_{1.48}Te_3$ [145]. As previously mentioned, low dimensional structures such as Bi_2Te_3/Sb_2Te_3 superlattices have been shown to exhibit large ZTs of up to 2.4 [10] [152].

2.4.2.4 Methods of synthesis

Many liquid and vapour phase techniques have been shown to fabricate different morphologies of Sb_2Te_3. Liquid phase techniques such as hydrothermal [164, 165] and electrochemical methods such as electrodeposition [166] [157] have been shown to synthesise thin films, nanoplates and nanobelts of Sb_2Te_3. Vapour phase techniques such as RF magnetron sputtering [167], ALD [168], MOCVD [169], PLD [170] and flash evaporation [153] have also been shown to synthesise different morphologies of Sb_2Te_3. Vapour phase methods are generally employed to prepare Sb_2Te_3 in doped forms as well as composites as they allow an accurate control over deposition conditions, parameters, dopant concentrations and crystallinity.

2.4.3 Titanium oxides – TiO_x

2.4.3.1 Crystal structure

TiO_2 is one of the most investigated metal oxides for a wide variety of photocatalytic, TE, solar cell, biosensing and gas sensing applications. TiO_2 has a bandgap of ~3.2 eV in its intrinsic form [171]. The most common polymorphs of TiO_2 are anatase, rutile and brookite. Rutile and anatase exhibit a tetragonal structure, while brookite is orthorhombic [172]. The transformation with increasing temperature usually follows the sequence: anatase→ brookite→ rutile. Generally in between room temperature and 598 K anatase is the dominant polymorph. Above 625 K, the anatase transforms to brookite [173]. Heating of titania in the temperature range of 873 to 1275 K leads to an alteration of phase stabilities, and it transforms almost completely to rutile. Many reviews on the various crystal structures, size and temperature dependence of the different polymorphs as well as different morphologies of stoichiometric and non-stoichiometric TiO_x exists [172-174].

2.4.3.2 TE properties of stoichiometric TiO_2

TiO_2 can be synthesised in many different morphologies such as spheroidal nanocrystallites, nanoparticles, nanotubes, nanosheets, nanofibers and epitaxial thin films [175]. The room temperature S of crystalline TiO_2 is reported to be approximately −600 μV/K, while σ of the order of 10^3 S/m is observed, resulting in a TPF of 360 μW/m.K^2. The κ at room temperature is ~ 5.8 W/m.K and is reduced with increasing temperature (~ 2.8 W/m.K at 1073 K) [176]. Owing to a moderate σ and high κ, the ZT in pure TiO_2 is low (< 0.025) [176, 177]. However, non-stoichiometric $TiO_{(2-x)}$ has been demonstrated to be promising for TE applications at both cryogenic [178] and elevated temperatures [177]. The TE properties of reduced, oxidized and doped TiO_2 are discussed next.

2.4.3.3 TE properties of non-stoichiometric, doped and composite TiO_x

Non-stoichiometric TiO_x can show fascinating TE properties both at elevated and cryogenic temperatures. Tsuyomoto *et al.* have shown that TiO_x (x=1.94) with an orthorhombic crystal structure, exhibits a peak S of – 518 μV/K and σ of 2×10^3 S/m at ~350 K. They demonstrated that both S and σ increase with temperature, resulting in a TPF of ~540 μW/m.K^2 at 343 K [179]. Interestingly, single crystal rutile TiO_2 reduced to $TiO_{(2-x)}$ *via* annealing in H_2 at elevated temperatures as high as 1050 K shows exceptionally high TPFs at cryogenic temperatures. $TiO_{(2-x)}$ generates enlarged phonon scattering by the defect planes, resulting in low thermal conductivities (0.83 W/m.K). Figure 2.3 (a,b) depict that $TiO_{(2-x)}$ can exhibit an extraordinary S of up to –60,000 μV/K, with TPF and ZT of ~ 1.7×10^4 μW/m.K^2 and 0.1, respectively, at temperatures in the range of 10 K [178]. Another study showed that non-stoichiometric $TiO_{(2-x)}$ with a rutile crystalline structure, formed after annealing and reduction in a carbon environment at 1373 K, demonstrates a TPF of 100 μW/m.K^2 at temperatures of up to 550 K [177]. Obviously, the introduction of oxygen vacancies in the TiO_2 crystal result in enhanced σ due to an increase in carrier concentration (Eq. 8). In contrast, a prolonged oxidation of TiO_2 at elevated temperatures, results in lower σ and S (– 600 to +150 μV/K) and therefore low TPFs and ZTs (<0.1). Additionally, a transition

from n-type to p-type is also observed in the oxidation process, at temperatures around 1300 K [180].

In addition to the change of stoichiometry, the doping technique is usually employed to tune the TE properties in TiO_2. As discussed in section 2.3.1, metallic dopants are useful as they result in enhanced electrical conductivities. Additionally, the doping process creates crystal disorder, which reduces the lattice thermal conductivities. It has been shown that Na doped titanate nanotubes (DTNTs) with a composition such as $Na_{2-x}H_xTi_3O_7$ result in TPFs ranging between 174 - 280 $\mu W/m.K^2$, and a peak ZT of 0.3, at elevated temperatures (745-1032 K) [181]. 2% Nb doped, anatase, n-type TiO_2 epitaxial films show a TPF and ZT of 250 $\mu W/m.K^2$ and 0.25, respectively, at 900 K [182]. Similar observations have also been made by Sheppard *et al.* at elevated temperatures [183, 184].

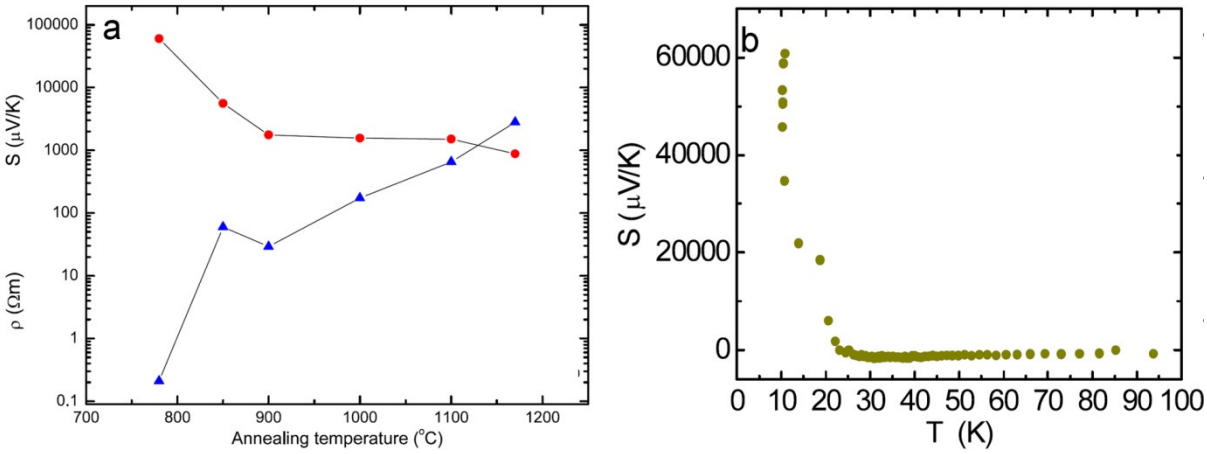

Figure 2.3: (a) Seebeck coefficient (red) and electrical resistivity (blue) of reduced single crystal rutile TiO_x as a function of annealing temperature and (b) Seebeck coefficient as a function of temperature for a sample annealed in H_2 at 1053 K. (Reproduced with permission from [178].)

A TiO_2 composite commonly investigated for its excellent TE properties is strontium titanate ($SrTiO_3$), also known as STO [55, 185, 186]. STO is a perovskite type oxide that exists in an isotropic cubic crystal structure at temperatures above 100 K. Additionally, it shows a strong structural tolerance to substitutional doping. Due to its *d*-band nature, the effective mass of carriers is quite large in STO, resulting in a high *S* (Eq.12). Additionally, STO exhibits a very high melting point (~2350 K), suggesting its stability at high temperatures [11].

In its pure form, STO is essentially an insulator; however, it can be tuned to be semiconducting or metallic by substitutional doping with La^{3+} or Nb^{5+} [55]. The highest TPF and ZT for La and Nb doped STO single crystal has been reported to be 3600 $\mu W/m.K^2$ and 0.1, respectively at room temperature, while the corresponding values at 1000 K, are 865 $\mu W/m.K^2$ and 0.27, respectively (Figure 2.4 (a-e)) [187] [185, 186] [188]. A number of studies on the TE properties of La and Nb doped STO thin films exist [182] [188] [189]. The ZT values are limited primarily due to its high κ (~11.0-3.2 W/m.K in the temperatures of 300-1000 K respectively) [11]. This high κ value can be ascribed to the perovskite type structure of STO, which even in the presence of dopant cations as point defects, lacks effective phonon scattering centers.

Muta *et al.* suggested that a Ca^{2+} substitution at Sr^{2+} sites may result in reduced κ, as it is established that such substitutions result in the introduction of defects that usually lower κ [190]. However, Yamamoto *et al.* have reported that such an approach results in a dramatic reduction of the TPF, which indicates that any further improvement in ZT is almost impossible to achieve in a conventional 3D bulk state of STO [191].

A reduction in the STO dimensionality is a strategy that is predicted to enhance TE properties by offering independent control of the key TE parameters (section 2.2). The fabrication of a two-dimensional electron gas (2DEG) can be useful as it results in a 2D quantum confinement of carriers. Ohta *et al.* utilized a high density 2DEG, which is confined within a layer of STO that has a thickness of a unit cell (0.3905 nm) [54]. Such 2DEG is realized in $SrTiO_3/SrTi_{0.8}Nb_{0.2}O_3$ superlattices and $TiO_2/SrTiO_3$ heterointerfaces. It was shown that in an optimised state, a 2DEG exhibits a massive TPF of 1.0×10^5 $\mu W/m.K^2$. The resultant ZT at room temperature was approximately 2.4 even if a κ value of a bulk single crystal STO is used (12 W/m.K). A recently published review article discusses new developments in STO based thermoelectrics in detail [89].

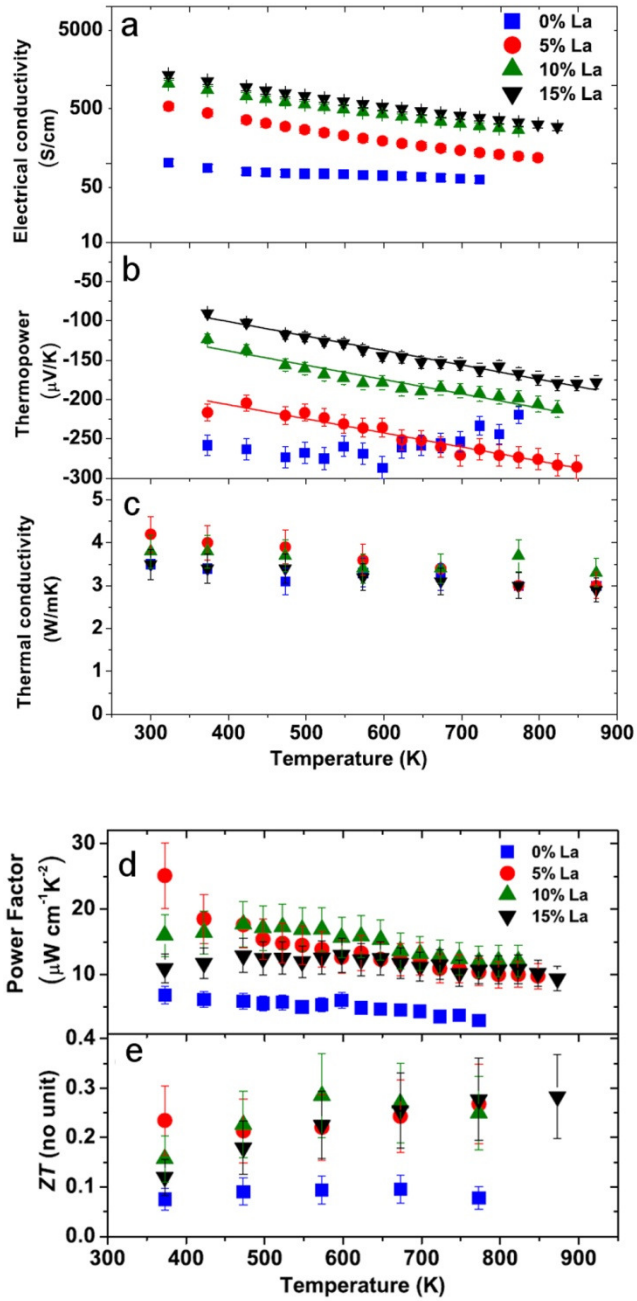

Figure 2.4: (a) Electrical conductivity, (b) Seebeck coefficient, (c) thermal conductivity, (d) TPF and (e) ZT *vs* temperature for different concentrations of La dopant in STO thin films. (Reproduced with permission from [188].)

2.4.3.4 Methods of synthesis

Many different vapour chemical based methods have been used for forming TE TiO_2 materials. Chemical synthesis which involves sol gel hydrolysis, electrochemical methods such as anodization of Ti and hydrothermal synthesis have been commonly used for

producing doped or non-stoichiometric TiO_2, as the concentration of dopants and metal/oxygen ratios can be readily controlled in such methods [175][192] [181].

Vapour deposition techniques including sputtering and pulsed laser deposition (PLD) have also been commonly used for forming highly crystalline TiO_2 with predetermined concentrations of dopants [182]. STO thin films doped with both La and oxygen vacancies have been shown to be synthesized using the PLD technique [188] [193]. PLD can also be used in forming 2DEG STO crystals comprised of superlattices of insulating/ Nb-doped layers of STO to achieve very high TPF of 1.0×10^5 μW/m.K^2 [54, 55].

2.4.4 Manganese oxides – MnO_x

2.4.4.1 Crystal structure

MnO_2, the most common form of manganese oxide, is a small bandgap (~ 1.3 eV), n-type semiconductor and is widely used for electrodes in supercapacitors, electrochemical batteries and microbial fuel cells [194] and as a catalytic material [195]. It exists in a number of structural forms [196, 197]. The most common polymorphs are the α-MnO_2 (psilomelane - monoclinic structure) and β-MnO_2 (pyrolusite - rutile structure) [194]. Other forms known as δ-, γ- and λ-MnO_2 also exist, and differ in the way in which the MnO_6 octahedra are linked [192, 198, 199]. A detailed study of various crystal phases of MnO_2 is presented elsewhere [197].

2.4.4.2 TE properties of stoichiometric MnO_2

β-MnO_2 has been reported to be promising for TE applications at elevated temperatures [51, 196]. Although, the semiconducting properties of α-, β- and γ-MnO_2 have been studied in detail [200], their TE properties have not been widely investigated, and only a limited number of studies exist. It has been reported that bulk and thin film β-MnO_2 exhibit S of approximately –300 μV/K and σ of 10^3 S/m, resulting in a TPF of 90 μW/m.K^2 [201]. Recently, Song *et al.* reported extremely high Seebeck coefficients in β-MnO_2 nanopowder [196]. The S and σ of the MnO_2 thin films have been shown to increase dramatically with temperature [51]. A Seebeck coefficient of approximately –1900 μV/K at a temperature of

623 K has been demonstrated. The σ of the thin films at such elevated temperatures is ~10^3 S/m, resulting in a TPF of 3600 μW/m.K^2. The κ for MnO_2 is reported to be approximately 4 W/m.K [51].

Although the TPF of MnO_2 is high, its ZT is still low. As suggested in section 2.3.3, nanostructuring can be used to tune the TE properties of a material. MnO_2 nanostructures such as nanorods and nanowires have been synthesized *via* various methods [51, 196].

2.4.4.3 TE properties of non-stoichiometric, doped and composite MnO_x

Doping and compositing are good strategies that can be used for increasing TE performance of MnO_x by introducing defects in the crystal structure, thereby impeding the lattice thermal conduction. Polycrystalline, bi-layered $LaSr_2Mn_{2-x}Co_xO_7$ (x<0.2) has been reported to exhibit extremely low TPFs [202]. However, the most commonly reported manganate stoichiometry for TE applications is the perovskite type $CaMnO_3$. It exhibits an orthorhombic symmetry in which each Mn atom is surrounded by six Mn neighbours. It occurs in two anti-ferromagnetic crystal phases: the A-type and G-type, out of which the G-type phase is more stable. The G-type phase exhibits an indirect bandgap of 0.7 eV, which accounts for its perfect semiconducting behavior [203]. The mixed valent, perovskite electron doped manganite $CaMnO_3$ has been shown to be a promising n-type TE material, especially at high temperatures [19]. This perovskite system exhibits S of –350 μV/K and σ of 50 S/m, resulting in a TPF of 6.1 μW/m.K^2, which is very low for TE applications. However, the electrical conductivity of such an oxide can be enhanced by introducing suitable dopants [11]. The manganate may be doped on either site. The most commonly used dopant is ytterbium (Y) on the calcium site and niobium (Nb) on the manganese site. The Y doping is particularly beneficial as it results in a lower κ and has been shown to be the most effective dopant [19, 89-91].

A peak TPF of 300 μW/m.K^2 has been reported in $CaMn_{0.96}Nb_{0.4}O_3$ at 1000 K. The highest reported value of ZT is 0.2 at 1000 K for the stoichiometry $Ca_{1-x}R_xMnO_3$, which is much less than the desired value of at least 1, to make it practically applicable in TE modules [204].

Unfortunately, it has been predicted, using the dynamical mean field theory, that ZT>1 in electron doped $CaMnO_3$ is rather unlikely to be achieved [19].

Koumoto *et al.* used a nanostructuring approach in an effort to enhance the TE performance as predicted in section 2.3.3 [11]. They showed that $Ca_{0.9}Yb_{0.1}MnO_3$ nanoparticles synthesised using gas phase reaction (GPR) show a higher TPF and ZT compared to those synthesised using solid state reaction (SSR) or liquid phase reaction (LPR). This is because GPR generally results in smaller and impurity-free particles due to the nature of the reaction medium. The highest value of the TPF was 190 $\mu W/m.K^2$ at 973 K, for the GPR synthesised nanoparticles, mainly due to lower electrical resistivity. The maximum ZT value was 0.13 at 1073 K for particles synthesised using the GPR, which was approximately 1.5 times higher compared to the one's synthesised using SSR at the same temperature [11]. In this case, there was no significant enhancement in the TPF and ZT after nanostructuring.

2.4.4.4 Methods of synthesis

Similar to other metal oxides, various liquid and gas phase synthesis techniques have been used for forming MnO_2. Electrochemical techniques such as anodization and electrodeposition are some of the commonly used liquid phase methods [205-208]. Chemical techniques such as the sol-gel and hydrothermal are also used to prepare crystalline α and β-MnO_2 [209-211]. Vapour phase techniques such as PLD, atomic layer deposition (ALD) and molecular beam epitaxy (MBE) have also been used to synthesise MnO_2 thin films [212-214].

2.4.5 Tungsten oxides – WO_x

2.4.5.1 Crystal structure

Tungsten oxides (WO_x) are widely studied for sensing, chromic and photocatalytic properties [58] and WO_3 is the most commonly investigated stoichiometry of WO_x. WO_3 is an n-type TMO with a perovskite-like structure. It is well known for its various properties in a non-stoichiometric form, as its lattice can support a significant concentration of oxygen vacancies [58, 215]. Crystals of WO_3 are formed by the corner and edge sharing of WO_6 octahedra.

Such corner sharing results in the following crystal phases: monoclinic I (γ), monoclinic II (ε), triclinic (δ), orthorhombic (β), tetragonal (α) and cubic (although cubic is not a commonly observed phase) [58]. Under different temperature conditions, bulk WO_3 follows the following sequence: monoclinic II (ε-WO_3 , < 230 K) → triclinic (δ-WO_3 , 230 to 290 K) → monoclinic I (γ-WO_3 , 290 K to 603 K) → orthorhombic (β-WO_3 , 603 K to 1013 K) → tetragonal (α-WO_3 , > 1013 K) [216, 217]. At room temperature, γ-WO_3 is the most stable crystal phase [58]. The bandgap of WO_3 ranges between 2.6-3.25 eV depending on the crystal phase and size [58]. Tungsten oxide, which is synthesised or manipulated in liquid media, is very commonly found in hydrated form ($yH_2O.WO_3$).

2.4.5.2 TE properties of stoichiometric WO_3

There are only a few studies that have examined the TE properties of stoichiometric WO_3 and WO_3 hydrates [218, 219]. WO_3 exhibits σ ranging between $10–10^{-2}$ S/m depending on the stoichiometry [220]. Additionally, σ is also influenced by the grain size, film thickness and dopants. Hence, the electrical properties are strongly dependent on the synthesis techniques and conditions [221]. It has been shown that the S of WO_3 hydrates is highly temperature dependent and generally increases linearly with temperatures between sub-zero to 323 K. Beyond 373 K, S decreases exponentially and it also gradually loses the water content at higher temperatures. A peak S with an absolute value of 480 μV/K is observed at 363 K [218]. Due to a low σ, the TPF is poor.

Hutchins *et al.* investigated the TE properties of α-WO_3 films of different thicknesses (100-500 nm) [222]. The S of the n-type WO_3 thin films varies with temperature (Figure 2.5 (a)), with the magnitude decreasing with increasing the film thickness, attaining a maximum absolute value of ~ 780 μV/K at a temperature of 350 K. Figure 2.5 (b) shows that σ of a 100 nm thick α-WO_3 film increases exponentially with temperature. The peak TPF of the α-WO_3 films was reported to be of the order of 1 $\mu W/m.K^2$ [222]. Additionally, Patil *et al.* demonstrated S of 600 μV/K in stoichiometric WO_3 films at a temperature of 473 K [219]. The κ of stoichiometric WO_3 thin films is 1.63 W/m.K [223]. Undoped WO_3 films thus

exhibit a maximum TPF of ~ 4 μW/m.K^2, which is rather too low to be considered for many TE applications except possibly in sensors for measuring temperatures.

2.4.5.3 TE properties of non-stoichiometric and doped WO*x*

Non-stoichiometric tungsten oxides have not shown any improvement in TE performance compared to the stoichiometric counterparts owing to the poor σ [224]. However, using other TMOs for doping WO_3 appears to be an effective approach to manipulate its TE properties. Recently, the TE properties of ZnO doped WO_3 ceramics were investigated [215]. The introduction of ZnO was shown to result in an increased σ, by approximately two orders of magnitude, while causing only a slight drop in *S*. A ZnO doping concentration of 0.5 % was found to be optimal, resulting in a maximum TPF of 1.34 μW/m.K^2 at 973 K, which is similar to the values reported in stoichiometric WO_3 and at least four orders of magnitude higher than that of non-stoichiometric WO_3 [225]. The variation of TPF with temperature for different levels of ZnO doping is shown in Figure 2.5 (c). Aluminium oxide (Al_2O_3) doping has also been shown to enhance σ of WO_3 by a factor of 10^4 [220]. Elevated σ was also observed by adding Co_3O_4, MnO_2, LiO_2 and TiO_2 dopants [226].

To make WO_3 a viable TE TMO, nanostructured WO_3 needs to be investigated for its TE properties. Although, WO_3 nanostructures are widely synthesised and reported for other applications, a detailed investigation of their TE properties has not been carried out.

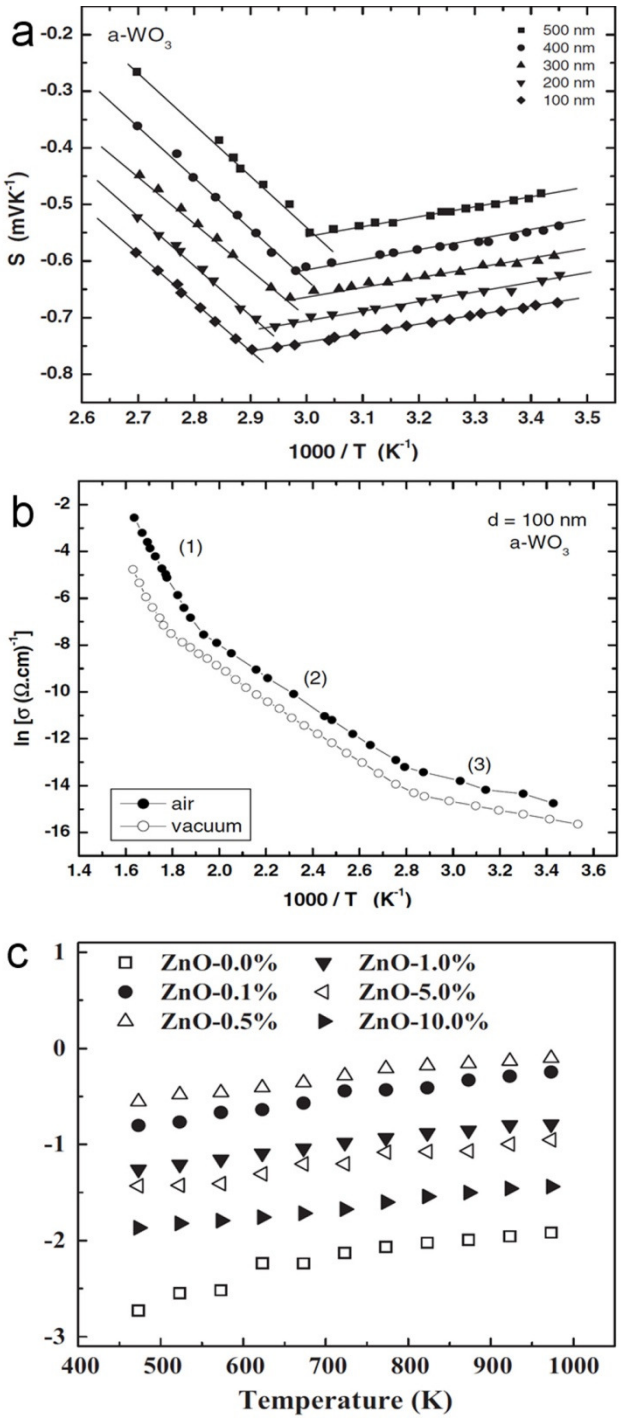

Figure 2.5: (a) Seebeck coefficient, (b) electrical conductivity variation with temperature for α-WO_3 films and (c) TPF obtained for varying ZnO doping concentrations in WO_3 ceramics. (Reproduced with permission from (a), (b) [222] and (c) [215].)

2.4.5.4 Methods of synthesis

Many liquid and vapour phase synthesis methods have been used to synthesise WO_3. Due to a high dependence of σ on the stoichiometry, the parameters of synthesis techniques play important roles in determining the TE properties of WO_3. The commonly used liquid phase

techniques to synthesise crystalline WO_3 are sol-gel, hydrothermal synthesis and electrochemical techniques such as anodization and electrodeposition [227-229] [58, 230, 231]. The most common vapour phase techniques include RF sputtering, PLD, electron beam evaporation and thermal evaporation [58, 232, 233]. A detailed review of synthesis techniques for various WO_3 is presented elsewhere [58].

2.4.6 Zinc oxides – ZnO

2.4.6.1 Crystal structure

ZnO is the most widely investigated TMO for a wide variety of photovoltaic, sensing, optoelectronic, piezoelectric and TE applications [39, 234-237]. ZnO is a direct bandgap binary n-type semiconductor with a bandgap of 3.3 eV at room temperature and substantial ionic character residing at the borderline between a covalent and an ionic semiconductor [238]. It can show either a hexagonal wurtzite, cubic zinc-blende (which are both tetrahedral) or rarely rocksalt structure (which is formed at very high pressures) [39] [238]. In wurtzite structure, every Zn atom is surrounded by four oxygen atoms. In zinc-blende structure, each oxygen atom is surrounded by four Zn atoms in a similar fashion. At ambient temperatures and pressure wurtzite is the stable polymorph and a stable zinc-blende structure is generally obtained when ZnO is grown on cubic substrates [238].

2.4.6.2 TE properties of stoichiometric ZnO

ZnO is considered as a promising high temperature TE material and can be synthesised in a variety of morphologies such as poly- and single crystal ceramics, epitaxial thin films, nanorods, nanobelts, nanorings, hierarchical nanostructures [39].

At ambient temperatures, pure ZnO shows a TPF of ~800 $\mu W/m.K^2$. However, it also exhibits a high κ (~40 W/m.K). The κ of ZnO reduces at higher temperatures (~5 W/m.K at 1000 K). This has been attributed to increased phonon scattering possibly as a result of large and substantially anisotropic thermal expansion of ZnO [239]. Another study showed that sputtered ZnO thin films can exhibit TPFs as high as 1.0×10^3 $\mu W/m.K^2$ [50].

Although it is possible to reach low κ's of 2-3 W/m.K at room temperature for nanograined ZnO ceramics [240], these structures exhibit highly reduced σ and therefore, neither TPF or ZTs improves. It has been postulated that the defects at grain boundaries are the major contributor to the drop in σ [240]. Overall, samples with larger grain sizes have been shown to exhibit higher σ.

As expected, nanostructuring approaches for bulk doped and undoped ZnO have also been shown to reduce κ [101, 240]. A large number of studies on TE properties of pure and doped ZnO have been conducted on polycrystalline ceramics [94-96, 98-100, 102, 103, 241-252]. TE properties of ZnO thin films [253-255] as well as nanostructures [97, 101, 104, 256, 257] have also been targeted in a number of studies. Commonly, nanostructuring results in a significant increase in *S*. As temperature increases, both *S* and σ are enhanced, resulting in higher TPFs and ZTs.

Of more interest however, are the TE properties of doped and co-doped ZnO, where the TPF and ZT can reach values as high as 1500 $\mu W/m.K^2$ and 0.65 respectively, making ZnO a viable candidate for a variety of TE applications.

2.4.6.3 TE properties of non-stoichiometric and doped ZnO

For heat scavenging applications, ZnO is commonly doped by n-type dopants such as Al, Ge, Ni and Ti to achieve improved TE properties. Al is the most common dopant for ZnO [93-104]. Generally, Al doping increases the carrier mobility and reduces the phonon mean free path in the crystal lattice of ZnO, resulting in higher σ and lower κ. ZT has been shown to increase to as high as 0.30 at 1273 K for Al concentrations of ~0.02 and a high TPF of 1500 $\mu W/m.K^2$ has been achieved at such elevated temperatures [93] Beneficial effects of Al doping can also be described in terms of its contribution to the high *c*-axis compression of the ZnO lattice leading to the increase in effective mass (m^*), resulting in enhanced *S* (Eq. 12) [99].

The dependence of TE properties of Al-doped ZnO (AZO), on the grain structure and secondary phases is further highlighted in a study by Jood *et al* [101]. Bulk pellets, obtained

by cold-pressing and sintering the nanocrystals that comprise of ZnO nanograins with $ZnAl_2O_4$ nanoprecipitates, were shown to reduce κ to very low values (1.5 W/m·K at 300 K). These nanocomposites also showed high σ and S, resulting in a significantly high TPF and ZT of 900 $\mu W/m.K^2$ and 0.44 respectively, at 1000 K.

There are also reports of co-doping ZnO with Al and other n-type dopants. Co-doping of Fe, Ni and Sm metals with AZO has not shown significant improvement in TE properties, with the highest TPF and ZT of 675 $\mu W/m.K^2$ and 0.126 respectively, for Ni-co-doped AZO at 1073 K [103]. On the other hand, co-doping of AZO with Ga resulted in significant improvement in ZT. Ga co-doping seemed to increase the solubility of Al in ZnO and strongly reduce the κ value at 2 mol% of Ga. Also, much larger TPFs than those of AZO have been observed in co-doped samples (Figure 2.6). The ZT value $Zn_{0.96}Al_{0.02}Ga_{0.02}O$ reached a maximum of 0.47 at 1000K and 0.65 at 1247 K, a significant enhancement over conventional AZO [98].

A study on co-doped $Zn_{0.97}Al_{0.03-y}Ti_yO$ has shown an enhancement in both σ and S, resulting in TPFs as high as 3.8×10^2 $\mu W/m.K^2$ for $Zn_{0.97}Al_{0.02}Ti_{0.01}O$ at 1073 K [96]. κ and ZT values of these samples have however not been reported. Ga doping has also been reported to improve TE properties of ZnO resulting in ZT values close to the best Al-doped ZnO ceramics [252].

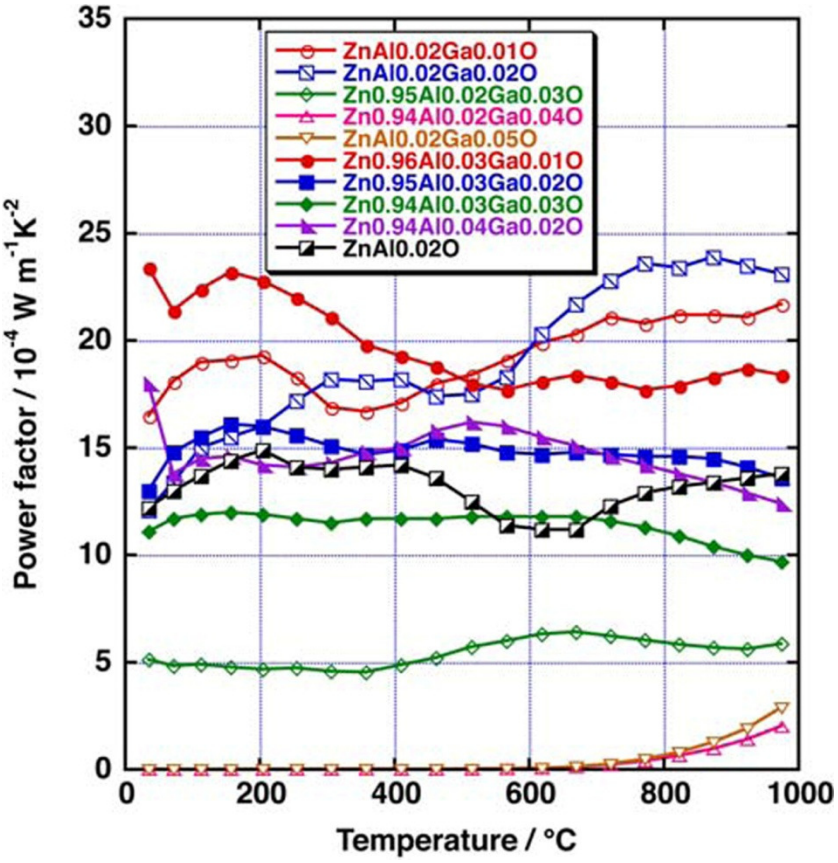

Figure 2.6: Temperature dependence of TPF of $Zn_{1-x-y}Al_xGa_yO$ ceramics. (Reproduced with permission from [98].)

2.4.6.4 Methods of synthesis

ZnO is widely synthesised using various liquid and vapour phase fabrication techniques. It can be synthesised in many different morphologies such as nanowires, nanospikes, nanopillars, nanorods and nanobelts. Over the years, liquid phase fabrication techniques such as hydrolysis, spray pyrolysis, sol-gel and hydrothermal synthesis have been employed to prepare ZnO for various applications [258-260] [261]. Other liquid phase methods to synthesise highly crystalline ZnO nanostructures include electrochemical techniques such as anodization and electrodeposition [262, 263].

Vapour deposition techniques such as RF/DC sputtering, ALD and MBE as well as chemical vapour deposition (CVD) technique and metal organic chemical vapour deposition (MOCVD) have been used to synthesise pure as well as doped ZnO thin films [264-267].

Other techniques such as spark plasma sintering (SPS) and PLD have also been widely used to synthesise densified ZnO in a powdered form [170][268, 269].

2.4.7 Copper oxides – Cu_2O and CuO

2.4.7.1 Crystal structure

Copper oxide occurs in two common phases: cuprous oxide (Cu_2O) and cupric oxide (CuO). Cu_2O (copper (I) oxide) has been commonly used for application in solar cells, catalysts, and sensors [270]. It exhibits a cubic crystal structure with a forbidden direct bandgap of ~1.9-2.2 eV, making it very challenging to study quantum confinement effects or modify its properties [271, 272]. Cu_2O has also been shown to depart from stoichiometry towards excess oxygen, leading to a p-type semiconducting nature and has been one of the most studied materials in semiconducting physics [273]. On the other hand, CuO (copper (II) oxide) belongs to the monoclinic crystal system with a direct bandgap of 1.2-1.5 eV and has been studied for photoconductive applications and is also the basis for several high temperature superconductors [271, 274]. In CuO, each Cu atom is coordinated by 4 oxygen atoms in an approximately square planar configuration. In a pure state and good stoichiometry, CuO behaves almost like an electrical insulator. However, non-stoichiometry leads to important semiconducting characteristics [275].

2.4.7.2 TE properties of stoichiometric copper oxides

A limited number of studies have been carried out on the TE properties of copper oxides in the 1990s. Jeong *et al.* examined the S and σ in uniaxially pressed CuO powder, which was subsequently sintered at different temperatures [276]. The CuO sample sintered at 1273 K in air, showed a peak S of ~650 μV/K between 400 to 500 K. Beyond 500 K, the S dropped rapidly. The corresponding σ as seen from Figure 2.7 (a) was approximately 1 S/m, resulting in a TPF of 0.42 $\mu W/m.K^2$ [276].

It has been shown that single crystal Cu_2O exhibits a high S at elevated temperatures (~1050 μV/K at 923 K) [273]. On the other hand, the S of CuO thin films has been shown to change with varying film thicknesses (340 nm to 620 nm) and exhibits a maximum value of

~ 500 μV/K for ~600 nm thick films (Figure 2.7 (b)) [275]. However, none of these works reported electrical or thermal conductivities. The full TE properties of intrinsic copper oxides are yet to be investigated.

2.4.7.3 TE properties of non-stoichiometric, doped and composite copper oxides

The doping technique has been shown to result in significant effect on the TE properties of copper oxides. Koffyberg *et al.* have demonstrated the TE effect in polycrystalline samples of Li doped CuO [277]. They have shown an average p-type S of 770 μV/K and σ of 6.25 S/m, resulting in a TPF of 3.7 $\mu W/m.K^2$ [277].

It seems that the most commonly investigated copper oxide composite for its TE properties is La_2CuO_4. It exhibits a simple layered structure comprising of 2D CuO_2 planes in a unit cell and is the parent compound for high temperature superconductivity, which is related to the excess oxygen content and the structural change as a result of phase transition [278]. This layered structure makes the anisotropy of conduction very strong. Due to the anisotropic nature of their electrical conduction, such composites are potential TE materials. A detailed overview of its crystal phases is provided elsewhere [279].

For enhancing the TE properties of La_2CuO_4 metallic dopants can be incorporated. In this regard, TE properties of $La_{2-x}R_xCuO_4$ polycrystalline ceramics, where R can be Pr, Y or Nb have been investigated [280]. In this study, it has been shown that the choice of dopants plays a crucial role in determining the TE properties. Figure 2.7 (c) shows the variation of the TPF of $La_{2-x}R_xCuO_4$ with temperature for different dopants. As can be seen, with increasing temperature the TPFs of all composites decrease, eventually becoming stable above 700 K [280]. Samples show S ranging between 200 to 620 μV/K. Amongst them $La_{1.98}Y_{0.02}CuO_4$ ceramics exhibit a high TPF of 10^3 $\mu W/m.K^2$. The maximum ZT was reported to be 0.17 at 330 K, which is around 3 times higher than pure La_2CuO_4 [280].

Studies on TE properties of n-type RE_2CuO_4 oxides, where RE is a rare earth element such as neodymium, samarium or gadolinium, have shown TPFs and ZTs of the order of

10 μW/m.K^2 and 0.005, respectively, at 950 K [281]. The electrical resistivities of such composites show a negative temperature dependence and is at least a magnitude higher than many conventional TE materials. Such RE_2CuO_4 type oxides exhibit a high κ of ~30 W/m.K at 300 K, which drops to ~ 8 W/m.K at 950 K [281], and can potentially be suitable for thermopower wave applications.

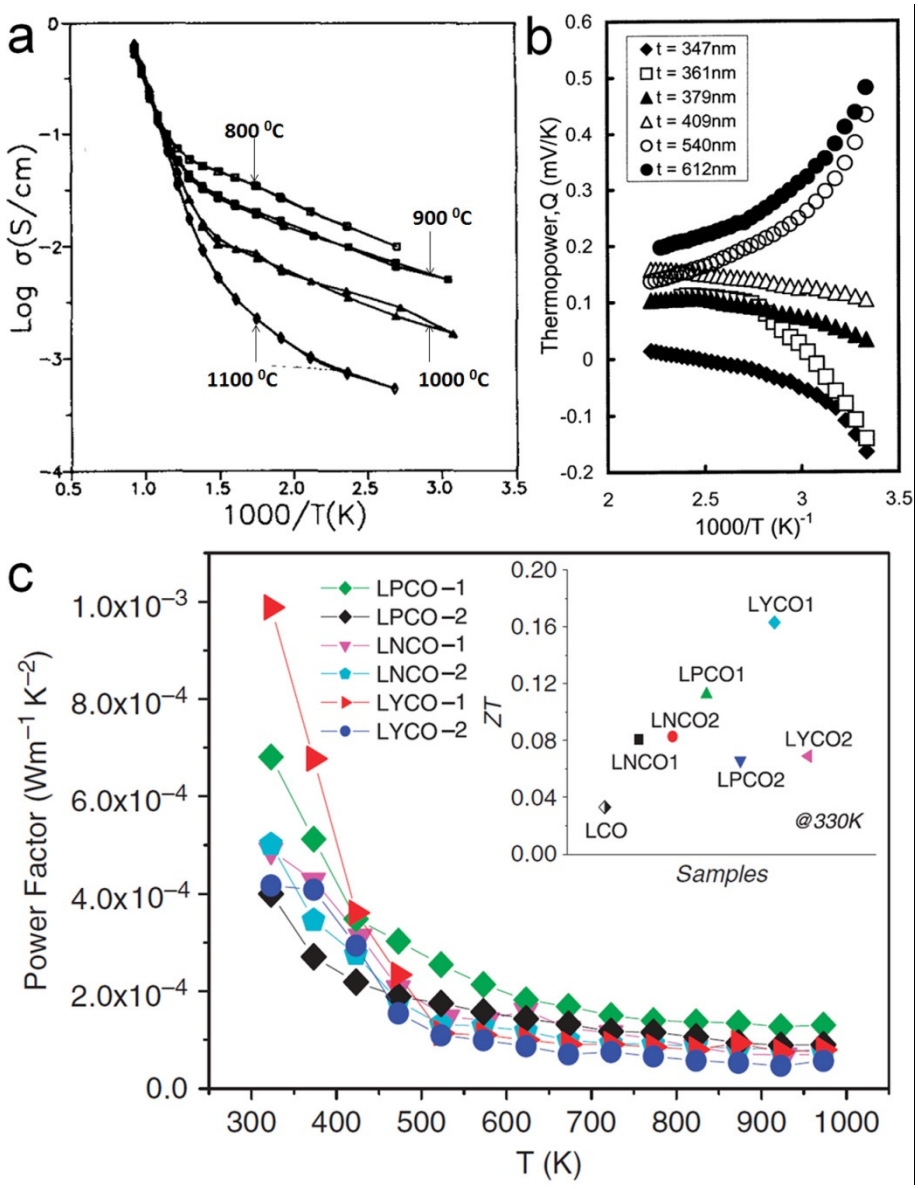

Figure 2.7: (a) Electrical conductivity variation of CuO sintered at different temperatures, (b) Seebeck coefficient variation with temperature for CuO films of different thicknesses and (c) Temperature dependence of TPF for various La_2CuO_4 ceramics, (inset shows ZT values at 330 K) [LNCO (Nb doped La_2CuO_4), LPCO (Pr doped La_2CuO_4), LYCO (Y doped La_2CuO_4)]. (Reproduced with permission from (a) [276], (b) [280] and (c) [275].)

2.4.7.4 Methods of synthesis

Many liquid and vapour phase methods are used for synthesising Cu_2O and CuO. Liquid phase techniques of for the sol-gel [282], hydrothermal [283] and spray pyrolysis [284] have been used for the synthesis of copper oxides. Other liquid phase techniques commonly employed to prepare high purity copper oxides include electrochemical methods such as anodization and electrodeposition [285, 286]. The chemical synthesis methods, especially hydrothermal are much desired for many applications as they are low cost, offer morphology control and facilitate low temperature synthesis and are therefore viable for large scale production [283]. Additionally, they result in a departure from stoichiometry when it is needed due to the introduction of point defects and impurities in the crystal lattice. Vapour phase techniques such as RF sputtering, PLD, various evaporation approaches and MBE have been demonstrated to synthesise crystalline copper oxide thin films at different oxygen contents [274]. Additionally, the CVD technique has also been utilized to synthesise copper oxides [287].

In most copper oxide synthesis methods a mixture of phases like Cu, Cu_2O and CuO is obtained. Post-deposition annealing or deposition at high temperature is usually needed to achieve the desired phase.

2.4.8 Vanadium oxides

2.4.8.1 Crystal structure

Vanadium oxide exists in many phases that include VO, VO_2, V_2O_3 or V_2O_5. However, only V_2O_5 demonstrates TE properties and shows highly anisotropic n-type electrical conduction [288]. It has a direct bandgap of ~2.4 eV and is a promising electrode material for energy storage systems such as Li-ion batteries [289-292] and possesses a high ionic storage capacity because of its layered structure [293]. Over the years, it has also been intensely investigated for its electrochromic properties [294, 295]. Unlike other configurations of vanadium oxide that have been known to exhibit multiple crystal phases, V_2O_5 exists only as an orthorhombic crystal, which is fundamentally comprised of VO_5 pyramids that form alternating double chains along the *b*-axis [296]. A detailed overview of the crystal structures of all phases of vanadium oxide is provided elsewhere [296].

2.4.8.2 TE properties of stoichiometric V_2O_5

Kounavis *et al.* have demonstrated that V_2O_5 gels exhibit a room temperature TPF of 0.3 $\mu W/m.K^2$ [297]. V_2O_5 films synthesised by sol-gel method exhibit *S* of ~ –200 $\mu V/K$, but have very high resistances of the order of 10^3 to 10^4 Ω [293]. Hence, it is evident that the σ of V_2O_5 films requires significant enhancement for practical refrigeration and energy scavenging applications.

2.4.8.3 TE properties of nanostructured, doped and composite V_2O_5

Bahgat *et al.* have synthesized highly oriented nanocrystalline, hydrated vanadium pentoxide, ($V_2O_5.nH_2O$) films of 200 nm thickness. The *S* and σ of such films have been shown to increase with temperature, resulting in a peak TPF of 101.25 $\mu W/m.K^2$ at 480 K (Figure 2.8 (a,b)) [298].

Iwanaga *et al.* have studied the TE properties of V_2O_5 thin films and reported that the introduction of metallic dopants (Na in this case) can improve the TPF values dramatically. This is primarily due to an increase in σ by a factor of up to ~ 10^4. At the same time, the *S* reduces to almost half its value. The direct measurements of TPF have shown an enhanced

TPF of 10 μW/m.K^2 (compared to ~10^{-2} μW/m.K^2 for pure V_2O_5 films) for 35 % Na doping [299].

Liu *et al.* have shown that polyethylene oxide (PEO) intercalated layered V_2O_5 xerogel nanocomposites result in low TPFs [300]. PbO and ZnO based vandates have also been shown to exhibit *S* of up to –400 μV/K at room temperature [301]. However, σ in such composites is low, so they can possibly be used only in temperature sensors.

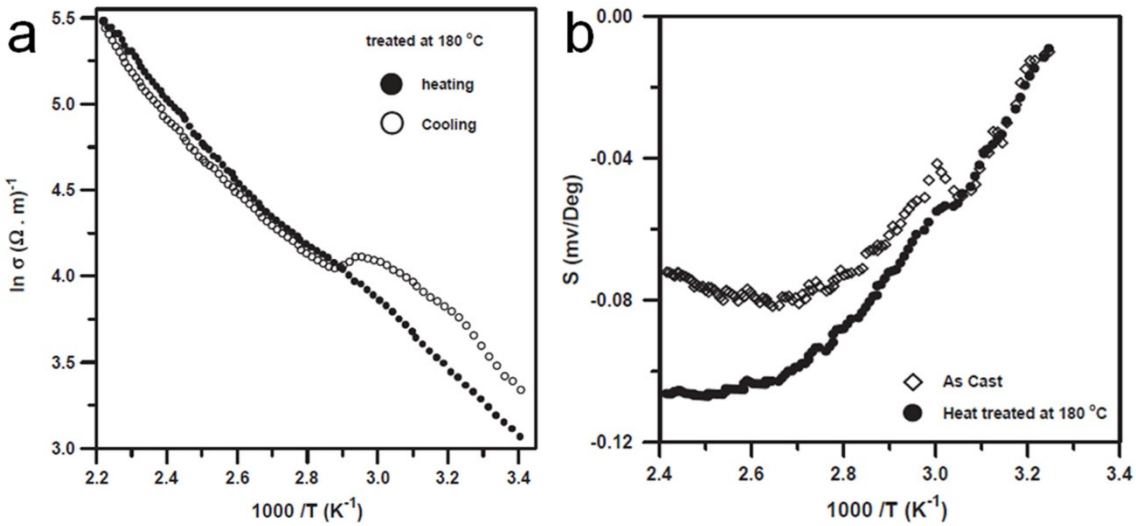

Figure 2.8: Temperature dependence of (a) electrical conductivity, (b) Seebeck coefficient for the as-cast and heat treated films during heating and cooling cycles of hydrated V_2O_5. (Reproduced with permission from [298].)

2.4.8.4 Methods of synthesis

V_2O_5 films can be synthesised using various liquid and vapour phase techniques [302]. Commonly used liquid phase methods for the synthesis of V_2O_5 thin films are the sol-gel and the hydrothermal synthesis technique in which hydrated forms are obtained. The sol-gel synthesised hydrated nanocrystalline V_2O_5 has been shown to exhibit the highest TPF [298]. A melt quench technique has also been employed to dope various concentrations of Na^+ ions into sol-gel solutions and subsequently, thin films of Na intercalated V_2O_5 can be prepared [297, 299]. Hydrothermal synthesis is often utilized to synthesise V_2O_5 nanostructures such as nanotubes and nanowires [303, 304]. Other liquid phase methods include the

electrodeposition and anodization techniques which have also been shown to synthesise V_2O_5 nanostructures [305-307].

Vapour phase techniques such as RF sputtering [308], ALD [309] and PLD [310] have also been shown to deposit crystalline V_2O_5 thin films of various phases. Additionally, the CVD method has also been demonstrated to form highly crystalline V_2O_5 thin films [311]. However, there are few reports on the TE properties of V_2O_5 prepared using vapour deposition techniques.

2.4.9 Cobalt oxides

2.4.9.1 Crystal structure

Cobalt oxide based materials have received great attention for their application in gas sensing, heterogeneous catalysts, intercalation compounds for energy storages, electrochromic devices and more recently as TE materials [312, 313]. Cobalt oxides are generally found in two stable oxide compounds: Co_3O_4 and CoO. Co_3O_4 is the more stable of these two. Both Co_3O_4 and CoO exhibit a cubic lattice. Co_3O_4 is a spinel with the presence of both Co^{2+} and Co^{3+} ions in its lattice. Co_3O_4 exhibits a bandgap in the range of 1.4-1.8 eV, while CoO has a higher energy bandgap of 2.2-2.8 eV. Both Co_3O_4 and CoO are usually non-stoichiometric with excess oxygen, leading to p-type semiconducting behaviours [313].

2.4.9.2 TE properties of stoichiometric cobalt oxides

So far, the TE properties of pure cobalt oxides have not been investigated widely, mainly due to the fact that high resistivities result in a poor TE performance for many energy scavenging applications. It has been shown that in a bulk form CoO exhibits a TPF of ~ 80 $\mu W/m.K^2$ at 1000 K [314]. However, the use of various approaches suggested in section 2.3 such as the addition of metallic dopants, substructuring, and reducing the dimensionality have made doped cobalt oxides the best TMOs for various TE applications.

2.4.9.3 TE properties of non-stoichiometric, doped, composite and nanostructured cobalt oxides

Rare-earth cobalt oxides ($RECoO_3$) with perovskite crystal structures have been studied for their TE properties for energy scavenging and cooling properties and have shown relatively large figure of merits around the room temperature [92]. Their high-temperature performance is however limited.

P-type cobalt oxide composites are among the TE metal oxides with the largest ZT values reported to date. The most promising cobaltite composites for such TE applications are Na_xCoO_2 and $Ca_3Co_4O_9$ [89]. The high ZT values are associated with their crystal structures, which consist of CoO_2^- planes composed of edge-sharing CoO_6 octahedra, and other structural components between these layers. Na_xCoO_2 exhibits a weak monoclininc distortion with respect to the hexagonal unit cell caused by the ordering of a layer of sodium ions in between CoO_2 planes, while $Ca_3Co_4O_9$ comprises of a distorted rock-salt type layer of Ca_2CoO_3, which lowers thermal conductivity by shortening the phonon mean free path (Eq. 2a), and is located between two CdI_2 type CoO_2 layers that are mainly responsible for providing the path for electrical conduction. Hence, these composites are a classic example of substructuring, which is predicted to enhance TE performance (section 2.3.3).

Terasaki *et al.* are the pioneers of layered cobalt oxide base TE materials. They were the first group to demonstrate large TPFs of the order of 5×10^3 $\mu W/m.K^2$ (compared to 4×10^3 $\mu W/m.K^2$ for Bi_2Te_3) and ZT as high as 0.75 in $NaCo_2O_4$ single crystals at room temperature [111]. Figure 2.9 (a,b) show the variation of resistivity and *S* with temperature for the $NaCo_2O_4$ single crystals [111]. Subsequent studies have shown that polycrystalline Na_xCoO_2 exhibits TPF as high as 1.4×10^3 $\mu W/m.K^2$ for $x = 0.85$ at room temperature [315, 316]. For Na_xCoO_2, silver (Ag) doping results in the enhancement of ZT [89]. Other metallic dopants such as Cu [105] and Zn [106] have also been shown to increase the TPFs, while Sr doping results in the improvement of ZT [317]. Polycrystalline Na_xCoO_2 typically shows a peak ZT of ~0.11. However, recently, two-dimensional (2D) and stacked Na_xCoO_2 nanostructures prepared by exfoliation/restacking method were reported to exhibit enhanced

TE properties for energy scavenging applications, as expected from the discussion in section 2.2 [318, 319]. The enhancement was attributed to the reduction of in-plane and cross-plane thermal conductivities in the super-lattice like structures, resulting in enhanced TPFs and ZTs of approximately 500 μW/m.K^2 and 0.4, respectively.

On the other hand, undoped $Ca_3Co_4O_9$ exhibits σ, S, κ, TPF and ZT of 10^4 S/m, 150 μV/K, 2 W/m.K, 225 μW/m.K^2 and 0.3, respectively, at elevated temperatures as large as 1000 K. Although, the room temperature TPFs performance of $Ca_3Co_4O_9$ is inferior to Na_xCoO_2, it is more commonly used in various TE applications due to its superior stability to compositional changes and better performance at high temperatures [89].

Similar to Na_xCoO_2, the addition of Ag as a dopant [320, 321] or a second phase composite [320, 322, 323] has been shown to improve TE properties of $Ca_3Co_4O_9$. A $Ca_{2.7}Ag_{0.3}Co_4O_9$/Ag-10 wt% composite showed an enhanced ZT of 0.5 at 1000 K. Bismuth (Bi) doping has also resulted in enhanced TPFs and reduced κ. However, the ZT of Bi-doped samples, is not as high as those of Ag doped oxides. $Ca_{2.75}Gd_{0.25}Co_4O_9$ ceramics have also been shown to exhibit TPF and ZT of 480 μW/m.K^2 and 0.23 respectively, at 923 K (Figure 2.9 (c)) [324]. It is seen that the $Ca_{2.75}Gd_{0.25}Co_4O_9$ ceramics synthesised using the SPS method exhibit slightly higher TPFs and ZTs compared to hot press (HP) synthesised samples (Figure 2.9 (c)). There are also reports on the doping of $Ca_3Co_4O_9$ with transition metals [325, 326] such as copper and nickel. Gallium addition has been demonstrated to improve TPFs and ZTs [327]. Doping with lanthanum and lanthanide elements has also been studied but the TE enhancements have not been as impressive [89].

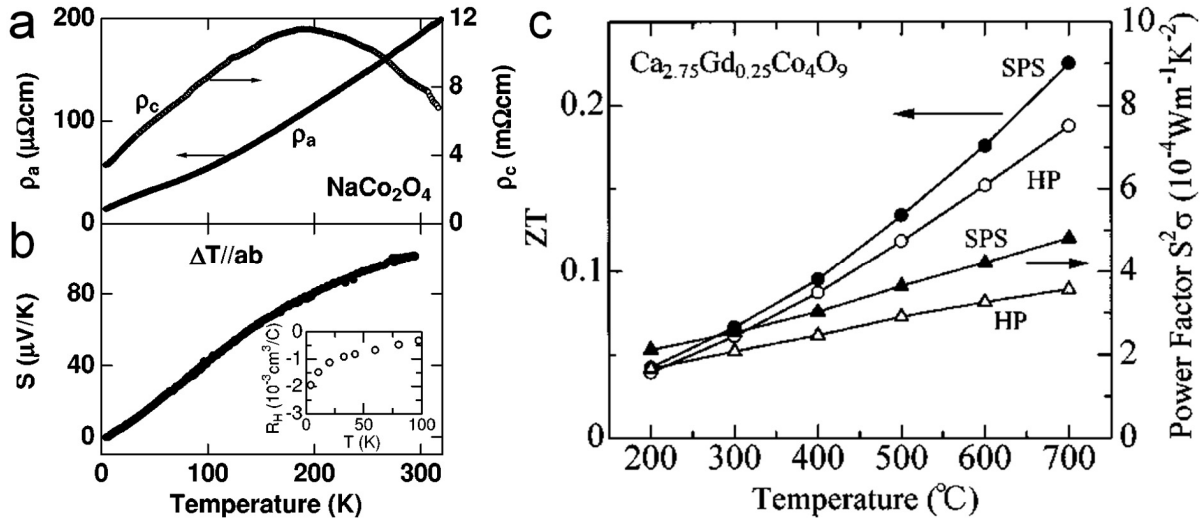

Figure 2.9: (a) Resistivity and (b) Seebeck coefficient variations with temperature for $NaCo_2O_4$ single crystals in plane (ρ_a) and out of plane (ρ_c) and (c) comparison of ZT and TPF for SPS and hot pressed (HP) synthesised $Ca_{2.75}Gd_{0.25}Co_4O_9$ samples. (Reproduced with permission from (a), (b) [111] and (c) [324].)

2.4.9.4 Methods of synthesis

Cobalt oxide can be synthesised using various liquid and vapour phase methods. Epitaxial thin films are generally preferred as they result in highly oriented structures [186, 328, 329]. Liquid phase techniques such as spray pyrolysis, sol-gel and hydrothermal have been employed to fabricate cobalt oxide thin films as well as nanostructures in various morphologies such as nanorods, hierarchical nanocolumns, nanocubes, nanowires and nanorods [312, 330-332]. Although, other liquid phase methods such as electrodeposition have also been employed [333]. An excellent review article summarises various liquid phase synthesis techniques for fabricating cobalt oxide nanostructures [332].

Vapour phase methods that include MBE, PLD and EBE have conventionally been used for the growth of epitaxial $Ca_3Co_4O_9$ films. For Na_xCo_2 films however, the volatility of sodium ions poses difficulties in controlling stoichiometry. The CVD synthesis technique has been shown to be advantageous since it allows accurate tailoring of system composition, structure, morphology *via* suitable choice of a precursor compounds and deposition conditions [312].

2.4.10 Rhodium oxides – RhO_x

2.4.10.1 Crystal structure

Rhodium oxides are generally found in two crystal oxide compounds: RhO_2 and Rh_2O_3. RhO_2 exhibits a tetragonal rutile structure, which transforms into corundum type α-Rh_2O_3 after annealing above 1000 K [334]. Heating above such temperatures results in a transformation to orthorhombic type β-Rh_2O_3 [335]. Rhodium oxides have been investigated primarily for applications in catalytic chemistry, electrochromisms and as a conductive transparent oxide [336-338]. Additionally, misfit-layered rhodium oxides with two-dimensional CdI_2-type crystal structures, analogous to that of cobalt oxides, are among the best candidates for forming p-type TE materials [57]. As in the case for cobalt oxides, their superior thermopower properties originate from CdI_2-type layers, which favour low spin state of Rh^{3+}/ Rh^{4+} with degeneracies of spin and orbital as the key factors [339]. The CdI_2-type layer has a hexagonal symmetry, while the misfit layer is generally a square lattice. However, a layered Bi-Sr-Rh-O system with fluorite-type misfit layers with a trigonal symmetry has also been reported to exhibit similar TE properties [57].

2.4.10.2 TE properties of stoichiometric RhO_x

There are no reports of stoichiometric RhO_x being employed in TE systems. What follows is a brief overview of the studies on rhodium oxide based metal oxide systems that are among the best p-type TE TMOs.

2.4.10.3 TE properties of non-stoichiometric, composite and doped RhO_x

Okada *et al.* initially reported the first synthesized misfit-layered rhodium based metal oxide in polycrystalline form [340]. Samples of $(Bi_{1-x}Pb_x)_{1.8}Sr_2Rh_{1.6}O_y$ (x=0, 0.1, 0.2) and $Bi_{1.8}Ba_2Rh_{1.9}O_y$ were investigated for their TE properties, with the most promising results being 125 μV/K, 213 S/m and 3.3 μW/m.K^2 for S, σ and TPF, respectively, at room temperature (see Figure 2.10 (a-c)). In another study, polycrystalline samples of Co and Rh mixed solutions $Bi_{1.7}Ba_2(Co_{1-z}Rh_z)O_y$ with hexagonal (Co, Rh)O_2 layers have been synthesized in an effort to further alter the TE properties by decreasing κ [341]. Although κ

was reduced in the solid solution, the σ also dropped due to the distortions made by different ionic size elements in (Co, Rh)O_2 layers and therefore, TE performance did not improve.

Kobayashi *et al.* have synthesized rhodium oxide based single crystals in Br-Sr-Rh-O systems with alternately stacked conductive RhO_x and insulating in $(Bi_{0.75}Sr_{0.25})O_{1.5}$ fluorite-type layers [57]. Interestingly, the misfit layer showed a trigonal symmetry with a rhombohedral unit cell, rather than the square-lattice usually observed in other oxides. Room temperature S of up to 63 μV/K and σ of 6.25×10^4 S/m were obtained for $Bi_{0.78}Sr_{0.4}RhO_{3+y}$ crystals. The TPF of such a composite was estimated to be 248 $\mu W/m.K^2$, which is comparable to the values for cobalt oxide based systems [57]. Additionally, single crystals of $Ba_{1.2}Rh_8O_{16}$ have been shown to exhibit κ and ZT values of 3 W/m.K and 0.02 at 200 K, respectively [342].

A recent first principle investigation of layered K_xRhO_2 composites based on ab-initio calculations and Boltzmann transport theory has suggested that the material system has the potential for exceptionally remarkable TE properties [343]. Calculations found large Seebeck coefficients in the temperature range of 0 to 700 K for hydrated phase of K_xRhO_2. Moreover a peak value of ZT = 0.3 is predicted for $K_{7/8}RhO_2$ at 100 K, which is higher than Na_xCoO_2 systems. Even at room temperature, TPFs higher than Na_xCoO_2 are predicted [343].

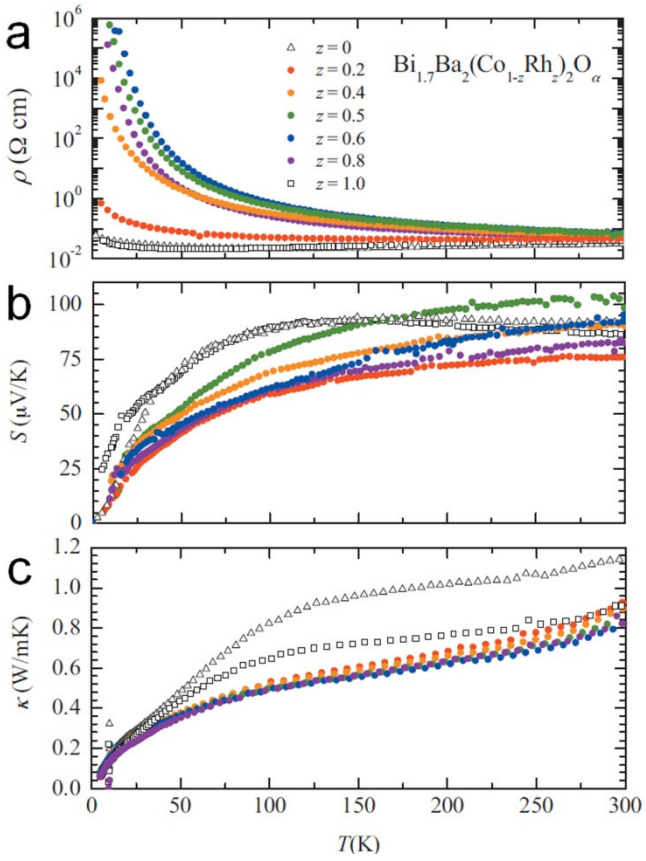

Figure 2.10: Temperature (T) dependence of (a) resistivity (ρ), (b) Seebeck coefficient (S), and (c) thermal conductivity (κ) for $Bi_{1.7}Ba_2(Co_{1-z}Rh_z)O_y$ of varying rhodium concentration (z) (Reproduced with permission from [341].)

2.4.10.4 Methods of synthesis

Many liquid and vapour phase techniques are employed to synthesise rhodium oxides. Amongst the liquid phase synthesis techniques, sol-gel and hydrothermal are the most commonly used methods to synthesise Rh_2O_3 in various morphologies [344-346]. Vapour phase techniques such as RF sputtering, electron beam evaporation (EBE) and the CVD method are used for preparing crystalline rhodium oxide thin films [347]. Misfit, layered rhodium oxide composites such as $(Bi_{1-x}Pb_x)_{1.8}Sr_2Rh_{1.6}O_y$ are synthesised using the SSR technique [340, 341]. It should be considered that RhO_2 is insoluble even in hot aqua regia, hence solution based synthesis techniques are not employed for forming RhO_2. SSR is therefore commonly utilized [348].

2.4.11 Molybdenum oxides – MoO_x

2.4.11.1 Crystal structure

The most common stoichiometries of MoO_x are MoO_2 and MoO_3. However, MoO_3 is the most widely investigated stoichiometry of MoO_x for a variety of applications such as gas sensing, photochromic devices, light emitting diodes (LEDs), batteries and organic solar cells [292, 349-356]. The most common crystal phases of MoO_3 are the thermodynamically stable α-MoO_3 and the metastable β-MoO_3 [357-360]. Bulk α-MoO_3 exhibits an indirect bandgap of ~3 eV and has an orthorhombic crystal structure, that comprises of dual layered planar crystals of distorted MoO_6 octahedra that are held together by weak van der Waals forces. β-MoO_3 on the other hand comprises of MoO_6 octahedra that share corners in all the three dimensions, resulting in a monoclinic 3D structure [356, 361]. At temperatures above 620 K, the β phase transforms into the more stable, layered α-MoO_3 phase [357, 358].

2.4.11.2 TE properties of stoichiometric MoO_x

There is no literature that reports the TE properties of stoichiometric molybdenum oxides, primarily due to their low σ. However, incorporation of various dopants and implementation of MoO_x composites have been shown to result in high TPFs.

2.4.11.3 TE properties of non-stoichiometric, doped and composite MoO_x

Non-stoichiometric and doped molybdenum oxides have been shown to exhibit high TPFs. Xu *et al.* investigated the TE properties of highly reduced molybdenum oxides (RMo_8O_{14}) where R=La, Ce, Nd and Sm. Figure 2.11 (a) shows the TPFs of the four composites at different temperatures. It is seen that $NdMo_8O_{18}$ exhibits a peak TPF and ZT of 177 $\mu W/m.K^2$ and 0.1, respectively, at 1000 K. The κ of the composite has been reported to be 3.19 W/m.K at 322 K, which drops to 2 W/m.K at 1164 K [362, 363]. It is evident that the TPF is certainly large enough to make these molybdenum oxide composites promising for high temperature energy scavenging applications.

It has also been shown that the use of composites can result in enhanced TE performance as suggested in section 2.3.4. A study reports that the TPFs of polyaniline (a typical conductive

polymer) molybdenum trioxide (PANI/MoO_3) composites, is high. A maximum TPF of ~10^2 μW/m.K^2 was observed for 10 wt% of MoO_3 (Figure 2.11 (b)) [364].

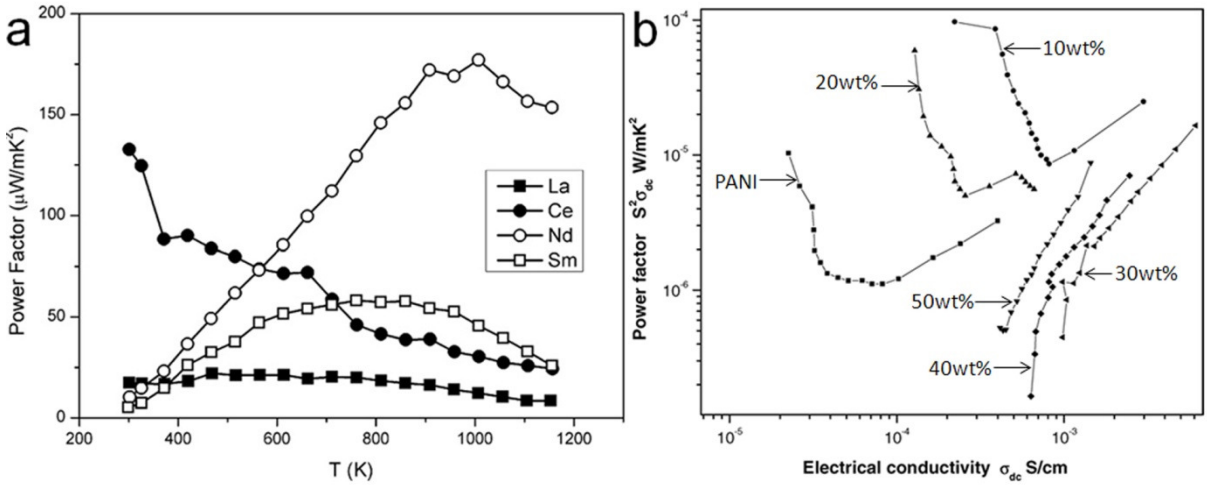

Figure 2.11: (a) Temperature dependence of TPF of RMo_8O_{14} (R:La, Ce, Nd, Sm) pellets, and (b) electrical conductivity *vs* TPF of PANI/MoO_3 composites *vs* MoO_3 concentration in the composite. (Reproduced with permission from (a) [363] and (b) [364].)

2.4.11.4 Methods of synthesis

Similar to other TMOs, MoO_3 can be synthesised using many different liquid and vapour phase techniques. The commonly used liquid phase techniques include sol-gel, hydrothermal, and electrodeposition [358]. Vapour phase techniques such as thermal evaporation, electron beam epitaxy, PLD, RF/DC sputtering, MBE and van der Waal epitaxy (VDWE) have been used for synthesising MoO_3 in various thin film and nanostructured forms. Amongst these, MBE and VDWE have been shown to synthesise ordered, layered MoO_3 structures. Additionally, CVD techniques are also employed to synthesise crystalline MoO_3. A detailed overview of the synthesis techniques to produce various morphologies of MoO_3 is provided elsewhere [356].

2.4.12 Other transition metal oxides and their TE properties

In this section, we will discuss other TMOs, whose TE properties have not been widely investigated. Most of these TMOs are wide bandgap materials, resulting in extremely poor electrical conductivities. However, a few oxides such as iron oxide, cadmium oxide, nickel oxide and doped zirconium oxide exhibit promising TE properties for various applications.

In this section, we provide a brief overview of the small number of reports on the TE properties of the remaining TMOs in their stoichiometric and/or doped states.

2.4.12.1 Iron oxides

There are many known stable iron oxide stoichiometries available. Amongst them, Fe_2O_3 is the iron oxide compound that has been studied for its TE properties. An analysis of a limited number of reports suggests that Fe_2O_3 can potentially be a promising TMO for TE applications at high temperatures as it exhibits high TPFs at room as well as elevated temperatures

Fe_2O_3 thin films have been shown to exhibit peak *S* of 1650 μV/K in the temperature range of 270-290 K. A peak σ of 5.5×10^3 S/m has been reported in the same temperature range, resulting in a high TPF of 1.5×10^4 μW/m.K^2 [365]. Li- doped α-Fe_2O_3 has been reported to exhibit a TPF of 5.5×10^3 μW/m.K^2 at temperature over 800 K for which a κ of 4 W/m.K has been reported [366]. Fe_2O_3-NiO composites have also been shown to exhibit high TPFs at elevated temperatures (900 μW/m.K^2 at 823 K) [367]. Nanostructuring technique has been predicted to enhance TE performance (section 2.3.3). Although, 1D electronic quantum confinement has been demonstrated in α-Fe_2O_3 nanorods, they have not been examined for their TE properties [368].

2.4.12.2 Chromium oxides

There exists many crystalline phases of chromium oxides however, Cr_2O_3 is the most stable bulk form of this TMO [369], with a few recent reports on its TE properties [365, 370].

Cr_2O_3 thin films have been shown to exhibit *S* of 3500-4500 μV/K at room temperature. However, we wish to add that such dramatically high *S* has not been confirmed by any other study so far. A σ of 5.8×10^3 S/m has been reported for stoichiometric Cr_2O_3 [365]. Another study demonstrates a TPF of 3.5 μW/m.K^2 at a temperature of 1300 K in Cr_2O_3 [370].

The effect of TiO_2 addition to Cr_2O_3 on its TE properties has also been investigated. A 2 % TiO_2 addition results in a slightly improved TPF of 5.6 μW/m.K^2 [371].

The TE properties of chromium oxide compounds such as $CuCrO_2$ have also been studied. A maximum TPF and ZT of 236 μW/m.K^2 and 0.1 at 1100 K has been obtained [372]. $CrO_{0.1}N_{0.9}$ polycrystalline samples have also been reported to show a TPF of 80 μW/m.K^2 at 300 K [373].

The above discussion shows that sufficiently large TPFs have been demonstrated for Cr_2O_3 and its compounds. However, further studies are required to establish chromium oxide as a viable TE TMO for many applications.

2.4.12.3 Scandium oxides

Scandium oxide is a wide band gap (6 eV) insulating material, and is therefore not useful for TE conversion applications [171]. Doping can slightly improve electrical conduction; however, it is still insufficient for any meaningful TE energy scavenging applications. Cu doped scandium oxide epitaxial thin films exhibit S and σ of 40 μV/K and 110 S/m, respectively, at room temperature, resulting in extremely low TPF of 0.18 μW/m.K^2 [374].

2.4.12.4 Zirconium oxides

Zirconium oxides are stable at extremely high temperatures and are generally used as ionic conductors at such temperatures. As such these oxides are frequently used in oxygen sensors and fuel cell membranes [375]. ZrO_2 is the most common crystal phase of zirconium oxides which is found in three phases: a cubic phase with a fluorite structure that occurs at temperatures >2850 K and transforms into a tetragonal phase at 2650 K, which on further cooling transforms to a monoclinic phase [376]. It exhibits a wide bandgap of 5 eV [171].

Pure ZrO_2 does not exhibit good TE properties due to its poor σ. However, $ZrO_2/CoSb_3$ nanocomposites show a peak S of 140 μV/K at 700 K for 5 % ZrO_2 and a corresponding σ and κ of 3.75×10^4 S/m and 2.75 W/m.K, respectively [129]. The resulting TPF and ZT is approximately 735 μW/m.K^2 and 0.2, respectively. Therefore, it is obvious that the incorporation of ZrO_2 can potentially be a good approach for obtaining enhanced TE properties for energy scavenging at elevated temperatures.

2.4.12.5 Cadmium oxides

Cadmium oxide is an n-type semiconductor, which exhibits a cubic rocksalt type crystal structure with a direct bandgap of ~2.1 eV at room temperature [377]. A study of highly crystalline CdO thin films have revealed high σ of the order of 10^5 S/m and a peak S of –90 μV/K, resulting in a high TPF of ~800 μW/m.K^2 [378]. Another study has demonstrated a TPF of 100 μW/m.K^2 at 700 K [379]. Other studies on pure as well as doped CdO have revealed similar order of magnitude TPFs [380-382]. Therefore, it is evident that CdO can potentially be a viable n-type TE TMO at elevated temperatures.

2.4.12.6 Nickel oxides

Nickel oxide is a p-type semiconductor that exhibits a cubic rocksalt type crystal structure with a rather large bandgap of 3.6-4.0 eV. Although the σ of stoichiometric NiO is extremely low, Ni^{2+} vacancies are easily formed in undoped NiO, resulting in dramatic improvements in σ [383].

In the past, a few studies have examined TE properties of NiO [384, 385]. One such study has reported S, σ of 101 μV/K and 10^{-2} S/m respectively, at room temperature. The TPF is extremely low primarily due to poor electrical conductivity [385].

The use of metallic dopants such as Li and Na has been shown to result in enhanced TE properties [386][387]. Li doped NiO exhibits TPFs of the order of 10^2 μW/m.K^2 at temperatures exceeding 1000 K, suggesting its suitability as a promising metal oxide for energy scavenging and thermopower wave sources [386].

2.4.12.7 Iridium oxides

IrO_2 is the most stable phase of iridium oxides and exhibits a TiO_2 like rutile crystal structure. The TE properties of pure IrO_2 have not been examined. However, Ca-Ir-O composites have been investigated for their TE properties by Keawprak *et al.* [388-390]. They reported low TPFs and ZTs (~35 μW/m.K^2 and 0.01, respectively).

2.4.12.8 Other TMOs

Other transition metals such as Nb, La, Ac Y, Ta, Re, Hf, Ag and Te are usually employed as dopants in other TE TMOs for tuning their various TE properties in order to achieve higher TPFs and ZTs. However, reports on their stoichiometric TMOs are rare and yet to be fully investigated.

2.5 Summary

In this chapter, the author presented the TE properties of Bi_2Te_3, Sb_2Te_3 as the conventional TE materials and a variety of TE TMOs. In addition, he presented the theory governing the key TE parameters (*S,* σ and κ) and strategies to alter these parameters *via* stoichiometric, dimensional and morphological changes. A major portion of this chapter was submitted for publication consideration in Journal of Progress in Materials Science.

Based on the analysis conducted in this chapter, the author made an informed choice of core TE materials for the thin film thermopower wave devices. These comprised of Bi_2Te_3 and Sb_2Te_3 as the conventional TE materials and zinc oxide (ZnO), manganese dioxide (MnO_2) as TE transition metal oxides TMOs that can provide advantageous properties to the thermopower wave systems. Bi_2Te_3 and Sb_2Te_3 were chosen at the first stage as they exhibit high Seebeck coefficient and electrical conductivities. However, in order to compensate for their low thermal conductivity, the author devised a successful strategy by placed them on thermally conductive Al_2O_3 substrates. The author then chose ZnO and MnO_2 for the development of thermopower wave systems. These two TE TMOs show exceptionally large Seebeck coefficients, high electrical conductivities and moderate thermal conductivities at elevated temperatures. A detailed description of thermopower wave systems based on the aforementioned core TE materials will be provided in Chapters 3, 4, 5 and 6.

In the next chapter, the author will demonstrate thermopower wave sources in a thin film geometry for the first time using Bi_2Te_3 as the core TE material. The exothermic

chemical reactions from a solid fuel will be coupled to charge carriers in Bi_2Te_3 layers to generate voltages and oscillations amplitudes higher than previously demonstrated MWNT based thermopower wave sources, while maintaining a high specific power.

References

[1] W. Choi, S. Hong, J. T. Abrahamson, J. H. Han, C. Song, N. Nair*, et al.*, "Chemically driven carbon-nanotube-guided thermopower waves," *Nature Materials,* vol. 9, pp. 423-429, 2010.

[2] G. J. Snyder and E. S. Toberer, "Complex thermoelectric materials," *Nature Materials,* vol. 7, pp. 105-114, 2008.

[3] T. M. Tritt, *Thermal conductivity: theory, properties, and applications*: Springer, 2005.

[4] A. A. Balandin, "Thermal properties of graphene and nanostructured carbon materials," *Nature Materials,* vol. 10, pp. 569-581, 2011.

[5] R. W. Keyes, "High-temperature thermal conductivity of insulating crystals-Relationship to the melting point," *Physical Review,* vol. 115, pp. 564-567, 1959.

[6] T. M. Tritt, "Thermoelectric Phenomena, Materials, and Applications," in *Annual Review of Materials Research, Vol 41*. vol. 41, D. R. Clarke and P. Fratzl, Eds., ed, 2011, pp. 433-448.

[7] L. D. Hicks and M. S. Dresselhaus, "Effect of quantum-well structures on the thermoelectric figure of merit " *Physical Review B,* vol. 47, pp. 12727-12731, 1993.

[8] A. Balandin and K. L. Wang, "Effect of phonon confinement on the thermoelectric figure of merit of quantum wells," *Journal of Applied Physics,* vol. 84, pp. 6149-6153, 1998.

[9] R. Venkatasubramanian, T. Colpitts, B. OQuinn, S. Liu, N. El-Masry, and M. Lamvik, "Low-temperature organometallic epitaxy and its application to superlattice structures in thermoelectrics," *Applied physics letters,* vol. 75, pp. 1104-1106, 1999.

[10] R. Venkatasubramanian, E. Siivola, T. Colpitts, and B. O'Quinn, "Thin-film thermoelectric devices with high room-temperature figures of merit," *Nature,* vol. 413, pp. 597-602, 2001.

[11] K. Koumoto, Y. F. Wang, R. Z. Zhang, A. Kosuga, and R. Funahashi, "Oxide 'Thermoelectric Materials: A Nanostructuring Approach," in *Annual Review of Materials Research, Vol 40*. vol. 40, D. R. Clarke, M. Ruhle, and F. Zok, Eds., ed, 2010, pp. 363-394.

[12] L. D. Hicks and M. S. Dresselhaus, "Thermoelectric figure of merit of a one-dimensional conductor," *Physical Review B,* vol. 47, pp. 16631-16634, 1993.

[13] J. Zou and A. Balandin, "Phonon heat conduction in a semiconductor nanowire," *Journal of Applied Physics,* vol. 89, pp. 2932-2938, 2001.

[14] X. B. Zhao, X. H. Ji, Y. H. Zhang, T. J. Zhu, J. P. Tu, and X. B. Zhang, "Bismuth telluride nanotubes and the effects on the thermoelectric properties of nanotube-containing nanocomposites," *Applied Physics Letters,* vol. 86, 2005.

[15] F. Xiao, C. Hangarter, B. Yoo, Y. Rheem, K. H. Lee, and N. V. Myung, "Recent progress in electrodeposition of thermoelectric thin films and nanostructures," *Electrochimica Acta,* vol. 53, pp. 8103-8117, 2008.

[16] J. H. Zhou, C. G. Jin, J. H. Seol, X. G. Li, and L. Shi, "Thermoelectric properties of individual electrodeposited bismuth telluride nanowires," *Applied Physics Letters,* vol. 87, 2005.

[17] M. Scheele, N. Oeschler, K. Meier, A. Kornowski, C. Klinke, and H. Weller, "Synthesis and Thermoelectric Characterization of Bi2Te3 Nanoparticles," *Advanced Functional Materials,* vol. 19, pp. 3476-3483, 2009.

[18] N. Peranio, O. Eibl, and J. Nurnus, "Structural and thermoelectric properties of epitaxially grown Bi_2Te_3 thin films and superlattices," *Journal of Applied Physics,* vol. 100, 2006.

[19] A. Mavrokefalos, A. L. Moore, M. T. Pettes, L. Shi, W. Wang, and X. G. Li, "Thermoelectric and structural characterizations of individual electrodeposited bismuth telluride nanowires," *Journal of Applied Physics,* vol. 105, 2009.

[20] Y. M. Zuev, J. S. Lee, C. Galloy, H. Park, and P. Kim, "Diameter dependence of the transport properties of antimony telluride nanowires," *Nano letters,* vol. 10, pp. 3037-3040, 2010.

[21] M. Law, J. Goldberger, and P. Yang, "Semiconductor nanowires and nanotubes," *Annu. Rev. Mater. Res.,* vol. 34, pp. 83-122, 2004.

[22] Z. R. Tian, J. A. Voigt, J. Liu, B. Mckenzie, M. J. Mcdermott, M. A. Rodriguez*, et al.*, "Complex and oriented ZnO nanostructures," *Nature materials,* vol. 2, pp. 821-826, 2003.

[23] Y. M. Lin, O. Rabin, M. S. Dresselhaus, Ieee, and Ieee, *Segmented nanowires: a theoretical study of thermoelectric properties*, 2002.

[24] Y.-M. Lin and M. S. Dresselhaus, "Thermoelectric properties of superlattice nanowires," *Physical Review B,* vol. 68, p. 075304, 2003.

[25] J. P. Heremans, "Low-dimensional thermoelectricity," *Acta Physica Polonica A,* vol. 108, pp. 609-634, 2005.

[26] G. G. Yadav, G. Zhang, B. Qiu, J. A. Susoreny, X. Ruan, and Y. Wu, "Self-templated synthesis and thermal conductivity investigation for ultrathin perovskite oxide nanowires," *Nanoscale,* vol. 3, pp. 4078-4081, 2011.

[27] N. Tsuda, K. Nasu, A. Fujimori, and K. Siratori, *Electronic conduction in oxides* vol. 94: Springer, 2000.

[28] L. Forro, O. Chauvet, D. Emin, L. Zuppiroli, H. Berger, and F. Levy, "High mobility n-type charge carriers in large single crystals of anatase (TiO_2)," *Journal of applied physics,* vol. 75, pp. 633-635, 1994.

[29] Y. Tokura and N. Nagaosa, "Orbital physics in transition-metal oxides," *science,* vol. 288, pp. 462-468, 2000.

[30] V. E. Henrich and P. A. Cox, *The surface science of metal oxides*: Cambridge university press, 1996.

[31] L. Forro, O. Chauvet, D. Emin, L. Zuppiroli, H. Berger, and F. Levy, "High mobility n type charge carriers in large single crystals of anatase (TiO_2)," *Journal of applied physics,* vol. 75, pp. 633-635, 1994.

[32] G. Wang and T. Cagin, "Investigation of effective mass of carriers in Bi_2Te_3 □Sb_2Te_3 superlattices via electronic structure studies on its component crystals," *Applied physics letters,* vol. 89, pp. 152101-152101-3, 2006.

[33] C. Bauer, G. Boschloo, E. Mukhtar, and A. Hagfeldt, "Ultrafast relaxation dynamics of charge carriers relaxation in ZnO nanocrystalline thin films," *Chemical Physics Letters,* vol. 387, pp. 176-181, 2004.

[34] E. Hendry, M. Koeberg, B. O'Regan, and M. Bonn, "Local field effects on electron transport in nanostructured TiO_2 revealed by terahertz spectroscopy," *Nano Letters,* vol. 6, pp. 755-759, 2006.

[35] J. C. Johnson, K. P. Knutsen, H. Yan, M. Law, Y. Zhang, P. Yang*, et al.*, "Ultrafast carrier dynamics in single ZnO nanowire and nanoribbon lasers," *Nano Letters,* vol. 4, pp. 197-204, 2004.

[36] E. Canadell and M. H. Whangbo, "Conceptual aspects of structure-property correlations and electronic instabilities, with applications to low-dimensional transition-metal oxides," *Chemical Reviews,* vol. 91, pp. 965-1034, 1991.

[37] S. Balendhran, J. Deng, J. Z. Ou, S. Walia, J. Scott, J. Tang*, et al.*, "Enhanced Charge Carrier Mobility in Two-Dimensional High Dielectric Molybdenum Oxide," *Advanced Materials,* vol. 25, pp. 109-114, 2013.

[38] K. Takada, H. Sakurai, E. Takayama-Muromachi, F. Izumi, R. A. Dilanian, and T. Sasaki, "Superconductivity in two-dimensional CoO_2 layers," *Nature,* vol. 422, pp. 53-55, 2003.

[39] Z. L. Wang, "Zinc oxide nanostructures: growth, properties and applications," *Journal of Physics: Condensed Matter,* vol. 16, p. R829, 2004.

[40] H. Sakaki, "Scattering suppression and high-mobility effect of size-quantized electrons in ultrafine semiconductor wire structures," *Jpn. J. Appl. Phys,* vol. 19, pp. L735-L738, 1980.

[41] E. B. Ramayya, D. Vasileska, S. M. Goodnick, and I. Knezevic, "Electron Mobility in Silicon Nanowires," *Nanotechnology, IEEE Transactions on,* vol. 6, pp. 113-117, 2007.

[42] J. G. Lu, P. Chang, and Z. Fan, "Quasi-one-dimensional metal oxide materials—Synthesis, properties and applications," *Materials Science and Engineering: R: Reports,* vol. 52, pp. 49-91, 2006.

[43] H. Hosono, "Ionic amorphous oxide semiconductors: Material design, carrier transport, and device application," *Journal of non-crystalline solids,* vol. 352, pp. 851-858, 2006.

[44] E. Comini, C. Baratto, G. Faglia, M. Ferroni, A. Vomiero, and G. Sberveglieri, "Quasi-one dimensional metal oxide semiconductors: Preparation, characterization and application as chemical sensors," *Progress in Materials Science,* vol. 54, pp. 1-67, 2009.

[45] A. Vomiero, I. Concina, E. Comini, C. Soldano, M. Ferroni, G. Faglia*, et al.*, "One-dimensional nanostructured oxides for thermoelectric applications and excitonic solar cells," *Nano Energy,* vol. 1, pp. 372-390, 2012.

[46] R. Y. Wang, J. P. Feser, J.-S. Lee, D. V. Talapin, R. Segalman, and A. Majumdar, "Enhanced thermopower in PbSe nanocrystal quantum dot superlattices," *Nano Letters,* vol. 8, pp. 2283-2288, 2008.

[47] M. S. Dresselhaus, G. Chen, M. Y. Tang, R. G. Yang, H. Lee, D. Z. Wang*, et al.*, "New directions for low-dimensional thermoelectric materials," *Advanced Materials,* vol. 19, pp. 1043-1053, 2007.

[48] P. Limelette, S. Hébert, V. Hardy, R. Frésard, C. Simon, and A. Maignan, "Scaling behavior in thermoelectric misfit cobalt oxides," *Physical review letters,* vol. 97, p. 46601, 2006.

[49] Y. Y. Wang, N. S. Rogado, R. J. Cava, and N. P. Ong, "Spin entropy as the likely source of enhanced thermopower in $Na_xCo_2O_4$," *Nature,* vol. 423, pp. 425-428, 2003.

[50] S. Walia, R. Weber, S. Balendhran, D. Yao, J. T. Abrahamson, S. Zhuiykov*, et al.*, "ZnO based thermopower wave sources," *Chemical Communications,* vol. 48, pp. 7462-7464, 2012.

[51] S. Walia, S. Balendhran, P. Yi, D. Yao, S. Zhuiykov, M. Pannirselvam*, et al.*, "MnO_2 based Thermopower Wave Sources with Exceptionally large Output Voltages," *Journal of Physical Chemistry C,* 10.1021/jp401731b, 2013.

[52] D. Medlin and G. Snyder, "Interfaces in bulk thermoelectric materials: A review for Current Opinion in Colloid and Interface Science," *Current Opinion in Colloid & Interface Science,* vol. 14, pp. 226-235, 2009.

[53] J. M. O. Zide, D. Vashaee, Z. X. Bian, G. Zeng, J. E. Bowers, A. Shakouri*, et al.*, "Demonstration of electron filtering to increase the Seebeck coefficient in $In_{(0.53)}Ga_{(0.47)}As/In_{(0.53)}Ga_{(0.28)}Al_{(0.19)}As$ superlattices," *Physical Review B,* vol. 74, 2006.

[54] H. Ohta, S. Kim, Y. Mune, T. Mizoguchi, K. Nomura, S. Ohta, *et al.*, "Giant thermoelectric Seebeck coefficient of two-dimensional electron gas in $SrTiO_3$," *Nature Materials,* vol. 6, pp. 129-134, 2007.

[55] H. Ohta, "Thermoelectrics based on strontium titanate," *Materials Today,* vol. 10, pp. 44-49, 2007.

[56] T. Motohashi, E. Naujalis, R. Ueda, K. Isawa, M. Karppinen, and H. Yamauchi, "Simultaneously enhanced thermoelectric power and reduced resistivity of NaCoO by controlling Na nonstoichiometry," *Applied Physics Letters,* vol. 79, p. 1480, 2001.

[57] W. Kobayashi, S. Hébert, D. Pelloquin, O. Pérez, and A. Maignan, "Enhanced thermoelectric properties in a layered rhodium oxide with a trigonal symmetry," *Physical Review B,* vol. 76, p. 245102, 2007.

[58] H. D. Zheng, J. Z. Ou, M. S. Strano, R. B. Kaner, A. Mitchell, and K. Kalantar-Zadeh, "Nanostructured Tungsten Oxide - Properties, Synthesis, and Applications," *Advanced Functional Materials,* vol. 21, pp. 2175-2196, 2011.

[59] M. Breedon, M. B. Rahmani, S.-H. Keshmiri, W. Wlodarski, and K. Kalantar-zadeh, "Aqueous synthesis of interconnected ZnO nanowires using spray pyrolysis deposited seed layers," *Materials Letters,* vol. 64, pp. 291-294, 2010.

[60] X. W. Lou and H. C. Zeng, "Hydrothermal synthesis of α-MoO_3 nanorods via acidification of ammonium heptamolybdate tetrahydrate," *Chemistry of materials,* vol. 14, pp. 4781-4789, 2002.

[61] A. Shakouri, "Recent developments in semiconductor thermoelectric physics and materials," *Materials Research,* vol. 41, p. 399, 2011.

[62] A. I. Boukai, Y. Bunimovich, J. Tahir-Kheli, J. K. Yu, W. A. Goddard, and J. R. Heath, "Silicon nanowires as efficient thermoelectric materials," *Nature,* vol. 451, pp. 168-171, 2008.

[63] G. D. Mahan and J. O. Sofo, "The best thermoelectric," *Proceedings of the National Academy of Sciences of the United States of America,* vol. 93, pp. 7436-7439, 1996.

[64] F. Borga, M. Bekele, Y. B. Tatek, and M. Tsige, "Efficiency, power, and period at two optimum operations of a thermoelectric single-level quantum dot," *Physical Review E,* vol. 86, 2012.

[65] J. Z. He, X. M. Wang, and Y. C. Zhang, "Performance characteristics of a quantum dot thermoelectric refrigerator," *International Journal of Modern Physics B,* vol. 26, 2012.

[66] K. I. Wysokinski, "Thermoelectric transport in the three terminal quantum dot," *Journal of Physics-Condensed Matter,* vol. 24, 2012.

[67] T. C. Harman, P. J. Taylor, M. P. Walsh, and B. E. LaForge, "Quantum dot superlattice thermoelectric materials and devices," *Science,* vol. 297, pp. 2229-2232, 2002.

[68] R. Y. Wang, J. P. Feser, J. S. Lee, D. V. Talapin, R. Segalman, and A. Majumdar, "Enhanced thermopower in PbSe nanocrystal quantum dot superlattices," *Nano Letters,* vol. 8, pp. 2283-2288, 2008.

[69] T. C. Harman, P. J. Taylor, D. L. Spears, and M. P. Walsh, "Thermoelectric quantum-dot superlattices with high ZT," *Journal of Electronic Materials,* vol. 29, pp. L1-L4, 2000.

[70] M. S. Dresselhaus, G. Chen, M. Y. Tang, R. Yang, H. Lee, D. Wang*, et al.*, "New Directions for Low-Dimensional Thermoelectric Materials," *Advanced Materials,* vol. 19, pp. 1043-1053, 2007.

[71] J. Jie, G. Wang, X. Han, and J. Hou, "Synthesis and characterization of ZnO: In nanowires with superlattice structure," *The Journal of Physical Chemistry B,* vol. 108, pp. 17027-17031, 2004.

[72] R. S. Devan, R. A. Patil, J. H. Lin, and Y. R. Ma, "One-Dimensional Metal-Oxide Nanostructures: Recent Developments in Synthesis, Characterization, and Applications," *Advanced Functional Materials,* vol. 22, pp. 3326-3370, 2012.

[73] L. E. Bell, "Cooling, heating, generating power, and recovering waste heat with thermoelectric systems," *Science,* vol. 321, pp. 1457-1461, 2008.

[74] J. Schieferdecker, R. Quad, E. Holzenkämpfer, and M. Schulze, "Infrared thermopile sensors with high sensitivity and very low temperature coefficient," *Sensors and Actuators A: Physical,* vol. 47, pp. 422-427, 1995.

[75] S. Walia, R. Weber, K. Latham, P. Petersen, J. T. Abrahamson, M. S. Strano*, et al.*, "Oscillatory Thermopower Waves Based on Bi_2Te_3 Films," *Advanced Functional Materials,* vol. 21, pp. 2072-2079, 2011.

[76] S. Walia, R. Weber, S. Sriram, M. Bhaskaran, K. Latham, S. Zhuiykov*, et al.*, "Sb_2Te_3 and Bi_2Te_3 based thermopower wave sources," *Energy & Environmental Science,* vol. 4, pp. 3558-3564, 2011.

[77] M. Zebarjadi, K. Esfarjani, M. S. Dresselhaus, Z. F. Ren, and G. Chen, "Perspectives on thermoelectrics: from fundamentals to device applications," *Energy & Environmental Science,* vol. 5, pp. 5147-5162, 2012.

[78] C. Chiritescu, D. G. Cahill, N. Nguyen, D. Johnson, A. Bodapati, P. Keblinski*, et al.*, "Ultralow Thermal Conductivity in Disordered, Layered WSe2 Crystals," *Science,* vol. 315, pp. 351-353, 2007.

[79] A. J. Minnich, M. S. Dresselhaus, Z. F. Ren, and G. Chen, "Bulk nanostructured thermoelectric materials: current research and future prospects," *Energy & Environmental Science,* vol. 2, pp. 466-479, 2009.

[80] S. Mukerjee and J. E. Moore, "Doping dependence of thermopower and thermoelectricity in strongly correlated materials," *Applied Physics Letters,* vol. 90, pp. 112107-3, 2007.

[81] G. S. Nolas, J. Sharp, and J. Goldsmid, *Thermoelectrics: basic principles and new materials developments* vol. 45: Springer, 2001.

[82] B. Poudel, Q. Hao, Y. Ma, Y. Lan, A. Minnich, B. Yu*, et al.*, "High-thermoelectric performance of nanostructured bismuth antimony telluride bulk alloys," *Science,* vol. 320, pp. 634-638, 2008.

[83] O. Yamashita, S. Tomiyoshi, and K. Makita, "Bismuth telluride compounds with high thermoelectric figures of merit," *Journal of Applied Physics,* vol. 93, pp. 368-374, 2003.

[84] D. Y. Chung, T. Hogan, P. Brazis, M. Rocci-Lane, C. Kannewurf, M. Bastea*, et al.*, "$CsBi_4Te_6$: A high-performance thermoelectric material for low-temperature applications," *Science,* vol. 287, pp. 1024-1027, 2000.

[85] O. Yamashita and S. Tomiyoshi, "Effect of annealing on thermoelectric properties of bismuth telluride compounds doped with various additives," *Journal of applied physics,* vol. 95, pp. 161-169, 2004.

[86] L. D. Ivanova, Y. V. Granatkina, N. V. Polikarpova, and E. I. Smirnova, "Selenium-doped Sb_2Te_3-Bi_2Te_3 crystals," *Inorganic Materials,* vol. 33, pp. 558-561, 1997.

[87] J. R. Sootsman, D. Y. Chung, and M. G. Kanatzidis, "New and Old Concepts in Thermoelectric Materials," *Angewandte Chemie-International Edition,* vol. 48, pp. 8616-8639, 2009.

[88] E. Guilmeau, D. Berardan, C. Simon, A. Maignan, B. Raveau, D. O. Ovono*, et al.*, "Tuning the transport and thermoelectric properties of In_2O_3 bulk ceramics through doping at In-site," *Journal of Applied Physics,* vol. 106, pp. 053715-7, 2009.

[89] J. W. Fergus, "Oxide materials for high temperature thermoelectric energy conversion," *Journal of the European Ceramic Society,* vol. 32, pp. 525-540, 2012.

[90] Y. Wang, Y. Sui, and W. H. Su, "High temperature thermoelectric characteristics of $Ca_{(0.9)}R_{(0.1)}MnO_{(3)}$ (R=La, Pr, Yb)," *Journal of Applied Physics,* vol. 104, 2008.

[91] Y. Wang, Y. Sui, X. J. Wang, and W. H. Su, "Enhancement of thermoelectric efficiency in (Ca, Dy)MnO_3-(Ca, Yb)MnO_3 solid solutions," *Applied Physics Letters,* vol. 97, 2010.

[92] J. W. Moon, Y. Masuda, W. S. Seo, and K. Koumoto, "Influence of ionic size of rare-earth site on the thermoelectric properties of $RCoO_3$-type perovskite cobalt oxides," *Materials Science and Engineering B-Solid State Materials for Advanced Technology,* vol. 85, pp. 70-75, 2001.

[93] M. Ohtaki, T. Tsubota, K. Eguchi, and H. Arai, "High-temperature thermoelectric properties of $(Zn_{1-x}Al_x)O$," *Journal of Applied Physics,* vol. 79, pp. 1816-1818, 1996.

[94] Y. Fujishiro, M. Miyata, M. Awano, and K. Maeda, "Characterization of thermoelectric metal oxide elements prepared by the pulse electric-current sintering method," *Journal of the American Ceramic Society,* vol. 87, pp. 1890-1894, 2004.

[95] H. Kaga, Y. Kinemuchi, H. Yihnaz, K. Watarl, H. Nakano, H. Nakano*, et al.*, "Orientation dependence of transport property and microstructural characterization of Al-doped ZnO ceramics," *Acta Materialia,* vol. 55, pp. 4753-4757, 2007.

[96] K. Park, K. Y. Ko, W. S. Seo, W. S. Cho, J. G. Kim, and J. Y. Kim, "High-temperature thermoelectric properties of polycrystalline $Zn_{1-x-y}Al_xTi_yO$ ceramics," *Journal of the European Ceramic Society,* vol. 27, pp. 813-817, 2007.

[97] H. Cheng, X. J. Xu, H. H. Hng, and J. Ma, "Characterization of Al-doped ZnO thermoelectric materials prepared by RF plasma powder processing and hot press sintering," *Ceramics International,* vol. 35, pp. 3067-3072, 2009.

[98] M. Ohtaki, K. Araki, and K. Yamamoto, "High Thermoelectric Performance of Dually Doped ZnO Ceramics," *Journal of Electronic Materials,* vol. 38, pp. 1234-1238, 2009.

[99] J. P. Wiff, Y. Kinemuchi, H. Kaga, C. Ito, and K. Watari, "Correlations between thermoelectric properties and effective mass caused by lattice distortion in Al-doped ZnO ceramics," *Journal of the European Ceramic Society,* vol. 29, pp. 1413-1418, 2009.

[100] N. Ma, J. F. Li, B. P. Zhang, Y. H. Lin, L. R. Ren, and G. F. Chen, "Microstructure and thermoelectric properties of $Zn_{1-x}Al_xO$ ceramics fabricated by spark plasma sintering," *Journal of Physics and Chemistry of Solids,* vol. 71, pp. 1344-1349, 2010.

[101] P. Jood, R. J. Mehta, Y. L. Zhang, G. Peleckis, X. L. Wang, R. W. Siegel*, et al.*, "Al-Doped Zinc Oxide Nanocomposites with Enhanced Thermoelectric Properties," *Nano Letters,* vol. 11, pp. 4337-4342, 2011.

[102] X. R. Qu, W. Wang, S. C. Lv, and D. C. Jia, "Thermoelectric properties and electronic structure of Al-doped ZnO," *Solid State Communications,* vol. 151, pp. 332-336, 2011.

[103] H. Yamaguchi, Y. Chonan, M. Oda, T. Komiyama, T. Aoyama, and S. Sugiyama, "Thermoelectric Properties of ZnO Ceramics Co-Doped with Al and Transition Metals," *Journal of Electronic Materials,* vol. 40, pp. 723-727, 2011.

[104] S. Teehan, H. Efstathiadis, and P. Haldar, "Thermoelectric power factor enhancement of AZO/In-AZO quantum well multilayer structures as compared to bulk films," *Journal of Alloys and Compounds,* vol. 539, pp. 129-136, 2012.

[105] K. Park, K. Jang, H. C. Kwon, J. G. Kim, and W. S. Cho, "Influence of partial substitution of Cu for Co on the thermoelectric properties of $NaCo_2O_4$," *Journal of alloys and compounds,* vol. 419, pp. 213-219, 2006.

[106] K. Park and J. Lee, "Enhanced thermoelectric properties of $NaCo_2O_4$ by adding ZnO," *Materials Letters,* vol. 62, pp. 2366-2368, 2008.

[107] A. Georges, G. Kotliar, W. Krauth, and M. J. Rozenberg, "Dynamical mean-field theory of strongly correlated fermion systems and the limit of infinite dimensions," *Reviews of Modern Physics,* vol. 68, p. 13, 1996.

[108] M. I. Katsnelson and A. I. Lichtenstein, "Electronic structure and magnetic properties of correlated metals," *The European Physical Journal B - Condensed Matter and Complex Systems,* vol. 30, pp. 9-15, 2002.

[109] O. Restrepo, K. Varga, and S. Pantelides, "First-principles calculations of electron mobilities in silicon: Phonon and Coulomb scattering," *Applied Physics Letters,* vol. 94, pp. 212103-212103-3, 2009.

[110] Z. Wang, S. Wang, S. Obukhov, N. Vast, J. Sjakste, V. Tyuterev*, et al.*, "Thermoelectric transport properties of silicon: Toward an ab initio approach," *Physical Review B,* vol. 83, p. 205208, 2011.

[111] I. Terasaki, Y. Sasago, and K. Uchinokura, "Large thermoelectric power in $NaCo_2O_4$ single crystals," *Physical Review B,* vol. 56, pp. 12685-12687, 1997.

[112] M. Zebarjadi, K. Esfarjani, Z. Bian, and A. Shakouri, "Low-Temperature Thermoelectric Power Factor Enhancement by Controlling Nanoparticle Size Distribution," *Nano letters,* vol. 11, p. 225, 2011.

[113] A. Weidenkaff, R. Robert, M. Aguirre, L. Bocher, T. Lippert, and S. Canulescu, "Development of thermoelectric oxides for renewable energy conversion technologies," *Renewable Energy,* vol. 33, pp. 342-347, 2008.

[114] A. Weidenkaff, R. Robert, M. H. Aguirre, L. Bocher, and L. Schlapbach, "Nanostructured thermoelectric oxides with low thermal conductivity," *Physica Status Solidi-Rapid Research Letters,* vol. 1, pp. 247-249, 2007.

[115] J. Callaway, "Model for Lattice Thermal Conductivity at Low Temperatures," *Physical Review,* vol. 113, pp. 1046-1051, 1959.

[116] D. Broido, M. Malorny, G. Birner, N. Mingo, and D. Stewart, "Intrinsic lattice thermal conductivity of semiconductors from first principles," *Applied Physics Letters,* vol. 91, pp. 231922-231922-3, 2007.

[117] A. Ward and D. Broido, "Intrinsic phonon relaxation times from first-principles studies of the thermal conductivities of Si and Ge," *Physical Review B,* vol. 81, p. 085205, 2010.

[118] N. de Koker, "Thermal conductivity of MgO periclase from equilibrium first principles molecular dynamics," *Physical review letters,* vol. 103, p. 125902, 2009.

[119] K. Esfarjani and H. T. Stokes, "Method to extract anharmonic force constants from first principles calculations," *Physical Review B,* vol. 77, p. 144112, 2008.

[120] A. S. Henry and G. Chen, "Spectral phonon transport properties of silicon based on molecular dynamics simulations and lattice dynamics," *Journal of Computational and Theoretical Nanoscience,* vol. 5, pp. 141-152, 2008.

[121] M. Lundstrom, *Fundamentals of carrier transport*: Cambridge University Press, 2009.

[122] C. B. Vining, "A model for the high-temperature transport properties of heavily doped n-type silicon-germanium alloys," *Journal of applied physics,* vol. 69, pp. 331-341, 1991.

[123] R. G. Yang, G. Chen, and M. S. Dresselhaus, "Thermal conductivity of simple and tubular nanowire composites in the longitudinal direction," *Physical Review B,* vol. 72, 2005.

[124] Y. Q. Cao, X. B. Zhao, T. J. Zhu, X. B. Zhang, and J. P. Tu, "Syntheses and thermoelectric properties of Bi_2Te_3/Sb_2Te_3 bulk nanocomposites with laminated nanostructure," *Applied Physics Letters,* vol. 92, 2008.

[125] P. Zhu, Y. Imai, Y. Isoda, Y. Shinohara, X. Jia, and G. Zou, "Enhanced thermoelectric properties of PbTe alloyed with Sb_2Te_3," *Journal of Physics: Condensed Matter,* vol. 17, p. 7319, 2005.

[126] G. Kavei and M. Karami, "Fabrication and characterization of the p-type (Bi_2Te_3) x (Sb_2Te_3) thermoelectric crystals prepared via zone melting," *Bull. Mater. Sci,* vol. 29, pp. 659-663, 2006.

[127] G. C. Christakudis, S. Plachkova, L. Shelimova, and E. Avilov, "Thermoelectric Figure of Merit of Some Compositions in the System $(GeTe)_{1-x}[(Ag_2Te)_{1-y}(Sb_2Te_3)_y]_x$," *physica status solidi (a),* vol. 128, pp. 465-471, 1991.

[128] A. Li Bassi, A. Bailini, C. Casari, F. Donati, A. Mantegazza, M. Passoni*, et al.*, "Thermoelectric properties of Bi–Te films with controlled structure and morphology," *Journal of Applied Physics,* vol. 105, pp. 124307-124307-9, 2009.

[129] C. Stiewe, Z. He, D. Platzek, G. Karpinski, E. Müller, S. Li*, et al.*, "Control of thermoelectric properties in ZrO2/CoSb3 nano-dispersed composites," *Materialwissenschaft und Werkstofftechnik,* vol. 38, pp. 773-776, 2007.

[130] S. Maekawa, T. Tohyama, S. E. Barnes, S. Ishihara, W. Koshibae, and G. Khaliullin, *Physics of transition metal oxides* vol. 144: Springer, 2004.

[131] P. A. Cox, *Transition metal oxides: an introduction to their electronic structure and properties*: Oxford Univ Pr, 2010.

[132] C. N. R. Rao and B. Raveau, *Transition Metal Oxides: Structure, Properties, and Synthesis of Ceramic Oxides*: Wiley, 1998.

[133] H. Goldsmid, "The electrical conductivity and thermoelectric power of bismuth telluride," *Proceedings of the Physical Society,* vol. 71, p. 633, 2002.

[134] S. Mishra, S. Satpathy, and O. Jepsen, "Electronic structure and thermoelectric properties of bismuth telluride and bismuth selenide," *Journal of Physics: Condensed Matter,* vol. 9, p. 461, 1999.

[135] B. Y. Yavorsky, N. Hinsche, I. Mertig, and P. Zahn, "Electronic structure and transport anisotropy of Bi_2Te_3 and Sb_2Te_3," *Physical Review B,* vol. 84, p. 165208, 2011.

[136] D. Teweldebrhan, V. Goyal, M. Rahman, and A. A. Balandin, "Atomically-thin crystalline films and ribbons of bismuth telluride," *Applied Physics Letters,* vol. 96, pp. 053107-053107-3, 2010.

[137] D. Teweldebrhan, V. Goyal, and A. A. Balandin, "Exfoliation and characterization of bismuth telluride atomic quintuples and quasi-two-dimensional crystals," *Nano letters,* vol. 10, pp. 1209-1218, 2010.

[138] H. Zhang, C.-X. Liu, X.-L. Qi, X. Dai, Z. Fang, and S.-C. Zhang, "Topological insulators in Bi_2Se_3, Bi_2Te_3 and Sb_2Te_3 with a single Dirac cone on the surface," *Nature Physics,* vol. 5, pp. 438-442, 2009.

[139] B. Y. Yoo, C. K. Huang, J. R. Lim, J. Herman, M. A. Ryan, J. P. Fleurial*, et al.*, "Electrochemically deposited thermoelectric n-type Bi_2Te_3 thin films," *Electrochimica Acta,* vol. 50, pp. 4371-4377, 2005.

[140] G. Zhang, B. Kirk, L. A. Jauregui, H. Yang, X. Xu, Y. P. Chen*, et al.*, "Rational Synthesis of Ultrathin n-Type Bi2Te3 Nanowires with Enhanced Thermoelectric Properties," *Nano letters,* vol. 12, pp. 56-60, 2011.

[141] J. Zhou, C. Jin, J. H. Seol, X. Li, and L. Shi, "Thermoelectric properties of individual electrodeposited bismuth telluride nanowires," *Applied Physics Letters,* vol. 87, pp. 133109-3, 2005.

[142] F. Xiao, B. Yoo, K. H. Lee, and N. V. Myung, "Synthesis of Bi_2Te_3 nanotubes by galvanic displacement," *Journal of the American Chemical Society,* vol. 129, pp. 10068-10069, 2007.

[143] Y. Lan, B. Poudel, Y. Ma, D. Wang, M. S. Dresselhaus, G. Chen*, et al.*, "Structure study of bulk nanograined thermoelectric bismuth antimony telluride," *Nano letters,* vol. 9, pp. 1419-1422, 2009.

[144] X. Zhao, X. Ji, Y. Zhang, T. Zhu, J. Tu, and X. Zhang, "Bismuth telluride nanotubes and the effects on the thermoelectric properties of nanotube-containing nanocomposites," *Applied Physics Letters,* vol. 86, pp. 062111-062111-3, 2005.

[145] W. Xie, X. Tang, Y. Yan, Q. Zhang, and T. M. Tritt, "High thermoelectric performance BiSbTe alloy with unique low-dimensional structure," *Journal of Applied Physics,* vol. 105, pp. 113713-113713-8, 2009.

[146] B. Yoo, F. Xiao, K. N. Bozhilov, J. Herman, M. A. Ryan, and N. V. Myung, "Electrodeposition of thermoelectric superlattice nanowires," *Advanced Materials,* vol. 19, pp. 296-299, 2007.

[147] J. P. Heremans, C. M. Thrush, D. T. Morelli, and M.-C. Wu, "Thermoelectric power of bismuth nanocomposites," *Physical review letters,* vol. 88, p. 216801, 2002.

[148] M. S. Sander, A. L. Prieto, R. Gronsky, T. Sands, and A. M. Stacy, "Fabrication of high-density, high aspect ratio, large-area bismuth telluride nanowire arrays by electrodeposition into porous anodic alumina templates," *Advanced Materials,* vol. 14, pp. 665-667, 2002.

[149] H. Huang, W.-l. Luan, and S.-t. Tu, "Influence of annealing on thermoelectric properties of bismuth telluride films grown via radio frequency magnetron sputtering," *Thin Solid Films,* vol. 517, pp. 3731-3734, 2009.

[150] A. Bailini, F. Donati, M. Zamboni, V. Russo, M. Passoni, C. Casari*, et al.*, "Pulsed laser deposition of Bi_2Te_3 thermoelectric films," *Applied Surface Science,* vol. 254, pp. 1249-1254, 2007.

[151] J. Dheepa, R. Sathyamoorthy, S. Velumani, A. Subbarayan, K. Natarajan, and P. Sebastian, "Electrical resistivity of thermally evaporated bismuth telluride thin films," *Solar energy materials and solar cells,* vol. 81, pp. 305-312, 2004.

[152] R. Venkatasubramanian, T. Colpitts, E. Watko, M. Lamvik, and N. El-Masry, "MOCVD of Bi_2Te_3, Sb_2Te_3 and their superlattice structures for thin-film thermoelectric applications," *Journal of crystal growth,* vol. 170, pp. 817-821, 1997.

[153] S. S. Garje, D. J. Eisler, J. S. Ritch, M. Afzaal, P. O'Brien, and T. Chivers, "A new route to antimony telluride nanoplates from a single-source precursor," *Journal of the American Chemical Society,* vol. 128, pp. 3120-3121, 2006.

[154] R. Lan, R. Endo, M. Kuwahara, Y. Kobayashi, and M. Susa, "Thermal conductivity measurements of solid Sb_2Te_3 by hot-strip method," *Japanese Journal of Applied Physics,* vol. 49, p. 8003, 2010.

[155] L. Goncalves, P. Alpuim, G. Min, D. Rowe, C. Couto, and J. Correia, "Optimization of Bi_2Te_3 and Sb_2Te_3 thin films deposited by co-evaporation on polyimide for thermoelectric applications," *Vacuum,* vol. 82, pp. 1499-1502, 2008.

[156] G.-H. Dong, Y.-J. Zhu, and L.-D. Chen, "Microwave-assisted rapid synthesis of Sb_2Te_3 nanosheets and thermoelectric properties of bulk samples prepared by spark plasma sintering," *Journal of Materials Chemistry,* vol. 20, pp. 1976-1981, 2010.

[157] C. Schumacher, K. G. Reinsberg, L. Akinsinde, S. Zastrow, S. Heiderich, W. Toellner*, et al.*, "Optimization of Electrodeposited p-Doped Sb_2Te_3 Thermoelectric Films by Millisecond Potentiostatic Pulses," *Advanced Energy Materials,* vol. 2, pp. 345-352, 2012.

[158] T. Ikeda, L. A. Collins, V. A. Ravi, F. S. Gascoin, S. M. Haile, and G. J. Snyder, "Self-assembled nanometer lamellae of thermoelectric PbTe and Sb_2Te_3 with epitaxy-like interfaces," *Chemistry of materials,* vol. 19, pp. 763-767, 2007.

[159] D. A. Tuan, J. Choi, Y. Shin, S. Cho, H. M. Park, W. Kim*, et al.*, "Structure and magnetic properties of Cu-doped Bi_2Te_3 and Sb_2Te_3 single crystals," *Journal of the Korean Physical Society,* vol. 61, pp. 1675-1678, 2012.

[160] O. C. Yelgel and G. P. Srivastava, "Thermoelectric properties of p-type $(Bi_2Te_3)_{(x)}(Sb_2Te_3)_{(1-x)}$ single crystals doped with 3 wt. % Te," *Journal of Applied Physics,* vol. 113, 2013.

[161] Z. J. Yue, X. L. Wang, Y. Du, S. M. Mahboobeh, F. F. Yun, Z. X. Cheng, *et al.*, "Giant and anisotropic magnetoresistances in p-type Bi-doped Sb_2Te_3 bulk single crystals," *Epl,* vol. 100, 2012.

[162] Y. Zhang, M. L. Snedaker, C. S. Birkel, S. Mubeen, X. Ji, Y. Shi, *et al.*, "Silver-Based Intermetallic Heterostructures in Sb_2Te_3 Thick Films with Enhanced Thermoelectric Power Factors," *Nano letters,* vol. 12, pp. 1075-1080, 2012.

[163] T. Thonhauser, T. Scheidemantel, J. Sofo, J. Badding, and G. Mahan, "Thermoelectric properties of Sb_2Te_3 under pressure and uniaxial stress," *Physical Review B,* vol. 68, p. 085201, 2003.

[164] W. D. Shi, L. Zhou, S. Y. Song, J. H. Yang, and H. J. Zhang, "Hydrothermal synthesis and thermoelectric transport properties of impurity-free antimony telluride hexagonal nanoplates," *Advanced Materials,* vol. 20, pp. 1892, 2008.

[165] W. Shi, J. Yu, H. Wang, and H. Zhang, "Hydrothermal synthesis of single-crystalline antimony telluride nanobelts," *Journal of the American Chemical Society,* vol. 128, pp. 16490-16491, 2006.

[166] G. Leimkuhler, I. Kerkamm, and R. Reineke-Koch, "Electrodeposition of antimony telluride," *Journal of the Electrochemical Society,* vol. 149, pp. C474-C478, 2002.

[167] T. Chen, P. Fan, Z. Zheng, D. Zhang, X. Cai, G. Liang, *et al.*, "Influence of Substrate Temperature on Structural and Thermoelectric Properties of Antimony Telluride Thin Films Fabricated by RF and DC Cosputtering," *Journal of electronic materials,* pp. 1-5, 2012.

[168] K. Knapas, T. Hatanpa, M. Ritala, and M. Leskela, "In Situ Reaction Mechanism Studies on Atomic Layer Deposition of Sb_2Te_3 and GeTe from $(Et_3Si)_2Te$ and Chlorides," *Chemistry of Materials,* vol. 22, pp. 1386-1391, 2009.

[169] A. Giani, A. Boulouz, F. Pascal-Delannoy, A. Foucaran, A. Boyer, B. Aboulfarah, *et al.*, "Electrical and thermoelectrical properties of Sb_2Te_3 prepared by the metal-organic chemical vapor deposition technique," *Journal of materials science letters,* vol. 18, pp. 541-543, 1999.

[170] K. Zhang, D. Nminibapiel, M. Tangirala, H. Baumgart, and V. Kochergin, "Fabrication of Sb_2Te_3 and Bi_2Te_3 Multilayer Composite Films by Atomic Layer Deposition," in *Meeting Abstracts*, 2012, pp. 2456-2456.

[171] A. V. Emeline, G. V. Kataeva, V. K. Ryabchuk, and N. Serpone, "Photostimulated generation of defects and surface reactions on a series of wide band gap metal-oxide solids," *Journal of Physical Chemistry B,* vol. 103, pp. 9190-9199, 1999.

[172] M. Matsui and M. Akaogi, "Molecular dynamics simulation of the structural and physical properties of the four polymorphs of TiO_2," *Molecular Simulation,* vol. 6, pp. 239-244, 1991.

[173] H. Z. Zhang and J. F. Banfield, "Understanding polymorphic phase transformation behavior during growth of nanocrystalline aggregates: Insights from TiO_2," *Journal of Physical Chemistry B,* vol. 104, pp. 3481-3487, 2000.

[174] U. Diebold, "The surface science of titanium dioxide," *Surface Science Reports,* vol. 48, pp. 53-229, 2003.

[175] D. V. Bavykin, J. M. Friedrich, and F. C. Walsh, "Protonated titanates and TiO_2 nanostructured materials: Synthesis, properties, and applications," *Advanced Materials,* vol. 18, pp. 2807-2824, 2006.

[176] Q. Y. He, Q. Hao, G. Chen, B. Poudel, X. W. Wang, D. Z. Wang, *et al.*, "Thermoelectric property studies on bulk TiO_x with x from 1 to 2," *Applied Physics Letters,* vol. 91, 2007.

[177] Y. Lu, M. Hirohashi, and K. Sato, "Thermoelectric properties of non-stoichiometric titanium dioxide TiO_{2-x} fabricated by reduction treatment using carbon powder," *Materials Transactions,* vol. 47, pp. 1449-1452, 2006.

[178] J. K. Tang, W. D. Wang, G. L. Zhao, and Q. Li, "Colossal positive Seebeck coefficient and low thermal conductivity in reduced TiO_2," *Journal of Physics-Condensed Matter,* vol. 21, 2009.

[179] I. Tsuyumoto, T. Hosono, and M. Murata, "Thermoelectric power in nonstoichiometric orthorhombic titanium oxides," *Journal of the American Ceramic Society,* vol. 89, pp. 2301-2303, 2006.

[180] T. Bak, M. K. Nowotny, L. R. Sheppard, and J. Nowotny, "Effect of prolonged oxidation on semiconducting properties of titanium dioxide," *Journal of Physical Chemistry C,* vol. 112, pp. 13248-13257, 2008.

[181] L. Miao, S. Tanemura, R. Huang, C. Y. Liu, C. M. Huang, and G. Xu, "Large Seebeck Coefficients of Protonated Titanate Nanotubes for High-Temperature Thermoelectric Conversion," *Acs Applied Materials & Interfaces,* vol. 2, pp. 2355-2359, 2010.

[182] D. Kurita, S. Ohta, K. Sugiura, H. Ohta, and K. Koumoto, "Carrier generation and transport properties of heavily Nb-doped anatase TiO_2 epitaxial films at high temperatures," *Journal of Applied Physics,* vol. 100, 2006.

[183] L. R. Sheppard, T. Bak, and J. Nowotny, "Electrical properties of niobium-doped titanium dioxide. 3. Thermoelectric power," *Journal of Physical Chemistry C,* vol. 112, pp. 611-617, 2008.

[184] L. R. Sheppard, T. Bak, and J. Nowotny, "Electrical properties of niobium-doped titanium dioxide. 1. Defect disorder," *Journal of Physical Chemistry B,* vol. 110, pp. 22447-22454, 2006.

[185] T. Okuda, K. Nakanishi, S. Miyasaka, and Y. Tokura, "Large thermoelectric response of metallic perovskites: $Sr_{1-x}La_xTiO_3$ ($0 <= x <= 0.1$)," *Physical Review B,* vol. 63, 2001.

[186] H. Ohta, K. Sugiura, and K. Koumoto, "Recent progress in oxide thermoelectric materials: p-type $Ca_3CO_4O_9$ and n-type $SrTiO_3$," *Inorganic Chemistry,* vol. 47, pp. 8429-8436, 2008.

[187] S. Ohta, T. Nomura, H. Ohta, and K. Koumoto, "High-temperature carrier transport and thermoelectric properties of heavily La- or Nb-doped $SrTiO_3$ single crystals," *Journal of Applied Physics,* vol. 97, 2005.

[188] J. Ravichandran, W. Siemons, D. W. Oh, J. T. Kardel, A. Chari, H. Heijmerikx*, et al.*, "High-temperature thermoelectric response of double-doped $SrTiO_3$ epitaxial films," *Physical Review B,* vol. 82, 2010.

[189] B. Jalan and S. Stemmer, "Large Seebeck coefficients and thermoelectric power factor of La-doped SrTiO3 thin films," *Applied Physics Letters,* vol. 97, 2010.

[190] H. Muta, K. Kurosaki, and S. Yamanaka, "Thermoelectric properties of rare earth doped $SrTiO_3$," *Journal of Alloys and Compounds,* vol. 350, pp. 292-295, 2003.

[191] M. Yamamoto, H. Ohta, and K. Koumoto, "Thermoelectric phase diagram in a $CaTiO_3$-$SrTiO_3$-$BaTiO_3$ system," *Applied Physics Letters,* vol. 90, 2007.

[192] B. B. Lakshmi, C. J. Patrissi, and C. R. Martin, "Sol-gel template synthesis of semiconductor oxide micro- and nanostructures," *Chemistry of Materials,* vol. 9, pp. 2544-2550, 1997.

[193] L. H. Zhang, T. Tosho, N. Okinaka, and T. Akiyama, "Thermoelectric properties of combustion-synthesized lanthanum-doped strontium titanate," *Materials Transactions,* vol. 48, pp. 1079-1083, 2007.

[194] W. F. Wei, X. W. Cui, W. X. Chen, and D. G. Ivey, "Manganese oxide-based materials as electrochemical supercapacitor electrodes," *Chemical Society Reviews,* vol. 40, pp. 1697-1721, 2011.

[195] W. Xiao, D. L. Wang, and X. W. Lou, "Shape-Controlled Synthesis of MnO_2 Nanostructures with Enhanced Electrocatalytic Activity for Oxygen Reduction," *Journal of Physical Chemistry C,* vol. 114, pp. 1694-1700, 2010.

[196] F. F. Song, L. M. Wu, and S. Liang, "Giant Seebeck coefficient thermoelectric device of MnO_2 powder," *Nanotechnology,* vol. 23, 2012.

[197] E. Cockayne and L. Li, "First-principles DFT+U studies of the atomic, electronic, and magnetic structure of alpha-MnO_2 (cryptomelane)," *Chemical Physics Letters,* vol. 544, pp. 53-58, 2012.

[198] J. E. Post, R. B. Vondreele, and P. R. Buseck, "Symmetry and cation displacements in hollandites-Structure refinements of hollandite, cryptomelane and priderite," *Acta Crystallographica Section B-Structural Science,* vol. 38, pp. 1056-1065, 1982.

[199] S. Devaraj and N. Munichandraiah, "Effect of crystallographic structure of MnO_2 on its electrochemical capacitance properties," *Journal of Physical Chemistry C,* vol. 112, pp. 4406-4417, 2008.

[200] E. Preisler, "Semiconductor properties of manganese dioxide," *Journal of Applied Electrochemistry,* vol. 6, pp. 311-320, 1976.

[201] A. Ul Islam, R. Islam, and K. A. Khan, "Studies on the thermoelectric effect in semiconducting MnO_2 thin films," *Journal of Materials Science-Materials in Electronics,* vol. 16, pp. 203-207, 2005.

[202] R. Ang, W. J. Lu, R. L. Zhang, B. C. Zhao, X. B. Zhu, W. H. Song*, et al.*, "Effects of Co doping in bilayered manganite $LaSr_2Mn_2O_7$: Resistivity, thermoelectric power, and thermal conductivity," *Physical Review B,* vol. 72, 2005.

[203] F. P. Zhang, Q. M. Lu, X. Zhang, and J. X. Zhang, "First principle investigation of electronic structure of $CaMnO_3$ thermoelectric compound oxide," *Journal of Alloys and Compounds,* vol. 509, pp. 542-545, 2011.

[204] D. Flahaut, T. Mihara, R. Funahashi, N. Nabeshima, K. Lee, H. Ohta*, et al.*, "Thermoelectrical properties of A-site substituted $Ca_{1-x}Re_xMnO_3$ system," *Journal of Applied Physics,* vol. 100, 2006.

[205] H. Sato, T. Enoki, M. Isobe, and Y. Ueda, "Transport properties and magnetism of a helically Hund-coupled conductor: beta-MnO_2," *Physical Review B,* vol. 61, pp. 3563-3569, 2000.

[206] X. Zhang, W. S. Yang, J. J. Yang, and D. G. Evans, "Synthesis and characterization of alpha-MnO2 nanowires: Self-assembly and phase transformation to beta-MnO_2 microcrystals," *Journal of Crystal Growth,* vol. 310, pp. 716-722, 2008.

[207] X. Wang and Y. D. Li, "Synthesis and formation mechanism of manganese dioxide nanowires/nanorods," *Chemistry-a European Journal,* vol. 9, pp. 300-306, 2003.

[208] M. Devenney, S. Donne, and S. Gorer, "Application of combinatorial methodologies to the synthesis and characterization of electrolytic manganese dioxide," *Journal of Applied Electrochemistry,* vol. 34, pp. 643-651, 2004.

[209] S. Chou, F. Cheng, and J. Chen, "Electrodeposition synthesis and electrochemical properties of nanostructured γ-MnO_2 films," *Journal of power sources,* vol. 162, pp. 727-734, 2006.

[210] B. Dong, T. Xue, C.-L. Xu, and H.-L. Li, "Electrodeposition of mesoporous manganese dioxide films from lyotropic liquid crystalline phases," *Microporous and Mesoporous Materials,* vol. 112, pp. 627-631, 2008.

[211] X. Wang, X. Wang, W. Huang, P. Sebastian, and S. Gamboa, "Sol–gel template synthesis of highly ordered MnO_2 nanowire arrays," *Journal of power sources,* vol. 140, pp. 211-215, 2005.

[212] O. Nilsen, H. Fjellvåg, and A. Kjekshus, "Growth of manganese oxide thin films by atomic layer deposition," *Thin Solid Films,* vol. 444, pp. 44-51, 2003.

[213] S. Isber, E. Majdalani, M. Tabbal, T. Christidis, K. Zahraman, and B. Nsouli, "Study of manganese oxide thin films grown by pulsed laser deposition," *Thin Solid Films,* vol. 517, pp. 1592-1595, 2009.

[214] L. W. Guo, D. L. Peng, H. Makino, T. Hanada, S. K. Hong, K. Sumiyama, *et al.*, "Structural characteristics and magnetic properties of MnO_2 films grown by plasma-assisted molecular beam epitaxy," *Journal of Applied Physics,* vol. 90, pp. 351-354, 2001.

[215] H. Q. Wang, X. Dong, S. J. Peng, L. Dong, and Y. Wang, "Improvement of thermoelectric properties of WO_3 ceramics by ZnO addition," *Journal of Alloys and Compounds,* vol. 527, pp. 204-209, 2012.

[216] E. K. H. Salje, S. Rehmann, F. Pobell, D. Morris, K. S. Knight, T. Herrmannsdorfer, *et al.*, "Crystal structure and paramagnetic behaviour of epsilon-WO_{3-x}," *Journal of Physics-Condensed Matter,* vol. 9, pp. 6563-6577, 1997.

[217] T. Vogt, P. M. Woodward, and B. A. Hunter, "The high-temperature phases of WO3," *Journal of Solid State Chemistry,* vol. 144, pp. 209-215, 1999.

[218] M. R. Goulding and C. B. Thomas, "Transport properties of amorphous films of tungstic oxide sublimed under different conditions," *Thin Solid Films,* vol. 62, pp. 175-188, 1979.

[219] P. S. Patil, P. R. Patil, and E. A. Ennaoui, "Characterization of ultrasonic spray pyrolyzed tungsten oxide thin films," *Thin Solid Films,* vol. 370, pp. 38-44, 2000.

[220] V. O. Makarov and M. Trontelj, "Sintering and electrical conductivity of doped WO3," *Journal of the European Ceramic Society,* vol. 16, pp. 791-794, 1996.

[221] R. S. Vemuri, K. K. Bharathi, S. K. Gullapalli, and C. V. Ramana, "Effect of Structure and Size on the Electrical Properties of Nanocrystalline WO3 Films," *Acs Applied Materials & Interfaces,* vol. 2, pp. 2623-2628, 2010.

[222] M. G. Hutchins, O. Abu-Alkhair, M. M. El-Nahass, and K. Abdel-Hady, "Electrical conduction mechanisms in thermally evaporated tungsten trioxide (WO_3) thin films," *Journal of Physics-Condensed Matter,* vol. 18, pp. 9987-9997, 2006.

[223] H. T. Wang, Y. B. Xu, M. Goto, Y. Tanaka, M. Yamazaki, A. Kasahara, *et al.*, "Thermal conductivity measurement of tungsten oxide nanoscale thin films," *Materials Transactions,* vol. 47, pp. 1894-1897, 2006.

[224] J. Molenda and A. Kubik, "Transport properties and reactivity of tungsten trioxide," *Solid State Ionics,* vol. 117, pp. 57-64, 1999.

[225] H. Q. Wang, Z. Q. Hua, S. J. Peng, X. Dong, L. Dong, and Y. Wang, "Effect of CeO_2 on the thermoelectric properties of WO_3-based ceramics," *Ceramics International,* vol. 38, pp. 1133-1137, 2012.

[226] P. S. Patil, S. H. Mujawar, A. I. Inamdar, P. S. Shinde, H. P. Deshmukh, and S. B. Sadale, "Structural, electrical and optical properties of TiO_2 doped WO_3 thin films," *Applied Surface Science,* vol. 252, pp. 1643-1650, 2005.

[227] B. Marsen, E. L. Miller, D. Paluselli, and R. E. Rocheleau, "Progress in sputtered tungsten trioxide for photoelectrode applications," *International Journal of Hydrogen Energy,* vol. 32, pp. 3110-3115, 2007.

[228] C. Cantalini, H. Sun, M. Faccio, M. Pelino, S. Santucci, L. Lozzi, *et al.*, "NO_2 sensitivity of WO_3 thin film obtained by high vacuum thermal evaporation," *Sensors and Actuators B: Chemical,* vol. 31, pp. 81-87, 1996.

[229] M. Breedon, P. Spizzirri, M. Taylor, J. du Plessis, D. McCulloch, J. Zhu, *et al.*, "Synthesis of Nanostructured Tungsten Oxide Thin Films: A Simple, Controllable, Inexpensive, Aqueous Sol– Gel Method," *Crystal Growth & Design,* vol. 10, pp. 430-439, 2009.

[230] S. Baeck, T. Jaramillo, G. Stucky, and E. McFarland, "Controlled electrodeposition of nanoparticulate tungsten oxide," *Nano Letters,* vol. 2, pp. 831-834, 2002.

[231] K. Kalantar-zadeh, A. Z. Sadek, H. Zheng, V. Bansal, S. K. Bhargava, W. Wlodarski, *et al.*, "Nanostructured WO_3 films using high temperature anodization," *Sensors and Actuators B: Chemical,* vol. 142, pp. 230-235, 2009.

[232] Y. Zhao, Z.-C. Feng, and Y. Liang, "Pulsed laser deposition of WO_3-base film for NO_2 gas sensor application," *Sensors and Actuators B: Chemical,* vol. 66, pp. 171-173, 2000.

[233] R. Sivakumar, R. Gopalakrishnan, M. Jayachandran, and C. Sanjeeviraja, "Preparation and characterization of electron beam evaporated WO_3 thin films," *Optical Materials,* vol. 29, pp. 679-687, 2007.

[234] B. A. Buchine, W. L. Hughes, F. L. Degertekin, and Z. L. Wang, "Bulk acoustic resonator based on piezoelectric ZnO belts," *Nano Letters,* vol. 6, pp. 1155-1159, 2006.

[235] J. H. He, C. L. Hsin, J. Liu, L. J. Chen, and Z. L. Wang, "Piezoelectric gated diode of a single ZnO nanowire," *Advanced Materials,* vol. 19, pp. 781-784, 2007.

[236] M.-P. Lu, J. Song, M.-Y. Lu, M.-T. Chen, Y. Gao, L.-J. Chen, *et al.*, "Piezoelectric nanogenerator using p-type ZnO nanowire arrays," *Nano Letters,* vol. 9, pp. 1223-1227, 2009.

[237] Z. L. Wang and J. Song, "Piezoelectric nanogenerators based on zinc oxide nanowire arrays," *Science,* vol. 312, pp. 242-246, 2006.

[238] V. Coleman and C. Jagadish, "Basic properties and applications of ZnO," *Zinc Oxide Bulk, Thin films and Nanostructures, Processing, Properties and Applications,* pp. 1-20, 2006.

[239] K. P. Ong, D. J. Singh, and P. Wu, "Analysis of the thermoelectric properties of n-type ZnO," *Physical Review B,* vol. 83, 2011.

[240] Y. Kinemuchi, M. Mikami, K. Kobayashi, K. Watari, and Y. Hotta, "Thermoelectric Properties of Nanograined ZnO," *Journal of Electronic Materials,* vol. 39, pp. 2059-2063, 2010.

[241] Y. Fujishiro, M. Miyata, M. Awano, and K. Maeda, "Effect of microstructural control on thermoelectric properties of hot-pressed aluminum-doped zinc oxide," *Journal of the American Ceramic Society,* vol. 86, pp. 2063-2066, 2003.

[242] K. H. Kim, S. H. Shim, K. B. Shim, K. Niihara, and J. Hojo, "Microstructural and thermoelectric characteristics of zinc oxide-based thermoelectric materials fabricated using a spark plasma sintering process," *Journal of the American Ceramic Society,* vol. 88, pp. 628-632, 2005.

[243] K. Park and K. Y. Ko, "Effect of TiO_2 on high-temperature thermoelectric properties of ZnO," *Journal of Alloys and Compounds,* vol. 430, pp. 200-204, 2007.

[244] K. Park and J. K. Seong, "Influence of simultaneous addition of Sb_2O_3 and SnO_2 on thermoelectric properties of $Zn_{1-x-y}Sb_xSn_yO$ prepared by tape casting," *Journal of Alloys and Compounds,* vol. 464, pp. 1-5, 2008.

[245] K. Park, J. K. Seong, Y. Kwon, S. Nahm, and W. S. Cho, "Influence of SnO_2 addition on the thermoelectric properties of $Zn_{1-x}Sn_xO(0.01 <= x <= 0.05)$," *Materials Research Bulletin,* vol. 43, pp. 54-61, 2008.

[246] K. Park, J. K. Seong, and S. Nahm, "Improvement of thermoelectric properties with the addition of Sb to ZnO," *Journal of Alloys and Compounds,* vol. 455, pp. 331-335, 2008.

[247] E. Guilmeau, A. Maignan, and C. Martin, "Thermoelectric Oxides: Effect of Doping in Delafossites and Zinc Oxide," *Journal of Electronic Materials,* vol. 38, pp. 1104-1108, 2009.

[248] K. Park, J. K. Seong, and G. H. Kim, "NiO added $Zn_{1-x}Ni_xO$ ($0 <= x <= 0.05$) for thermoelectric power generation," *Journal of Alloys and Compounds,* vol. 473, pp. 423-427, 2009.

[249] D. Berardan, C. Byl, and N. Dragoe, "Influence of the Preparation Conditions on the Thermoelectric Properties of Al-Doped ZnO," *Journal of the American Ceramic Society,* vol. 93, pp. 2352-2358, 2010.

[250] H. Colder, E. Guilmeau, C. Harnois, S. Marinel, R. Retoux, and E. Savary, "Preparation of Ni-doped ZnO ceramics for thermoelectric applications," *Journal of the European Ceramic Society,* vol. 31, pp. 2957-2963, 2011.

[251] Y. Michiue, T. Mori, A. Prytuliak, Y. Matsushita, M. Tanaka, and N. Kimizuka, "Electrical, optical, and thermoelectric properties of $Ga_2O_3(ZnO)_{(9)}$," *Rsc Advances,* vol. 1, pp. 1788-1793, 2011.

[252] K. H. Jung, K. H. Lee, W. S. Seo, and S. M. Choi, "An enhancement of a thermoelectric power factor in a Ga-doped ZnO system: A chemical compression by enlarged Ga solubility," *Applied Physics Letters,* vol. 100, 2012.

[253] G. K. Paul and S. K. Sen, "Sol-gel preparation, characterization and studies on electrical and thermoelectrical properties of gallium doped zinc oxide films," *Materials Letters,* vol. 57, pp. 742-746, 2002.

[254] O. J. Gregoryz and M. Amani, "Thermoelectric Properties of $Zn_xIn_yO_{x+1.5y}$ Films," *Journal of the Electrochemical Society,* vol. 158, pp. J15-J19, 2011.

[255] D. K. Seo, S. Shin, H. H. Cho, B. H. Kong, D. M. Whang, and H. K. Cho, "Drastic improvement of oxide thermoelectric performance using thermal and plasma treatments of the InGaZnO thin films grown by sputtering," *Acta Materialia,* vol. 59, pp. 6743-6750, 2011.

[256] L. H. Shi, J. Chen, G. Zhang, and B. W. Li, "Thermoelectric figure of merit in Ga-doped 0001 ZnO nanowires," *Physics Letters A,* vol. 376, pp. 978-981, 2012.

[257] Y. Yang, K. C. Pradel, Q. Jing, J. M. Wu, F. Zhang, Y. Zhou*, et al.*, "Thermoelectric Nanogenerators Based on Single Sb-Doped ZnO Micro/Nanobelts," *ACS nano,* vol. 6, pp. 6984-9, 2012.

[258] G. Rodríguez-Gattorno, P. Santiago-Jacinto, L. Rendon-Vazquez, J. Németh, I. Dékány, and D. Díaz, "Novel synthesis pathway of ZnO nanoparticles from the spontaneous hydrolysis of zinc carboxylate salts," *The Journal of Physical Chemistry B,* vol. 107, pp. 12597-12604, 2003.

[259] M. Caglar, S. Ilican, Y. Caglar, and F. Yakuphanoglu, "The effects of Al doping on the optical constants of ZnO thin films prepared by spray pyrolysis method," *Journal of Materials Science: Materials in Electronics,* vol. 19, pp. 704-708, 2008.

[260] J. Zhang, L. Sun, J. Yin, H. Su, C. Liao, and C. Yan, "Control of ZnO morphology via a simple solution route," *Chemistry of Materials,* vol. 14, pp. 4172-4177, 2002.

[261] M. Kamalasanan and S. Chandra, "Sol-gel synthesis of ZnO thin films," *Thin Solid Films,* vol. 288, pp. 112-115, 1996.

[262] K.-S. Choi, H. C. Lichtenegger, G. D. Stucky, and E. W. McFarland, "Electrochemical synthesis of nanostructured ZnO films utilizing self-assembly of surfactant molecules at solid-liquid interfaces," *Journal of the American Chemical Society,* vol. 124, pp. 12402-12403, 2002.

[263] S. He, M. Zheng, L. Yao, X. Yuan, M. Li, L. Ma*, et al.*, "Preparation and properties of ZnO nanostructures by electrochemical anodization method," *Applied Surface Science,* vol. 256, pp. 2557-2562, 2010.

[264] A. Banerjee, C. Ghosh, K. Chattopadhyay, H. Minoura, A. K. Sarkar, A. Akiba*, et al.*, "Low-temperature deposition of ZnO thin films on PET and glass substrates by DC-sputtering technique," *Thin Solid Films,* vol. 496, pp. 112-116, 2006.

[265] G.-C. Yi, C. Wang, and W. I. Park, "ZnO nanorods: synthesis, characterization and applications," *Semiconductor Science and Technology,* vol. 20, p. S22, 2005.

[266] S.-Y. Pung, K.-L. Choy, X. Hou, and C. Shan, "Preferential growth of ZnO thin films by the atomic layer deposition technique," *Nanotechnology,* vol. 19, p. 435609, 2008.

[267] I. Gonzalez-Valls and M. Lira-Cantu, "Vertically-aligned nanostructures of ZnO for excitonic solar cells: a review," *Energy & Environmental Science,* vol. 2, pp. 19-34, 2009.

[268] K. H. Kim, S. H. Shim, K. B. Shim, K. Niihara, and J. Hojo, "Microstructural and Thermoelectric Characteristics of Zinc Oxide-Based Thermoelectric Materials Fabricated Using a Spark Plasma Sintering Process," *Journal of the American Ceramic Society,* vol. 88, pp. 628-632, 2005.

[269] B. Jin, S. Im, and S. Lee, "Violet and UV luminescence emitted from ZnO thin films grown on sapphire by pulsed laser deposition," *Thin Solid Films,* vol. 366, pp. 107-110, 2000.

[270] X. Gou, G. Wang, J. Yang, J. Park, and D. Wexler, "Chemical synthesis, characterisation and gas sensing performance of copper oxide nanoribbons," *Journal of Materials Chemistry,* vol. 18, pp. 965-969, 2008.

[271] T. Ito, H. Yamaguchi, K. Okabe, and T. Masumi, "Single-crystal growth and characterization of Cu_2O and CuO," *Journal of Materials Science,* vol. 33, pp. 3555-3566, 1998.

[272] M. Yin, C.-K. Wu, Y. Lou, C. Burda, J. T. Koberstein, Y. Zhu*, et al.*, "Copper oxide nanocrystals," *Journal of the American Chemical Society,* vol. 127, pp. 9506-9511, 2005.

[273] M. H. Zirin and D. Trivich, "Thermoelectric effect in single-crystal cuprous oxide at high temperatures," *Journal of Chemical Physics,* vol. 39, pp. 870-&, 1963.

[274] B. Balamurugan and B. Mehta, "Optical and structural properties of nanocrystalline copper oxide thin films prepared by activated reactive evaporation," *Thin Solid Films,* vol. 396, pp. 90-96, 2001.

[275] M. Muhibbullah, M. O. Hakim, and M. G. M. Choudhury, "Studies on Seebeck effect in spray deposited CuO thin film on glass substrate," *Thin Solid Films,* vol. 423, pp. 103-107, 2003.

[276] Y. K. Jeong and G. M. Choi, "Nonstoichiometry and electrical conduction of CuO," *Journal of Physics and Chemistry of Solids,* vol. 57, pp. 81-84, 1996.

[277] F. P. Koffyberg and F. A. Benko, "A Photo-Electrochemical determination of the position of the conduction and valence band edges of p type CuO," *Journal of Applied Physics,* vol. 53, pp. 1173-1177, 1982.

[278] J. D. Yu, Y. Inaguma, M. Itoh, M. Oguni, and T. Kyomen, "Effect of oxygen content on the anomalies at successive phase transitions of $La_2CuO_{4+delta}$ single crystal below 320 K," *Physical Review B,* vol. 54, pp. 7455-7461, 1996.

[279] R. Hord, H. Luetkens, G. Pascua, A. Buckow, K. Hofmann, Y. Krockenberger*, et al.*, "Enhanced two-dimensional behavior of metastable T-La_2CuO_4, the parent compound of electron-doped cuprate superconductors," *Physical Review B,* vol. 82, 2010.

[280] Y. Liu, Y. H. Lin, B. P. Zhang, H. M. Zhu, C. W. Nan, J. L. Lan*, et al.*, "High-Temperature Thermoelectric Properties in the $La_{2-x}R_xCuO_4$ (R: Pr, Y, Nb) Ceramics," *Journal of the American Ceramic Society,* vol. 92, pp. 934-937, 2009.

[281] S. Yamanaka, H. Kobayashi, and K. Kurosaki, "Thermoelectric properties of layered rare earth copper oxides," *Journal of Alloys and Compounds,* vol. 349, pp. 321-324, 2003.

[282] L. Armelao, D. Barreca, M. Bertapelle, G. Bottaro, C. Sada, and E. Tondello, "A sol–gel approach to nanophasic copper oxide thin films," *Thin Solid Films,* vol. 442, pp. 48-52, 2003.

[283] S. Li, H. Zhang, Y. Ji, and D. Yang, "CuO nanodendrites synthesized by a novel hydrothermal route," *Nanotechnology,* vol. 15, p. 1428, 2004.

[284] T. Kosugi and S. Kaneko, "Novel Spray-Pyrolysis Deposition of Cuprous Oxide Thin Films," *Journal of the American Ceramic Society,* vol. 81, pp. 3117-3124, 2005.

[285] N. K. Allam and C. A. Grimes, "Electrochemical fabrication of complex copper oxide nanoarchitectures copper anodization in aqueous and non-aqueous electrolytes," *Materials Letters,* vol. 65, pp. 1949-1955, 2011.

[286] J. A. Switzer, H. M. Kothari, P. Poizot, S. Nakanishi, and E. W. Bohannan, "Enantiospecific electrodeposition of a chiral catalyst," *Nature,* vol. 425, pp. 490-493, 2003.

[287] T. Maruyama, "Copper oxide thin films prepared by chemical vapor deposition from copper dipivaloylmethanate," *Solar energy materials and solar cells,* vol. 56, pp. 85-92, 1998.

[288] V. Eyert and K.-H. Höck, "Electronic structure of V_2O_5: Role of octahedral deformations," *Physical Review B,* vol. 57, p. 12727, 1998.

[289] A. M. Cao, J. S. Hu, H. P. Liang, and L. J. Wan, "Self-assembled vanadium pentoxide (V_2O_5) hollow microspheres from nanorods and their application in lithium-ion batteries," *Angewandte Chemie-International Edition,* vol. 44, pp. 4391-4395, 2005.

[290] C. R. Sides and C. R. Martin, "Nanostructured electrodes and the low-temperature performance of Li-ion batteries," *Advanced Materials,* vol. 17, pp. 125-+, 2005.

[291] J. Liu, H. Xia, D. F. Xue, and L. Lu, "Double-Shelled Nanocapsules of V_2O_5-Based Composites as High-Performance Anode and Cathode Materials for Li Ion Batteries," *Journal of the American Chemical Society,* vol. 131, pp. 12086-+, 2009.

[292] N. A. Chernova, M. Roppolo, A. C. Dillon, and M. S. Whittingham, "Layered vanadium and molybdenum oxides: batteries and electrochromics," *Journal of Materials Chemistry,* vol. 19, pp. 2526-2552, 2009.

[293] Z. S. El Mandouh and M. S. Selim, "Physical properties of vanadium pentoxide sol gel films," *Thin Solid Films,* vol. 371, pp. 259-263, 2000.

[294] A. Talledo and C. G. Granqvist, "Electrochromic vanadium-pentoxide based films-Structural,Electrochemical and optical properties," *Journal of Applied Physics,* vol. 77, pp. 4655-4666, 1995.

[295] C. R. Xiong, A. E. Aliev, B. Gnade, and K. J. Balkus, "Fabrication of silver vanadium oxide and V_2O_5 nanowires for electrochromics," *Acs Nano,* vol. 2, pp. 293-301, 2008.

[296] R. B. Darling and S. Iwanaga, "Structure, properties, and MEMS and microelectronic applications of vanadium oxides," *Sadhana-Academy Proceedings in Engineering Sciences,* vol. 34, pp. 531-542, 2009.

[297] P. Kounavis, A. Vomvas, E. Mytilineou, M. Roilos, and L. Murawski, "Thermopower, conductivity and the Hall-effect in V_2O_5 gels," *Journal of Physics C-Solid State Physics,* vol. 21, pp. 967-973, 1988.

[298] A. A. Bahgat, F. A. Ibrahim, and M. M. El-Desoky, "Electrical and optical properties of highly oriented nanocrystalline vanadium pentoxide," *Thin Solid Films,* vol. 489, pp. 68-73, 2005.

[299] S. Iwanaga, M. Marciniak, R. B. Darling, and F. S. Ohuchi, "Thermopower and electrical conductivity of sodium-doped V_2O_5 thin films," *Journal of Applied Physics,* vol. 101, 2007.

[300] Y. J. Liu, J. L. Schindler, D. C. DeGroot, C. R. Kannewurf, W. Hirpo, and M. G. Kanatzidis, "Synthesis, structure, and reactions of poly(ethylene oxide) V_2O_5 intercalative nanocomposites," *Chemistry of Materials,* vol. 8, pp. 525-534, 1996.

[301] K. V. Ramesh and D. L. Sastry, "Transport properties of ZnO substituted lead vanadate glass system at eutectic composition," *Materials Science and Engineering B-Solid State Materials for Advanced Technology,* vol. 126, pp. 66-73, 2006.

[302] S. Beke, "A review of the growth of V_2O_5 films from 1885 to 2010," *Thin Solid Films,* vol. 519, pp. 1761-1771, 2011.

[303] T. Chirayil, P. Y. Zavalij, and M. S. Whittingham, "Hydrothermal synthesis of vanadium oxides," *Chemistry of Materials,* vol. 10, pp. 2629-2640, 1998.

[304] D. Pan, Z. Shuyuan, Y. Chen, and J. Hou, "Hydrothermal preparation of long nanowires of vanadium oxide," *Journal of materials research,* vol. 17, pp. 1981-1984, 2002.

[305] K. Takahashi, S. J. Limmer, Y. Wang, and G. Cao, "Synthesis and electrochemical properties of single-crystal V_2O_5 nanorod arrays by template-based electrodeposition," *The Journal of Physical Chemistry B,* vol. 108, pp. 9795-9800, 2004.

[306] K. Takahashi, S. J. Limmer, and G. Cao, "Template-based growth of V2O5 nanorods by electrodeposition," in *Optical Science and Technology, SPIE's 48th Annual Meeting*, 2003, pp. 33-42.

[307] G. Stefanovich, A. Pergament, A. Velichko, and L. Stefanovich, "Anodic oxidation of vanadium and properties of vanadium oxide films," *Journal of Physics: Condensed Matter,* vol. 16, p. 4013, 2004.

[308] C. Navone, J. Pereira-Ramos, R. Baddour-Hadjean, and R. Salot, "High-capacity crystalline V_2O_5 thick films prepared by RF sputtering as positive electrodes for rechargeable lithium microbatteries," *Journal of the Electrochemical Society,* vol. 153, pp. A2287-A2293, 2006.

[309] J.-C. Badot, A. Mantoux, N. Baffier, O. Dubrunfaut, and D. Lincot, "Electrical properties of V_2O_5 thin films obtained by atomic layer deposition (ALD)," *J. Mater. Chem.,* vol. 14, pp. 3411-3415, 2004.

[310] C. Ramana, R. Smith, O. Hussain, and C. Julien, "Growth and surface characterization of V_2O_5 thin films made by pulsed-laser deposition," *Journal of Vacuum Science & Technology A: Vacuum, Surfaces, and Films,* vol. 22, pp. 2453-2458, 2004.

[311] D. Barreca, L. Armelao, F. Caccavale, V. Di Noto, A. Gregori, G. A. Rizzi*, et al.*, "Highly oriented V_2O_5 nanocrystalline thin films by plasma-enhanced chemical vapor deposition," *Chemistry of materials,* vol. 12, pp. 98-103, 2000.

[312] D. Barreca, C. Massignan, S. Daolio, M. Fabrizio, C. Piccirillo, L. Armelao*, et al.*, "Composition and microstructure of cobalt oxide thin films obtained from a novel cobalt(II) precursor by chemical vapor deposition," *Chemistry of Materials,* vol. 13, pp. 588-593, 2001.

[313] J. Wollenstein, M. Burgmair, G. Plescher, T. Sulima, J. Hildenbrand, H. Bottner*, et al.*, "Cobalt oxide based gas sensors on silicon substrate for operation at low temperatures," *Sensors and Actuators B-Chemical,* vol. 93, pp. 442-448, 2003.

[314] K. Kowalski, M. Ijjaali, T. Bak, B. Dupre, C. Gleitzer, J. Nowotny*, et al.*, "Semiconducting Properties of CoO Thin Films," *Ionics,* vol. 7, pp. 394-399, 2001.

[315] X. C. Tong, "Thermoelectric Cooling Through Thermoelectric Materials," in *Advanced Materials for Thermal Management of Electronic Packaging*. vol. 30, ed, 2011, pp. 477-525.

[316] M. Lee, L. Viciu, L. Li, Y. Y. Wang, M. L. Foo, S. Watauchi*, et al.*, "Large enhancement of the thermopower in Na_xCoO_2 at high Na doping," *Nature Materials,* vol. 5, pp. 537-540, 2006.

[317] T. Nagira, M. Ito, S. Katsuyama, K. Majima, and H. Nagai, "Thermoelectric properties of $(Na_{1-y}M_y)_xCo_2O_4$(M= K, Sr, Y, Nd, Sm and Yb; y= 0.01- 0.35)," *Journal of alloys and compounds,* vol. 348, pp. 263-269, 2003.

[318] J. Y. Kim, J. I. Kim, and W. S. Seo, "Exfoliation Route to Nanostructured Cobalt Oxide with Enhanced Thermoelectric Performance," *Applied Physics Express,* vol. 4, 2011.

[319] J.-Y. Kim, J.-I. Kim, S.-M. Choi, Y. S. Lim, W.-S. Seo, and H. J. Hwang, "Nanostructured thermoelectric cobalt oxide by exfoliation/restacking route," *Journal of Applied Physics,* vol. 112, pp. 113705-8, 2012.

[320] Y. Wang, Y. Sui, J. Cheng, X. Wang, and W. Su, "Comparison of the high temperature thermoelectric properties for Ag-doped and Ag-added $Ca_3Co_4O_9$," *Journal of Alloys and Compounds,* vol. 477, pp. 817-821, 2009.

[321] F. Zhang, Q. Lu, and J. Zhang, "Synthesis and high temperature thermoelectric properties of $Ba_xAg_yCa_{3-x-y}Co_4O_9$ compounds," *Journal of Alloys and Compounds,* vol. 484, pp. 550-554, 2009.

[322] Y. Song, Q. Sun, L. Zhao, F. Wang, and Z. Jiang, "Synthesis and thermoelectric power factor of $(Ca_{0.95}Bi_{0.05})_3Co_4O_9$/Ag composites," *Materials Chemistry and Physics,* vol. 113, pp. 645-649, 2009.

[323] Y. Wang, Y. Sui, J. Cheng, X. Wang, and W. Su, "Efficient room temperature thermoelectric characteristics of $Ca_{3-x}Ag_xCo_4O_{9+\delta}/Ag_y$ composites," *Journal of Physics D: Applied Physics,* vol. 41, p. 045406, 2008.

[324] I. Matsubara, R. Funahashi, T. Takeuchi, and S. Sodeoka, "Thermoelectric properties of spark plasma sintered $Ca_{2.75}Gd_{0.25}Co_4O_9$ ceramics," *Journal of Applied Physics,* vol. 90, pp. 462-465, 2001.

[325] Q. Yao, D. Wang, L. Chen, X. Shi, and M. Zhou, "Effects of partial substitution of transition metals for cobalt on the high-temperature thermoelectric properties of $Ca_3Co_4O_{9+\delta}$," *Journal of applied physics,* vol. 97, pp. 103905-103905-5, 2005.

[326] Y. Wang, Y. Sui, X. Wang, W. Su, and X. Liu, "Enhanced high temperature thermoelectric characteristics of transition metals doped $Ca_3Co_4O_{9+\delta}$ by cold high-pressure fabrication," *Journal of Applied Physics,* vol. 107, pp. 033708-033708-9, 2010.

[327] N. Nong, C. J. Liu, and M. Ohtaki, "Improvement on the high temperature thermoelectric performance of Ga-doped misfit-layered $Ca_3Co_{4-x}Ga_xO_{9+\delta}$(x= 0, 0.05, 0.1, and 0.2)," *Journal of Alloys and Compounds,* vol. 491, pp. 53-56, 2010.

[328] K. Sugiura, H. Ohta, K. Nomura, M. Hirano, H. Hosono, and K. Koumoto, "High electrical conductivity of layered cobalt oxide $Ca_3Co_4O_9$ epitaxial films grown by topotactic ion-exchange method," *Applied physics letters,* vol. 89, p. 032111, 2006.

[329] K. Sugiura, H. Ohta, K. Nomura, M. Hirano, H. Hosono, and K. Koumoto, "Fabrication and thermoelectric properties of layered cobaltite, gamma-$Sr_{0.32}Na_{0.21}CoO_2$ epitaxial films," *Applied Physics Letters,* vol. 88, 2006.

[330] G. Wang, X. Shen, J. Horvat, B. Wang, H. Liu, D. Wexler*, et al.*, "Hydrothermal synthesis and optical, magnetic, and supercapacitance properties of nanoporous cobalt oxide nanorods," *The Journal of Physical Chemistry C,* vol. 113, pp. 4357-4361, 2009.

[331] Y. Shao, J. Sun, and L. Gao, "Hydrothermal Synthesis of Hierarchical Nanocolumns of Cobalt Hydroxide and Cobalt Oxide," *The Journal of Physical Chemistry C,* vol. 113, pp. 6566-6572, 2009.

[332] X. W. Xie and W. J. Shen, "Morphology control of cobalt oxide nanocrystals for promoting their catalytic performance," *Nanoscale,* vol. 1, pp. 50-60, 2009.

[333] I. G. Casella, "Electrodeposition of cobalt oxide films from carbonate solutions containing Co (II)–tartrate complexes," *Journal of Electroanalytical Chemistry,* vol. 520, pp. 119-125, 2002.

[334] M. E. Grillo, "Stability of corundum- versus rutile-type structures of ruthenium and rhodium oxides," *Physical Review B,* vol. 70, 2004.

[335] S. Music, A. Saric, S. Popovic, and M. Ivanda, "Formation and characterisation of nanosize alpha-Rh2O3 particles," *Journal of Molecular Structure,* vol. 924-26, pp. 221-224, 30 2009.

[336] P. Watson and G. Somorjai, "The hydrogenation of carbon monoxide over rhodium oxide surfaces," *Journal of Catalysis,* vol. 72, pp. 347-363, 1981.

[337] W. Dautremont-Smith, "Transition metal oxide electrochromic materials and displays: a review: Part 2: oxides with anodic coloration," *Displays,* vol. 3, pp. 67-80, 1982.

[338] D. A. J. M. Ligthart, R. A. van Santen, and E. J. M. Hensen, "Supported Rhodium Oxide Nanoparticles as Highly Active CO Oxidation Catalysts," *Angewandte Chemie International Edition,* vol. 50, pp. 5306-5310, 2011.

[339] W. Koshibae, K. Tsutsui, and S. Maekawa, "Thermopower in cobalt oxides," *Physical Review B,* vol. 62, pp. 6869-6872, 2000.

[340] S. Okada and I. Terasaki, "Physical properties of Bi-based rhodium oxides with RhO_2 hexagonal layers," *Japanese Journal of Applied Physics Part 1-Regular Papers Brief Communications & Review Papers,* vol. 44, pp. 1834-1837, 2005.

[341] S. Okada, A. Sakai, T. Kanno, S. Yotsuhashi, and H. Adachi, "Thermoelectric properties of bismuth based cobalt-rhodium oxides with hexagonal $(Co,Rh)O_2$ layers," *Journal of Applied Physics,* vol. 105, 2009.

[342] W. Kobayashi, W. Tamura, and I. Terasaki, "Thermal conductivity of thermoelectric rhodium oxides measured by a modified Harman method," *Journal of the Physical Society of Japan,* vol. 77, 2008.

[343] Y. Saeed, N. Singh, and U. Schwingenschlögl, "Colossal Thermoelectric Power Factor in $K_{7/8}RhO_2$," *Advanced Functional Materials,* vol. 22, pp. 2792-2796, 2012.

[344] H. H. Wang, M. M. Yan, and Z. Y. Jiang, "Electrochromic properties of rhodium oxide films prepared by a sol-gel method," *Thin Solid Films,* vol. 401, pp. 211-215, 2001.

[345] H. H. Wang, C. J. Zhao, M. M. Yan, and Z. Y. Jiang, "Preparation of rhodium oxide films and its electrochromic study," *Acta Chimica Sinica,* vol. 60, pp. 1203-1208, 2002.

[346] E. Moran-Miguelez and M. Alario-Franco, "Hydrothermal synthesis and reactivity of rhodium dioxide and oxyhydroxide," *Thermochimica Acta,* vol. 60, pp. 181-186, 1983.

[347] L. Marot, D. Mathys, G. D. Temmerman, and P. Oelhafen, "Characterization of sub-stoichiometric rhodium oxide deposited by magnetron sputtering," *Surface Science,* vol. 602, pp. 3375-3380, 2008.

[348] O. Muller and R. Roy, "Formation and stability of the platinum and rhodium oxides at high oxygen pressures and the structures of Pt_3O_4, β-PtO_2 and RhO_2," *Journal of the Less Common Metals,* vol. 16, pp. 129-146, 1968.

[349] J. N. Yao, K. Hashimoto, and A. Fujishima, "Photochromism induced in an electrolytically pretreated MoO_3 thin film by visible light," *Nature,* vol. 355, pp. 624-626, 1992.

[350] T. He and J. N. Yao, "Photochromism in composite and hybrid materials based on transition-metal oxides and polyoxometalates," *Progress in Materials Science,* vol. 51, pp. 810-879, 2006.

[351] A. M. Azad, S. G. Mhaisalkar, L. D. Birkefeld, S. A. Akbar, and K. S. Goto, "Behavior of a new ZrO_2-MoO_3 sensor for carbon-monoxide detection," *Journal of the Electrochemical Society,* vol. 139, pp. 2913-2920, 1992.

[352] Q. Y. Ouyang, L. Li, Q. S. Wang, Y. Zhang, T. S. Wang, F. N. Meng*, et al.*, "Facile synthesis and enhanced H_2S sensing performances of Fe-doped alpha-MoO_3 micro-structures," *Sensors and Actuators B-Chemical,* vol. 169, pp. 17-25, 2012.

[353] D. W. Zhao, X. W. Sun, C. Y. Jiang, A. K. K. Kyaw, G. Q. Lo, and D. L. Kwong, "Efficient tandem organic solar cells with an Al/MoO_3 intermediate layer," *Applied Physics Letters,* vol. 93, 2008.

[354] L. Cattin, F. Dahou, Y. Lare, M. Morsli, R. Tricot, S. Houari*, et al.*, "MoO_3 surface passivation of the transparent anode in organic solar cells using ultrathin films," *Journal of Applied Physics,* vol. 105, 2009.

[355] F. J. Zhang, X. W. Xu, W. H. Tang, J. Zhang, Z. L. Zhuo, J. Wang*, et al.*, "Recent development of the inverted configuration organic solar cells," *Solar energy materials and solar cells,* vol. 95, pp. 1785-1799, 2011.

[356] S. Balendhran, S. Walia, H. Nili, J. Z. Ou, S. Zhuiykov, R. B. Kaner*, et al.*, "Two-Dimensional Molybdenum Trioxide and Dichalcogenides," *Advanced Functional Materials,* p. 10.1002/adfm.201300125, 2013.

[357] P. F. Carcia and E. M. McCarron, "Synthesis and properties of thin film polymorphs of molybdenum trioxide," *Thin Solid Films,* vol. 155, pp. 53-63, 1987.

[358] D. Di Yao, J. Z. Ou, K. Latham, S. Zhuiykov, A. P. O'Mullane, and K. Kalantar-zadeh, "Electrodeposited alpha- and beta-Phase MoO_3 Films and Investigation of Their Gasochromic Properties," *Crystal Growth & Design,* vol. 12, pp. 1865-1870, 2012.

[359] K. Kalantar-zadeh, J. S. Tang, M. S. Wang, K. L. Wang, A. Shailos, K. Galatsis*, et al.*, "Synthesis of nanometre-thick MoO_3 sheets," *Nanoscale,* vol. 2, pp. 429-433, 2009.

[360] D. O. Scanlon, G. W. Watson, D. J. Payne, G. R. Atkinson, R. G. Egdell, and D. S. L. Law, "Theoretical and Experimental Study of the Electronic Structures of MoO3 and MoO2," *Journal of Physical Chemistry C,* vol. 114, pp. 4636-4645, 2010.

[361] D. O. Scanlon, G. W. Watson, D. Payne, G. Atkinson, R. Egdell, and D. Law, "Theoretical and Experimental Study of the Electronic Structures of MoO_3 and MoO_2," *The Journal of Physical Chemistry C,* vol. 114, pp. 4636-4645, 2010.

[362] J. X. Xu, M. Sonne, N. Pryds, and H. Kleinke, "Thermoelectric properties of molybdenum oxides $LnMo_{(8)}O_{(14)}$ (Ln = La, Ce, Pr, Nd and Sm)," *Journal of Alloys and Compounds,* vol. 489, pp. 353-356, 2010.

[363] J. X. Xu, M. Sonne, S. I. Yanangiya, N. Van Nong, N. Pryds, M. Nygren*, et al.*, "High thermoelectric performance of reduced lanthanide molybdenum oxides densified by spark plasma sintering," *Journal of Alloys and Compounds,* vol. 500, pp. 22-25, 2010.

[364] K. R. Anilkumar, A. Parveen, G. R. Badiger, and M. Prasad, "Thermoelectric Power Factor for Polyaniline/Molybdenum Trioxide Composites," *Ferroelectrics,* vol. 386, pp. 88-93, 2009.

[365] S. A. Mulenko, "Synthesis of nanometric iron and chromium oxide films by reactive pulsed laser deposition for photo-thermo sensors," in *Fundamentals of Laser-Assisted Micro- and Nanotechnologies 2010*. vol. 7996, V. P. Veiko and T. A. Vartanyan, Eds., ed Bellingham: Spie-Int Soc Optical Engineering, 2011.

[366] S. Sugihara, C. Suzuki, and R. Kameya, "High thermoelectric performance of metal substituted samples of α Fe_2O_3 and computation of their electronic structures by the DVXα method," *International Journal of Quantum Chemistry,* vol. 109, pp. 2788-2792, 2009.

[367] S. Rajendran and V. S. Rao, "An anomalous behaviour in the phase stability of the system Fe2O3 and NiO," *Journal of Materials Science,* vol. 29, pp. 5673-5679, 1994.

[368] L. Vayssieres, C. Sathe, S. M. Butorin, D. K. Shuh, J. Nordgren, and J. Guo, "One-Dimensional Quantum-Confinement Effect in α-Fe_2O_3 Ultrafine Nanorod Arrays," *Advanced Materials,* vol. 17, pp. 2320-2323, 2005.

[369] F. Maldonado, C. Novillo, and A. Stashans, "Ab initio calculation of chromium oxide containing Ti dopant," *Chemical Physics,* vol. 393, pp. 148-152, 2012.

[370] E. W. A. Young, J. H. Gerretsen, and J. H. W. Dewit, "The oxygen partial pressure dependence of the defect structure of chromium(III) oxide," *Journal of the Electrochemical Society,* vol. 134, pp. 2257-2260, 1987.

[371] H. Nagai and K. Ohbayashi, "Effect of TiO_2 on the Sintering and the Electrical Conductivity of Cr_2O_3," *Journal of the American Ceramic Society,* vol. 72, pp. 400-403, 1989.

[372] K. Hayashi, K. Sato, T. Nozaki, and T. Kajitani, "Effect of doping on thermoelectric properties of delafossite-type oxide $CuCrO_2$," *Japanese Journal of Applied Physics,* vol. 47, pp. 59-63, 2008.

[373] P. Tomes, D. Logvinovich, J. Hejtmanek, M. H. Aguirre, and A. Weidenkaff, "Magnetic influence on thermoelectric properties of $CrO_{0.1}N_{0.9}$," *Acta Materialia,* vol. 59, pp. 1134-1140, 2011.

[374] Y. Kakehi, K. Satoh, T. Yotsuya, A. Ashida, T. Yoshimura, and N. Fujimura, "Electrical and optical properties of excess oxygen intercalated $CuScO_2$(0001) epitaxial films prepared by oxygen radical annealing," *Thin Solid Films,* vol. 516, pp. 5785-5789, 2008.

[375] S. Zhuiykov, *Electrochemistry of zirconia gas sensors*: CRC Press, 2010.

[376] F. Zandiehnadem, R. A. Murray, and W. Y. Ching, "Electronic structures of three phases of zirconium oxide," *Physica B+C,* vol. 150, pp. 19-24, 1988.

[377] P. H. Jefferson, S. Hatfield, T. D. Veal, P. King, C. F. McConville, J. Zúñiga-Pérez*, et al.*, "Bandgap and effective mass of epitaxial cadmium oxide," *Applied Physics Letters,* vol. 92, pp. 022101-022101-3, 2008.

[378] K. Gurumurugan, D. Mangalaraj, S. K. Narayandass, and Y. Nakanishi, "DC reactive magnetron sputtered CdO thin films," *Materials Letters,* vol. 28, pp. 307-312, 1996.

[379] R. Wright, "The Variation with Temperature of the Electrical Properties of a Degenerate Electronic Semiconductor as exemplified by Cadmium Oxide," *Proceedings of the Physical Society. Section A,* vol. 64, p. 350, 2002.

[380] R. R. Salunkhe, D. S. Dhawale, T. P. Gujar, and C. D. Lokhande, "Structural, electrical and optical studies of SILAR deposited cadmium oxide thin films: Annealing effect," *Materials Research Bulletin,* vol. 44, pp. 364-368, 2009.

[381] K. Gurumurugan, D. Mangalaraj, S. K. Narayandass, K. Sekar, and C. G. Vallabhan, "Characterization of transparent conducting CdO films deposited by spray pyrolysis," *Semiconductor Science and Technology,* vol. 9, p. 1827, 1999.

[382] B. Li and J. Zhang, "Electrical Conductivity of Cadmium Oxide—Antimony Oxide System Ceramics," *Journal of the American Ceramic Society,* vol. 72, pp. 2377-2380, 1989.

[383] M. D. Irwin, D. B. Buchholz, A. W. Hains, R. P. Chang, and T. J. Marks, "p-Type semiconducting nickel oxide as an efficiency-enhancing anode interfacial layer in polymer bulk-heterojunction solar cells," *Proceedings of the National Academy of Sciences,* vol. 105, pp. 2783-2787, 2008.

[384] G. Parravano, "Thermoelectric Behavior of Nickel Oxide," *The Journal of Chemical Physics,* vol. 23, p. 5, 1955.

[385] P. S. Patil and L. D. Kadam, "Preparation and characterization of spray pyrolyzed nickel oxide (NiO) thin films," *Applied Surface Science,* vol. 199, pp. 211-221, 2002.

[386] W. Shin and N. Murayama, "Li-doped nickel oxide as a thermoelectric material," *Japanese Journal of Applied Physics,* vol. 38, pp. L1336-L1338, 1999.

[387] M. B. Dutt, R. Banerjee, and A. K. Barua, "Transport properties of Lithium and Sodium doped Nickel oxide," *Physica Status Solidi a-Applied Research,* vol. 65, pp. 365-370, 1981.

[388] N. Keawprak, R. Tu, and T. Goto, "Thermoelectricity of $CaIrO_3$ ceramics prepared by spark plasma sintering," *Journal of the Ceramic Society of Japan,* vol. 117, pp. 466-469, 2009.

[389] N. Keawprak, R. Tu, and T. Goto, "Thermoelectric Properties of Ca-Ir-O Compounds Prepared by Spark Plasma Sintering," *Materials Transactions,* vol. 50, pp. 853-858, 2009.

[390] N. Keawprak, R. Tu, and T. Goto, "Thermoelectric properties of Sr–Ir–O compounds prepared by spark plasma sintering," *Journal of Alloys and Compounds,* vol. 491, pp. 441-446, 2010.

Chapter 3

Oscillatory Thermopower Wave Sources based on Bi_2Te_3

3.1 Introduction

In chapter 1, it was highlighted that prior to the commencement of the author's PhD candidature, only one thermopower wave system that incorporated multi-walled carbon nanotubes (MWNTs) as the thermoelectric (TE) cores had been reported (by Strano group at MIT) [1]. However, the main limitation of that work was that their system generated low voltages (generally 30-50 mV) and oscillation amplitudes. This highlighted the need for investigating other core thermoelectric (TE) materials that exhibit high Seebeck coefficients (S), electrical conductivities (σ) and moderate thermal conductivities (κ) so that the output voltages from such sources could be increased, while maintaining a high specific power. In order to identify the potential core TE materials that exhibit the aforementioned properties, the author reviewed the TE properties of conventional TE materials such as bismuth telluride (Bi_2Te_3), antimony telluride (Sb_2Te_3) and TE transition metal oxides (TMOs) in the previous chapter. Based on the analysis carried out in chapter 2, the author of this thesis identified Bi_2Te_3 as one of the potential candidates due to its high S (~ –200 μV/K) and σ (10^5 S/m).

In this chapter, the author will demonstrate thin film thermopower wave generation systems based on n-type Bi_2Te_3 as the core TE material. As a moderate to high thermal conductivity is essential to sustain the self-propagation of the thermopower waves, the author will compensate for the low κ of Bi_2Te_3 by depositing it on thermally conductive alumina (Al_2O_3) substrates. Subsequently, highly exothermic chemical reaction of a solid fuel (nitrocellulose) will be coupled to charge carriers in the Bi_2Te_3 layers to generate self-propagating thermopower waves which entrain charge carriers of Bi_2Te_3 to generate voltage and power.

The author will conduct a comprehensive theoretical analysis of the Bi_2Te_3 based thermopower wave system by adapting the theory of combustion waves to assess and predict the behaviour of the thermopower waves in thin film geometries. A thorough analysis of the system will be carried out by characterizing the Bi_2Te_3 films before and after the thermopower wave propagation. The influence of the mass of fuel on the voltage and power generated will be studied. Terracotta substrates, which exhibit contrastingly low thermal conductivity compared to Al_2O_3 will also be used to study the role of the substrate thermal conductivity on the behaviour of thermopower waves. Additionally, the influence of the Bi_2Te_3 film thickness on the output voltage will also be investigated by the author. The work in this chapter was published as a full article in the journal Advanced Functional Materials.

3.2 Experimental

3.2.1 Synthesis of Bi_2Te_3 films

RF magnetron sputtering was used to deposit Bi_2Te_3 films. High purity (99%) Bi_2Te_3 sputtering target (Vin Karola Instruments) was used in the process [2]. The sputtering process was started after the chamber was pumped down to 2×10^{-5} torr. Al_2O_3 and terracotta, with dimensions in the order of 5 to 25 mm, were used as substrates after being adequately cleaned using acetone, isopropanol and distilled water successively, and dried using a high pressure air gun. The choice of substrates was based on their contrasting thermal conductivities. Al_2O_3 has a thermal conductivity of over 20 W/m.K while terracotta has a thermal conductivity of approximately 1 W/m.K [3, 4]. This difference enabled the author to test the performance of the system for two extremely different thermal conductivities and compare the results with our theoretical model which is described in section 3.3 of this chapter. The substrates were kept at 100 ºC during the sputtering process. RF sputtering power of 100 W was used throughout the deposition process. The sputtering process was carried out under an atmosphere of 100% Argon (Ar). A sputtering time of 90 min resulted in 5 µm Bi_2Te_3 layer. Adhesive conductive

silver (Ag) paste (42469, Alfa Aesar) was used to make electrical contacts between the copper tape electrodes and the Bi_2Te_3 samples. Their resistance ranged from 2 Ω to 10 Ω.

3.2.2 Preparation of the fuel

Nitrocellulose [C_6H_8 $(NO_2)_2O_5$] was used as the fuel due to its large enthalpy of reaction. Nitrocellulose was prepared by dissolving millipore nitrocellulose membranes (N8645, Sigma Aldrich) in acetonitrile (15g/L). This solution was dropped onto the Bi_2Te_3 film using a pipette and left to dry in ambient air. The acetonitrile evaporated, leaving a layer of adhesive nitrocellulose coating. Sodium azide (NaN_3) (14314, Alfa Aesar) in aqueous solution (50mg/mL) was then added on top of the nitrocellulose layer using a pipette to serve as a primary igniter. The total thickness of the fuel layers was approximately 240 µm. A schematic representation of a fuel/Bi_2Te_3/substrate thermopower wave device is shown in Figure 3.1.

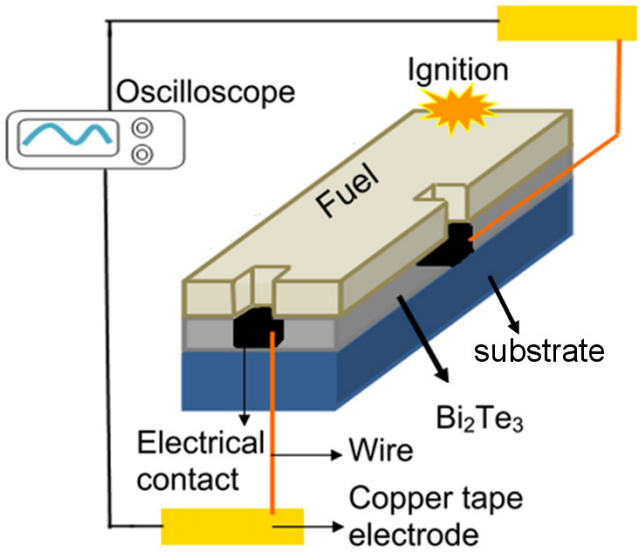

Figure 3.1: Schematic representation of a fuel/Bi_2Te_3/substrate system (not to scale).

3.2.3 Characterization of the Bi_2Te_3 film surface

Scanning electron microscopy was conducted using the FEI Nova Nano SEM to investigate the structure of the Bi_2Te_3 films to assess their porosity. Figures 3.2 (a,b) show SEM images of the Bi_2Te_3 film for two different thicknesses (5 and 10 µm) on

Al_2O_3 substrates. Figures 3.2 (c,d) show their cross-sectional view. The images show clearly that the Bi_2Te_3 film is not smooth but consists of layers made of nano sized flakes of irregular shape and size.

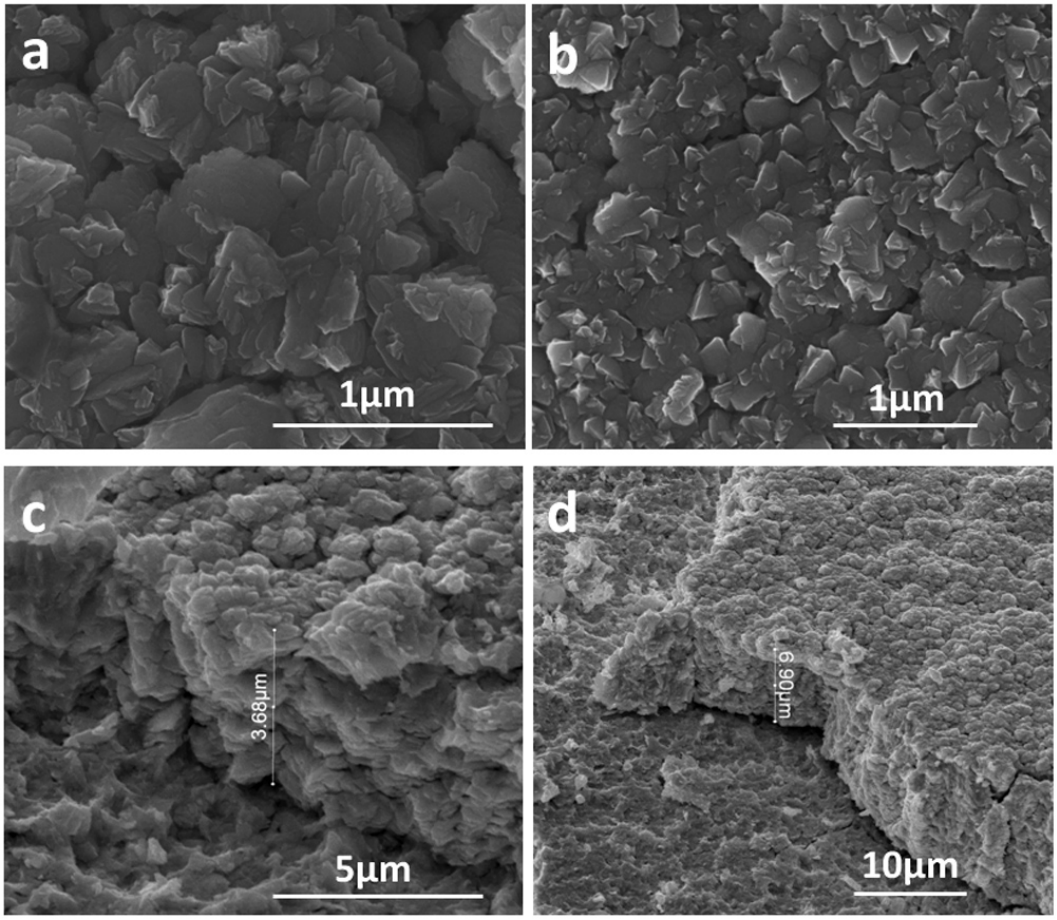

Figure 3.2: SEM image of Bi_2Te_3 film (a) 5 µm thick on Al_2O_3, (b) 10 µm thick on Al_2O_3. Cross-sectional SEM images of (c) 5 µm Bi_2Te_3 film on Al_2O_3 substrate and (d) a 10 µm Bi_2Te_3 film on Al_2O_3 substrate, The samples in (c,d) were tilted at an angle of 45^o when the SEM images were taken. Hence, the thickness of the Bi_2Te_3 films in (c) & (d) are $3.68\sqrt{2}$ = 5.2 µm and $6.9\sqrt{2}$ = 9.8 µm, respectively.

An AMBIOS Technology (XP-2 SERIES) profiler was used in order to further investigate the morphology of the Bi_2Te_3 surface. Figures 3.3 (a,b) show the surface profile of the 5 and 10 µm Bi_2Te_3 films, respectively, as well as the surface profile of the Al_2O_3 substrate. The standard deviation of approximately 0.6 and 0.7 µm was obtained for Bi_2Te_3 surface roughness for 5 and 10 µm films, respectively, indicating their almost similar porous natures. Obviously, a greater porosity enables more fuel to be placed on

the surface of the film, resulting in a sustained reaction propagation. Additionally, porosity is also important to increase the thermal conductivity between the fuel and the TE films.

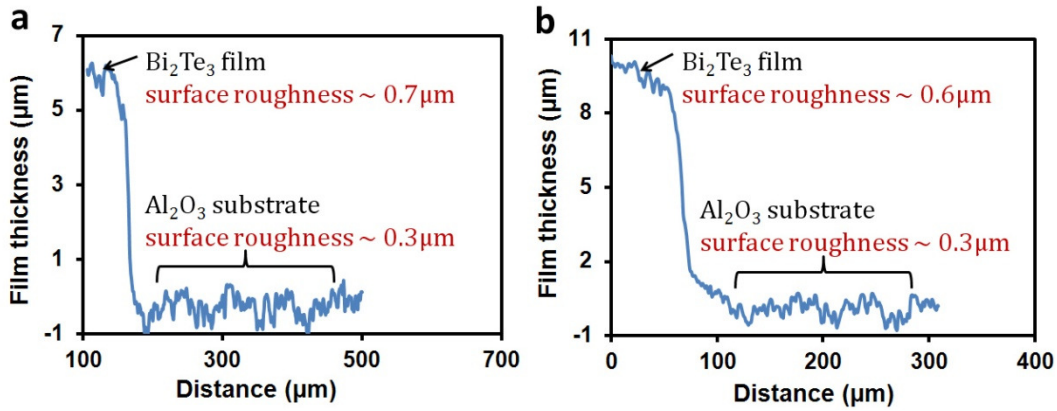

Figure 3.3: Surface profile of (a) 5 µm Bi_2Te_3 film on Al_2O_3 substrate, and (b) surface profile of 10 µm Bi_2Te_3 film on Al_2O_3 substrate.

In order to observe the crystalline structure of Bi_2Te_3, and the effect of nitrocellulose on the crystallinity of the sample, x-ray diffraction (XRD) was carried out using a Bruker D8 DISCOVER microdiffractometer fitted with a GADDS (General Area Detector Diffraction System). Data was collected at room temperature using CuKα radiation (λ = 1.54178 Å) with a potential of 40 kV and a current of 40 mA, and filtered with a graphite monochromator in the parallel mode (175 mm collimator with 0.5 mm pinholes). The effect of NaN_3 could not be investigated using XRD due to its low reaction threshold. The XRD data (Figures 3.4 (a,b)) show that the crystallinity of Bi_2Te_3 changes slightly with a change in film thickness. The XRD pattern of Bi_2Te_3 also reveals its polycrystalline nature [5]. Deposition of nitrocellulose on the Bi_2Te_3 film also influences the XRD pattern. The Bi_2Te_3 peak at around 18.1° 2θ ((006) plane for rhombohedral Bi_2Te_3– ICDD No. [1-75-0921]) is no longer exhibited in the Bi_2Te_3 samples with nitrocellulose (Figures 3.4 (c,d)). The disappearance of this peak may be due to incoherent scattering and adsorption effects. It is possible, that on coating the Bi_2Te_3 sample with the nitrocellulose surface was effectively masked, inhibiting the penetration of x-rays to, and collection of scattering data from, the lower Bi_2Te_3 surface. This effect is

particularly acute for the relatively low intensity (006) Bi_2Te_3 peak, which occurs in the same region as the principal XRD reflections for nitrocellulose (ICDD No. [03-0114]). This argument is confirmed further by XRD data from samples following consumption of the nitrocellulose, where the (006) peak reappears (Figure 3.4 (e)).

The effect of adding nitrocellulose on the 18.1º 2θ peak is slightly different for the 5 and 10 µm Bi_2Te_3 films. This observation may be due to slightly different porosities of the two Bi_2Te_3 thicknesses, resulting in different behaviour of incoherent scattering and adsorption effects.

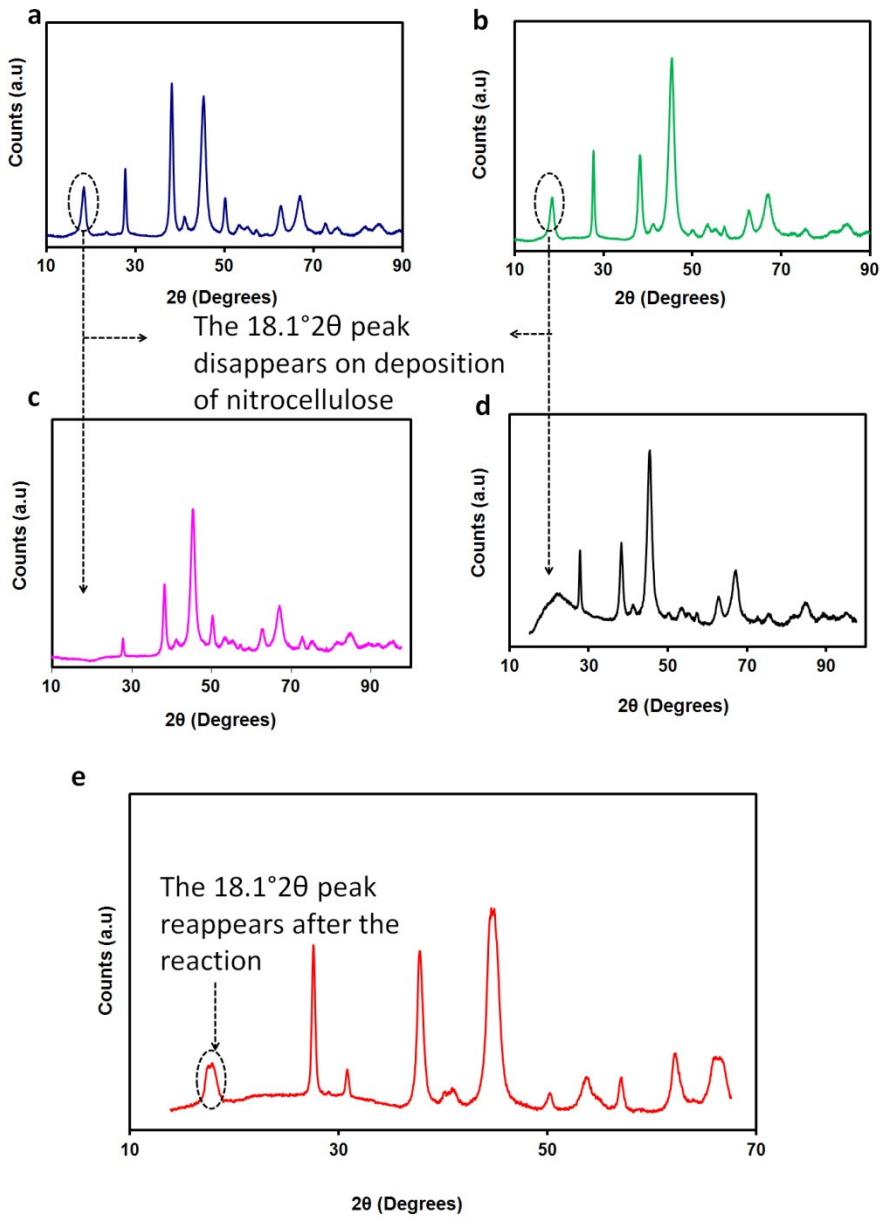

Figure 3.4: XRD pattern of: (a) 5 µm thick Bi_2Te_3 film, (b) 10 µm thick Bi_2Te_3 film, (c) 5 µm thick Bi_2Te_3 film after depositing a layer of nitrocellulose, and (d) 10 µm thick Bi_2Te_3 film after depositing a layer of nitrocellulose and (e) the Bi_2Te_3 film after the reaction (note: traces of oxidized Bi_2Te_3 (ICDD No. [24-0154]) and carbon are also present in the after the reaction XRD pattern. The oxidation of Bi_2Te_3 may be the reason for the emergence of the 31° 2θ that appears in (e) after the consumption of nitrocellulose.

3.2.4 Thermal conduction of Al_2O_3 and terracotta substrates

In order to show the difference in thermal conductivities of the Al_2O_3 and terracotta substrates, both were heated at one end for the same duration using a custom-made blowtorch and the temperature profile was obtained at the other end to see how fast thermal conduction occurs through the substrate.

As seen from Figure 3.5, the temperature for Al_2O_3 rises rapidly to about 130 ^oC in about 40 sec. The terracotta substrate however reaches a maximum temperature of around 40 ^oC and takes about twice the time taken by Al_2O_3 to reach peak temperature. It should be noted that the temperature continues to rise even after the heat source is withdrawn. This is because heat takes time to travel from one end to the other and finally dissipates, depending on the thermal conductivity of the material. Therefore, the peak temperature is obtained a few seconds after the heat source is turned off. However we can see that terracotta takes approximately 60 seconds longer than Al_2O_3 to reach its peak temperature. A similar observation is made in the cooling durations of the two substrates. While Al_2O_3 cools down to room temperature in about 150 seconds from the point of its peak temperature, terracotta takes approximately 240 seconds to cool down to room temperature. These observations clearly demonstrate that the thermal conduction through terracotta is significantly slower than Al_2O_3.

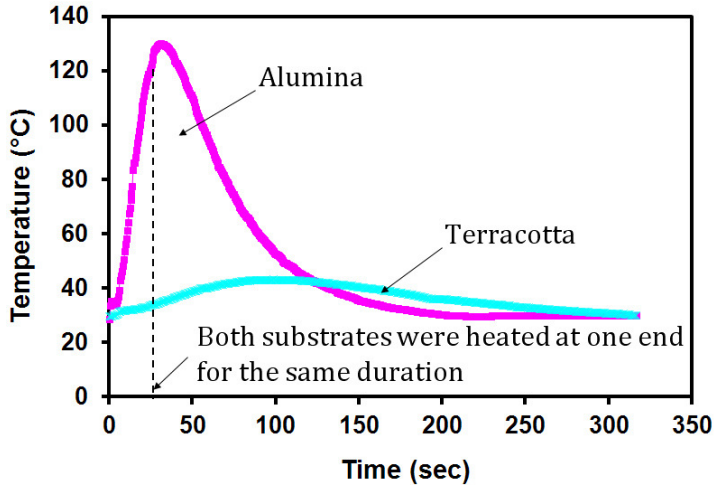

Figure 3.5: Difference in the thermal conduction rate of Al_2O_3 and terracotta substrates.

3.2.5 Calculation of Specific Power

In order to obtain the specific power, the masses of the fuel (nitrocellulose & sodium azide) and Bi_2Te_3 films were considered. The relationship between mass, density and volume was used for calculating the mass of the Bi_2Te_3 as: $m = \rho \times V$ where, m is the mass in grams (g), ρ is the density in g/cm^3 and V is the volume in cm^3.

For Bi_2Te_3 ρ=7.7 g/cm^3 [6] and V depends on the dimensions of the sample and is calculated using the formula $V = l \times w \times h$, where l is the length, w is the width and h is the thickness of the Bi_2Te_3 film in cm, respectively.

For fuels, nitrocellulose and NaN_3 in our case, we knew the concentration of the two in their respective solutions. As mentioned in Section 3.2.2, 15g/L nitrocellulose and 20g/L NaN_3 were used by drop casting. Hence, we know the amount of solution for each fuel and therefore the corresponding mass for each sample, depending on the volume of the liquid placed on the Bi_2Te_3 films. The sum of the masses of the Bi_2Te_3 film and the fuels gives the total mass of the materials used. The corresponding power from the sample is then scaled to per kg of the materials to obtain the specific power of the sample in kW/kg.

3.3 Theory of Thermopower Wave oscillations

In order to assess the behaviour of the thermopower waves the author adapted the theory of combustion waves to describe coupled thermal waves in fuel/ Bi_2Te_3/ Al_2O_3 or fuel/ Bi_2Te_3/ terracotta systems. The Bi_2Te_3 layer is comparatively thin (5 or 10 μm compared to 100 μm Al_2O_3 substrate), so the main path for thermal conduction is through the substrate. Additionally, our experimental systems are much longer than they are wide. As a result, one-dimensional approximations for both the fuel/Al_2O_3 system and the fuel/terracotta system are considered in the calculations. It means that fuel either exchanges heat with a thermally conductive substrate of alumina with κ=20 W.m^{-1}.K^{-1} or much less thermally conductive substrate of terracotta with κ=1 W/m.K (see Figure 3.5).

The theoretical approach is of particular importance as it can be used to predict the behaviour of the system, the velocity of the wave front and the possibility of oscillations. It is assumed that the solid fuel combustion is exothermic, oxygen is supplied in excess, and governed by Arrhenius kinetics with volumetric heat loss, the dimensional equations for the conservation of heat and mass are [7]:

$$\rho c_p \frac{\partial T}{\partial t} = k\frac{\partial^2 T}{\partial x^2} + \rho QAwe^{-E/RT} - \frac{hS}{V}(T - T_a) \quad (1)$$

$$\rho\frac{\partial w}{\partial t} = -\rho Awe^{-E/RT} \quad (2)$$

where T and w denote the temperature and the concentration of the fuel, respectively; x and t describe space and time variables, ρ is the density of the fuel (kg/m^3), c_p is the specific heat of the fuel (J/kg.K), k is the thermal conductivity of the fuel (J/s.m.K), Q is the heat of reaction (J/kg), A is the pre-exponential rate constant (/s), E is the activation energy (J/mol), R is the universal gas constant (8.314 J/mol.K). Heat is transferred from the fuel layer to the Bi_2Te_3/substrate layer and to the surroundings. As we are using a one-dimensional averaged model, the term $\frac{hS}{V}(T - T_a)$ models both the transfer to Bi_2Te_3/substrate and the Newtonian cooling to the ambient surrounding, which is at a temperature T_a [7]. In the latter case, S/V is the surface-area-to-volume ratio of the fuel (/m) and h is the heat transfer coefficient from the fuel to the quiescent surroundings (J/s.m^2.K^1) [7] which is typically quite small. The term $\rho QAwe^{-E/RT}$ in Equation (1) accounts for the exponential decomposition reaction of the fuel.

As a first step towards analysing the combustion, the model presented by Mercer *et al.*[7] is applied. Defining the non-dimensional temperature to be $u = \frac{RT}{E}$ and re-scaling space and time co-ordinates by $\sqrt{\frac{\rho QAR}{kE}}$ and $\frac{QAR}{c_p E}$, respectively, leads to the non-dimensional version of the governing equations:

$$\frac{\partial u}{\partial t} = \frac{\partial^2 u}{\partial x^2} + we^{-1/u} - \ell(u - u_a) \qquad (1a)$$

$$\frac{\partial w}{\partial t} = -\beta we^{-1/u} \qquad (2a)$$

where we define $\beta = \frac{\mathrm{Ec_p}}{\mathrm{QR}}$, a parameter related to the properties of the fuel, and the non-dimensional volumetric heat transfer, $\ell = \frac{\mathrm{hSE}}{\mathrm{VR}\rho\mathrm{QA}}$.

Depending on the value of system parameters, thermopower waves with or without oscillations can be predicted [8, 9]. For simplification in the theoretical analysis, we start with a one-dimensional space model and transform it to a non-dimensional system to predict the occurrence of oscillatory combustion linked to the heat losses.

The determination of all the necessary parameter values is the key to being able to apply the model to a real system. The solution of the model presented by Mercer *et al.*, [7] assumes that the ambient temperature is absolute zero (u_a=0). Ambient temperatures are typically very small compared to the reaction temperature and hence this assumption has little effect on the overall behaviour of the solutions to this model.

For the fuel (which is a combination of nitrocellulose and sodium azide in our case) the values parameters are as follows: S/V=1/240 /μm , ρ = 1600 kg/m^3, c_p =1596 J/kg.K, Q = 4.75 ×10^6 J/kg, E = 1.26× 10^5 J/mol, A = 10^5 /s and h=2 × 10^{-3} J/s.m^2.K. In all cases the β value is 5.09 for the nitrocellulose fuel layer. Two extreme conditions are now considered for the substrate:

3.3.1 A thermally conductive substrate (κ=20 W/m.K)

This system is similar to the schematic, which is shown in Figure 3.1. The fuel is deposited on Al_2O_3 (with a thin layer of Bi_2Te_3 in between) with a thermal conductivity

of approximately 20 W/m.K. This results in the non- dimensional heat loss parameter ℓ = 1.7 ×10^{-4}. The oscillation period is directly related to β and ℓ. For β = 5.09 the critical heat loss value for the onset of oscillations can be estimated from Figure 3.6 as being smaller than ℓ/β = 0.000035. Furthermore, the model predicts that there would be a time of approximately 0.05 seconds between peaks in the oscillating signal. In this case an oscillatory behaviour is predicted hence, the slower and faster propagation speeds are strongly dependent on very fine scale details of the solution to the model; the slower one being of the order of 0.002m/sec and the faster one, an order of magnitude higher.

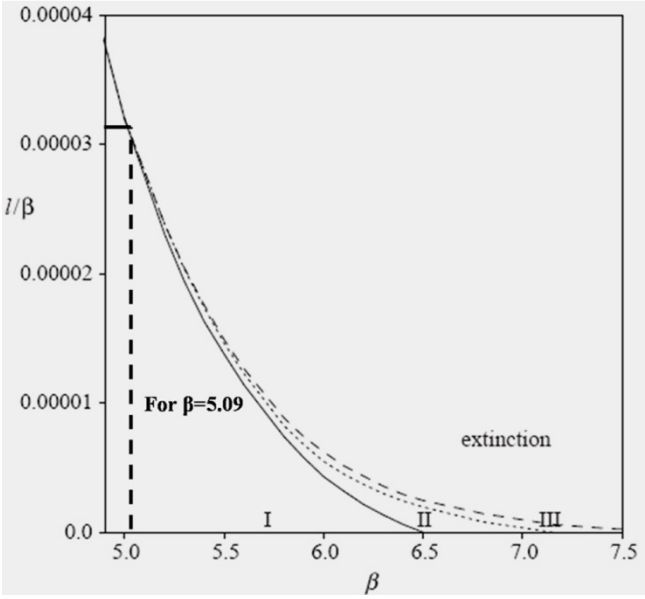

Figure 3.6**:** Region in the parameter (β, ℓ / β) space where combustion waves and extinction occurs.

Due to the oscillatory behaviour, a two dimensional model will better account for the various paths of heat conduction to provide accurate velocity predictions in this case.

3.3.2 A substrate with a low thermal conductivity (κ=1 W/m.K)

This system is similar to the schematic which is shown in Figure 3.1**.** The fuel is deposited on terracotta (with a thin layer of Bi_2Te_3 in between) with a thermal conductivity of approximately 1 W/m.K. The change in thermal conductivity of the substrate effects the heat loss parameter. In case of terracotta the heat loss parameter is

obtained as $\ell = 2\times10^{-5}$ which according to Figure 3.6 predicts that oscillations will cease to exist.

Next, the model proposed by McIntosh *et al.* is applied to predict the reaction propagation velocity for the fuel/terracotta system [11]. The equation is as follows:

$$c - \frac{\ell}{c} = \frac{1}{c} e^{-\beta} (e^{2\ell\beta / c^2} - e^{-\beta}) \qquad (3)$$

where c is the wave speed in m/sec. Using Equation (3), it is estimated that the reaction average propagation velocity is approximately 0.007m/sec. The velocity measured in the author's experiments for the fuel/terracotta system was about 0.009m/sec so the simulation agrees reasonably well with our measurements. Hence, the mathematical model is able to reasonably predict the oscillation period and the reaction propagation velocity.

3.4 Results and discussion

A schematic of a Bi_2Te_3 based thermopower device is shown in Figure 3.1. Ignition is initiated at one end of this system using a custom-made blow torch with a fine tip and the resulting reaction wave self-propagates to the other end. We show that such self-propagating thermal waves result in either oscillating or non-oscillating wave front velocities [12].

For the self-propagation of an exothermic reaction, heat must be generated through the reaction faster than it is removed by thermal diffusion [13]. Hence, nitrocellulose [$C_6H_8(NO_2)_2O_5$] is used as the fuel due to its large enthalpy of reaction. Sodium azide (NaN_3) in aqueous solution (50mg/mL) is then added to serve as a primary igniter to lower activation energy (40kJ/mol for NaN_3, compared to 110 – 150 kJ/mol for nitrocellulose) [14, 15]. Samples with low nitrocellulose and/or NaN_3 weights showed no sustained reaction under any conditions. The Bi_2Te_3 layer generally survived the thermopower

wave propagation and remained intact after the reaction, which is proved by the optical observation and X-ray diffraction (XRD) pattern, shown in Figure 3.3 (e).

Several samples using different masses of the fuel and two different thicknesses of Bi_2Te_3 (5 μm and 10 μm) were prepared and tested. A high speed camera tracked the propagation of the reaction front. Figure 3.7 depicts the propagation of one such reaction along a fuel/Bi_2Te_3/Al_2O_3 sample at different times.

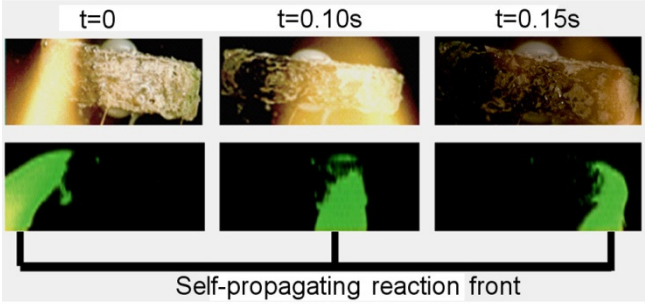

Figure 3.7: Images of the self-propagating reaction front using a high speed camera. Ignition occurs at the left corner and the wave self-propagates across the surface to the other end. The length of the sample is ~14 mm. The propagation of the combustion wave was filmed using a high speed video camera (Phantom v4.3, Vision Research Inc.) with a 105 mm f/2.8 Micro-Nikkor lens at 1000 frames per second with an exposure time of 25 μs for each frame.

The accelerated reaction wave drives a simultaneous wave of electrons. This wave of electrons results in oscillatory, followed by non-oscillatory, voltage output. An oscilloscope (Agilent MSO7014) was used for voltage acquisition from the thermopower experiments. The voltage signal was positive for waves emanating from the negative electrode (Figure 3.8 (a)). This observation can be attributed to the negative Seebeck coefficient of Bi_2Te_3 (−287μV/K). The voltage signal is of the same duration as the corresponding reaction wave, thereby enabling the calculation of the reaction propagation velocity for the sample.

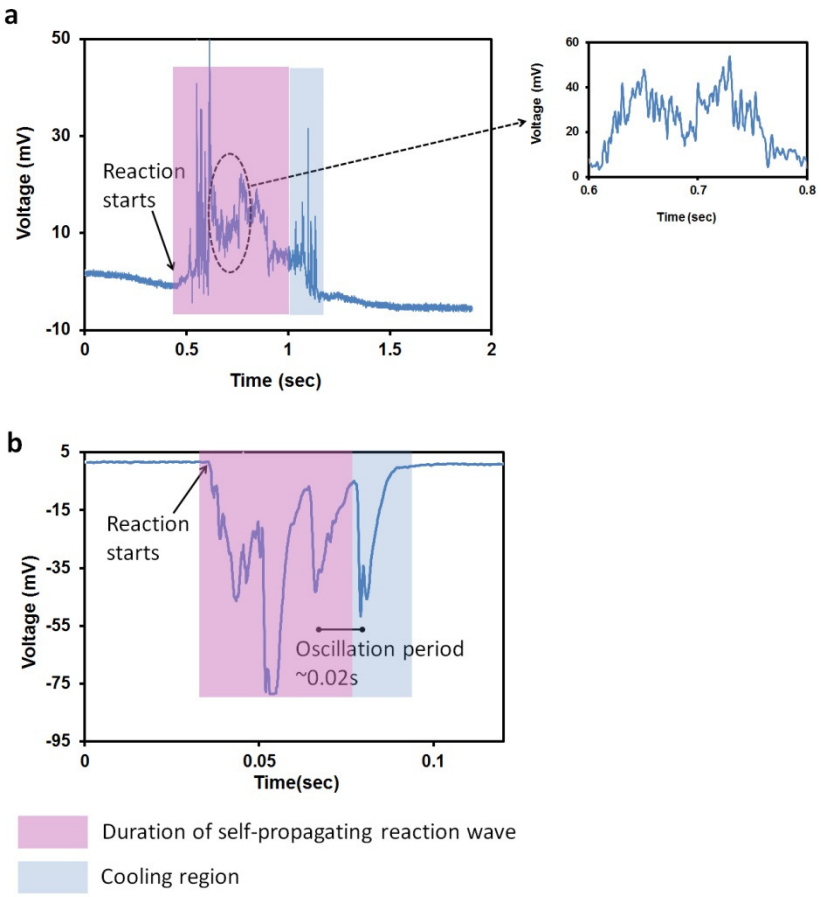

Figure 3.8: Thermopower voltage signals in reaction and cooling zones. The voltage signal is divided into two phases: the initial oscillation phase indicates reaction time and the smooth phase reflects the cooling time. The voltage returns to zero after the temperature across the sample reaches equilibrium. (a) Negative voltage generation with clear oscillating regions. (b) Positive voltage generation with oscillating zones after reversing the measurement system electrodes.

The chemically driven thermopower waves with high propagation velocities have a constant polarity depending on the direction of the reaction. This suggests that the wave passes through the system faster than the cooling time of the region it left behind, resulting in a highly efficient direction of energy [1].

3.4.1 System based on a thermally conducting substrate (Al_2O_3)

The average wave front propagation velocity is in the order of 0.01 to 0.9 m/sec with the median of 0.4 m/sec for Al_2O_3 substrate and it was mostly oscillatory, particularly for large velocity reactions. Very wide ranges of velocity were also observed by Strano *et al.* [1] The oscillatory nature of the system based on thermally conductive Al_2O_3 (20 W/m.K) was discussed in section 3.3.1 of this chapter and clearly observed in experimentally obtained

output signals. Sustained reaction waves specifically along the direction of the Bi_2Te_3 layer (Figure 3.7) were observed at velocities up to 10 orders of magnitude larger than the bulk combustion rate of nitrocellulose (20 – 70 mm/sec) under atmospheric conditions [1, 16]. The high speed videos of the reaction waves also show that in some cases combustion behind the main wavefront may be interrupted till the arrival of the next transverse wave. The reason for the emergence of the transverse wave may be due to the combustion wave being spatially unstable [17]. This interrupted combustion pattern may also be responsible for the large oscillations seen in the voltage. Figures 3.8 (a,b) show the voltage measurements across two samples of the fuel/ Bi_2Te_3/Al_2O_3 system (the measurement system electrodes were connected in reverse for Figure 3.8 (b). The voltage profiles in Figure 3.8 can be classified into two phases: an initial reaction phase and a cooling phase [12]. The high speed videos show that the oscillation region corresponds to the period when the reaction waves are propagating. The reaction phase consists of a region of rising voltage as the wavefront spreads radially across the sample until all the combustion fuel is consumed. This is followed by a region of exponential decay [12]. Large temperature gradients result in voltages with peak magnitudes in the range of 40 to 150 mV and oscillations with peak-to-peak amplitude of up to 140 mV. The peak power obtained from these devices is as large as 10 mW. By comparing Figures 3.8 (a,b) it can be seen that after swapping the electrodes of the measurement system the voltage polarity was also reversed. This implies that the polarity of the reaction depends on the Seebeck coefficient of Bi_2Te_3 and the direction of the reaction.

The shape and magnitude of the voltage signals varied through different samples. Figures 3.9 (a,b) show the respective velocity profiles of two starkly different voltage signals shown in Figures 3.9 (c,d)**.** The velocity profiles for the corresponding voltage profiles are obtained from the high speed videos. The profiles illustrate that the reaction velocities also exhibit an oscillatory behaviour. Additionally, it seems that the voltage oscillations are correlated with the velocity profiles. Further work is required to accurately establish the relation between the

velocity and voltage oscillations. The shape of the velocity profiles again proves that the propagation of the combustion wave is not linear and is highly oscillatory.

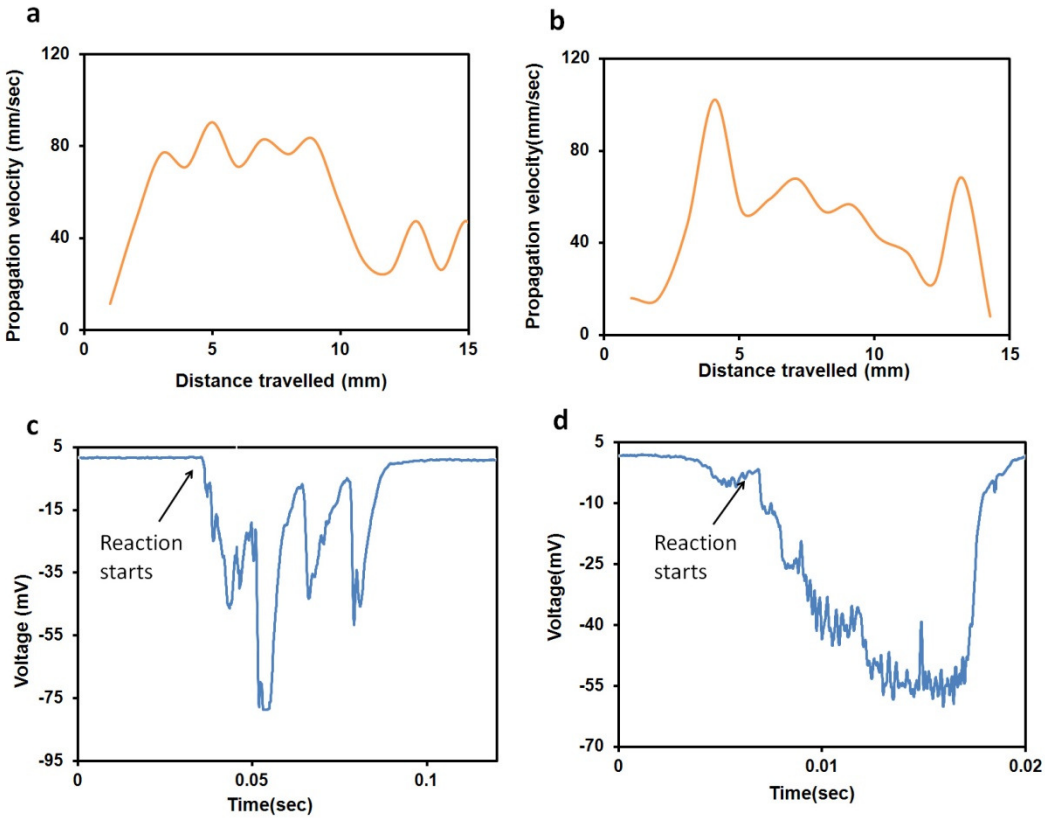

Figure 3.9: Velocity profiles (a,b) along with the corresponding voltage signals (c , d). Reaction velocity also exhibits an oscillatory behaviour. The oscillations in voltage seem to follow the velocity oscillations in general. The velocity profiles are extracted from the high speed videos. The x axis of the velocity graphs show the distance travelled by the self-propagating wavefront from the point of ignition. Velocity of this wavefront is obtained at different points during the course of its propagation. Velocity oscillations in the reaction wave may be responsible for the significant oscillations in the voltage signal. The reaction time corresponds to the duration of the voltage signal.

The magnitude of the voltage depends on the sample mass, particularly the amount of fuel. Larger mass results in a higher peak value of the voltage signal as well as higher output power, as shown in Figures 3.10 (a,b) Analysis of the voltage and power *vs* mass data indicates an optimal mass range, where both the voltage and power obtained are maximized, about 24 – 27 mg. The data indicate that a very low mass of fuel cannot supply enough heat to sustain exothermic reaction waves. On the other hand, too much fuel may provide more heat energy but the non-reacted regions require a large amount of

energy, and consequently the propagation may not be sustained. As a result, we may expect that there is an optimal mass range to promote sustained reaction propagation, which is also suggested by Strano *et al* [1].

As can be seen in Figure 3.10 (c) both generated voltages for samples with Bi_2Te_3 films of 5 and 10 µm thicknesses have fairly similar patterns. The voltages produced for 10 µm sample were slightly larger than the 5 µm samples due to their higher sheet resistance. Additionally, there was no obvious relation between the propagation velocity and magnitude of voltage produced, as can be seen in Figure 3.10 (d).

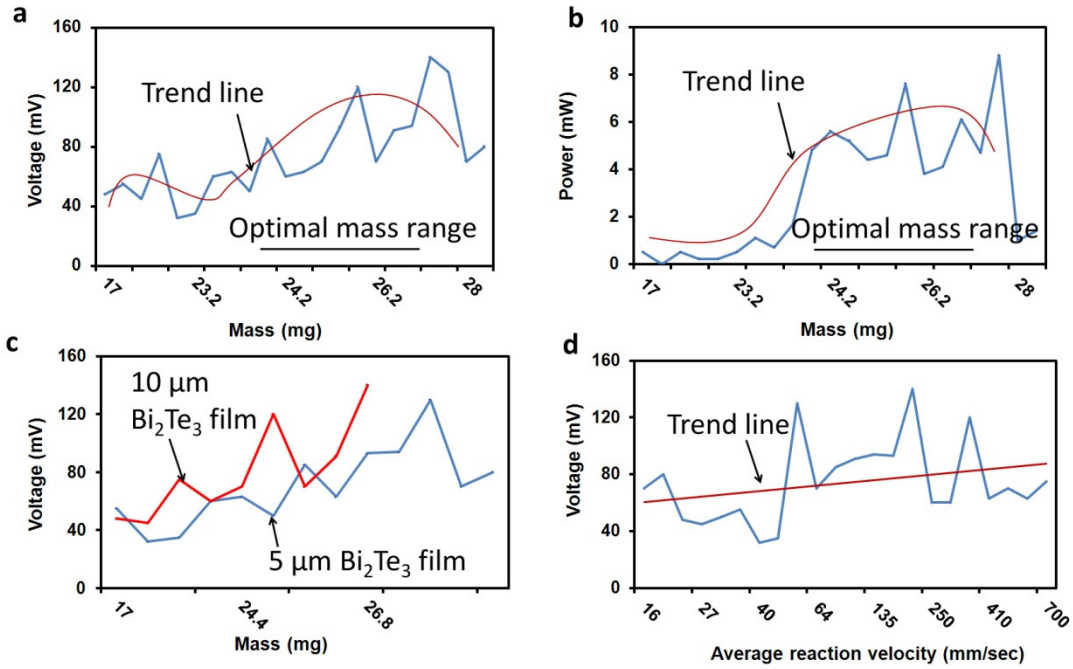

Figure 3.10: (a) Variation of peak voltage with mass of (fuel & Bi_2Te_3). The trend line indicates that peak voltage increases with the mass of the materials. (b) Power plotted as a function of system mass. The optimal mass range corresponds to the one for peak voltage. (c) Variation of peak voltage with mass for two different thicknesses of the Bi_2Te_3 film. (d) Voltage as a function of the propagation velocity.

However, very thick Bi_2Te_3 films (>30 µm) effectively reduced the thermal conductivity effect of the Al_2O_3 substrate, and hence, oscillations ceased. This was both predicted by our theoretical model and shown by experiments. For these systems, the oscillation almost stopped and the produced voltage was relatively low. The cross-sectional SEM of

thick Bi_2Te_3 film (thickness >30 µm) sample and the corresponding voltage signal are shown in Figures 3.11 (a) and 3.11 (b), respectively.

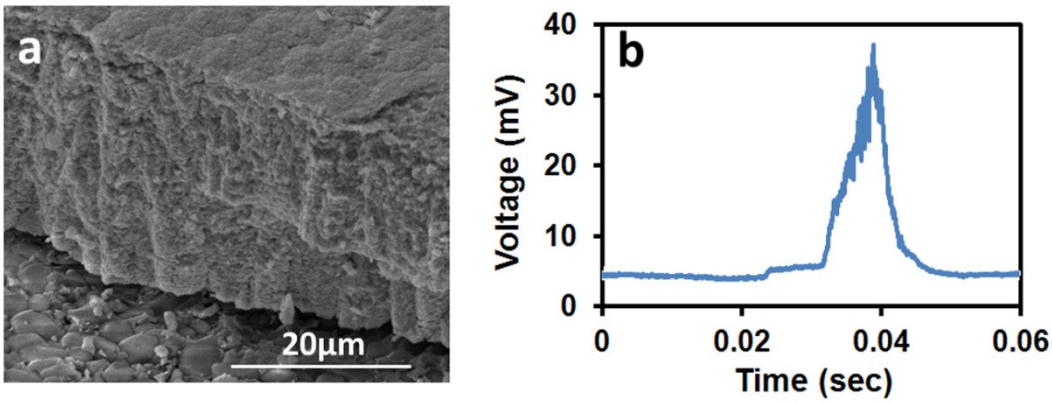

Figure 3.11: (a) Cross-sectional SEM image of Bi_2Te_3 film with thickness of >30 µm on Al_2O_3 substrate and (b) the corresponding thermopower voltage signal. It can be seen that the magnitude of voltage has been reduced compared to thinner Bi_2Te_3 films and there is nearly no oscillations.

3.4.2 System based on substrate with low thermal conductivity (terracotta)

The thermal conductivity of the substrate determines the oscillatory behaviour and the wave front velocity. Due to the low thermal conductivity of terracotta, which is of the order of 1 W/m.K, no oscillation was predicted as per section 3.3.2 of this chapter. In addition, the theoretical calculations also suggested that the propagation velocity would be reduced dramatically. Confirming these predictions, the wave propagation velocity for the fuel/Bi_2Te_3/terracotta system was consistently measured to be lower, on average approximately ~0.01 m/sec (30-40 times less than the Bi_2Te_3/Al_2O_3 films on average). Figure 3.12 is an example output signal of a fuel/Bi_2Te_3/terracotta system, which illustrates the voltage generated peaks of 7 mV with no oscillations. The difference in propagation velocities using the two substrates closely follows the difference in thermal conductivities of the two substrates. The thermal conductivity of Al_2O_3 is 20 times that of terracotta, and we consequently observe significant difference in wave front propagation velocities in the order of 30-40. This further proves that thermal conduction from the fuel layer to the substrate drives reaction wave propagation.

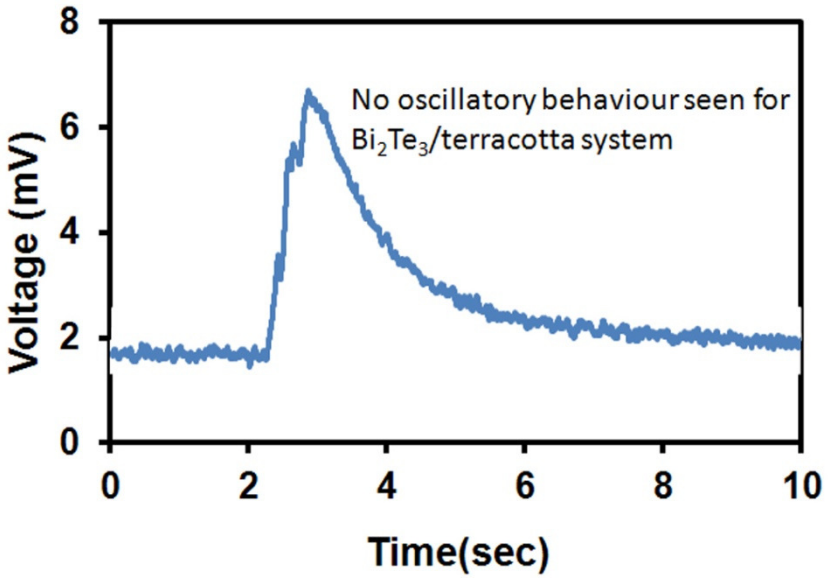

Figure 3.12: Voltage signal obtained using a Bi_2Te_3 layer on a terracotta substrate (low thermal conductivity). It shows that the oscillations cease to exist if the effective thermal conductivity is low. This observation is in line with the prediction made by the author's theoretical model. Furthermore, it also shows that the thermal conductivity of the substrate plays an important part in determining whether oscillations occur.

3.5 Summary

In this chapter, the author demonstrated a thin film thermopower wave system based on Bi_2Te_3 as the core TE material. It was shown that the generation of directionally dependant thermopower waves using a fuel/ Bi_2Te_3/Al_2O_3 system resulted in oscillatory voltages as high as 150 mV and powers up to 10 mW. At the same time a high specific power in the order of 1 kW/kg was maintained. This can be ascribed to the high *S* of Bi_2Te_3 (~ –200 μV/K) and high electrical conductivities of the order of 10^5 S/m.

A full analysis of the system was carried out and it was observed that when using the thermally conductive substrate of alumina, the output showed strong oscillatory behaviour, while there were no oscillations seen when terracotta substrates with a low thermal conductivity were used. This behaviour was described well by the theoretical model using the heat transfer equations with suitable boundary conditions. It was also shown using characterization techniques such as XRD that the Bi_2Te_3 films remained intact at the end of the thermopower wave propagation.

Furthermore, it was demonstrated that the mass of the fuel played an important role in determining the magnitude of the output voltage. A higher fuel mass generally resulted in larger output voltages. However, it was observed that the amount of fuel exhibited an optimal mass range in which the output voltages were maximised.

This work conducted by the author of this thesis is of utmost importance as it demonstrates thermopower wave systems in a thin film geometry for the first time. The use of thin films is important as it will enable the incorporation and testing of a wide variety of core TE materials in order to increase the output voltage and specific power outputs from such sources. By developing thermopower wave sources based on Bi_2Te_3, a common TE material, output voltages higher than MWNT based thermopower sources (>150%) were generated while maintaining large specific power. This is an important step towards the realisation of thermopower waves systems as a new category of micro power sources.

In the next chapter, the author will use a novel combination of two commonly used TE materials with complimentary semiconducting properties (p-type Sb_2Te_3 and n-type Bi_2Te_3) in order to generate voltage signals with alternating polarities. A detailed comparison of p-type Sb_2Te_3 and n-type Bi_2Te_3 based thermopower wave sources will be presented.

References

[1] W. Choi, S. Hong, J. T. Abrahamson, J. H. Han, C. Song, N. Nair*, et al.*, "Chemically driven carbon-nanotube-guided thermopower waves," *Nature Materials,* vol. 9, pp. 423-429, May 2010.

[2] H. Huang, W.-l. Luan, and S.-t. Tu, "Influence of annealing on thermoelectric properties of bismuth telluride films grown via radio frequency magnetron sputtering," *Thin Solid Films,* vol. 517, pp. 3731-3734, 2009.

[3] M. M. Safarov and K. Madzhidov, "Effective thermal conductivity of aluminum oxide with metallic fillers in gaseous media and a vacuum at various temperatures," *Journal of Engineering Physics and Thermophysics,* vol. 50, pp. 341-346, 1986.

[4] S. Kam, J. Bathiébo, L. Zerbo, J. Soro, K. Traoré, P. Blanchart*, et al.*, "Experimental determination of some micro-structural and hydrous properties of a terra cotta and modelisation of hygrothermal transfers," *Journal of Applied Sciences,* vol. 9, pp. 3424-3432, 2009.

[5] P. Pradyumnan, "Thermoelectric properties of Bi_2Te_3 and Sb_2Te_3 and its bilayer thin films," *Indian journal of pure & applied physics,* vol. 48, pp. 115-120, 2010.

[6] G. R. Miller and C.-Y. Li, "Evidence for the existence of antistructure defects in bismuth telluride by density measurements," *Journal of Physics and Chemistry of Solids,* vol. 26, pp. 173-177, 1965.

[7] G. N. Mercer, R. O. Weber, and H. S. Sidhu, "An oscillatory route to extinction for solid fuel combustion waves due to heat losses," *Proceedings of the Royal Society of London Series a-Mathematical Physical and Engineering Sciences,* vol. 454, pp. 2015-2022, Jul 1998.

[8] V. Zarko and A. Kiskin, "Numerical modeling of nonsteady powder combustion under the action of a light flux," *Combustion, Explosion, and Shock Waves,* vol. 16, pp. 650-654, 1980.

[9] A. Bayliss and B. J. Matkowsky, "From travelling waves to chaos in combustion " *Siam Journal on Applied Mathematics,* vol. 54, pp. 147-174, Feb 1994.

[10] S. Walia, R. Weber, K. Latham, J. T. Abrahamson, M. S. Strano, and K. Kalantar-zadeh, "Oscillatory Thermopower waves based on Bi_2Te_3 Films," *Advanced Functional Materials,* 2011.

[11] A. C. McIntosh, R. O. Weber, and G. N. Mercer, "Non-adiabatic combustion waves for general Lewis numbers: Wave speed and extinction conditions," *Anziam Journal,* vol. 46, pp. 1-16, Jul 2004.

[12] J. T. Abrahamson, W. Choi, J.-H. Han, N. S. Schonenbach, J. Park, M. P. Walsh*, et al.*, " Wave Front Velocity Oscillations of Carbon Nanotube-Guided Thermopower Waves:Nanoscale Alternating Current Sources," *ACS Nano,*vol. 5, pp. 367-375 2010.

[13] A. J. Gavens, D. Van Heerden, A. B. Mann, M. E. Reiss, and T. P. Weihs, "Effect of intermixing on self-propagating exothermic reactions in Al/Ni nanolaminate foils," *Journal of Applied Physics,* vol. 87, pp. 1255-1263, Feb 2000.

[14] A. K. Burnham and L. E. Fried, "Kinetics of PBX9404 Aging," presented at the 27th Aging, Compatibility and Stockpile Stewardship Conference, Los Alamos, USA, 2006.

[15] K. Katoh, S. Ito, S. Kawaguchi, E. Higashi, K. Nakano, Y. Ogata*, et al.*, "Effect of heating rate on the thermal behavior of nitrocellulose," *Journal of Thermal Analysis and Calorimetry,* vol. 100, pp. 303-308, 2010.

[16] R. C. Sausa and W. R. Anderson, " Burn-Rate Modeling and Combustion Diagnostics for Environmentally Friendly, Solid Rocket Propellants," US Army Research Laboratory2006.

[17] V. N. Marshakov, A. G. Istratov, and V. M. Puchkov, "Combustion-front non-one-dimensionality in single- and double-base propellants," *Combustion Explosion and Shock Waves,* vol. 39, pp. 452-457, Jul-Aug 2003.

Chapter 4

Comparison of p-type Sb_2Te_3 and n-type Bi_2Te_3 based Thermopower Wave Sources

4.1 Introduction

In the previous chapter, the author demonstrated thin film thermopower wave devices based on thermoelectric (TE) cores of n-type bismuth telluride (Bi_2Te_3) for the first time. Voltages and oscillation amplitudes larger (>150%) than previously developed thermopower wave system based on (MWNTs) were demonstrated, while maintaining a high specific powers in the order of 1 kW/kg. However, as discussed in chapter 1, voltage signals with alternating polarities are highly desirable for practical applications. This could potentially be achieved by implementing a combination of p and n-type TE core materials. However, it was not known whether the phenomenon of thermopower waves extends to p-type materials which have holes as the majority charge. Subsequently, based on the analysis presented in chapter 2, the author chose to develop thermopower wave sources based on a novel combination of p-type antimony telluride (Sb_2Te_3) and n-type Bi_2Te_3. Sb_2Te_3, a conventional TE material was chosen as the complimentary core TE material due to its high Seebeck coefficient (~180 μV/K) and electrical conductivity (10^4 S/m).

In this chapter, the author will demonstrate thermopower wave sources by incorporating p-type Sb_2Te_3 and n-type Bi_2Te_3 as the core TE materials. In order to compensate for the low thermal conductivity of Sb_2Te_3 and Bi_2Te_3, the author will place them on thermally conductive alumina (Al_2O_3) substrates. Subsequently, highly exothermic chemical reaction of a solid fuel (nitrocellulose) will be coupled to charge carriers in Sb_2Te_3 and Bi_2Te_3 layers to generate self-propagating thermopower waves which entrain holes and

electrons in Sb_2Te_3 and Bi_2Te_3 respectively, to generate voltage and power. The theory of combustion waves will be adapted to understand the behaviour of thermopower waves in the Sb_2Te_3 and Bi_2Te_3 based thermopower wave devices. The author will present detailed characterizations of the Sb_2Te_3 and Bi_2Te_3 films before and after thermopower wave propagation. The role of thermal conductivity of the substrates on the behaviour of thermopower waves will be assessed by depositing Sb_2Te_3 and Bi_2Te_3 on terracotta (baked natural polysilicate) which exhibits a contrastingly low thermal conductivity compared to Al_2O_3. The influence of the mass of fuel on the voltage and power generated will be studied. A detailed comparison of the output voltages, specific powers, oscillatory behaviours and thermopower wave propagation velocities for Sb_2Te_3 and Bi_2Te_3 based thermopower wave devices will also be presented in this chapter. The outcome of this work was published as a full article in the journal Energy & Environmental Science.

4.2 Experimental

4.2.1 Deposition of Sb_2Te_3 and Bi_2Te_3 films

The Sb_2Te_3 and Bi_2Te_3 films were deposited on Al_2O_3 and terracotta substrates using RF magnetron sputtering, under identical deposition conditions. High purity (99%) Sb_2Te_3 and Bi_2Te_3 targets (Vin Karola Instruments) were used for sputtering. The chamber was pumped down to a pressure of 2×10^{-5} Torr before starting the sputtering process. Al_2O_3 and terracotta substrates with linear dimensions of 12-15 mm (L) × 4-6 mm (W) × 100 µm (H) were utilised after being cleaned using acetone, isopropyl alcohol, and distilled water. The substrates were held at a constant temperature of 100 ºC throughout the sputtering process, in which a power of 100 W and an argon atmosphere with 10 mTorr process pressure were used. Sputtering time of 90 mins resulted in a 6 µm thick Sb_2Te_3 and 5 µm Bi_2Te_3 films, repectively. Electrical contacts between the copper tape electrodes and the thermoelectric layer were made using adhesive conductive silver paste (42469, Alfa Aesar). The resistance between the

electrodes for Sb_2Te_3 films and Bi_2Te_3 films ranged from 6-12 Ω and 2-10 Ω, respectively [1].

4.2.2 Preparation of fuel

The fuel used for the exothermic reaction was a combination of nitrocellulose ($C_6H_8(NO_2)_2O_5$) and sodium azide (NaN_3). Nitrocellulose was used due to its large enthalpy of reaction (4.75×10^6 J/kg). It was prepared by dissolving millipore nitrocellulose membranes (N8645, Sigma Aldrich) in acetonitrile (15g/L). This solution was then dropcast on the Bi_2Te_3 and Sb_2Te_3 films using a pipette and left to dry. The acetonitrile evaporated leaving an adhesive and solid nitrocellulose layer deposited on top of the thermoelectric materials. NaN_3 was used to serve as a primary igniter due to its low activation energy (40 kJ/mol for NaN_3 compared to 110-150 kJ/mol for nitrocellulose) [2, 3]. NaN_3 (14314, Alfa Aesar) in aqueous solution (50 mg/mL) was then added on top of the nitrocellulose layer using a pipette. The total thickness of the fuel layer was ~240 µm.

4.2.3 Characterization of Sb_2Te_3 and Bi_2Te_3 films

Figures 4.1 (a,b) show scanning electron micrographs (SEM) of Sb_2Te_3 and Bi_2Te_3 films, respectively. The images clearly show the difference between the structures of the two films with Bi_2Te_3 exhibiting a more irregular structure compared to Sb_2Te_3. This confirms the polycrystalline nature of Bi_2Te_3 [1]. The SEM images also show that Bi_2Te_3 films are more porous than Sb_2Te_3, when deposited on Al_2O_3 substrates under identical conditions.

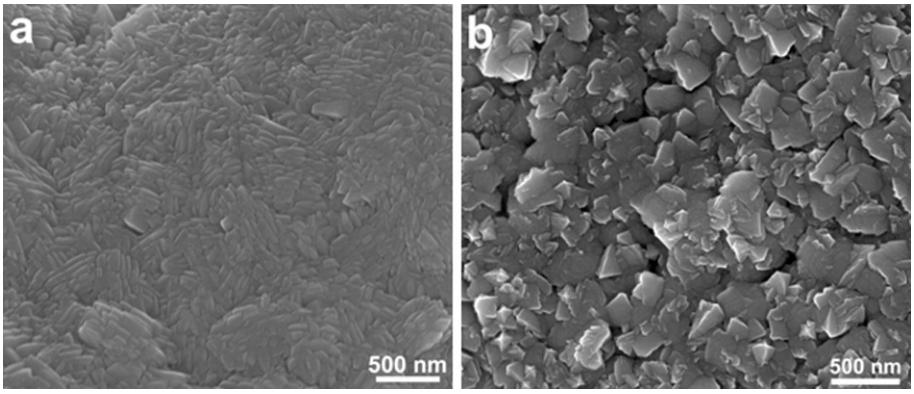

Figure 4.1: The SEM images of: (a) Sb_2Te_3 film on Al_2O_3 (b) Bi_2Te_3 film on Al_2O_3.

A surface profilometer (Ambios Technology XP-2) was used to further investigate the morphology of the Sb_2Te_3 and Bi_2Te_3 surfaces and that of the substrate (Figure 4.2 (a,b)). The average surface roughness of Sb_2Te_3 and Bi_2Te_3 was determined to be 0.4 and 0.7 µm, respectively. This indicates that the Bi_2Te_3 films are more porous; thereby, confirming the earlier observation made from the micrograph in Figure 4.1 (b). A greater porosity enables more fuel to be placed on the surface of the films. Additionally, a higher porosity is also important to facilitate increased thermal conduction between the fuel and thermoelectric films [1], resulting in a more sustained reaction propagation.

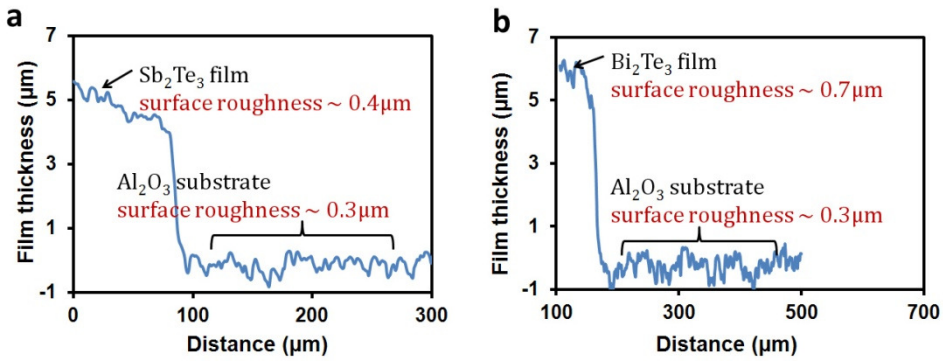

Figure 4.2: (a) surface profile of a 6 µm Sb_2Te_3 film on Al_2O_3 substrate, (b) surface profile of 6 µm Bi_2Te_3 film on Al_2O_3 substrate.

X-ray diffraction (XRD) measurements were carried out on the Sb_2Te_3 and Bi_2Te_3 samples in order to assess the crystallinity of the films. The XRD was conducted using a Bruker D8 DISCOVER microdiffractometer fitted with a GADDS (General Area Detector Diffraction System). The XRD pattern for Sb_2Te_3 (Figure 4.3 (a), 1] shows three

well defined peaks, which indicate its crystalline structure. In case of Bi_2Te_3, the XRD pattern reveals a more polycrystalline structure (Figure 4.3 (b), 1] [4]. On addition of nitrocellulose different effects on the XRD patterns of Sb_2Te_3 and Bi_2Te_3 are observed (Figure 4.3 (c), 2 and Figure 4.3 (d), 2]. For Bi_2Te_3 the peak at 18.1° 2θ (006) plane for rhombohedral Bi_2Te_3 – ICDD No. [1-75-0921]) is no longer exhibited in the samples with nitrocellulose (Figure 4.3 (d), 1). Possibly incoherent scattering and adsorption effects may be responsible for the disappearance of this peak. It is also probable that the nitrocellulose coating on both the Sb_2Te_3 and Bi_2Te_3 samples effectively masks the surface, thus inhibiting the penetration of X-rays to, and collection of scattering data from this particular peak. This effect is particularly acute for the relatively low intensity (006) Bi_2Te_3 peak, which lies in the same region as the principal XRD reflections for nitrocellulose (ICDD No. [03-0114]) [1]. Sb_2Te_3 on the other hand does not show any significant diffraction peaks in this region. Thus, the masking effect caused by the nitrocellulose layer only results in a general decrease in diffraction intensity across its entire diffraction pattern. The XRD patterns of the samples following consumption of the nitrocellulose are also shown (Figure 4.3 (c), 3 and Figure 4.3 (d), 3], and will be discussed later.

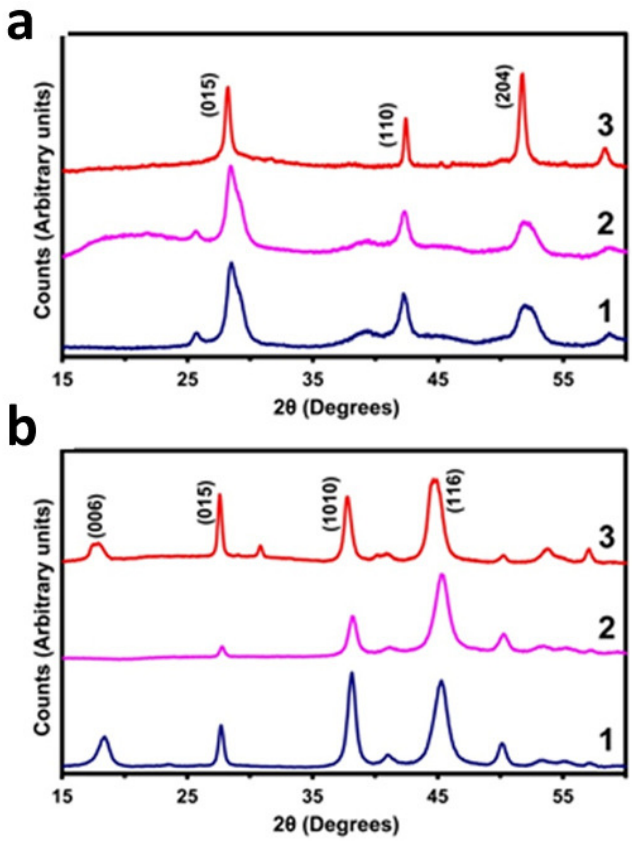

Figure 4.3: (a) 1. The XRD pattern of Sb_2Te_3 before thermopower wave propagation, 2. after adding nitrocellulose and 3. after thermopower wave propagation (b) 1. The XRD pattern of Bi_2Te_3 before thermopower wave propagation, 2. after adding nitrocellulose and 3. after thermopower wave propagation.

4.2.4 Comparison of thermal conduction rate of Sb_2Te_3 and Bi_2Te_3

In order to show the difference in the thermal conduction rates of Sb_2Te_3 and Bi_2Te_3, the measurement set up Figure 4.4 (a) is used. The Sb_2Te_3/Al_2O_3 and Bi_2Te_3/Al_2O_3 samples of ~ 12 mm length were used for the measurement and the thickness of both Sb_2Te_3 and Bi_2Te_3 films were equal to 6 μm. A heater with a sharp tip was used as the heating source and was positioned at one end on the sample. The temperature profile was acquired at the opposite end using a TENMA 727730 thermocouple. The heat source was kept in place until the temperature at the other end reached a constant value (approximately 200 s) in equilibrium with the ambient. Figure 4.4 (b) shows the temperature profile for the two samples. It shows that the temperature rises to approximately 47 ºC for both samples. However, the rate of rise is approximately 2.2 times higher for the Al_2O_3/Sb_2Te_3 sample which is analogous to the

ratio of the thermal conductivities of Sb_2Te_3 and Bi_2Te_3. Therefore, the rate of heat conduction in Sb_2Te_3 is ~2.5 times faster than that in Bi_2Te_3.

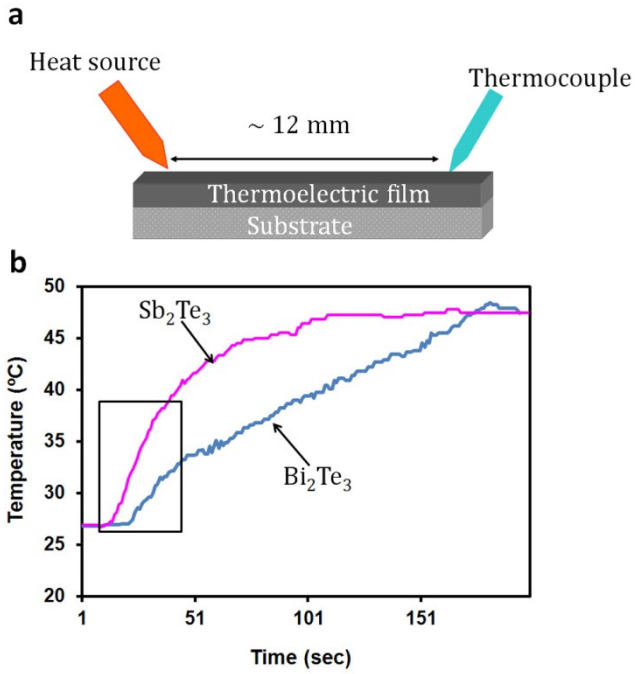

Figure 4.4: (a) Measurement set up, (b) Difference in thermal conduction of Sb_2Te_3 and Bi_2Te_3 films.

4.2.5 Electrical conductivities of Sb_2Te_3 and Bi_2Te_3 films

In order to compare the electrical conductivities of the two films four point probe measurements were carried out on Sb_2Te_3 and Bi_2Te_3. The resistivity can be calculated using the equation $\rho = R_{Sh} \times t$ in which ρ is the resistivity of the film in Ω.m, R_{Sh} is the sheet resistance of the film in Ω/□ and t is the thickness of the film in m.

4.2.5.1 Sb_2Te_3 film

The four point probe showed that the sheet resistance of the Sb_2Te_3 film was 3.103 Ω/□ for the Sb_2Te_3 film of approximately 6μm. Therefore the resistivity of the film was calculated to be 1.86×10^{-5} Ω.m. Inverse of the resistivity gives the conductivity. Thus, the electrical conductivity of the Sb_2Te_3 film was found to be 5.3×10^4 S/m.

4.2.5.2 Bi_2Te_3 film

A similar approach was used to calculate the electrical conductivity of the Bi_2Te_3 film. The sheet resistance of the Bi_2Te_3 film was found to be 1.75 Ω/□. Therefore the electrical conductivity of the film was calculated to be 1.1×10^5 S/m. The above measurements show that the electrical conductivity of Bi_2Te_3 is an order of magnitude higher than Sb_2Te_3. The values obtained are also comparable with the literature values of 10^4 and 10^5 S/m for Sb_2Te_3 and Bi_2Te_3 films respectively [5-7].

4.2.6 Calculation of Specific Power

In order to obtain the specific power, the masses of the fuel (nitrocellulose & sodium azide) and thermoelectric films were considered. The relationship between mass, density and volume was used for calculating the mass of the Sb_2Te_3 and Bi_2Te_3 films as: $m = \rho \times V$,where, m is the mass in grams (g), ρ is the density in g/cm^3 and V is the volume in cm^3.

ρ=6.5 g/cm^3 and 7.7 g/cm^3 for Sb_2Te_3 and Bi_2Te_3 respectively [8, 9]. and V depends on the dimensions of the sample and is calculated using the formula, $V = l \times w \times h$ where l is the length, w is the width and h is the thickness of the thermoelecteric film in cm, respectively.

For fuels, nitrocellulose and NaN_3 in our case, we knew the concentration of the two in their respective solutions. As mentioned in section 4.2.2, 15g/L nitrocellulose and 20g/L NaN_3 were used by drop casting. Hence, we know the amount of solution for each fuel and therefore the corresponding mass for each sample, depending on the volume of the liquid placed on the thermoelectric films. The sum of the masses of the thermoelectric film and the fuels gives the total mass of the materials used. The corresponding power from the sample is then scaled to per kg of the materials to obtain the specific power of the sample in kW/kg.

4.3 Results and Discussion

4.3.1 Comparison of Sb_2Te_3 and Bi_2Te_3 based thermopower devices

4.3.1.1 Thermopower devices based on Al_2O_3 substrate

Figure 4.5 shows the schematic of the set-up used for the thermopower experiments. Ignition takes place at one end of this system and the reaction self-propagates to the other end.

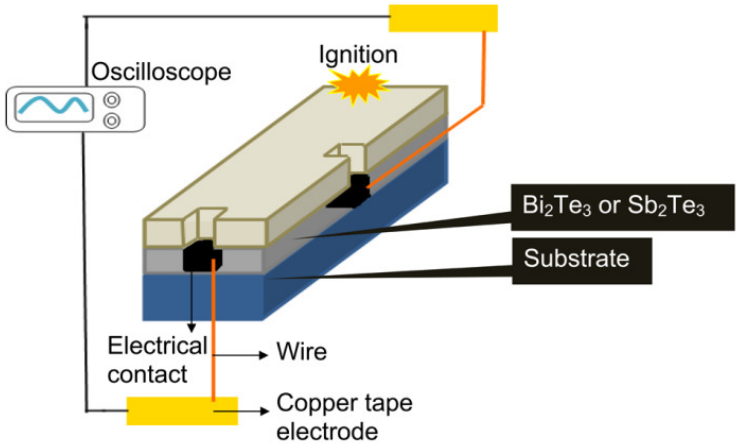

Figure 4.5: Schematic of the fuel/thermoelectric material/substrate thermopower wave generation system. Ignition at one end of the fuel (combination of nitrocellulose and sodium azide) layer results in a self-propagating exothermic reaction. (not to scale)

A custom-made blow torch with a localized flame tip is used to initiate the reaction. Samples with low mass of nitrocellulose or NaN_3 (masses below 15 mg per 75 mm^2) showed no sustained wavefront propagation in any direction. Several samples using different mass of the fuels were prepared and tested. For both Bi_2Te_3 and Sb_2Te_3 systems identical masses were used to ensure statistical comparison. Ignition at one end of the system, shown in Figure 4.5, results in an accelerated self-propagating reaction wave that drives a simultaneous wave of free carriers. This wave of carriers results in a flow of current and voltage across the devices. The voltage signal exhibited a positive polarity for waves initiating at the positive electrode for p-type Sb_2Te_3 and the opposite polarity for the n-type Bi_2Te_3. The duration of the output signal corresponds to the reaction time, thus enabling us to calculate the reaction propagation velocity. Even in oscillatory mode, the thermopower waves always exhibit a constant polarity during the reaction, depending on

the direction of wavefront propagation. This suggests that the wave passes through the system faster than the cooling time of its posterior region [1, 10].

The thermal conductivity of Al_2O_3 is much higher than Bi_2Te_3 and Sb_2Te_3. Both Bi_2Te_3 and Sb_2Te_3 films are comparatively thin (<10 µm compared to the ~100 µm thick Al_2O_3 substrate). Thus we can assume that the Al_2O_3 substrate will dominate the thermal conduction process [1].

Figures 4.6 (a,b) show typical voltage measurements across the fuel/Sb_2Te_3/Al_2O_3 and the fuel/Bi_2Te_3/Al_2O_3 systems, respectively. The voltage profiles of Figures 4.6 (a,b) can be divided into an initial reaction phase followed by a cooling down phase. The reaction phase consists of a rising voltage and continues until all the combustion fuel is consumed. This is followed by a region of exponential decay [11]. The voltage generated depends on the sample mass, especially the amount of fuel used (which is a combination of nitrocellulose and sodium azide). Sb_2Te_3-based devices generated voltages as large as 200 mV with oscillations in the range of 10-40 mV. On the other hand, Bi_2Te_3 devices generated voltages as large as 140 mV with larger oscillations generally within the range of 40-140 mV. The Bi_2Te_3-based devices occasionally showed voltages as high as 300-400 mV; however, due to lack of consistency these results are not included. Figures 4.6 (a,b) also show the difference in the oscillation amplitudes of the Sb_2Te_3 and Bi_2Te_3 devices. The reason for the difference in oscillatory behaviour can be attributed to the larger thermal conductivity of Sb_2Te_3 (2.5 times that of Bi_2Te_3). Oscillation amplitude difference between the two devices corresponds to the difference in thermal conductivities of the two materials. A larger effective thermal conductivity means that the reaction will propagate faster, potentially affecting the oscillation amplitude. Previously, we have theoretically demonstrated that a change in thermal conductivity affects the rate of heat loss and hence the oscillations [1].

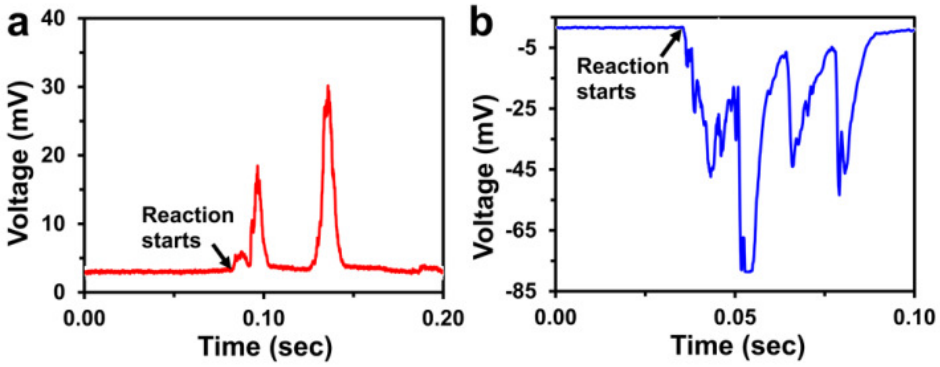

Figure 4.6: Comparison of oscillations between Sb_2Te_3 and Bi_2Te_3 based thermopower devices. (a) Oscillatory thermopower voltage signal for Sb_2Te_3 device using Al_2O_3 substrate.(b) Oscillatory thermopower voltage signal for Bi_2Te_3 device using Al_2O_3 substrate. We can see that Bi_2Te_3 based devices exhibit amplitudes approximately 3 times larger than that of Sb_2Te_3 based devices. The difference is similar to the variation in the thermal conductivities of Bi_2Te_3 and Sb_2Te_3.

For simplification in our theoretical analysis, we started with a one-dimensional space model and transformed it to a non-dimensional system to predict the occurrence of oscillatory combustion linked to the heat losses. As a first step towards analysing the combustion, we applied the model presented by Mercer *et al.*[12] Assuming that the solid fuel combustion is exothermic, oxygen is supplied in excess, and governed by Arrhenius kinetics with volumetric heat loss and defining the non-dimensional temperature u to be:

$$u = \frac{\mathrm{R}T}{\mathrm{E}} \qquad (1)$$

The non-dimensional equations for the conservation of heat and mass are:

$$\frac{\partial u}{\partial t} = \frac{\partial^2 u}{\partial x^2} + we^{-1/u} - \ell(u - u_a) \qquad (2)$$

$$\frac{\partial w}{\partial t} = -\beta we^{-1/u} \qquad (3)$$

in which T and w denote the temperature and concentration of the fuel, respectively, and x and t are the defined space and time variables. We define as $\beta = \frac{\mathrm{Ec_p}}{\mathrm{QR}}$, a parameter related to the properties of the fuel, and the non-dimensional volumetric heat transfer,

$\ell = \frac{hSE}{VR\rho QA}$ where, $\frac{S}{V}$ is the surface-area-to-volume ratio of the fuel (/m) and and h is the heat transfer coefficient from the fuel to the quiescent surroundings (J/s.m^2.K), ρ is the density of the fuel (kg/m^3), c_p is the specific heat of the fuel (J/kg.K), Q is the heat of reaction (J/kg), A is the pre-exponential rate constant (/s), E is the activation energy (J/mol), R is the universal gas constant (8.314 J/mol.K). The heat transfer coefficient h is an estimate for all the losses in the averaged model that we have used. For the purpose of gaining an understanding of the process, we estimated the heat losses to the substrate and the environment and lumped them together in h. Heat is transferred from the fuel layer to the (Bi_2Te_3 or Sb_2Te_3) thermoelectric/substrate layer and to the surroundings. Depending on the value of system parameters, we can predict the oscillatory behaviour of the thermopower waves. The determination of all the necessary parameter values is the key to being able to apply the model to a real system. The solution of the model presented by Mercer *et al*. [12], assumes that the ambient temperature is absolute zero (u_a=0). Ambient temperatures are very small relative to the reaction temperature, and hence, this inference has little effect on the overall behaviour of the solutions to this model. For the fuel, the value of the parameters is as follows: S/V=1/240 /μm, ρ = 1600 kg/m^3, c_p =1596 J/kg.K, Q = 4.75 ×10^6 J/kg, E = 1.26× 10^5 J/mol, A = 10^5 /s and h=2 × 10^{-3} J/s.m^2.K. In all cases the β value is 5.09 for the nitrocellulose fuel layer. The oscillation period is directly related to β and ℓ. For β = 5.09, the critical heat loss value for the onset of oscillations can be estimated as being smaller than ℓ/β = 0.000035 (Figure 4.7). The change in thermal conductivity affects the heat loss parameter. The higher thermal conductivity of Sb_2Te_3 compared to Bi_2Te_3 will enhance heat transfer (section 4.2.4). Hence, faster combustion velocities are predicted for Sb_2Te_3-based devices and that the system would be closer to the parameter values where oscillations in the combustion occur. However, as the model is based on a one-dimensional average over all the layers, the resultant changes predicted are not as dramatic as observed in the

experiments. Abrahamson *et al.* [11, 13] have employed a similar averaged one-dimensional model. They have solved their model numerically (rather than use the asymptotic results that we have) with a set of estimated parameter values and found corresponding results to those reported in this work, albeit for carbon nanotube guided thermopower waves, which are on a smaller scale than our experiments.

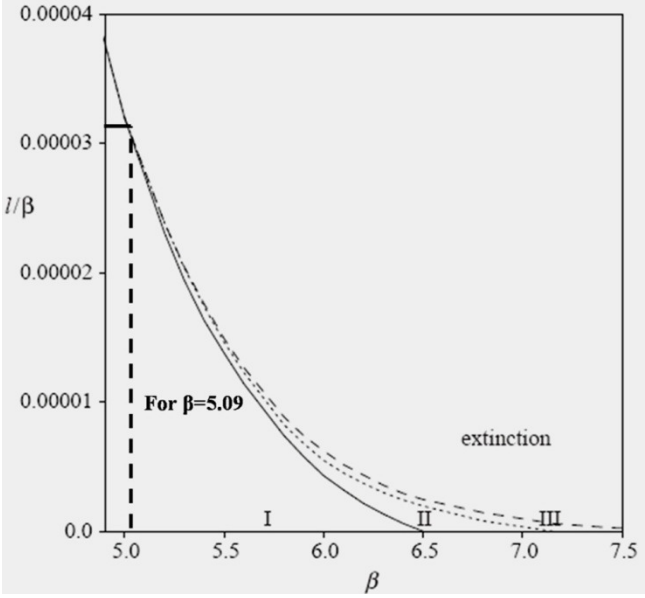

Figure 4.7**:** Region in the parameter (β, ℓ / β) space where combustion waves and extinction occurs.

The analysis of voltage and power as a function of mass shows an optimal mass range for both Sb_2Te_3 and Bi_2Te_3 based devices. A very low amount of fuel does not generate enough heat to sustain the propagation of the exothermic reaction. Too much fuel, on the other hand may provide more heat energy, but the unreacted accumulated fuel mass renders the reaction unsustainable [1]. As a result, we observed an optimal mass range (22-26 mg for ~75 mm^2 samples) that sustained the wavefront propagation. Almost both type devices exhibited well-matched trends in terms of the relation between voltage and mass (Figure 4.8 (a)).

Comparison of peak power *vs.* mass for the two different materials is shown in Figure 4.8(b). The peak power was determined using the equation: $P = \frac{V^2}{R}$ in which P is the peak power in watts, V is the peak output voltage in volts and R the resistance in Ω.

The resistance of the Sb_2Te_3 films ranged from 6-12 Ω, while Bi_2Te_3 films resistances were between 2-10 Ω. The difference between the resistances can be attributed to the larger electrical conductivity of Bi_2Te_3 (section 4.2.5). Hence, we expect the power output from Bi_2Te_3-based devices to be higher. Experimental observations show that the peak power generated by Sb_2Te_3-based devices is ~6 mW, while Bi_2Te_3-based devices on an average generate 67% larger power with the peak value of ~10 mW. The resistance of the thermoelectric films remains almost the same even after the end of the reactions. The resistance dependence on temperature is defined by the following equation:

$$R(T) = R_o [1+\alpha (T-T_o)] \qquad (4)$$

where T is the temperature, T_0 is the reference temperature, R_o is the resistance at T_o and α is the temperature coefficient of resistivity of the material. Since, Sb_2Te_3 and Bi_2Te_3 are semiconductors they exhibit negative temperature coefficient of resistivity [14, 15]. Hence, it is expected that the resistance actually decreases during the reaction propagation in our case.

Additionally, the XRD pattern of the samples after the thermopower wave propagation, confirm that the structures of Sb_2Te_3 and Bi_2Te_3 remain unchanged (Figure 4.3 (a), 3 and Figure 4.3 (b), 3), as the peaks remain dominantly unaltered. The average wavefront propagation velocity for Sb_2Te_3-based devices was approximately 0.7 m/s compared to ~0.3 m/s average propagation velocity for Bi_2Te_3-based devices. Propagation velocities for Sb_2Te_3-based devices were generally 2-2.5 times higher than the velocity for Bi_2Te_3-based devices (Figure 4.8(c)), which nicely corresponds to the difference in the thermal conductivities of the two thermoelectric materials. A higher thermal conductivity of the

thermoelectric material provides an extra path for heat conduction (*i.e.* the surface of the Sb_2Te_3 film) in addition to the path provided by the thermally conductive Al_2O_3 substrate. This will consequently cause the wave to travel faster on Sb_2Te_3, as the thermal wave generated from the exothermic reaction travels approximately 2.5 times faster than on Bi_2Te_3 (section 4.2.4).

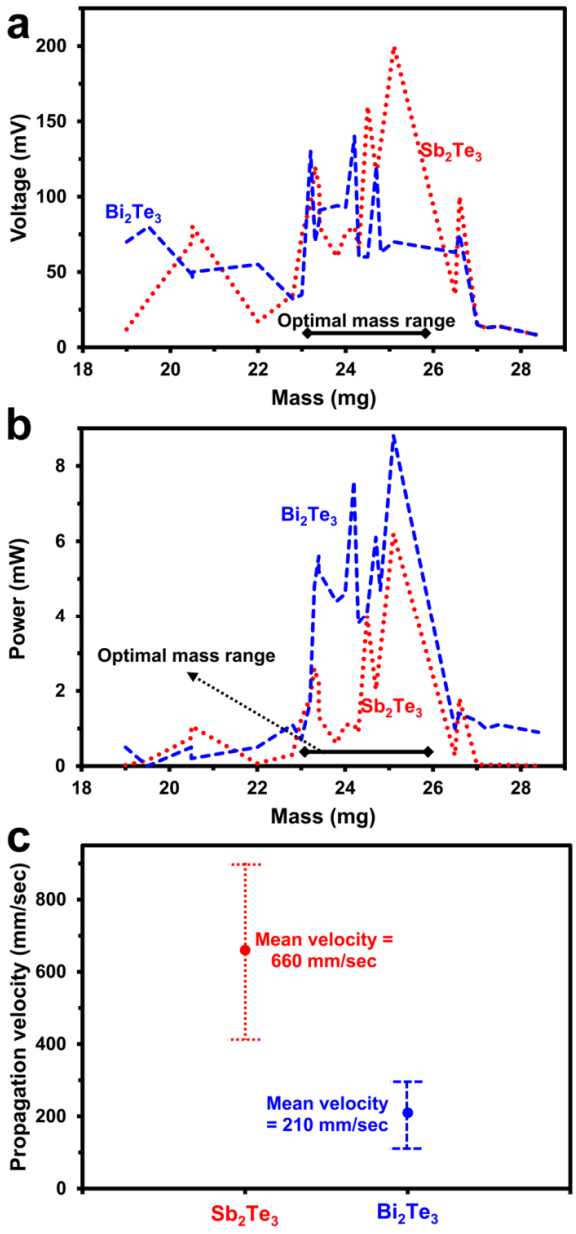

Figure 4.8: (a) Comparison of voltage generated as a function of mass (of fuel and thermoelectric material) for Sb_2Te_3 and Bi_2Te_3 based thermopower devices. (b) Power as a function of mass. (c) Comparison of the reaction propagation velocity for Sb_2Te_3 and Bi_2Te_3 based devices.

4.3.1.2 Thermopower devices based on terracotta substrate

The oscillatory behaviour and wave front velocities strongly depend on the thermal conductivity of the substrate. Terracotta has an identical thermal conductivity to Bi_2Te_3. However, thermal conductivity of Sb_2Te_3 is 2.5 times higher. Consequently, we expect the rate of heat conduction for Sb_2Te_3-based devices to be approximately 2.5 times faster than Bi_2Te_3-based thermopower devices (section 4.2.4).

Figures 4.9 (a,b) show the voltage signals obtained for Sb_2Te_3/terracotta and Bi_2Te_3/terracotta systems, respectively. In line with our expectation, we can see that the reaction propagation for the Sb_2Te_3/terracotta device is ~3 times faster than the Bi_2Te_3/terracotta device. This endorses our explanation that the reaction propagation velocity depends on the thermal conductivity of the material (see section 4.2.4). The voltages generated by both devices are comparatively low. The reason is that a high thermal conductivity is essential for a sustained thermopower wave propagation and to maintain a high reaction temperature [1].

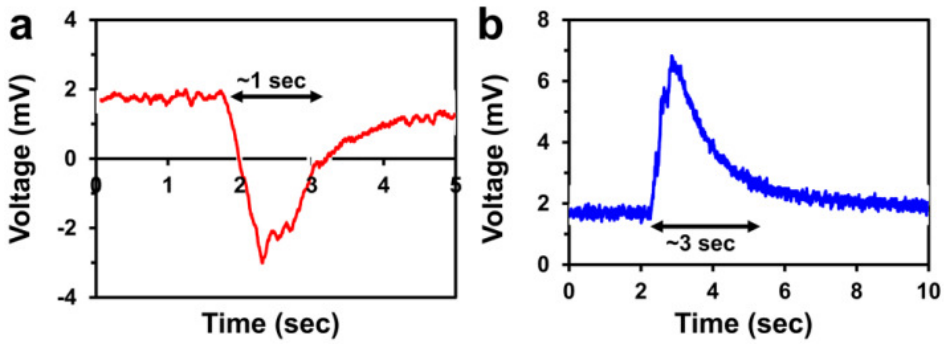

Figure 4.9: Comparison of thermopower voltage signals on terracotta substrates for: (a) Sb_2Te_3 films, (b) Bi_2Te_3 films.

4.4 Summary

In this chapter, the author demonstrated a thermopower wave system based on a novel combination of two complementary thermoelectric materials; p-type Sb_2Te_3 and n-type Bi_2Te_3. A highly thermally conductive substrate of Al_2O_3 accelerated the thermopower waves, which entrained free electrical carriers (holes in Sb_2Te_3 and electrons in Bi_2Te_3) to

produce oscillatory voltages with alternating polarities, while maintaining high specific powers (0.6 kW/kg and 1 kW/kg for Sb_2Te_3 and Bi_2Te_3 based devices respectively).

A full analysis of the system was conducted and it was observed that the thermally conductive substrate of alumina resulted in oscillatory output signals , while there were no oscillations seen when terracotta substrates with a low thermal conductivity were used. This behaviour was also described by developing a theoretical model using the heat transfer equations with suitable boundary conditions. Furthermore, it was observed that the amount of fuel exhibited an optimal mass range in which the output voltages were maximised. A detailed comparison of Sb_2Te_3 and Bi_2Te_3 based thermopower wave systems revealed that devices based on Bi_2Te_3 generated higher specific powers (~67%) mainly owing to the larger electrical conductivity of Bi_2Te_3. It was also shown that the Sb_2Te_3 and Bi_2Te_3 films survived the thermopower wave reaction largely intact.

This work conducted by the author is extremely important as it demonstrates thermopower wave propagation using a p-type (hole dominant electrical conduction) core TE material for the first time. It also shows that output voltage signals with alternating polarities could be obtained using a combination of p and n-type core TE materials. This is an important milestone towards making practically useful thermopower wave systems.

However, in order to establish thermopower wave sources as a viable energy generation technology, even larger output voltages and oscillation amplitudes than demonstrated in this work are required, while maintaining a high specific power. As a result, the author conducted a comprehensive study on the TE properties of transition metal oxides (TMOs) as presented in chapter 2. Based on the analysis, ZnO, which is a TE TMO was identified as an outstanding potential core TE material due to its high Seebeck coefficient, electrical conductivity and moderate thermal conductivity at elevated temperatures.

In the next chapter, the author will demonstrate thermopower wave systems by incorporating thin films of ZnO as the core TE material for the first time.

References

[1] S. Walia, R. Weber, K. Latham, P. Petersen, J. T. Abrahamson, M. S. Strano*, et al.*, "Oscillatory Thermopower Waves Based on Bi_2Te_3 Films," *Advanced Functional Materials,* vol. 21, pp. 2072-2079, 2011.

[2] A. K. Burnham and L. E. Fried, "Kinetics of PBX9404 Aging," presented at the 27th Aging, Compatibility and Stockpile Stewardship Conference, Los Alamos, USA, 2006.

[3] K. Katoh, S. Ito, S. Kawaguchi, E. Higashi, K. Nakano, Y. Ogata*, et al.*, "Effect of heating rate on the thermal behavior of nitrocellulose," *Journal of Thermal Analysis and Calorimetry,* vol. 100, pp. 303-308, 2010.

[4] P. P. Pradyumnan and Swathikrishnan, "Thermoelectric properties of Bi_2Te_3 and Sb_2Te_3 and its bilayer thin films," *Indian Journal of Pure & Applied Physics,* vol. 48, pp. 115-120, Feb 2010.

[5] C. B. Satterthwaite and R. W. Ure, "Electrical and thermal properties of Bi_2Te_3," *Physical Review,* vol. 108, pp. 1164-1170, 1957.

[6] B. Lv, S. B. Hu, W. Li, X. Di, L. H. Feng, J. Q. Zhang*, et al.*, "Preparation and Characterization of Sb_2Te_3 Thin Films by Coevaporation," *International Journal of Photoenergy,* 2010.

[7] K. Wojciechowski, E. Godlewska, K. Mars, R. Mania, G. Karpinski, P. Ziolkowski*, et al.*, "Characterization of thermoelectric properties of layers obtained by pulsed magnetron sputtering," *Vacuum,* vol. 82, pp. 1003-1006, 2008.

[8] G. Miller and C.-Y. Li, "Evidence for the existence of antistructure defects in bismuth telluride by density measurements," *Journal of Physics and Chemistry of Solids,* vol. 26, pp. 173-177, 1965.

[9] N. N. Greenwood, A. Earnshaw, and A. Earnshaw, *Chemistry of the Elements* vol. 1341: Butterworth-Heinemann Oxford, 1997.

[10] W. Choi, S. Hong, J. T. Abrahamson, J. H. Han, C. Song, N. Nair*, et al.*, "Chemically driven carbon-nanotube-guided thermopower waves," *Nature Materials,* vol. 9, pp. 423-429, May 2010.

[11] J. T. Abrahamson, W. Choi, N. S. Schonenbach, J. Park, J.-H. Han, M. P. Walsh*, et al.*, "Wavefront Velocity Oscillations of Carbon-Nanotube-Guided Thermopower Waves: Nanoscale Alternating Current Sources," *ACS Nano,* vol. 5, pp. 367-375, 2010.

[12] G. N. Mercer, R. O. Weber, and H. S. Sidhu, "An oscillatory route to extinction for solid fuel combustion waves due to heat losses," *Proceedings of the Royal Society of London Series a-Mathematical Physical and Engineering Sciences,* vol. 454, pp. 2015-2022, Jul 1998.

[13] J. T. Abrahamson and M. S. Strano, "Analytical Solution to Coupled Chemical Reaction and Thermally Diffusing Systems: Applicability to Self-Propagating

Thermopower Waves," *Journal of Physical Chemistry Letters,* vol. 1, pp. 3514-3519, Dec 2010.

[14] V. D. Das and N. Soundararajan, "Size and temperature effects on the thermoelectric power and electrical resistivity of bismuth telluride thin films," *Physical Review B,* vol. 37, pp. 4552-4559, Mar 1988.

[15] V. D. Das, N. Soundararajan, and M. Pattabi, "Electrical conductivity and thermoelectric power of amorphous Sb_2Te_3 thin films and amorphous crystalline transition," *Journal of Materials Science,* vol. 22, pp. 3522-3528, Oct 1987.

Chapter 5

ZnO based Thermopower Wave Sources

5.1 Introduction

In the previous chapter, the author demonstrated thermopower wave systems based on a novel combination of two conventional thermoelectric (TE) materials with complementary semiconducting properties (p-type Sb_2Te_3 and n-type Bi_2Te_3). Oscillatory voltages with alternating polarities were obtained while maintaining a high specific power of at least 0.6 kW/kg. However, there are still some fundamental deficiencies regarding thermopower wave systems based on Bi_2Te_3 and Sb_2Te_3. The maximum voltages obtained were in the order of only 200 mV. To make such systems practically applicable, larger output voltages while maintaining high specific powers are desired. Additionally, materials such as Bi_2Te_3 and Sb_2Te_3 pose a health hazard and are rare earth. As a result, the author decided to search for alternatives. In chapter 2, the author showed that transition metal oxides (TMOs) can potentially solve these problems. They are generally non-toxic, naturally abundant and a wealth of information about their synthesis is available. Furthermore, some of them can offer a high Seebeck coefficient (S) and electrical conductivity (σ) as well as moderate thermal conductivity (κ) simultaneously.

As presented in chapter 2, ZnO which is a n-type semiconducting transition metal oxide (TMO) is an outstanding candidate as the core TE material for thermopower based energy sources as it exhibits a high Seebeck coefficient which increases with temperature, a high electrical conductivity at elevated temperatures, moderate thermal conductivity and good chemical stability, all of which are highly desirable features.

In this chapter, the author will incorporate thin films of ZnO, a common TE TMO as the core material in thermopower wave sources. Exothermic chemical reactions from a reactive fuel (nitrocellulose) will be coupled to charge carriers in the ZnO film to generate voltage and power. In order to gain a complete understanding of the system, the author will conduct a full analysis by characterizing the ZnO films before and after the thermopower wave reaction. The thermopower wave propagation velocities will also be assessed with respect to the thermal conductivity of the core TE material. The outcome of this work was published as a communication in the journal Chemical Communications.

5.2 Experimental

5.2.1 Deposition of ZnO films

The ZnO films were deposited using RF magnetron sputtering. High purity (99%) ZnO sputtering target (Vin Karola Instruments) was used in the process. The sputtering process was started after the chamber was pumped down to 2×10^{-5} torr. Previous works carried out on RF sputtered ZnO films shows that their resistivity can vary up to 8 orders of magnitude depending on the sputtering power and the substrate temperature [1-3]. Consequently, in this work the author used a high sputtering power (160 W) and no substrate heating in order to synthesise crystalline and electrically conductive ZnO thin films (~1.2 μm). The sputtering process was carried out under an atmosphere of 100% Argon (Ar). Al_2O_3 substrates were used after being adequately cleaned using acetone, isopropanol and distilled water successively, and dried using a high pressure nitrogen gun. Adhesive conductive silver (Ag) paste (42469, Alfa Aesar) was used to make electrical contacts between the copper tape electrodes and the ZnO samples. Nitrocellulose [$C_6H_8(NO_2)_2O_5$] was used as the fuel, due to its large enthalpy of reaction (4.75×10^6 J kg^{-1}) [4]. Sodium azide (NaN_3) in aqueous solution (50 mg/mL) was then added to serve as a primary igniter to lower activation energy (40 kJ/mol for NaN_3, compared to 110–150 kJ/mol for nitrocellulose. Nitrocellulose [C_6H_8 $(NO_2)_2O_5$] was used as the fuel due to its large enthalpy of reaction. Nitrocellulose was prepared by

dissolving millipore nitrocellulose membranes (N8645, Sigma Aldrich) in acetonitrile (15g/L). This solution was drop-cast onto the ZnO film and dried at 50º C. The acetonitrile evaporated, leaving a layer of adhesive nitrocellulose coating. Sodium azide (NaN_3) (14314, Alfa Aesar) in aqueous solution (50mg/mL) was then added on top of the nitrocellulose layer using a pipette to serve as a primary igniter.

5.2.2 SEM and AFM analysis of the ZnO film surface

Scanning electron microscopy (SEM) was conducted using the FEI Nova Nano SEM to investigate the structure of the ZnO films. The SEM image (Figure 5.1(a)) shows that the ZnO film is composed of crystals of varying sizes (250 nm to 1 µm).

Atomic force microscopy (AFM) was carried out on the ZnO films using a AFM-Bruker D3100 in order to assess their surface roughness. The ZnO films exhibit a root mean squared roughness of ~250 nm indicating strong porous nature of the films. A higher porosity is important for an increased thermal conduction between the fuel layer and the ZnO surface thereby resulting in a more sustained reaction propagation. Figure 5.1 (b,c) shows the 2D and 3D profiles of the ZnO film surface sample, respectively.

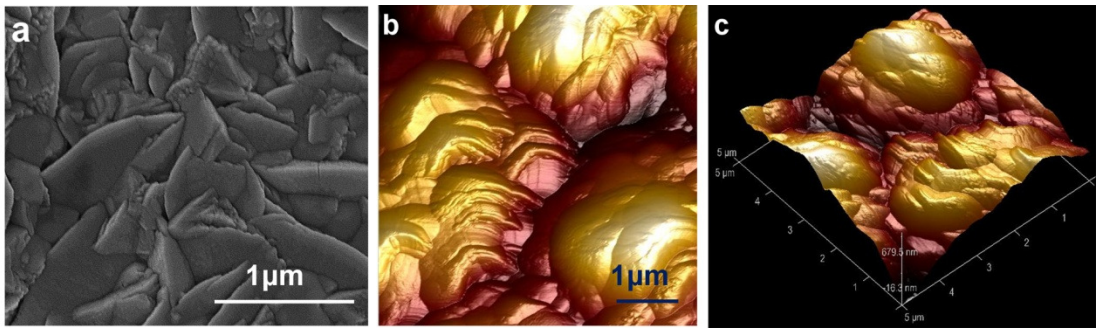

Figure 5.1: (a) SEM micrograph of ZnO film, (b) 2D AFM image of the ZnO film surface (b) 3D AFM profile of the ZnO film surface.

5.2.3 Effect of annealing on the ZnO thin film

The author has previously shown that in a thin film thermopower system configuration, incorporating nitrocellulose as the fuel, the reaction temperature remains under 300 ºC (chapters 2 & 3).To emulate the effect of surface heating on ZnO film during the

thermopower propagation reaction, a ZnO/Al_2O_3 sample was annealed at 300 ºC for 1 min in a vacuum furnace. Its thermal conduction behaviour was compared with the non-annealed sample. Additionally, its crystal structure was also examined after annealing.

In order to make the thermal conductivity comparison, one end of the sample with ZnO film was rested on a heater at 40 ºC and the temperature was recorded at the opposite end. Figure 5.2 shows the results after 150 seconds of measurements. The slope of the rise in temperature with time highlights the rate at which heat is transferred from one end to the other. The slope of the temperature rise was calculated to be 0.28 ºC /s before annealing while it decreased slightly to 0.22 ºC/s after annealing. This directly translates into less than 25% decrease in thermal conductivity. As a result, the thermal conductivity shows a small reduction in value after annealing.

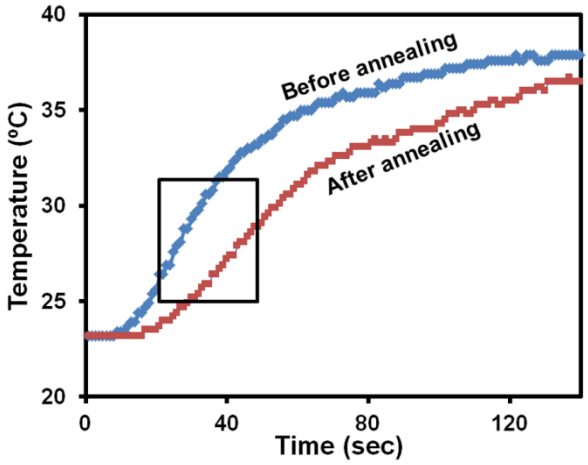

Figure 5.2: Change in thermal conduction of the ZnO films before and after annealing at 300 ºC.

Figure 5.3 (a, b) show the Raman spectra and XRD patterns of the ZnO films before and after annealing, respectively. The Raman spectra were recorded with a system incorporating an Ocean Optics QE 6500 spectrometer, and a 532 nm 40 mW laser as the excitation source. XRD was carried out using a Bruker D8 DISCOVER microdiffractometer fitted with a GADDS (General Area Detector Diffraction System). Data was collected at room temperature using CuKα radiation (λ = 1.54178 Å) with a potential of 40 kV and a current of 20 mA, and filtered with a graphite monochromator

in the parallel mode (175 mm collimator with 0.5 mm pinholes).

The XRD shows that the relative intensity of the dominant (002) to the (101) peak increases slightly (approximately 7%) after annealing [5]. This indicates the *c* axis directional orientation of the ZnO enhanced marginally after annealing. Additionally, the Raman spectra also does not identify any significant change as a result of annealing. This shows that the ZnO films are expected to be stable after the thermopower wave reaction.

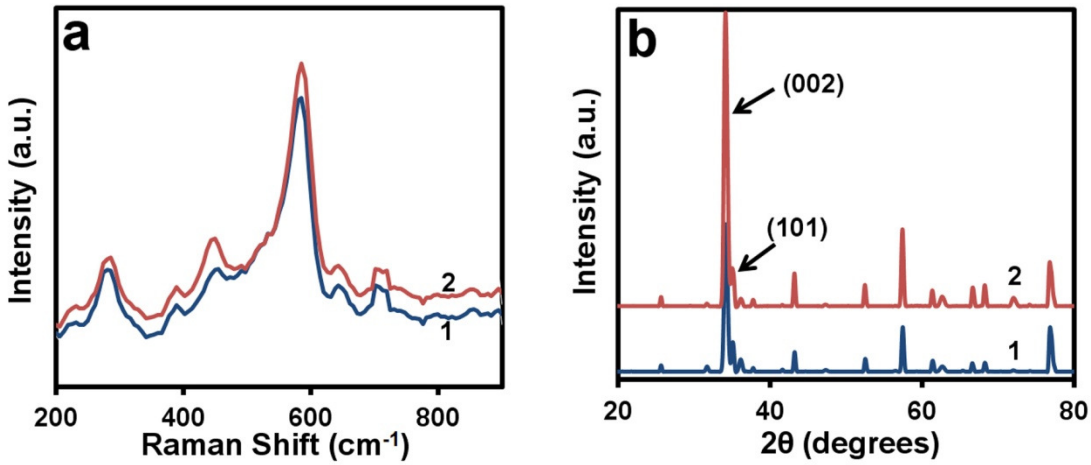

Figure 5.3: (a) Raman peaks of ZnO films 1. before and 2. after thermal annealing at 300 ºC, (b) XRD pattern of 1.ZnO film before and 2. after annealing.

5.2.4 Calculation of specific power

In order to obtain the specific power, the masses of the fuel (nitrocellulose & sodium azide) and thermoelectric films were considered. The relationship between mass, density and volume was used for calculating the mass of the ZnO films as: $m = \rho \times V$,where, m is the mass in grams (g), ρ is the density in g/cm^3 and V is the volume in cm^3.

ρ=5.6 g/cm^3 for ZnO and V depends on the dimensions of the sample and is calculated using the formula, $V = l \times w \times h$ where l is the length, w is the width and h is the thickness of the thermoelectric film in cm, respectively. For fuels, nitrocellulose and NaN_3 in our case, we knew the concentration of the two in their respective solutions. As mentioned in the main manuscript, 15g/L nitrocellulose and 20g/L NaN_3 were used by drop casting.

Hence, we know the amount of solution for each fuel and therefore the corresponding mass for each sample, depending on the volume of the liquid placed on the thermoelectric films. The sum of the masses of the thermoelectric film and the fuels gives the total mass of the materials used. The corresponding power from the sample is obtained using the equation: $P = \frac{V^2}{R}$ in which P is the peak power in watts, V is the peak output voltage in volts and R the resistance in Ω. The output power is then scaled to per kg of the materials to obtain the specific power of the sample in kW/kg.

5.3 Results and Discussion

5.3.1 Output voltage and power

A schematic of the fuel/ZnO/Al_2O_3 is shown in Figure 5.4.

Ignition was initiated at one end using a blow torch with a fine tip resulting in self-propagating reaction waves that travels at a rapid pace to the opposite end. This accelerated reaction wave entrains a simultaneous wave of electrical carriers resulting in an oscillatory voltage output.

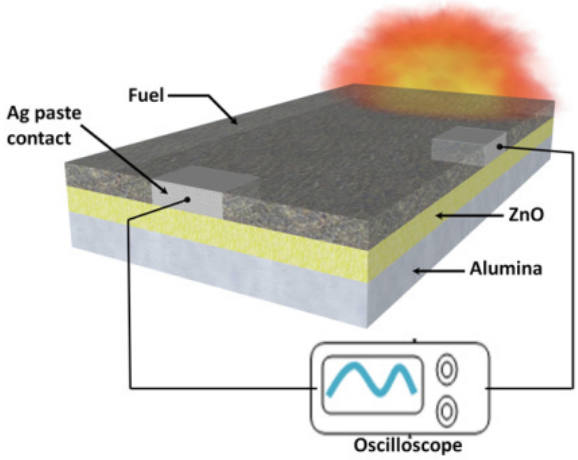

Figure 5.4: Schematic of a fuel/ZnO/Al_2O_3 thermopower wave generation system (not to scale).

The optical photos of the samples before and after the reaction are shown in Figure 5.5 (a). A typical thermopower voltage signal obtained across a sample of the fuel/

ZnO/Al_2O_3 system is shown in Figure 5.5 (b). The voltage profile exhibits two distinct regions: an initial phase during the wave propagation and a cooling down phase until the temperature across the ZnO film reaches equilibrium. The initial reaction phase is a region of rising voltage as the wavefront spreads across the sample until all the combustion fuel is consumed. This is followed by a region of exponential decay. The moving temperature gradient results in voltages with peak magnitudes of up to 500 mV and oscillations with peak-to-peak amplitude of up to 400 mV. The power and specific power obtained from these devices can be as large as 1 mW and 0.5 kW/kg respectively.

The author previously (chapter 2 & 3) adapted the theory of combustion waves to describe coupled thermal waves in fuel/Bi_2Te_3/Al_2O_3 and fuel/Sb_2Te_3/Al_2O_3 systems [6, 7]. Using the model presented by Mercer *et al.* and McIntosh *et al.* the author was able to predict the oscillatory behaviour and the propagation velocity of the thermopower waves [8, 9]. The theoretical analysis concluded that the oscillatory behaviour and wave front velocities strongly depend on the thermal conductivity. A change in thermal conductivity affects the heat loss parameters of the system. It was demonstrated that a higher thermal conductivity enhances the heat transfer through the thermoelectric core, resulting in a proportional increase in combustion velocities. Consequently, Sb_2Te_3 based systems exhibited combustion velocities that were almost 2.5 times faster than the Bi_2Te_3 based devices reflecting the difference in the thermal conductivities of the two materials [7].

Hence, based on the aforementioned analysis it is expected that a higher thermal conductivity of ZnO (~15.0 W/m.K) compared to Bi_2Te_3 (1.0 W/m.K) and Sb_2Te_3 (2.5 W W/m.K) would result in a faster wave velocity and larger oscillations. The author assessed the velocity of the waves in this system by using the duration in which the output voltage exists. As demonstrated previously by the author, the duration of the voltage signal corresponds to the reaction wave propagation time which enables the calculation of the linear propagation velocity of the thermopower waves [6, 7]. A high thermal conductivity of the ZnO thermoelectric material provides an extra path for heat conduction (i.e. the surface of the ZnO film) in addition to the path provided by the

thermally conductive Al_2O_3 substrate. As a result, it was expected that the rate of heat conduction for ZnO-based devices would be approximately 15 times faster than Bi_2Te_3-based thermopower devices. Propagation velocities for the ZnO based devices were measured to range between 12–35 m/sec (Figure 5.5 (c)) which was generally 15–25 times higher than the velocities for Sb_2Te_3 (1.2 m/sec) and Bi_2Te_3 (0.4 m/sec) based devices demonstrated in the author's previous work (chapter 3 and 4) [6, 7]. This difference nicely corresponds to the variation in the thermal conductivities of these materials and is in excellent agreement with theoretical expectations.

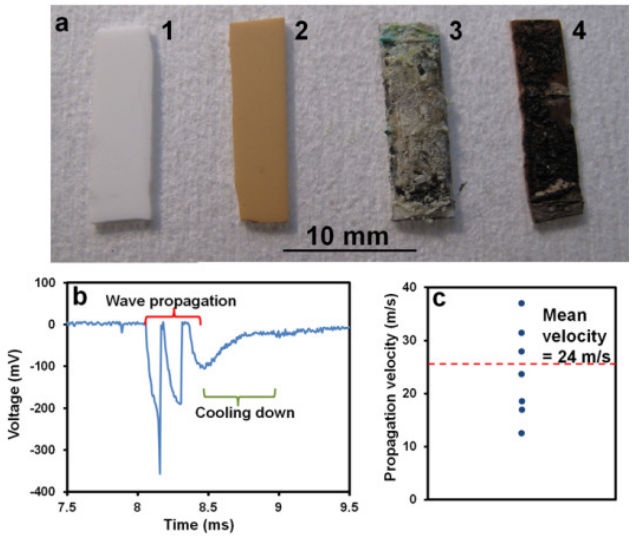

Figure 5.5: (a) Photo of the 1. Al_2O_3 substrate, 2. ZnO deposited on Al_2O_3 substrate, 3. fuel/ZnO/Al_2O_3 sample and 4. Sample after thermopower wave propagation. (b) Oscillatory thermopower voltage signal obtained using the fuel/ZnO/Al_2O_3 device. (c) Reaction propagation velocities for the fuel/ZnO/Al_2O_3 thermopower systems.

5.3.2 Seebeck coefficient and resistance profiles

The author has already shown that in a thin film thermopower system configuration, incorporating nitrocellulose as the fuel, the reaction temperature remains under 300 ºC (chapters 2 & 3) [6, 7]. As a result, an estimation of the Seebeck coefficient and resistance of the ZnO films was required within this range to understand the behaviour of the ZnO based thermopower devices.

The experimental set up to measure the Seebeck coefficient is shown in Figure 5.6 (a). The temperature difference was attained using two Peltier modules. The sample was placed such

that one edge rested on the hot side of one Peltier module while the other edge rested on the cold side of the other module. Micromanipulator probes were then used to measure the voltage generated as a result of the temperature difference. An infrared camera (FLIR Systems, Thermo Vision A320, Sweden) with a lateral resolution of ~ 600 μm was interfaced with ThermaCAM Researcher software to accurately measure the temperature at the two ends of the sample. The temperature gradient between the two ends of the sample was in the range of 10-20 ºC. Measurements were made up to a temperature of 350 ºC with an uncertainty of ± 2%. The uncertainty in the measured Seebeck coefficient values is < ± 5%. A hot plate was used to elevate the temperature of the sample to the required level whereas the Peltier modules were used to create a temperature difference.

Kim *et al.* have shown that the Seebeck coefficient of ZnO increases with temperature. In their work, it has been demonstrated that the Seebeck coefficient of ZnO is approximately −300 μV/K at 85 ºC [10]. In the author's measurements the Seebeck coefficient of the ZnO films was measured to be approximately −360 μV/K. (Figure 5.6 (b)) At 300 ºC the Seebeck coefficient is expected to be approximately −500 μV/K based on linear extrapolation (Figure 5.6 (b)) [10]. Figure 5.6 (b) also shows a comparison of the measured Seebeck coefficient at different temperatures with the literature values. The Seebeck coefficient obtained at 85 ºC was approximately −360 μV/K. It shows that the measurement values are comparable to those obtained by Kim *et al.*[10] The increase in S ($\Delta V/\Delta T$) was observed to be non-linear with $\Delta V/\Delta T$ tending to increase at higher temperatures. A detailed explanation of such temperature dependant behaviour of S has been provided on Pg. 162 of the thesis.

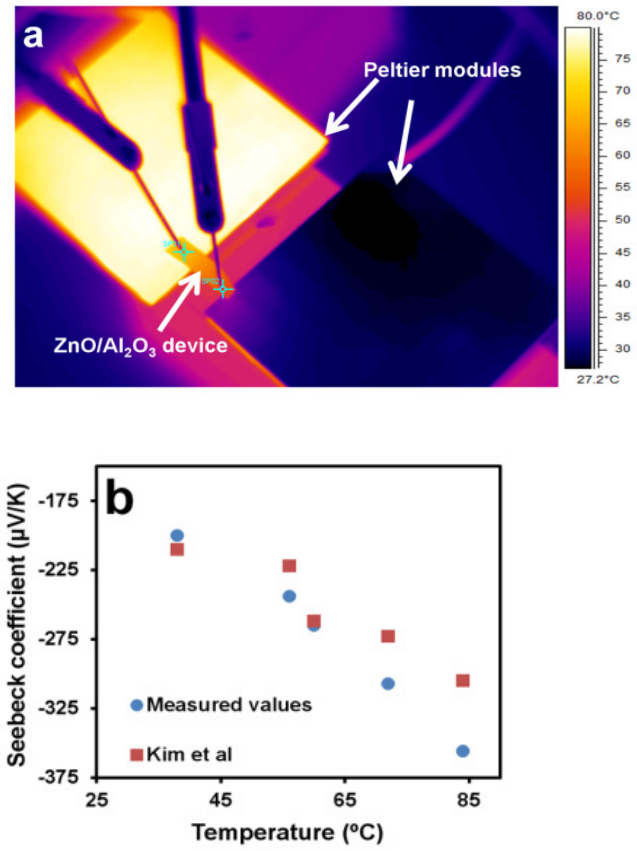

Figure 5.6: (a) Measurement set up used to calculate the Seebeck coefficient. The above image has been obtained using an infrared camera , (b) Measured and literature values of the Seebeck coefficient at different temperatures.

It has been reported that ZnO exhibits a negative temperature coefficient of resistance at temperatures up to 350 ºC [11, 12]. The author measured ZnO film resistance at temperatures of up to 300 ºC as shown in Figure 5.7, which is in close agreement with the value of the temperature coefficient of resistance suggested in the work of Caillaud *et al.* (approximately -3.5×10^{-3} /ºC) [12]. At 300 ºC the resistance was reduced to approximately 250 Ω. This is not an ideal internal impedance for a power source, however it resulted in the maximum current of the order of 2 mA in a short circuit load condition.

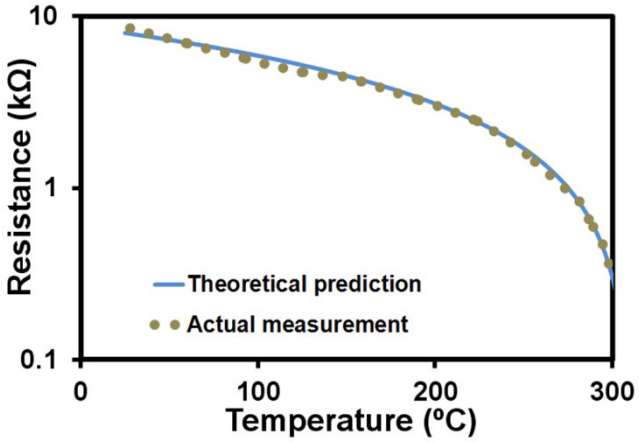

Figure 5.7: Change of resistance of ZnO film with temperature.

5.3.3 ZnO film structure before and after thermopower wave propagation

Figure 5.8(a), 1 illustrates the Raman spectra (indicated as '1') of the as-grown ZnO structure. The peaks observed at around 436 and 576 cm^{-1} correspond to the E_2 (high) and the dominant A_1 (LO) modes, respectively. The E_2 (high) is a characteristic mode of the ZnO hexagonal wurtzite type lattice [13]. In a wurtzite ZnO crystal there are 4 atoms per unit cell and a total of 12 phonon modes. These include one longitudinal-acoustic (LA), two transverse-acoustic (TA), three longitudinal-optical (LO) and six transverse-optical (TO) branches. The A_1 and E_1 branches are both Raman and infrared active while the two non-polar E_2 branches are Raman active only. For lattice vibrations with A_1 symmetries the atoms move parallel to the *c* axis while the high frequency E_2 mode involves the vibrations of the oxygen atoms. If the incident light is normal to the surface and only, A_1(LO) and E_2 modes are observed, it implies that the film is highly oriented. The E_2 (high) is a characteristic mode of the ZnO hexagonal wurtzite type lattice [13]. Therefore, the Raman results prove that the fabricated ZnO films are highly oriented.

The Raman peaks after the deposition of nitrocellulose (spectrum '2' in Figure 5.8 (a)) shows the presence of strong C–H and NO_2 bonds [14]. After the thermopower wave propagation the C–H and NO_2 bonds disappear, while carbon peaks appear on the Raman spectra (spectrum '3' in Figure 5.8 (a)). The exothermic reaction causes the C–H bonds

to decompose, while carbon is left behind as the residual product.

The X-ray diffraction (XRD) pattern Figure 5.8 (b) reveals that the ZnO films are highly crystalline with a strong *c*-directional (002) preferred orientation. Addition of nitrocellulose results in an acute reduction in intensity of the 25.3º 2θ Al_2O_3 substrate peak. This is because the 25.3º 2θ Al_2O_3 substrate peak lies in the same region as the principal XRD reflections for nitrocellulose (ICDD No. 03-0114). A general decrease in diffrraction intensity due to the nitrocellulose coating inhibiting X-ray peneration is observed [7]. The XRD pattern following thermopower wave propagation shows strong ZnO peaks (Figure 5.8 (b)) verifying that ZnO remained largely intact at the end of the process.

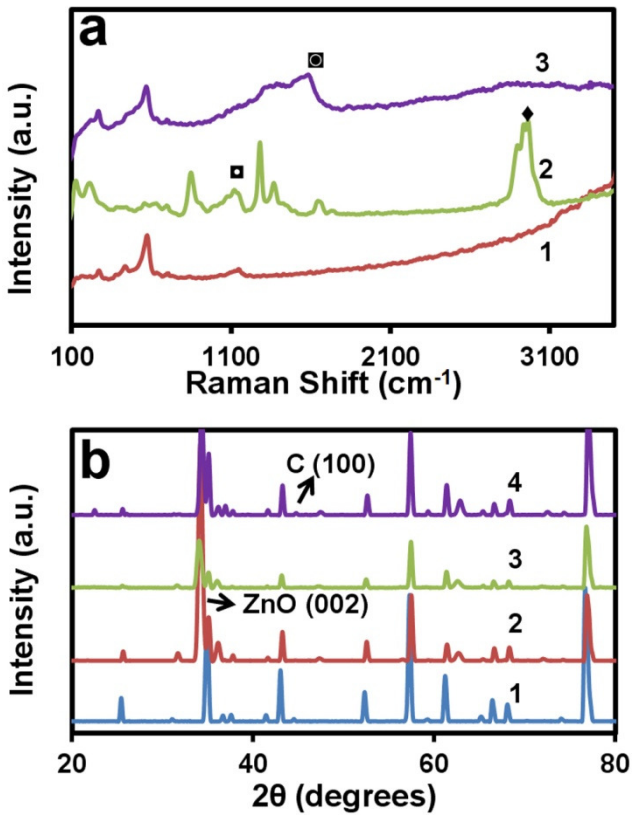

Figure 5.8: (a) Raman spectra of 1. ZnO film, 2. Nitrocellulose coated ZnO film (◘ peak denotes strong NO_2 bonds, ♦ denotes strong C–H bonds), 3. After the reaction (◙ peak denotes carbon), (b) XRD pattern of 1. Al_2O_3 substrate , 2. ZnO before thermopower wave propagation, 3. after adding nitrocellulose and 4. after thermopower wave propagation.

5.4 Summary

In this chapter, the author demonstrated thermopower wave sources based on ZnO, a TE TMO for the first time. It was shown that the incorporation of ZnO as the core TE material resulted in oscillatory output voltages as large as 500 mV, which was at least 200 % larger than previously demonstrated thermopower wave sources based on MWNTs, Bi_2Te_3 and Sb_2Te_3. At the same time a high specific power in the order of 0.5 kW/kg was maintained. The generation of large voltages was due to the high *S* of ZnO at elevated temperatures (–500 μV/K at 300 °C). At the same time the resistance of the ZnO films also dropped with increasing temperature (from ~8 kΩ at room temperature to 250 Ω at 300 °C).

A full analysis of the system was also carried out by characterizing the ZnO films before and after the thermopower wave propagation. It was shown that the ZnO films survived the thermopower wave propagation largely intact.

This work conducted by the author is of utmost importance as it is the first thermopower wave system based on a TMO. By demonstrating the generation of high amplitude alternating voltages (up to 500 mV), this work conducted by the author shows significantly larger voltages and oscillations than previously demonstrated thermopower wave systems. This work also highlights that the incorporation of TMOs in thermopower wave sources will potentially allow their application as a new class of micro-power sources.

After the development of ZnO based thermopower wave sources, the author reviewed other TE TMOs in an effort to identify materials that can result in increasing the output voltages from thermopower wave sources even further. Based on the analysis, MnO_2 appeared to be an outstanding candidate as a core TE material, as it exhibited an extremely high Seebeck coefficient and moderate electrical conductivity at elevated temperatures. In the next chapter, the author will demonstrate thermopower wave sources based on thin films of TE MnO_2 to

show the generation of voltages higher than any thermopower wave system demonstrated previously.

References

[1] M. K. Jayaraj, A. Antony, and M. Ramachandran, "Transparent conducting zinc oxide thin film prepared by off-axis rf magnetron sputtering," *Bulletin of Materials Science,* vol. 25, pp. 227-230, Jun 2002.

[2] S. J. Lim, S. J. Kwon, and H. Kim, "ZnO thin films prepared by atomic layer deposition and rf sputtering as an active layer for thin film transistor," *Thin Solid Films,* vol. 516, pp. 1523-1528, Feb 2008.

[3] M. A. Martínez, J. Herrero, and M. T. Gutiérrez, "Properties of RF sputtered zinc oxide based thin films made from different targets," *Solar Energy Materials and Solar Cells,* vol. 31, pp. 489-498, 1994.

[4] E. Lemieux and R. E. Prud'Homme, "Heats of decomposition, combustion and explosion of nitrocelluloses derived from wood and cotton," *Thermochimica Acta,* vol. 89, pp. 11-26, 1985.

[5] J. Kim, M. C. Kim, J. Yu, and K. Park, "H_2/Ar and vacuum annealing effect of ZnO thin films deposited by RF magnetron sputtering system," *Current Applied Physics,* vol. 10, pp. S495-S498, May 2010.

[6] S. Walia, R. Weber, K. Latham, P. Petersen, J. T. Abrahamson, M. S. Strano*, et al.*, "Oscillatory Thermopower Waves Based on Bi_2Te_3 Films," *Advanced Functional Materials,* vol. 21, pp. 2072-2079, Jun 2011.

[7] S. Walia, R. Weber, S. Sriram, M. Bhaskaran, K. Latham, S. Zhuiykov*, et al.*, "Sb_2Te_3 and Bi_2Te_3 based thermopower wave sources," *Energy & Environmental Science,* vol. 4, pp. 3558-3564, Sep 2011.

[8] A. C. McIntosh, R. O. Weber, and G. N. Mercer, "Non-adiabatic combustion waves for general Lewis numbers: Wave speed and extinction conditions," *Anziam Journal,* vol. 46, pp. 1-16, Jul 2004.

[9] G. N. Mercer, R. O. Weber, and H. S. Sidhu, "An oscillatory route to extinction for solid fuel combustion waves due to heat losses," *Proceedings of the Royal Society of London Series a-Mathematical Physical and Engineering Sciences,* vol. 454, pp. 2015-2022, Jul 1998.

[10] K. H. Kim, S. H. Shim, K. B. Shim, K. Niihara, and J. Hojo, "Microstructural and thermoelectric characteristics of zinc oxide-based thermoelectric materials fabricated using a spark plasma sintering process," *Journal of the American Ceramic Society,* vol. 88, pp. 628-632, Mar 2005.

[11] N. H. Al-Hardan, M. J. Abdullah, and A. A. Aziz, "Sensing mechanism of hydrogen gas sensor based on RF-sputtered ZnO thin films," *International Journal of Hydrogen Energy,* vol. 35, pp. 4428-4434, May 2010.

[12] F. Caillaud, A. Smith, and J.-F. Baumard, "Effect of oxygen chemisorption on the electrical conductivity of zinc oxide films prepared by a spray pyrolysis method," *Journal of the European Ceramic Society,* vol. 7, pp. 379-383, 1991.

[13] U. Ozgur, Y. I. Alivov, C. Liu, A. Teke, M. A. Reshchikov, S. Dogan*, et al.*, "A comprehensive review of ZnO materials and devices," *Journal of Applied Physics,* vol. 98, Aug 2005.

[14] D. S. Moore and S. D. McGrane, "Comparative infrared and Raman spectroscopy of energetic polymers," *Journal of Molecular Structure,* vol. 661, pp. 561-566, Dec 2003.

Chapter 6

MnO_2 based Thermopower Wave Sources with Exceptionally large Output Voltages

6.1 Introduction

In the previous chapter, the author of this thesis demonstrated thermopower wave sources by incorporating thin film thermoelectric (TE) cores of ZnO, which is a transition metal oxide (TMO), for the first time. The implementation of a TE TMO turned out to be a great approach and output voltages (as large as ~500 mV) and oscillatory amplitudes that were at least 200% higher than previously reported thermopower wave systems based on MWNT, Bi_2Te_3 and Sb_2Te_3 were obtained, while maintaining a high specific power in the order of 0.5 kW/kg. It was also shown that the Seebeck coefficient (S) and the electrical conductivity (σ) of the ZnO films increased with temperature underlining its suitability as a core TE material for thermopower wave sources. However, in order to establish thermopower wave sources as a viable energy generation technology, voltages more than 1.2 V, exceeding those of small batteries, are desirable. The results obtained by incorporating ZnO as the core TE material demonstrated the potential of employing TE TMOs in thermopower wave sources. Subsequently, the author comprehensively investigated TMOs other than ZnO and selected manganese dioxide (MnO_2) as the potential candidate. As presented in chapter 2, MnO_2 exhibits an exceptionally high Seebeck coefficient. MnO_2 is also an n-type semiconductor with an electrical conductivity that increases at elevated temperatures, thereby resulting in a high thermoelectric power factor (TPF-'$S^2\sigma$'). A high TPF is vital to increase the output voltage and power from thermopower wave sources and the choice of MnO_2 as the core TE material was based on this highly desirable characteristic of MnO_2.

In this chapter, the author will demonstrate thermopower wave sources based on thin films of TE MnO_2, as the core material. Exothermic chemical reactions from a solid fuel (nitrocellulose) will be coupled to charge carriers of the MnO_2 layers to generate voltage and power. The author will also present a full analysis of the system by characterizing the Seebeck coefficient and the electrical resistivity of the MnO_2 based thermopower wave devices before and after the thermopower wave reaction. The influence of the thermal conductivity of the core TE material on the reaction propagation velocities will be assessed and a comparison with previously demonstrated thin film thermopower wave sources will be carried out. The work in this chapter was published as a full article in the Journal of Physical Chemistry C.

6.2 Experimental details

6.2.1 Synthesis of MnO_2 thin films

MnO_2 films were prepared using ball-milled MnO_2 powder (42250, Alfa Aesar). The MnO_2 powder was ball-milled for 20 h at 500 rpm with a ball-to-powder mass ratio of 10:1 in order to reduce the size of the crystals. This MnO_2 nanopowder was then mixed with acetone (25 mg/mL) and the solution was subsequently drop-casted on to alumina substrates and dried in ambient conditions. Alumina with a thickness of ~100 μm was used as the substrate as it exhibits high thermal conductivity and can assist in the propagation of the thermopower waves [1-3]. The as fabricated samples were then annealed in air at 400 ºC for 4 h in a MTI V1200X furnace to improve the crystallinity, adhesion and consequently the electrical conductivity of the films. Scanning electron microscopy (SEM) was conducted using the FEI Nova Nano SEM to investigate the structure of the MnO_2 films. Figure 6.1 (a, b) shows the SEM images of the MnO_2 surface before and after the annealing process.

Annealing results in an improvement in the crystallization state of the film by lowering the number of grain boundary barriers, thereby facilitating the mobility of charge carriers resulting in a reduced resistivity [4].

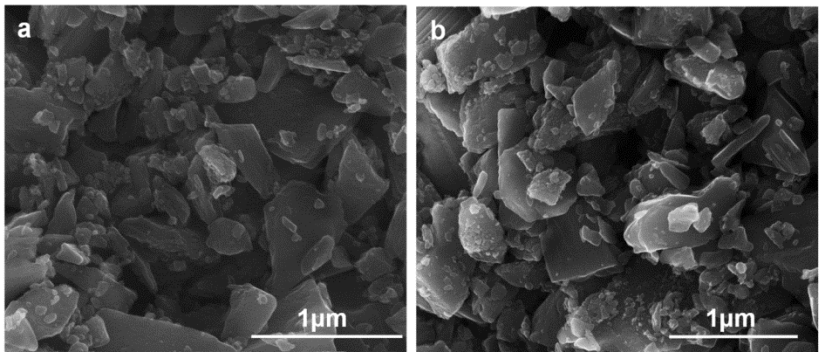

Figure 6.1: SEM images of the MnO_2 film surfaces: (a) before annealing and (b) after annealing.

6.2.2 Effect of ball-milling

SEM micrographs (Figure 6.2 (a,b)) show that the as-purchased powder is composed of crystals of dimensions in the order of 4-6 µm. Ball milling was used to increase the surface-to-volume ratio (thereby increasing the possibility of the phonon exchange between the fuel and MnO_2). Following ball milling the MnO_2 powder comprised of crystals ranging from 400-700 nm in size, as suggested by Song *et al*. [6] The SEM micrographs also illustrate the highly porous nature of the films. BET analysis of the MnO_2 films (carried out using an ASAP 2000 Surface Area Analyser) revealed an average pore diameter of ~ 12 nm further confirming the porous nature of the MnO_2 films.

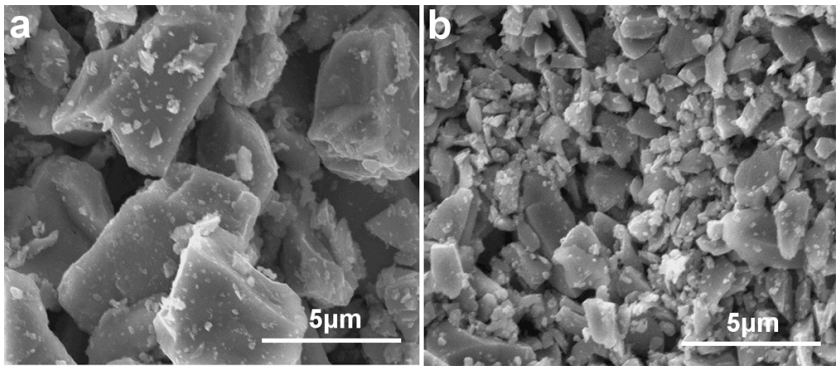

Figure 6.2: SEM micrograph of the (a) MnO_2 film before ball milling, (b) after ball milling.

However, no enhancement in Seebeck coefficients was observed as a result of ball-milling which was in contrast with the claim made by Song *et al.* [6] (Figure 6.3). Figure 6.3 shows that the Seebeck coefficient values for the MnO_2 films synthesised using ball-milled and non ball-milled powder were quite similar. The experimental set-up used to measure the Seebeck coefficient was identical to the one described in section 5.3.2 of chapter 5.

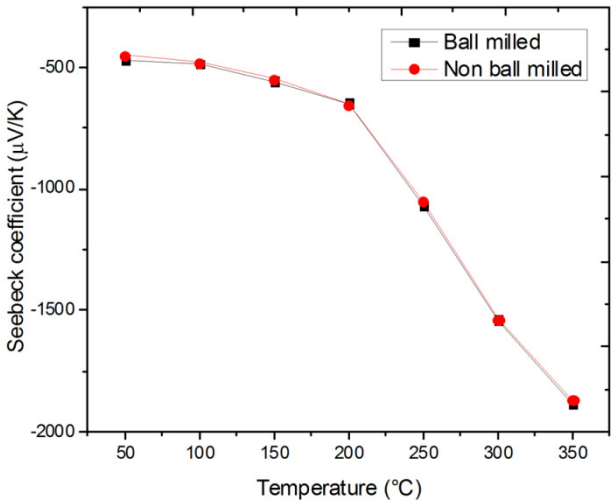

Figure 6.3: Seebeck coefficient *vs* temperature for MnO_2 films synthesised using ball-milled and non-ball milled MnO_2 powder.

6.2.3 Preparation of the fuel

Nitrocellulose [$C_6H_8(NO_2)_2O_5$] was used as the fuel, due to its large enthalpy of reaction (4.75×10^6 J/kg). Sodium azide (NaN_3) in aqueous solution (50 mg/mL) was then added to serve as a primary ignition source to lower activation energy (40 kJ/mol for NaN_3, compared to 110–150 kJ/mol for nitrocellulose).

6.2.4 Device schematic and voltage measurement set up

A pictorial representation of a MnO_2 based thermopower wave device is shown in Figure 6.4 (a). Electrical contacts between the copper tape electrodes and the TE layer were made using an adhesive conductive silver paste (42469, Alfa Aesar). The MnO_2 films (2-2.5 μm thick) were subsequently coated with ~ 220-260 μm thick solid fuel layer (nitrocellulose & sodium azide in this case) and integrated with electrodes to complete the system.

An Agilent MSO7014 oscilloscope (set at an input impedance of 1 MΩ) was used for acquiring the output voltage signals from the thermopower wave devices. A load resistance of 1 kΩ was also added in parallel to the input of the oscilloscope in order to ensure that power is generated. A schematic of the measurement set up is shown in Figure 6.4 (b).

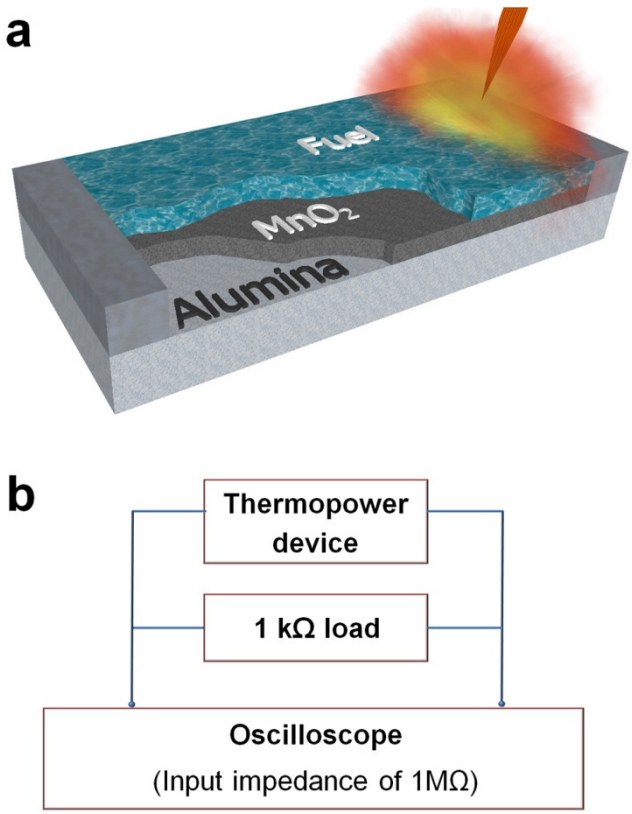

Figure 6.4: Schematic of (a) a thermopower wave generation device (not to scale) and (b) the measurement set up for a fuel/MnO_2/Al_2O_3 thermopower wave device.

6.2.5 Calculation of specific power

In order to obtain the specific power, the masses of the fuel (nitrocellulose & sodium azide) and thermoelectric films were considered. The relationship between mass, density and volume was used for calculating the mass of the MnO_2 films as: $m = \rho \times V$,where, m is the mass in grams (g), ρ is the density in g/cm^3 and V is the volume in cm^3.

For MnO_2, ρ=5.026 g/cm^3 and V depends on the dimensions of the sample and is calculated using the formula $V = l \times w \times h$, where l is the length, w is the width and h is the thickness of the TE film in cm, respectively. For fuels, nitrocellulose and NaN_3, the concentration in their respective solutions is known. As mentioned in the experimental section, 15g/L nitrocellulose and 20g/L NaN_3 were used by drop casting. Hence, we know the amount of solution for each fuel and therefore the corresponding mass for each sample, depending on the volume of the liquid placed on the thermoelectric films. The

sum of the masses of the thermoelectric film (~ 0.60 mg) and the fuels (~3.2 mg) gives the total mass of the materials used. The corresponding power from the sample is obtained using the equation: $P = \frac{V^2}{R}$, in which P is the peak power in watts, V is the peak output voltage in volts and R is the load resistance in Ω. The output power is then scaled to per kg of the materials to obtain the specific power of the sample in kW/kg.

6.3 Results and Discussion

6.3.1 Output voltage and power

A schematic of the fuel/MnO_2/Al_2O_3 system is shown in Figure 6.4 (a). A fine tip blowtorch was employed to initiate the reaction at one end. This resulted in a self-propagating reaction wave that travels rapidly to the other end, simultaneously entraining electrical carriers along its path, resulting in an output signal. A typical thermopower voltage signal of the fuel/MnO_2/Al_2O_3 system is shown in Figure 6.5 (a). The voltage signal was positive for waves emanating from the negative electrode. This can be ascribed to the n-type semiconducting nature of MnO_2. Additionally, the polarity of the voltage signal depends on the direction of the thermopower wave propagation. The voltage profiles can be divided into two distinct regions (Figure 6.5 (a)). An initial phase during the thermopower wave propagation, which lasts until the combustion fuel is consumed followed by a decaying phase which is the cooling down region. During the initial phase the moving temperature gradient across the surface of MnO_2 results in a voltage output, while in the decay phase the voltage drops back to zero as the temperature reaches equilibrium with the room temperature environment. This thermal wave propagation results in peak voltages as large as 1.8 V ± 5% and fluctuations of the order of 400 mV ± 5% in the output voltage signal (Figure 6.5 (a)). A peak output power as large as 3.24 mW ± 10% was also observed.

The specific power obtained from the MnO_2-based thermopower wave devices was of the order of ~1.0 kW/kg ± 15%. Voltage and power outputs obtained from seven MnO_2-based thermopower devices are shown in Figure 6.5 (b).

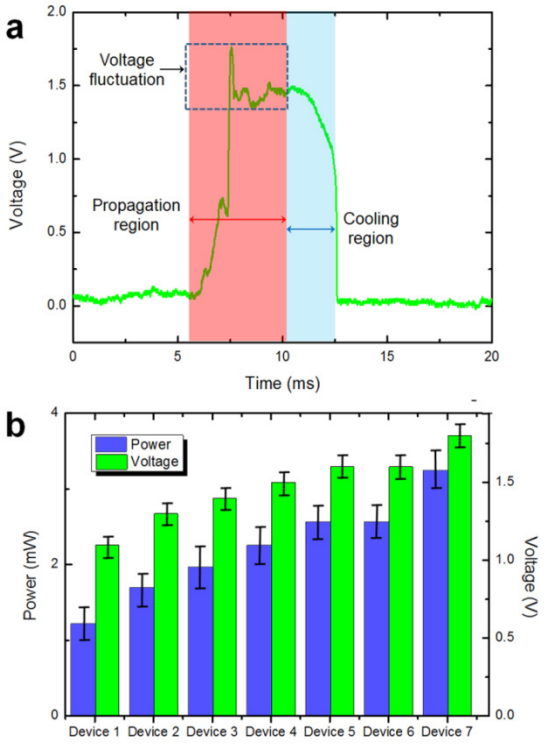

Figure 6.5: (a) A thermopower voltage signal obtained using the fuel/MnO_2/Al_2O_3 device. (b) Power and voltage outputs obtained from the fuel/MnO_2/Al_2O_3 thermopower devices.

The reaction temperature remains in the region of 300-400 ºC similar to the author's previous experiments [1-3]. There is a large variation in the output voltage and consequently power. This is due to the chaotic nature of thermopower waves. This chaotic behaviour is an intrinsic part of the thermopower wave propagation front, which is described by the equations governing the system and have been discussed by the author in Chapters 1 and 2. This produces disordered changes in the temperature of the areas near the wavefronts. As both internal resistivity and Seebeck coefficient change with temperature (Figure 6.6), variation in the output values of thermopower wave devices is inherently large even for those devices with very similar fabrication parameters. As such, this chaotic behaviour can be observed in the output voltage profiles (Figure 6.5 (a)).

6.3.2 Resistivity and Seebeck coefficient profiles before and after the reaction

To understand the performance of the system, the resistivity and Seebeck coefficient of MnO_2 films were characterized as a function of temperature. These two parameters are sufficient to assess and predict the output of the system as the power, voltage and current generated are directly dependent on these two properties.

An accurate value of the resistance is required in order to calculate the output power from the devices as well as the internal resistivity of the source. The author measured the MnO_2 film resistance at temperatures as large as 300 ºC. The resistivity profile of the MnO_2 films as a function of temperature is shown in Figure 6.6**.** From these results the thermal coefficient of resistance is estimated to be equal to -2.85×10^{-3} /ºC, which is a negative value for the n-type MnO_2. At room temperature the resistivity of the film was 0.43 Ω.cm ± 8% which was reduced to 0.1 Ω.cm ± 8% at 300 ºC. In order to evaluate the stability of the film, the resistivity profile was also obtained after the thermopower wave propagation (Figure 6.7 (a)). The resistivity profile after the reaction followed a similar trend as the one before the reaction. It can be seen that the resistivity of the film slightly increased after the reaction. Such an increase in resistivity is ascribed to a slight damage (the surface was chipped at a few locations) to the MnO_2 films. However, it proves that the MnO_2 films remain fairly stable after the thermopower wave propagation.

The Seebeck coefficient of the MnO_2 films was also measured for temperatures up to 350 ºC (Figure 6.6). The room temperature Seebeck coefficient was measured to be −460 μV/K ± 5%. Interestingly, the Seebeck coefficient shows a significant increase in magnitude at elevated temperatures, attaining a value of −1900 μV/K ± 5% at 350 ºC. It is expected that the absolute value of Seebeck coefficient increases even further up to a temperature of approximately 500 ºC, after which MnO_2 starts transforming into Mn_2O_3 [7]. The Seebeck coefficient profile of the film after the thermopower wave propagation was very similar to the one before the reaction (Figure 6.7 (b)).

The aforementioned measurements also followed the trend reported by Klose *et al.* and Khan *et al.* [8, 9] Furthermore, such behaviour explains the generation of such high output voltages in the MnO_2 based thermopower wave systems developed by the author.

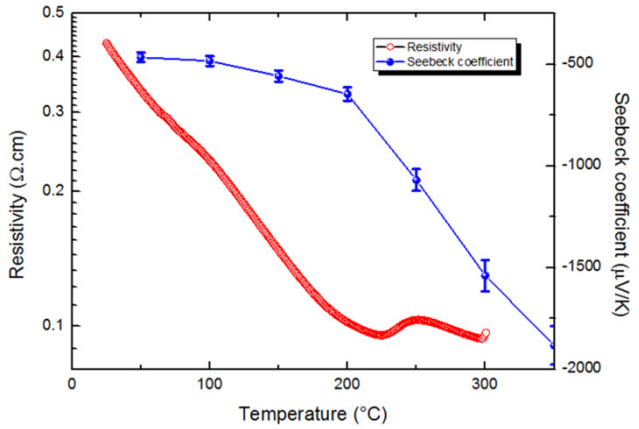

Figure 6.6: Changes of resistivity and Seebeck coefficient of the MnO_2 film with temperature.

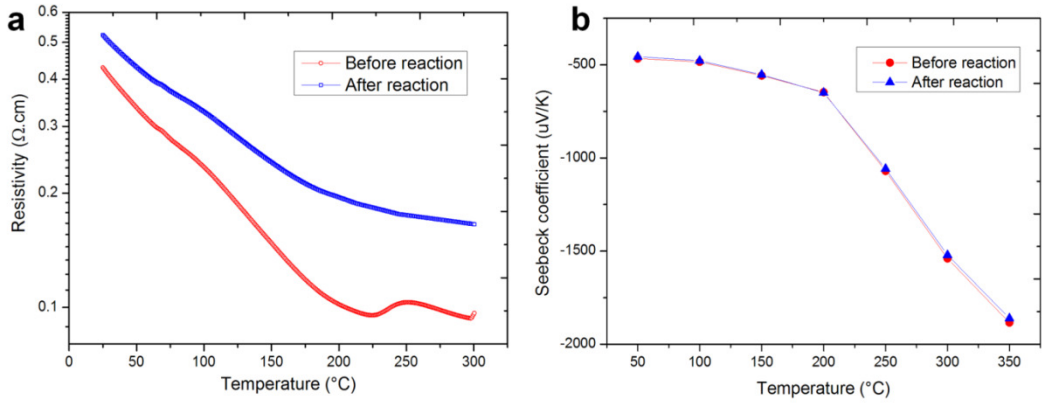

Figure 6.7: (a) Resistivity profiles of the MnO_2 films before and after thermopower wave propagation, (b) Seebeck coefficient profiles before and after thermopower wave propagation.

In order to explain the observation of enhanced Seebeck coefficient (S) with an increase in temperature, the following expression can be used to describe S for semiconducting materials (which is also a good approximation for several μm thick films made of micro/nanostructured grains) [10]:

$$S = \frac{8m^*\pi^2 k_B^2}{3eh^2} T \left(\frac{\pi}{3n}\right)^{2/3} \quad (1)$$

where, n is the carrier concentration, m^* is the carrier effective mass, e is the electronic charge, T is the temperature, h is Planck's constant and k_B is the Boltzmann constant.

From Eq. 1, it is predicted that in general an increase in temperature linearly enhances S. Eq.1 also shows that a higher m^* results in larger Seebeck coefficients. Additionally, the equation shows that, any decrease in carrier concentration can also enhances S.

The author has previously shown that the Seebeck coefficient of ZnO rises significantly with increasing temperature [1]. The calculations demonstrate that room temperature carrier concentration of our ZnO film (considering a typical carrier mobility of ~1 $cm^2/V.s$ for ZnO thin films [11]) is ~10^{19} /cm^3, while ZnO electron effective mass is relatively high (0.28) [12]. Obviously, the carrier concentration of ZnO increases with temperature due to the thermionic effect [13]. However, the influence of temperature on S is more dominant than the carrier concentration for temperatures smaller than 350 ºC, after which S starts falling [14]. Hence, an overall enhancement of Seebeck coefficient is observed at the temperatures in which ZnO based thermopower wave systems operate.

The author proposes that the enhanced S at elevated temperatures for MnO_2 can also be similarly described. To date, there are no reliable studies regarding the effective mass of electrons in MnO_2 films. Although, the reported very low electron mobility for MnO_2 (0.1 $cm^2/V.s<$) should be partially as a result of a relatively high electron effective mass [15]. In the MnO_2 films synthesised by the author, the carrier concentration is in the order of n = ~10^{18} /cm^3 for the upper limit of mobility of approximately 0.1 $cm^2/V.s$ (calculated from $n=\sigma/e\mu$ where μ is the mobility and σ is the electrical conductivity), which is an order of magnitude smaller than that of the ZnO film based thermopower wave system in our previous work [1]. As such for MnO_2, the effect of electron concentration should take effect and dominate at temperatures higher than 600 ºC and the absolute value of its Seebeck coefficient should increase with temperature linearly up to those temperatures.

Increase in Seebeck coefficients with temperature has been demonstrated in other transition metal oxides such as TiO_2 and WO_3 [16, 17], but such dramatically high values, which are observed for MnO_2, have not been reported for those transition metal oxides at elevated temperatures.

6.3.3 XRD of MnO_2 films before and after the reaction

The author also observed that the MnO_2 films are very stable both before and after the reaction. XRD was carried out using a Bruker D8 DISCOVER microdiffractometer fitted with a GADDS (General Area Detector Diffraction System). Data was collected at room temperature using CuKα radiation (λ = 1.54178 Å) with a potential of 40 kV and a current of 20 mA, and filtered with a graphite monochromator in the parallel mode (175 mm collimator with 0.5 mm pinholes). The X-ray diffraction (XRD) patterns shown in Figure 6.8 reveal the presence of the signature MnO_2 peaks (ICCD 01-072-1984), showing that the films are highly crystalline and exhibit a rutile crystal structure [18]. The XRD pattern after the wave propagation (Figure 6.8) shows the principal MnO_2 peaks which proves that the MnO_2 films remain largely intact after the reaction. Additionally, the XRD peaks after the reaction do not show any presence of Mn_2O_3 suggesting that the reaction temperature remained under 500 ºC.

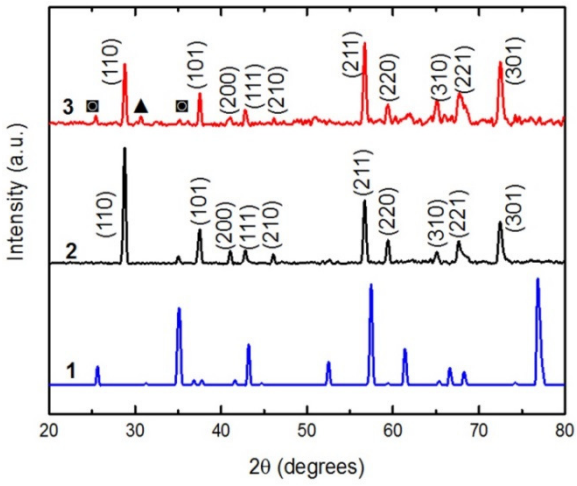

Figure 6.8: XRD pattern of 1. Al_2O_3 substrate , 2. MnO_2 before thermopower wave propagation, and 3. after thermopower wave propagation. The symbols ◙ and ▲ denote the XRD peaks of the Al_2O_3 substrate and sodium azide (NaN_3) respectively.

6.3.4 Comparison of thermal conduction rates and thermopower wave propagation velocities for different core TE materials

The author previously developed a model for the thermopower wave propagation by adapting the theory of combustion waves as described by McIntosh *et al.* and Mercer *et al.* [19, 20] This model demonstrated that the thermal conductivity of the core material affects the propagation velocity as well as the chaotic behaviour of the thermopower waves. Furthermore, it showed that a higher thermal conductivity facilitates the transfer of heat through the thermoelectric core, resulting in a proportional increase in combustion velocities [1-3]. The thermal conductivity of MnO_2 is 4.0 W/m.K compared to previously investigated core thermoelectric materials such as Bi_2Te_3 (1.0 W/m.K), Sb_2Te_3 (2.5 W/m.K) and ZnO (15.0 W/m.K) [21-26]. Based on the theoretical model, it is expected that the propagation velocity for the MnO_2 devices would be higher than Bi_2Te_3, Sb_2Te_3 and lower than ZnO based devices.

In order to experimentally demonstrate the difference between the thermal conduction behaviour of different thermoelectric core materials; Bi_2Te_3, Sb_2Te_3, MnO_2 and ZnO films on Al_2O_3 substrates with identical dimensions were heated using a micro heater at one end. Figure 6.9 (a) shows the measurement set up.

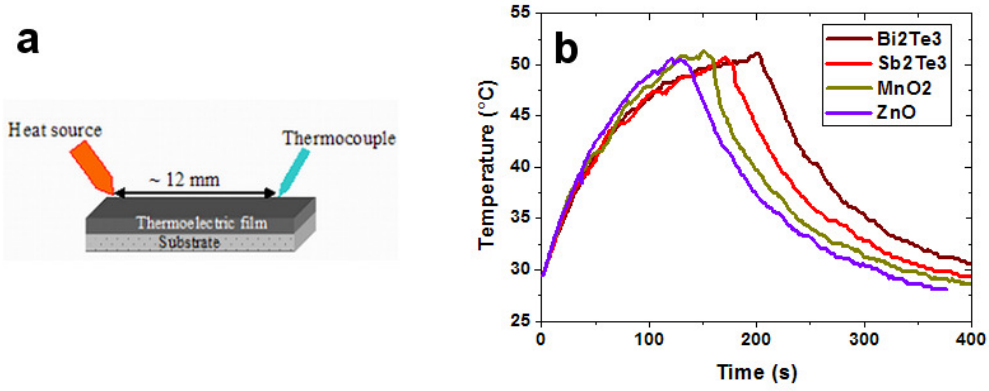

Figure 6.9: (a) Measurement set up to compare the thermal conduction rates of different thermoelectric films, (b) Difference between thermal conduction rates of Bi_2Te_3, Sb_2Te_3, MnO_2 and ZnO.

A heater with a sharp tip was used as the heating source and was positioned at one end on the sample. The temperature profile was acquired at the opposite end using a TENMA 727730

thermocouple. The heat source was withdrawn as soon as the temperature at the opposite end reached 50 ºC. Figure 6.9 (b) shows the temperature profile for the samples. A faster approach to 50 ºC indicates a higher rate of thermal conduction and therefore a higher thermal conductivity. Figure 6.9 (b) shows that Bi_2Te_3 sample takes 197 s to reach 50 ºC while Sb_2Te_3, MnO_2 and ZnO take 168, 150 and 126 s, respectively. Hence, it can be concluded that Bi_2Te_3 exhibits the lowest thermal conductivity followed by Sb_2Te_3, MnO_2 and ZnO in ascending order.

The velocity of the thermopower waves was assessed experimentally to test the influence of thermal conductivity on the wave propagation velocities. The duration of the output signal corresponds to the time of the wave propagation which enables the author to calculate the linear propagation velocity of the wave. The author has previously shown that the average combustion velocities for Bi_2Te_3, Sb_2Te_3 and ZnO based thermopower devices are 0.2, 0.7 and 23.0 m/sec, respectively with an error of ±10% [1-3]. Figure 6.10 shows that the average combustion velocity for the MnO_2-based devices is 3.9 m/sec. Due to the chaotic nature of the thermopower waves, the propagation velocities exhibit a wide range for all thermopower wave systems as shown in Figure 6.10 [1-3]. The difference in the propagation velocities corresponds well to the variation in the thermal conductivities of the core thermoelectric materials and is in excellent agreement with the theoretical expectations.

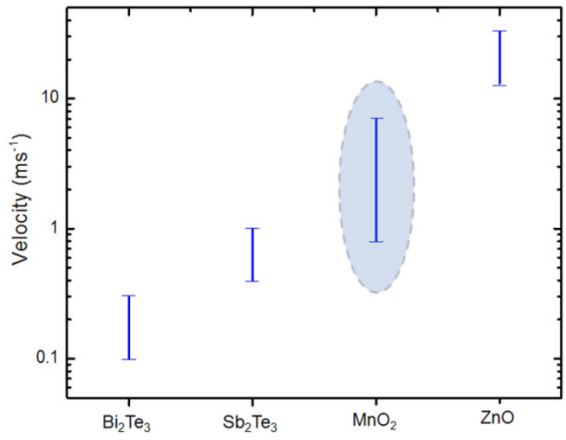

Figure 6.10: Reaction propagation velocities for thermopower systems based on different core thermoelectric materials.

6.4 Summary

In this chapter, the author demonstrated thermopower wave propagation using MnO_2 as the core TE material. The MnO_2 based thermopower wave devices resulted in extremely large output voltages of up to 1.8 V, which was at least 300% higher than any previously demonstrated thermopower wave system. At the same time, a high specific power in the order of ~1 kW/kg was maintained. The achievement of such large output voltages and specific power was primarily due to the large *S* exhibited by MnO_2 at elevated temperatures (–1900 μV/K at 350 °C) in which thermopower wave systems with nitrocellulose as the reactive fuel operate. Its electrical resistivity also dropped significantly with an increase in temperature (0.43 Ω.cm at room temperature to 0.1 Ω.cm at 300 °C). Consequently, a high TPF in the order of ~10^3 μW/m.K^2 was achieved at elevated temperatures.

The author also provided important fundamental insights to explain the observation of enhanced Seebeck coefficients with increasing temperatures in TMOs such as ZnO and MnO_2. A full analysis of the system by characterizing the device before and after the thermopower wave reaction was conducted and it was shown that the MnO_2 films survived the thermopower wave propagation largely intact and retained their large TPFs. It was also shown that the thermopower wave propagation velocities were strongly influenced by the thermal conductivity of the core TE material.

This work conducted by the author is very important as it is the first demonstration of voltages that are high enough to power small electronic circuits. Furthermore, this work conducted by the author underscores the crucial role that TMOs can play to make thermopower wave sources a viable future energy generation technology.

In the next chapter the author will present a summary of his PhD thesis and discusses future work related to his PhD research project.

References

[1] S. Walia, R. Weber, S. Balendhran, D. Yao, J. T. Abrahamson, S. Zhuiykov*, et al.*, "ZnO based thermopower wave sources," *Chemical Communications,* vol. 48, pp. 7462-7464, 2012.

[2] S. Walia, R. Weber, K. Latham, P. Petersen, J. T. Abrahamson, M. S. Strano*, et al.*, "Oscillatory Thermopower Waves Based on Bi_2Te_3 Films," *Advanced Functional Materials,* vol. 21, pp. 2072-2079, 2011.

[3] S. Walia, R. Weber, S. Sriram, M. Bhaskaran, K. Latham, S. Zhuiykov*, et al.*, "Sb_2Te_3 and Bi_2Te_3 based thermopower wave sources," *Energy & Environmental Science,* vol. 4, pp. 3558-3564, 2011.

[4] P. Fau, J. P. Bonino, and A. Rousset, "Electrical properties of sputterd MnO_2 thin films," *Applied Surface Science,* vol. 78, pp. 203-210, 1994.

[5] S. Walia, S. Balendhran, P. Yi, D. Yao, S. Zhuiykov, M. Pannirselvam*, et al.*, "MnO_2-Based Thermopower Wave Sources with Exceptionally Large Output Voltages," *The Journal of Physical Chemistry C,* 2013.

[6] F. F. Song, L. M. Wu, and S. Liang, "Giant Seebeck coefficient thermoelectric device of MnO_2 powder," *Nanotechnology,* vol. 23, 2012.

[7] S. H. Kim, S. J. Kim, and S. M. Oh, "Preparation of layered MnO_2 via thermal decomposition of $KMnO_4$ and its electrochemical characterizations," *Chemistry of Materials,* vol. 11, pp. 557-563, 1999.

[8] P. H. Klose, "Electrical properties of manganese dioxide and manganese sesquioxide," *Journal of the Electrochemical Society,* vol. 117, pp. 854-&, 1970.

[9] A. Ul Islam, R. Islam, and K. A. Khan, "Studies on the thermoelectric effect in semiconducting MnO_2 thin films," *Journal of Materials Science-Materials in Electronics,* vol. 16, pp. 203-207, 2005.

[10] G. J. Snyder and E. S. Toberer, "Complex thermoelectric materials," *Nature materials,* vol. 7, pp. 105-114, 2008.

[11] H. S. Bae, M. H. Yoon, J. H. Kim, and S. Im, "Photodetecting properties of ZnO-based thin-film transistors," *Applied Physics Letters,* vol. 83, pp. 5313-5315, 2003.

[12] D. P. Norton, Y. Heo, M. Ivill, K. Ip, S. Pearton, M. F. Chisholm*, et al.*, "ZnO: growth, doping & processing," *Materials today,* vol. 7, pp. 34-40, 2004.

[13] D. C. Look, "Recent advances in ZnO materials and devices," *Materials Science and Engineering: B,* vol. 80, pp. 383-387, 2001.

[14] X. Qu, W. Wang, S. Lv, and D. Jia, "Thermoelectric properties and electronic structure of Al-doped ZnO," *Solid State Communications,* vol. 151, pp. 332-336, 2011.

[15] X. Xi, L. Hong, and Z. H. Chen, "The study of semiconduction properties of gamma-MnO_2 with different degrees of reduction," *Journal of the Electrochemical Society,* vol. 136, pp. 266-271, 1989.

[16] Q. Y. He, Q. Hao, G. Chen, B. Poudel, X. W. Wang, D. Z. Wang, *et al.*, "Thermoelectric property studies on bulk TiO_x with x from 1 to 2," *Applied Physics Letters,* vol. 91, 2007.

[17] M. Hutchins, O. Abu-Alkhair, M. El-Nahass, and K. Abdel-Hady, "Electrical conduction mechanisms in thermally evaporated tungsten trioxide (WO_3) thin films," *Journal of Physics: Condensed Matter,* vol. 18, p. 9987, 2006.

[18] Y. Ren, P. G. Bruce, and Z. Ma, "Solid-solid conversion of ordered crystalline mesoporous metal oxides under reducing atmosphere," *Journal of Materials Chemistry,* vol. 21, pp. 9312-9318, 2011.

[19] A. C. McIntosh, R. O. Weber, and G. N. Mercer, "Non-adiabatic combustion waves for general Lewis numbers: Wave speed and extinction conditions," *Anziam Journal,* vol. 46, pp. 1-16, 2004.

[20] G. N. Mercer, R. O. Weber, and H. S. Sidhu, "An oscillatory route to extinction for solid fuel combustion waves due to heat losses," *Proceedings of the Royal Society of London Series a-Mathematical Physical and Engineering Sciences,* vol. 454, pp. 2015-2022, 1998.

[21] H. J. Goldsmid, "The thermal conductivity of bismuth telluride," *Proceedings of the Physical Society of London Section B,* vol. 69, pp. 203-209, 1956.

[22] P. Jood, R. J. Mehta, Y. L. Zhang, G. Peleckis, X. L. Wang, R. W. Siegel, *et al.*, "Al-Doped Zinc Oxide Nanocomposites with Enhanced Thermoelectric Properties," *Nano Letters,* vol. 11, pp. 4337-4342, 2011.

[23] K. H. Kim, S. H. Shim, K. B. Shim, K. Niihara, and J. Hojo, "Microstructural and thermoelectric characteristics of zinc oxide-based thermoelectric materials fabricated using a spark plasma sintering process," *Journal of the American Ceramic Society,* vol. 88, pp. 628-632, 2005.

[24] R. Lan, R. Endo, M. Kuwahara, Y. Kobayashi, and M. Susa, "Thermal Conductivity Measurements of Solid Sb_2Te_3 by Hot-Strip Method," *Japanese Journal of Applied Physics,* vol. 49, 2010.

[25] E. Preisler, "Semiconductor properties of manganese dioxide," *Journal of Applied Electrochemistry,* vol. 6, pp. 311-320, 1976.

[26] W. Wang, X. Yan, B. Poudel, Y. Ma, Q. Hao, J. Yang, *et al.*, "Chemical synthesis of anisotropic nanocrystalline Sb_2Te_3 and low thermal conductivity of the compacted dense bulk," *Journal of Nanoscience and Nanotechnology,* vol. 8, pp. 452-456, 2008.

Chapter 7

Conclusions and future works

7.1 Concluding remarks

The author's vision for this PhD involved developing thermopower wave sources to obtain output voltages, large enough for being employed in practical applications, while maintaining a high specific power. The author's vision was realised by developing thermopower wave sources in thin film geometries. The implementation of thermoelectric (TE) thin films for the propagation of thermopower waves turned out to be a crucial step as the author was able to employ a variety of core TE materials ranging from conventional TE materials such as Bi_2Te_3 and Sb_2Te_3 to TE transition metal oxide (TMOs) such as ZnO and MnO_2 to generate large magnitude voltages oscillatory, both oscillatory and non-oscillatory, while maintaining high specific powers.

In the course of conducting this research the author studied many reports on conventional TE materials such as Bi_2Te_3, Sb_2Te_3 and various TE TMOs. However, a comprehensive review on the TE properties of TMOs was lacking. As a result, the author prepared a comprehensive review article that provided the readers with a detailed description of TE properties of various TMOs in bulk and low dimensional morphologies as well as potential TE applications that they offer. Various tuning strategies to alter their TE properties via changes in morphology and stoichiometry were also discussed. The article highlighted the need to investigate many TMOs as viable TE materials, a research area where information is lacking. It was also noticed that prior to the author's research, only one thermopower wave system that was based on MWNTs had been reported (by Strano group at MIT). That system generated low voltages and oscillation amplitudes and it was obvious that the output voltages and oscillation amplitudes from thermopower wave sources needed to increase significantly to make it a viable technology. This highlighted the need for investigating other core TE

materials that exhibit high Seebeck coefficients, electrical conductivities and moderate thermal conductivities. It was also highlighted that thermopower wave propagation had not been demonstrated using p-type core materials which exhibit hole dominant electrical conduction. The review conducted by the author identified the potential of conventional TE materials such as Bi_2Te_3, Sb_2Te_3 and TE TMOs as possible candidates for being used as the core materials in thermopower wave sources due to their high TPFs. As such, the author's research was organised and conducted so as to target the identified research deficiencies.

In the first stage he demonstrated thermopower wave devices based on thin films of n-type Bi_2Te_3. Bi_2Te_3 was chosen due to its high S and σ. However, as its thermal conductivity was low, the author designed a viable system by depositing Bi_2Te_3 on the thermally conductive substrate of Al_2O_3 to compensate for this deficiency. This was the first demonstration of thermopower wave devices based on thin films. Subsequently, in the second stage the author developed thermopower wave devices based on p-type Sb_2Te_3 and n-type Bi_2Te_3 thin films to generate voltages with alternating polarities. This was the first demonstration of thermopower wave propagation using a p-type TE core material. In the third stage, the author for the first time implemented ZnO, a TE TMO as the core material in thermopower wave sources owing to its high TPF at elevated temperatures in which thermopower wave systems operate. The ZnO based thermopower wave system resulted in high voltage and oscillations amplitudes (>200%) compared to any previous thermopower wave system. Finally, in the fourth stage, prompted by the excellent results obtained by incorporating ZnO, the author implemented MnO_2, another TMO as the core TE material in thermopower wave sources to obtain significantly larger voltage (~1.8 V) and oscillations amplitudes than any previously developed thermopower wave system.

The major findings of each stage of this PhD research project are summarised as follows:

7.1.1 Stage 1

- In the first stage, the author demonstrated thermopower wave systems in a thin film geometry for the first time. n-type Bi_2Te_3 was incorporated as the core TE layer and exothermic chemical reactions from a solid fuel (nitrocellulose) were coupled to charge carriers of the Bi_2Te_3 layer to generate self-propagating thermopower waves. Bi_2Te_3 was used due to its high S and σ. However, the author compensated for its low κ by placing it on a thermally conductive substrate of Al_2O_3. Output voltages and oscillation amplitudes at least 150% higher than the previously reported MWNT based thermopower wave systems were achieved, while maintaining a high specific power of the order of 1 kW/kg.
- In addition to employing a thermally conductive substrate of Al_2O_3, the author also deposited Bi_2Te_3 on a substrate with extremely low thermal conductivity (terracotta). This was important in order to observe the effect of substrate thermal conductivity on the behaviour of thermopower waves and it was shown that a moderate to high thermal conductivity is an important requirement for generating oscillatory voltage signals of high magnitude.
- The author adapted the theory of combustion waves to theoretically analyse the fuel/Bi_2Te_3/Al_2O_3 and fuel/Bi_2Te_3/terracotta systems. Using a 1D approximation, the author estimated the thermopower wave propagation velocities and voltage oscillation frequencies. These estimations were also experimentally confirmed with an acceptable degree of accuracy.
- The author also examined the effect of the fuel mass and wave propagation velocities on the output voltage. It was observed that there was an optimal mass range of the fuel for which output voltages were maximised.
- The author employed the XRD technique to show that the Bi_2Te_3 films remained intact even after the thermopower wave propagation. This is an important observation as it can allow for developing reusable thermopower wave devices in the future.
- To the best of the author's knowledge, this was the first demonstration of thermopower

wave systems in a thin film geometry with highly oscillatory voltage signals and high specific power. The development of thin film thermopower wave systems is of utmost importance due to several advantages that thin films offer. Thin films allow the synthesis of different layers of varying TE properties that can be used for manipulating the propagation of the thermopower waves. Additionally, it allows for altering of the surface roughness which can be employed to increase the amount of solid fuel that can be placed over the TE layer. These advantages will certainly lead to the investigation of a wide variety and combination of TE cores for thermopower wave devices.

7.1.2 Stage 2

- In this stage the author developed thermopower wave devices based on a novel combination of two TE materials with complimentary semiconducting properties. The author employed p-type Sb_2Te_3 and n-type Bi_2Te_3 thin films as the TE cores. This unique combination of p and n-type materials with high S and σ resulted in output voltage signals with alternating polarities and higher magnitudes than MWNT based thermopower wave systems (at least 100 % higher in general). At the same time the devices generated a high specific power (0.6-1 kW/kg). Such oscillatory voltages along with high specific powers are highly desirable for practical applications.
- Thin films of the Sb_2Te_3 and Bi_2Te_3 were deposited on substrates with contrasting thermal conductivities (thermally conducting Al_2O_3 and thermally insulating terracotta) in order to assess the influence of the substrate thermal conductivity on the output voltages and the thermopower wave propagation velocities. It was observed that the substrate's thermal conductivity played a crucial role in the propagation of thermopower waves. Devices based on low thermal conductivity substrate of terracotta generated very low voltages with no oscillations.
- The author conducted a theoretical analysis of the Sb_2Te_3 and Bi_2Te_3 based thermopower wave devices to assess and predict the behaviour of thermopower waves. Using the theoretical model, the author was able to predict the oscillation frequencies

and thermopower wave propagation velocities with an acceptable accuracy.

- The author compared the performance of the thermopower wave sources based on the two p and n-type TE materials, and experimentally assessed the influence of thermal conductivity of the substrate and the core TE material on the propagation velocity and the output voltages. It was shown that the specific power obtained from Bi_2Te_3 based devices was higher, primarily due to the higher electrical conductivity of Bi_2Te_3. It was also shown that the difference in thermopower wave propagation velocities correspond to the difference in the thermal conductivities of the core TE materials, when deposited on identical substrates.
- Characterization techniques such as XRD were employed to assess the structure of the Sb_2Te_3 and Bi_2Te_3 films before and after the thermopower wave propagation. They showed that the films survived the reaction and remained largely intact.
- For the first time, the author showed that the phenomenon of thermopower waves was not just limited to n-type materials, but extended to p-type TE materials as well. This work is of utmost importance as it opens the opportunity of investigating other p-type materials, especially p-type TE TMOs as the core TE materials in thermopower wave sources. Additionally, this work shows that by using a combination of p and n-type materials also has the potential to generate ac voltage signals from such sources.

7.1.3 Stage 3

- In this stage, the author incorporated ZnO, a TE TMO, as the core material in thermopower wave devices for the first time. The author showed that the Seebeck coefficient and electrical conductivity of the ZnO thin films was enhanced in the temperature regimes in which thermopower wave systems operate, resulting in a high TPF. This made ZnO an outstanding choice as a core TE material in thermopower wave sources
- It was shown that ZnO based thermopower wave sources generated output voltages and oscillations at least 200% higher, while maintaining a high specific power (~0.5 kW/kg)

than any previously demonstrated thermopower wave system.

- Characterization techniques such as Raman spectroscopy and XRD were used to assess the structure of the ZnO film before and after thermopower wave propagation. It revealed that the ZnO films remained intact after the completion of the reaction.
- This was the first implementation of a TE TMO as the core material for thermopower wave sources. It also showed that TE TMOs were attractive candidates for thermopower wave sources due to their highly desirable properties (high S, σ and moderate κ). The success of this work formed the basis of further work conducted by the author by employing another TE TMO as described in stage 4.

7.1.4 Stage 4

- In this stage, the author implemented MnO_2 which is another TE TMO, as the core material in thermopower wave sources. The Seebeck coefficient and electrical conductivity of the MnO_2 thin films was assessed at elevated temperatures of up to 350 ºC. It was observed that both S and σ were dramatically enhanced at such elevated temperatures in which thermopower wave systems operate. The author also provided new fundamental insights into the observation of enhanced Seebeck coefficient with temperature. As expected, MnO_2 based thermopower wave systems generated voltages as high as 1.8 V, while maintaining high specific powers of the order of 1 kW/kg.
- Characterisation techniques such as SEM, BET and AFM were carried out to assess the surface roughness and porosity of the MnO_2 films. XRD was also carried out and revealed that the MnO_2 surface remained intact after the thermopower wave propagation.
- The Seebeck coefficient and electrical resistivity profiles were also obtained after the reaction to show that the MnO_2 films still retained their structure and properties after the reaction. Such behaviour is an important feature for the development of reusable thermopower wave devices in the future.
- The influence of thermal conductivity of the core TE material on the reaction

propagation velocities was assessed and a comparison with previously demonstrated thin film thermopower wave sources was conducted to prove that reaction propagation velocities are strongly influenced by the thermal conductivity of the core TE materials.

- This work is highly significant due to the generation of output voltages as high as 1.8 V, while maintaining a high specific power of the order of 1 kW/kg. Such voltages are enough to power small electronic circuits. It further highlighted the important role TMOs can play in making thermopower wave sources a viable energy generation technology in the future.

In conclusion, this research project has successfully brought new ideas and knowledge to the field of thermopower wave sources as well as the thermoelectric field in general. As such, the outcomes of this PhD research have been published in prestigious peer reviewed scientific journals. A complete list of publications by the author since the beginning of his PhD research project, are as follows:

7.2 Journal publications:

The work conducted by the author of this thesis during his PhD candidature has resulted in eight journal papers (five as the first author) in prestigious journals such as Advanced Functional Materials, Energy & Environmental Science, Chemical Communications, Journal of Physical Chemistry C and Advanced Materials. The list of author's scientific papers is presented below:

- **S. Walia**, R. Weber, K. Latham, P. Petersen, J. T. Abrahamson, M. S. Strano and K. Kalantar-zadeh, "Oscillatory Thermopower Waves Based on Bi_2Te_3 Films," *Advanced Functional Materials,* vol. 21, pp. 2072-2079, 2011.
- **S. Walia**, R. Weber, S. Sriram, M. Bhaskaran, K. Latham, S. Zhuiykov and K. Kalantar-zadeh, "Sb_2Te_3 and Bi_2Te_3 based thermopower wave sources," *Energy & Environmental Science,* vol. 4, pp. 3558-3564, 2011.

- **S. Walia**, R. Weber, S. Balendhran, D. Yao, J. T. Abrahamson, S. Zhuiykov, M. Bhaskaran, S. Sriram M. S. Strano and K. Kalantar-zadeh, "ZnO based thermopower wave sources," *Chemical Communications*, vol. 48, pp. 7462-7464, 2012.
- **S. Walia**, S. Balendhran, P. Yi, D. Yao, S. Zhuiykov, M. Pannirselvam, R. Weber, M. S. Strano, M. Bhaskaran, S. Sriram and K. Kalantar-zadeh, "MnO_2 based Thermopower Wave Sources with Exceptionally Large Output Voltages," *Journal of Physical Chemistry C*, 10.1021/jp401731b, 2013.
- **S. Walia**, S. Balendhran, H. Nili, S. Zhuiykov, G. Rosengarten, Q. H Wang, "Transition metal oxides-thermoelectric properties," *Progress in materials science*, Under review.
- S. Balendhran, J. Deng, J. Z. Ou, **S. Walia**, J. Scott, J. Tang, *et al*., "Enhanced Charge Carrier Mobility in Two-Dimensional High Dielectric Molybdenum Oxide," *Advanced Materials*, vol. 25, pp. 109-114, 2013.
- S. Balendhran, **S. Walia**, H. Nili, J. Z. Ou, S. Zhuiykov, R. B. Kaner, et al., "Two-Dimensional Molybdenum Trioxide and Dichalcogenides," *Advanced Functional Materials*, 10.1002/adfm.201300125, 2013.
- P. J. Gutruf, C. M. Shah, **S. Walia**, A. S. Zoolfakar, C. Karnutsch, K. Kalantar-zadeh, S. Sriram, and M. Bhaskaran, "Transparent functional oxide stretchable electronics: Micro-tectonics enabled high strain electrodes," *NPG Asia Materials,* Under review.

7.3 Conference publications:

In addition to the journal papers, the author of this thesis has had the opportunity to attend prestigious conferences such as the Materials Research Society meeting in San Francisco, USA and the International Conference on Nanoscience and Nanotechnology (ICONN) held in Perth, Australia to present the outcomes of his PhD research. Additionally, it resulted in the following publication in the proceedings of the ICONN conference:

- **S. Walia**, Sriram, M. Bhaskaran, S. Balendhran, S. Zhuiykov, and K. Kalantar-zadeh, "A combination of silicon and multi-walled carbon nanotubes with controllable thermoelectric parameters", in Brendan Griffin, Lorenzo Faraone, Mariusz Martyniuk (ed.) *Proceedings of the APMC 10 / ICONN 2012 / ACMM 22, Perth, Australia, 5-9 February 2012* 151, 2012.

7.4 Recommendations for future works

Significant strides have been made in the development of thermopower waves' based energy sources as part of this PhD project, however the author feels that there still exists numerous opportunities for continuing research in alignment with those presented in this thesis, and recommends the following as future work:

- The evolution of thin film thermopower wave devices allow for investigation of more TE core materials, especially TMOs. The high TPFs of many TMOs at elevated temperatures makes them attractive materials for thermopower wave sources. Modification strategies based on reducing dimensions of TE TMOs have already resulted in enhanced TPFs through engineering of their density of states. Enhanced TPFs can certainly be achieved by nanostructuring, substructuring, compositing, doping and changing the stoichiometry of TMOs. Considering that significant enhancements in TPF can be obtained in TMOs, the author of this thesis suggests that achieving output voltages as high as 10 V in thermopower wave sources based on TMOs is possible.
- Another future prospect for the development of viable thermopower wave systems would be the integration of liquid and gaseous fuels. As the thin films of the TE cores easily survive the thermopower wave propagation, the use of liquid and gaseous fuels will provide the opportunity to develop reusable/re-fuellable thermopower wave systems. Additionally, it will also provide the opportunity of using many highly intense fuels in gas and liquid phases, which can result in larger temperature gradients, producing higher output voltages.

- The physics of thermopower waves still needs to be fully understood. In this context, the development of a 3D theoretical model for thermopower wave systems is certainly an important proposition for future work. Such a model will allow researchers to accurately assess the influence of every parameter of the fuel, core TE material and the substrate on the behaviour of thermopower waves. This knowledge has the potential for the development of thermopower wave sources in which the frequency of the output voltage oscillations can be controlled.
- The efficiency of thermopower wave systems is still very low. This is mainly because a large portion of the heat generated from the exothermic chemical reaction of the fuel is dissipated to the ambient surroundings. Methods to minimise this heat dissipation need to be explored to increase the efficiency of thermopower wave systems.